Many-body cavity QED

The Dicke model, phase transitions, and engineering of multipartite entangled atomic states

Stuart J. Masson

A thesis submitted in fulfilment of the requirements for the degree
of Doctor of Philosophy in Physics, the University of Auckland, 2019.

Abstract

The interaction of matter with an electromagnetic field is an old problem. We performed theoretical modelling for experiments simulating a fundamental model of this interaction: the Dicke model. We then made use of this model, and the methods used to simulate it, to propose the production of a variety of entangled many-body states of an atomic ensemble.

Our research focussed on engineering interactions between a gas of cold atoms and light, in particular laser fields and modes of an optical cavity. These interactions are engineered via cavity-assisted Raman transitions: two-photon transitions where one photon is provided by a laser field and the other is associated to a mode of an optical cavity. Two types of interactions were considered: between the cavity mode and the gas, and within the gas *via* the cavity mode.

Results of our research included contributions to the experiments of our collaborators, who mapped out phase boundaries of the Dicke model, giving a fundamental insight into how atoms interact with a field. Using these methods in the context of a generalised Dicke model with an added non-linear coupling, we discovered the presence of strong entanglement for atoms *in steady state* and proposed how to access such entanglement.

A key concept of the thesis is the introduction of spinor atoms - i.e. atoms with integer spin - to many-body cavity QED. We showed that the Dicke model, and more simply a Tavis-Cummings model, acting on a particular state of spin-1 atoms produces highly entangled states heralded by measurement of the cavity output. In the context of interactions within the gas, we proposed the emulation and extension of physics currently accessible only to spinor Bose-Einstein condensates. We then proposed the use of those engineered interactions to emulate a particular experiment performed in spinor Bose-Einstein condensates, creating a novel type of squeezing and entanglement in a spinor gas.

Our research has not only helped explain how light and matter interact and given specific methods to produce interesting many-body states using those interactions, but it also implies a rich field of novel results for spinor atoms in many-body cavity QED systems.

Acknowledgements

I landed in Auckland four years ago, almost to the day, “ready” to start my PhD. Nervous, excited, enthusiastic to get started. Four years ago, it seems… well, it seems that much has been written about the passing of time by much more eloquent scholars than me, so I think I will avoid making any clichéd comments on the topic. Instead, I will simply say that it has been a time of my life that I will always look back on fondly, and never want to repeat. I reserve the rest of the self-indulgence for thanking the various people who have helped me get to this point, four years later, as I put the final touches on my thesis.

First of all, I should thank Scott Parkins for his supervision and support throughout my PhD. On arrival, naïve and optimistic, I had not really considered the importance of the relationship between student and supervisor. I don’t think I truly grasped what Scott was going to be expecting of me nor what I should expect from Scott. Looking back I realise that my choice of supervisor was, of course, extraordinarily important for my development. I am obviously pretty lucky, since I cannot conceive of a supervisor better suited to me, though I suppose I do not have any other first hand experience… At all times, I have been treated with respect, listened to and allowed to function as independently as I wanted. I have felt as if I were a real scientist, for which I will be forever grateful.

I also wish to thank Murray Barrett and his group at the Centre for Quantum Technologies. I have often been heard to say that experiments are my favourite part of physics, and, just as frequently, that doing experiments does not suit my particular set of skills. To be able to work alongside experiments and feel part of the work without actually having to try and work out what goes where has been a great pleasure. Thank you also for the funding help for my visits to Singapore.

I would like to acknowledge the role of the quantum optics group both in Auckland and as part of the Dodd-Walls Centre. The history of quantum optics in New Zealand is, of course, a proud and illustrious one. To have been able to forge my own small part of that history, surrounded by those whose contributions ring so loudly, has been an honour.

I should more personally thank the rest of the Auckland quantum optics PhD students with whom I have shared this experience. Workplace acquaintances doesn't even begin to cover it…Thank you Ricardo, Victor and Niki. Thank you for your kindness, wisdom and countless conversations on research, quantum optics and, on extremely rare occasion, somewhat more frivolous matters.

To list all the friends I have made in Auckland seems like an egregious boast, and not wanting to draw a line that excludes people who will never read this anyway, I will instead just thank my friends generically. From my first invite to Friday drinks to the, presumably, civilised lunch beers that will follow the submission of this thesis, I have always felt welcome and at home here. Thanks.

I should also acknowledge the role of my family. Thanks to Mum and Dad. Without your assistance I would never have been able to leave the UK; who knew a visa medical cost that much… More importantly, your advice has always been cherished, if not always solicited, and, most importantly, your unwavering support of my best interests, in the face of a relocation that was probably not in yours, has been a constant inspiration and a testament to a strength I have always admired. Thank you to Anna, for your unequivocal caring and love, and for braving the long flight and sharing a holiday with us that has left me with some of my favourite memories of this country. Thank you to Katherine, and to Bethany and Dominic. Having to watch and hear from afar as your young family grows has been one of the hardest parts of being so far from home. Thank you for the frequent cute pictures, silly videos, and stories that remind me of what is really important when I am stressed about nonsense.

Most importantly, I should thank Emily. I think I probably could still have finished a different PhD with a different supervisor in a different place surrounded by different people and different friends, but there is no chance I would have managed with a different you. Helping me check near 250 pages of highly technical text and equations on a topic you have absolutely no interest in has exemplified exactly why I love you. I love you for your patience. I love you for your loyalty. I love you for your selflessness. I hope you know how much I appreciate your support and your company. Thanks pal.

All I do, is sit down at the typewriter, and start hittin' the keys. Getting them in the right order, that's the trick.

That's the trick.

Garth Marenghi

Horror writer, dreamweaver, visionary, plus actor.

Contents

List of figures

List of publications

Included in the thesis

Masson, S. J., Barrett, M. D., & Parkins, S.
Cavity QED engineering of spin dynamics and squeezing in a spinor gas
Physical Review Letters **119**, 213601 (2017)

Masson, S. J. & Parkins, S.
Preparing the spin-singlet state of a spinor gas in an optical cavity
Physical Review A **99**, 013819 (2019)

Masson, S. J. & Parkins, S.
Extreme spin squeezing in the steady state of a generalized Dicke model
Physical Review A **99**, 023822 (2019)

Masson, S. J., & Parkins, S.
Rapid production of many-body entanglement in spin-1 atoms via cavity output photon counting
Physical Review Letters **122**, 103601 (2019)

Other publications

Zhang, Z. *et al*
Nonequilibrium phase transition in a spin-1 Dicke model
Optica **4**, 4 (2017)

Zhang, Z. *et al*
Dicke-model simulation via cavity-assisted Raman transitions
Physical Review A **97**, 043858 (2018)

THE UNIVERSITY OF AUCKLAND
Te Whare Wānanga o Tāmaki Makaurau
NEW ZEALAND

School of Graduate Studies
AskAuckland Central
Alfred Nathan House
The University of Auckland
Tel: +64 9 373 7599 ext 81321
Email: postgradinfo@auckland.ac.nz

Co-Authorship Form

This form is to accompany the submission of any PhD that contains published or unpublished co-authored work. **Please include one copy of this form for each co-authored work**. Completed forms should be included in all copies of your thesis submitted for examination and library deposit (including digital deposit), following your thesis Acknowledgements. Co-authored works may be included in a thesis if the candidate has written all or the majority of the text and had their contribution confirmed by all co-authors as not less than 65%.

Please indicate the chapter/section/pages of this thesis that are extracted from a co-authored work and give the title and publication details or details of submission of the co-authored work.

Chapter 10. Cavity QED Engineering of Spin Dynamics and Squeezing in a Spinor Gas. Phys Rev Lett. 2017 Nov;119:213601.

Nature of contribution by PhD candidate	Calculated model. Developed idea for the squeezing. Performed simulations. Interpreted the data. Made figures and wrote the letter.
Extent of contribution by PhD candidate (%)	75

CO-AUTHORS

Name	Nature of Contribution
Murray Barrett	Developed the idea for the model. Assisted with writing of the letter.
Scott Parkins	Developed the idea for the model and for the squeezing. Supervised calculation of model and interpretation of data. Assisted with writing of the letter.

Certification by Co-Authors

The undersigned hereby certify that:

- the above statement correctly reflects the nature and extent of the PhD candidate's contribution to this work, and the nature of the contribution of each of the co-authors; and
- that the candidate wrote all or the majority of the text.

Name	Signature	Date
Scott Parkins	A S Parkins	11 October 2018
Murray Barrett	M D Barrett	11 October 2018

Last updated: 28 November 2017

THE UNIVERSITY OF
AUCKLAND
Te Whare Wānanga o Tāmaki Makaurau
NEW ZEALAND

School of Graduate Studies
AskAuckland Central
Alfred Nathan House
The University of Auckland
Tel: +64 9 373 7599 ext 81321
Email: postgradinfo@auckland.ac.nz

Co-Authorship Form

This form is to accompany the submission of any PhD that contains published or unpublished co-authored work. **Please include one copy of this form for each co-authored work**. Completed forms should be included in all copies of your thesis submitted for examination and library deposit (including digital deposit), following your thesis Acknowledgements. Co-authored works may be included in a thesis if the candidate has written all or the majority of the text and had their contribution confirmed by all co-authors as not less than 65%.

Please indicate the chapter/section/pages of this thesis that are extracted from a co-authored work and give the title and publication details or details of submission of the co-authored work.

Chapter 8. Rapid production of many-body entanglement in spin-1 atoms via cavity output photon counting. Submitted to Physical Review Letters, available at arXiv:1810.00524

Nature of contribution by PhD candidate	Developed the idea. Performed simulations. Interpreted the data. Made figures and wrote the letter.
Extent of contribution by PhD candidate (%)	80

CO-AUTHORS

Name	Nature of Contribution
Scott Parkins	Supervised development of idea and interpretation of data. Assisted with writing of the letter.

Certification by Co-Authors

The undersigned hereby certify that:

- ❖ the above statement correctly reflects the nature and extent of the PhD candidate's contribution to this work, and the nature of the contribution of each of the co-authors; and
- ❖ that the candidate wrote all or the majority of the text.

Name	Signature	Date
Scott Parkins	A S Parkins	11 October 2018

Last updated: 28 November 2017

School of Graduate Studies
AskAuckland Central
Alfred Nathan House
The University of Auckland
Tel: +64 9 373 7599 ext 81321
Email: postgradinfo@auckland.ac.nz

Co-Authorship Form

This form is to accompany the submission of any PhD that contains published or unpublished co-authored work. **Please include one copy of this form for each co-authored work**. Completed forms should be included in all copies of your thesis submitted for examination and library deposit (including digital deposit), following your thesis Acknowledgements. Co-authored works may be included in a thesis if the candidate has written all or the majority of the text and had their contribution confirmed by all co-authors as not less than 65%.

Please indicate the chapter/section/pages of this thesis that are extracted from a co-authored work and give the title and publication details or details of submission of the co-authored work.

Chapter 11. Preparing the spin singlet state of a spinor gas in an optical cavity. Submitted to Physical Review A, available at arXiv:1810.08353

Nature of contribution by PhD candidate	Developed the idea. Performed simulations. Interpreted the data. Made figures and wrote the paper.
Extent of contribution by PhD candidate (%)	80

CO-AUTHORS

Name	Nature of Contribution
Scott Parkins	Supervised development of idea and interpretation of data. Assisted with writing of the paper.

Certification by Co-Authors

The undersigned hereby certify that:

- the above statement correctly reflects the nature and extent of the PhD candidate’s contribution to this work, and the nature of the contribution of each of the co-authors; and
- that the candidate wrote all or the majority of the text.

Name	Signature	Date
Scott Parkins	A S Parkins	29 October 2018

School of Graduate Studies
AskAuckland Central
Alfred Nathan House
The University of Auckland
Tel: +64 9 373 7599 ext 81321
Email: postgradinfo@auckland.ac.nz

Co-Authorship Form

This form is to accompany the submission of any PhD that contains published or unpublished co-authored work. **Please include one copy of this form for each co-authored work**. Completed forms should be included in all copies of your thesis submitted for examination and library deposit (including digital deposit), following your thesis Acknowledgements. Co-authored works may be included in a thesis if the candidate has written all or the majority of the text and had their contribution confirmed by all co-authors as not less than 65%.

Please indicate the chapter/section/pages of this thesis that are extracted from a co-authored work and give the title and publication details or details of submission of the co-authored work.

Chapter 6. Extreme spin squeezing in the steady state of a generalized Dicke model. Submitted to Physical Review A, available at arXiv:1810.11176

Nature of contribution by PhD candidate	Developed the idea. Performed simulations. Interpreted the data. Made figures and wrote the paper.
Extent of contribution by PhD candidate (%)	80

CO-AUTHORS

Name	Nature of Contribution
Scott Parkins	Supervised development of idea and interpretation of data. Assisted with writing of the paper.

Certification by Co-Authors

The undersigned hereby certify that:

- the above statement correctly reflects the nature and extent of the PhD candidate's contribution to this work, and the nature of the contribution of each of the co-authors; and
- that the candidate wrote all or the majority of the text.

Name	Signature	Date
Scott Parkins	A S Parkins	29 October 2018

Last updated: 28 November 2017

Glossary of terms

This is a list of technical terms frequently used in this thesis. The list is not intended to be exhaustive. Where relevant, links to useful parts of the text are included.

Adiabatic elimination	Tracing over part of a system which has time evolution on a much different scale to the rest of the system.
Adiabatic transformation	Manipulating the ground state of a system by varying Hamiltonian parameters slowly enough that the system wavefunction adapts to the new Hamiltonian and remains in the ground state.
Annihilation operator	An operator that removes one excitation from a bosonic field, see Section 2.2.2.
Bloch sphere	Visual representation that maps the state of a two-level system to a sphere, see Section 3.4.1. For a collective spin of fixed length, the atomic Q-function on the collective Bloch sphere can be used, see Section 3.4.5.
Bose-Einstein condensate	A state of matter where the atoms belong to the same macroscopic state, see Section 3.3.3.
Cavity	A device that confines light into a small volume, most typically with mirrors, see Section 4.1.
Cavity mode	Resolved mode of the electromagnetic field with a particular frequency and polarisation that can exist within a cavity, see Section 4.1.1.
Clebsch-Gordan coefficients	Numbers that describe angular momentum couplings, relevant to this thesis as the relative strength of angular momentum transitions.
Coherent states	States of a bosonic field formed by the displacement of the vacuum, see Section 2.2.3.
Coherent spin states	States of a collective spin analogous to coherent states, see Section 3.4.5.
Creation operator	An operator that adds one excitation to a bosonic field, see Section 2.2.2.

Dark state	An eigenstate of the Hamiltonian that is decoupled from dissipation, see Section 2.3.2.
Degeneracy	When more than one eigenstate of an operator has the same eigenvalue.
Detuning	Difference in frequency between an atomic transition and an electromagnetic field mode.
Dicke model	A fundamental model of the interaction of a single mode of the electromagnetic field with an ensemble of two-level systems, see Section 4.4.
Dicke states	Collective states of an atomic ensemble with a definite total angular momentum and magnetic projection, see Section 3.4.3.
Dipole trap	Trap that uses the dipole force to attract atoms to points of maximum intensity, see Section 3.3.2.
Doppler shift	Shift in frequency observed by a moving system due to the expansion or compression of the observed oscillations.
Dressed states	A composite picture where excitations are shared between field and atoms, see Section 4.2.
Entanglement	Phenomenon where the wavefunction of two systems needs to be described compositely such that measurements of the two systems have quantum correlations between them, see Section 2.1.1.
Entanglement depth	Number of atoms in the largest set where all atoms in the set are entangled to all other atoms.
Environment	Everything the considered quantum system interacts with that is not part of the system, see Section 2.3.1.
Fock states	States of a bosonic field with an exact number of excitations, see Section 2.2.2.
Heisenberg limit	The fundamental limit to precision for an atomic ensemble allowing for entanglement, see Section 3.4.6.
Heralding	A protocol that is deemed successful by a particular measurement of the output.
Hyperfine level	A level with particular angular momentum summed over the angular momentum and spin of the electron and the spin of the nucleus, see Section 3.1.3.
Jaynes-Cummings model	A fundamental model for the interaction of a single mode of the electromagnetic field with a single two-level system, see Section 4.2.
Jump operator	Operator that acts on the system as part of the interaction with the environment, see Sections 2.3.1 and 2.3.2.

Ladder operator	Operators that move the magnetic projection of a spin up or down by one quanta, see Section 3.4.4.
Light shift	Shift to an energy level of an atom caused by the presence of a light field, see Section 3.1.4.
Markovianity	Property of an environment such that any information sent there is lost, see Section 2.3.1.
Master equation	Describes the evolution of a system in the presence of unmonitored losses to an environment, see Section 2.3.1.
Multipartite entanglement	Entanglement between a set of more than two particles. Genuine multipartite entanglement is where any pair of atoms in that set are entangled.
Nematic tensor	A higher order operator that describes properties of a spin-1 atom, see Section 3.4.2.
Number operator	An operator that counts the number of excitations in a bosonic field, see Section 2.2.2.
Optical lattice	A pattern of dipole traps that forms a periodic lattice for the atoms, see Section 3.3.2.
Phase sensitivity	Precision available to a state for the estimation of a phase imprinted on that state.
Q-function	A visual representation of a bosonic field state formed by mapping out the overlap with the coherent states, see Section 2.2.3.
Quantum Fisher information	A measure of the phase sensitivity available to a system, see Section 8.1.1.
Quantum metrology	The use of quantum correlated states to perform precision measurements.
Quantum trajectory	Describes the stochastic evolution of a system in the presence of monitored losses, see Section 2.3.2.
Quench	Instantaneous change of a Hamiltonian parameter that takes the system across a phase transition.
Rabi frequency	The frequency of oscillations driven between the levels of a two-level system, see Section 3.2.1.
Rabi oscillations	Oscillations, driven by a light field, between the levels of a two-level system, see Section 3.2.1.
Raman transitions	Two-photon transitions that move an atom between two states via some intermediary state, see Section 3.2.4.
Resonant	Matched frequencies of an atomic transition and an electromagnetic field mode.
Schrödinger equation	Describes the evolution of a system in the absence of losses, see Section 2.1.4.

Self-organisation	Process by which atoms in a cavity move to a particular pattern, for example, to optimise scattering into the cavity, see Section 4.4.3.
Shelved state	A state which is not strongly coupled to the active levels of the system such that the atom stays there.
Single-mode approximation	Where the spin states of a spinor Bose-Einstein condensate have the same spatial wavefunction such that it can be integrated out, see Section 9.1.2.
Spin	Intrinsic angular momentum of fundamental particles, see Section 3.1.2.
Spinor physics	Study of atoms with integer spin, see Section 3.4.2.
Spin singlet	Collective state of an ensemble of atoms with zero collective angular momentum, see Section 11.1.1.
Spin squeezing	Redistribution of noise from one angular momentum component of a collective spin to another such that the former features quantum correlations and entanglement, see Section 3.4.6.
Spontaneous emission	Process by which a system transitions from an excited state to a lower energy state by emission of a photon, see Section 3.2.2.
Squeezing	Redistribution of noise from one variable to another non-commuting variable such that the former features quantum correlations, see Section 2.2.4.
Standard quantum limit	The limit to precision for an atomic ensemble without accounting for quantum correlations, see Section 3.4.6.
Superoperator	A generalised function that performs a set of operations on a state.
Superradiance	Collective enhancement of emission into a shared field, see Sections 4.3 and 4.4.
Tavis-Cummings model	A fundamental model for the interaction of a single mode of the electromagnetic field with an ensemble of two-level systems under the rotating wave approximation, see Section 4.3.
Thermal states	States of a bosonic field at equilibrium at a non-zero temperature, see Section 2.2.5.
Thermodynamic limit	Where the number of atoms is taken to be so large as to be able to ignore quantum fluctuations, strictly only true with infinite atom number.
Zeeman shift	Shift of the atomic energy level caused by the presence of a magnetic field, see Section 3.1.4.

Glossary of abbrevations

This is a list of abbreviations used in this thesis. The list is not intended to be exhausted.

BEC	Bose-Einstein condensate
CQT	Centre for Quantum Technologies
CSS	Coherent spin state
MOT	Magneto-optical trap
QED	Quantum electrodynamics
QFI	Quantum Fisher information
SPCM	Single-photon counting module
SQL	Standard quantum limit
TC	Tavis-Cummings

Glossary of symbols

This is a list of symbols commonly used in this thesis. The list is not intended to be exhaustive. Every effort has been made not to use symbols for more than one purpose; where that is not possible both definitions are listed here and it should be clear from context which definition is relevant.

$\hat{a}, \hat{a}^\dagger$	Annihilation and creation operator for a photon
$\mathbf{B}$	Magnetic field vector
$\hat{b}_m, \hat{b}_m^\dagger$	Annihilation and creation operator for atoms with magnetic quantum number m
c	Speed of light, 2.9979×10^8 m/s
$\mathcal{D}$	Dissipative superoperator
$D_{1,2}$	Transition lines
E	Energy
$\mathbf{E}$	Electric field vector
e	Elementary charge, $e = 1.6022 \times 10^{-19}$C
F	Total angular momentum quantum number
$\mathcal{F}$	Quantum Fisher information
$\mathfrak{F}$	Cavity finesse
$\hat{G}$	Generator over which the Quantum Fisher information is calculated
g	Single atom-cavity coupling
$g^{(2)}(\tau)$	Second-order correlation function
$\hat{H}$	Hamiltonian operator
$\mathcal{H}$	Hilbert space
h	Planck constant, $h = 6.6261 \times 10^{-34}$Js
$\hbar$	Reduced Planck constant, $\hbar = h/2\pi = 1.0546 \times 10^{-34}$ Js/rad
I	Nuclear spin quantum number
J	Electron angular momentum quantum number
$\hat{J}$	Jump operator
$\mathbf{k}$	Wavevector
k_B	Boltzmann constant, $k_B = 1.3806 \times 10^{-23}$J/K
$\mathcal{L}$	Liouvillian superoperator

l	Angular momentum quantum number
M	Mass of a single atom
m	Magnetic quantum number
m_e	Mass of the electron, 9.1094×10^{-31}kg
m_F	Total magnetic quantum number
N	Number of atoms
n	Principal quantum number
n	Number of quanta in a bosonic field
$\bar{n}$	Average occupation of a thermal bosonic field
$\hat{n}$	Number operator for a bosonic field
$\lvert n\rangle$	Fock state of n bosons
$\hat{\mathcal{O}}$	Generic operator
$\langle\hat{\mathcal{O}}\rangle$	Expectation value of an operator
$(\Delta\hat{\mathcal{O}})^2$	Variance of the expectation value of an operator
$\hat{P}_{\lvert\phi\rangle}$	Projector operator for a state $\lvert\phi\rangle$
$\hat{Q}, \hat{Q}'$	Sums of transition terms necessary for adiabatic elimination of the excited states in a detuned Raman transition scheme
$\hat{\mathbf{Q}}$	Nematic tensor for an ensemble
$\hat{Q}_{ij}$	Element of the nematic tensor for an ensemble
q	Quadratic Zeeman shift
$\hat{\mathbf{q}}$	Nematic tensor for a single atom
$\hat{q}_{ij}$	Element of the nematic tensor for a single atom
$\mathbf{r}$	Position, $r = (x, y, z)$ or $r = (r, \theta, \varphi)$ depending on chosen coordinates
S	Collective angular momentum quantum number
$\hat{\mathbf{S}}$	Collective spin operator
$\hat{S}_{x,y,z}$	Collective spin operator on the x, y, z-axis
$\hat{S}_\pm$	Collective ladder operator
$\lvert S, m\rangle$	Dicke state with angular momentum S and magnetic projection m
s	Spin quantum number
T	Temperature
t	Time
$\mathrm{tr}(\cdot)$	Trace
U	Cavity-driven light shift in the effective Dicke model
$\hat{V}$	Potential operator
$\bar{v}$	Route mean-square velocity of a Maxwell-Boltzmann distribution
$\lvert\alpha\rangle$	Coherent state with eigenvalue α for the annihilation operator
Γ	Cavity-mediated decay rate on the collective spin operator after adiabatic elimination of the cavity mode
γ	Spontaneous emission rate
Δ	Detuning between a light field and an atomic transition

δ_{ij}	Kronecker delta function, zero for $i \neq j$ and one for $i = j$
ε_0	Permittivity of free space, 8.8542×10^{-12}F/m
η	Quantum efficiency of a single-photon detector
$\|\eta\rangle$	Coherent spin state centred on spherical coordinates (θ, φ)
κ	Half width of the cavity
Λ	Effective interaction strength for spinor models after adiabatic elimination of the cavity mode
λ	Wavelength
λ	Collective coupling of an ensemble of atoms to a cavity mode, $\lambda = \sqrt{N}g$
λ_c	Critical coupling in the Dicke model above which superradiance exists
λ_-, λ_+	Collective coupling for the rotating and counter-rotating terms of the Dicke model respectively
μ_0	Permeability of free space, $4\pi \times 10^{-7}$H/m
ξ_D	Dicke squeezing parameter
ξ_R^2	Spin squeezing parameter for Ramsey interferometry
ξ_S^2	Spin squeezing parameter
ξ_x^2	Spin-nematic squeezing parameter
ρ	Density matrix of the system
$\hat{\sigma}_{x,y,z}$	Spin operator on the x, y, z-axis for a single atom
$\hat{\sigma}_\pm$	Ladder operators for single spins
$\|\psi\rangle$	Wavefunction of the system
$\|\psi_{\mathrm{REC}}\rangle$	Wavefunction of the system conditioned on a particular scattering record
Ω	Rabi frequency
ω	Frequency of an electromagnetic field
ω_z	Linear Zeeman shift
ω_0	Frequency difference of a two-level system
ζ	Frequency difference between the $F = 1$ and $F = 2$ lines
$\|-1\rangle$	Lowest magnetic state of a spin-1 atom
$\|0\rangle$	Ground state of a two-level system or central magnetic state of a spin-1 atom
$\|1\rangle$	Excited state of a two-level system or highest magnetic state of a spin-1 atom
$\mathbb{1}$	Identity matrix

Chapter 1

Introduction

Over the last few decades, progress in experimental atomic and quantum optical physics has gone from groundbreaking proof of principle experiments to a point where precisely manipulating and measuring such systems can be performed on an almost routine basis. As recently as the early 1990s, there was discussion as to whether Bose-Einstein condensates could even exist, yet now they can be created for a wide variety of atomic species and controlled with exquisite precision. Similarly, the ability to strongly couple atoms to single modes of the electromagnetic field was a tremendous breakthrough only a few decades ago. Now we can build such systems, not only with atoms between mirrors as in those first experiments, but in a variety of equivalent setups. They can be built making use of extremely thin optical fibres or tiny donut shaped resonators where the atoms are trapped in, and coupled to, an evanescent field. Even more exotic architectures can be used, such as superconducting circuits and tiny dots of semiconductor material where the "atoms" are actually quantised elements of a macroscopic system.

These advances allow us to test fundamental aspects of quantum mechanics. We know now that the properties of two particles, even if separated by huge distances, can be correlated in ways that make no sense in terms of a 19th century understanding of physics. We know that a single particle can create interference patterns with itself. We know that two particles can arrive at two inputs to a beamsplitter and exit through the same output *every single time*. It was these fascinating, and, quite frankly, *weird* phenomena that first piqued my interest in quantum physics.

Modern techniques have now brought us to a point where we can not only test the correctness of quantum mechanics, we can *harness* quantum mechanics. We store, transfer and manipulate bits of information held in quantum states. We make chains of trapped ions answer maths questions. We measure time with an error of a fraction of a second in the *age of the universe*. We have made Schrödinger's infamous cats, though obviously not with actual cats. A focus on the *cool stuff* belies the fact that quantum physics underlies huge swathes of technology used around the world every single day. Computers, phones, GPS, internet traffic, DVD players, MRI machines, and even those low-wattage environmentally friendly light bulbs that save the planet and your wallet at the same time. All those things could not have been invented without our understanding of quantum physics. A century ago, quantum mechanics was just an interesting mathematical theory, but now, without our understanding of it, my thesis would have been written on a typewriter and, let's face it, would be a lot less interesting.

As our experimental prowess advances, the quest for new understanding and new technologies advances with it. This thesis deals with my contributions to both aspects. These contributions include theoretical modelling of experiments performed at the Centre for Quantum Technologies in Singapore of the simulation of a classic model for the interaction of light and matter, first discussed in 1954 but only recently realised. I also propose methods to engineer other models, some of which can be used to produce exotic quantum states useful for precision measurements.

In theory, if read (thoroughly) from front to back, the thesis *should* be accessible to anyone with a basic knowledge of physics. However, practical concerns mean that this may not be quite as simple as intended. In particular, the introduction to many key concepts is somewhat brief and so a rudimentary understanding of quantum mechanics and atomic physics is probably very useful if not essential. A reasonable understanding of certain aspects of classical physics, in particular classical optics and electromagnetism, is assumed. It is necessary, given the nature of the thesis, for there to be significant mathematical content. Long derivations are presented more in the vein of transparency to the methods than as essential content. For those with less interest or knowledge in the mathematical side of the work, a physical intuition of the equations is given where it is deemed necessary.

Chapters 2, 3 and 4 act as an introduction, providing the background material needed to understand the rest of the text. Chapter 2 introduces the key aspects of quantum mechanics and quantum optics, and the mathematical frameworks used both in the rest of the text and to perform the majority of the computational work. Chapter 3 is an introduction to atomic physics. This includes the electronic level structure of atoms and how those atoms interact with light. I then introduce the basics of how to prepare cold atoms for experiments, as well as the mathematical structures used to describe those atoms theoretically. In Chapter 4, I introduce the field of cavity quantum electrodynamics. I will show how the building blocks of alkali atoms and optical cavities can be used to build the types of experiments discussed throughout the rest of the thesis, as well as simple models for its behaviour that will also be of relevance later.

Chapters 5 and 7 describe the experiments performed at the Centre for Quantum Technologies and my contributions to that work. This includes a brief explanation of those experiments and the results, and a more in-depth discussion of my theoretical modelling of both systems. Chapter 7 is an introduction to perhaps the most important and fundamental development of the PhD: the combination of many-body spinor physics and cavity QED systems. Chapter 9 moves to a limit where the cavity mode itself becomes a tool by which to engineer interactions between the particles and so create "pure" spinor systems.

Chapters 6, 8, 10 and 11 describe proposals for experiments, all of which are presented as papers published during the course of the PhD. These have been reformatted to fit with the aesthetic of the thesis and in some cases have had minor edits such as the insertion of supplemental material into the main text or alterations to notation so as to be consistent with other sections of the thesis. All such changes are noted in the introductions to those Chapters.

In Chapter 12, I discuss how this project might be extended. This includes discussion of speculative ideas on the range of physics accessible with the methods developed in the thesis, as well as more specific ideas that arose during the PhD and are currently being further explored.

This introduction, in its frequent use of technical terms that are yet to be introduced, may immediately undermine the intention for the thesis to be accessible from front to back. However, I hope that it gives some sense of why this field is so exciting and the broad motivation behind my work. I hope it gives an idea of the value of my work and perhaps even the motivation to read the thesis. I hope those who do read it come away with at least a grasp on how these ideas are of interest to the scientific community. At the very least, I hope any reader can come back and understand those technical terms...

Chapter 2

Quantum mechanics & quantum optics

Quantum physics is inherently based on the concept of quantisation: the idea that the measurement of *things* results in discrete quantities. These *things* might be a particle's energy, its angular momentum or the projection of that angular momentum on some spatial axis. Upon measurement, the particle can only exist with those discrete properties. In between, the particle can exist in one of those states or in some *superposition* of them. It is this fundamental principle, which dates back to Boltzmann, Planck and Einstein, that underlies much of quantum mechanics. In this Chapter I dissect the key postulates of quantum mechanics, as well as introducing the mathematical framework necessary to understand them. I discuss how to describe the quantum state of a particle or system, how that state can feature superpositions and entanglement, how to define variables, and how to describe measurement. I then quantise the electromagnetic field, discuss useful states associated with that photon picture and introduce how to evolve states in quantum optics.

2.1 Postulates of quantum mechanics

Quantum mechanics relies on certain *postulates* upon which our understanding is based. Here I introduce those postulates, how I will represent them mathematically and their important implications with respect to this thesis.

2.1.1 States

Associated to any system is a wavefunction that describes all information that can be known about the system.

The global wavefunction of a system describes *every* aspect of the system. However, in general, there will be some aspects of the system that we are interested in, and others which are neither relevant nor coupled to those interesting aspects. The wavefunction, $|\psi\rangle^1$, will thus describe the *relevant* aspects of the system. The wavefunction of a system lives in a *Hilbert space*, defined as the space that contains all possible wavefunctions.

Wavefunctions evolve over time and take different forms over the course of that evolution. We can denote, for example, a set of possibilities for the state as $\{\ |\ \phi_i\rangle\ \}$. If any possible wavefunction for the system can be expressed using the members of that set then the set is *complete*. If the set is such that $\langle\phi_i|\phi_j\rangle = \delta_{ij}$, where δ_{ij} is the Kronecker delta function, then that set is *orthonormal* and that expression is *unique*. If both are true, then we have a complete orthonormal basis of the Hilbert space.

The system can obviously take on any one of these basis states but also *superpositions* of them. For simplicity, we consider two states such that

$$|\psi\rangle = \alpha\,|\phi_1\rangle + \beta\,|\phi_2\rangle \tag{2.1}$$

where α, β are any complex numbers that are normalised such that $|\alpha^2| + |\beta|^2 = 1$. More generally, such superpositions can be of anywhere from two states to an infinite space with the condition that $\langle\psi|\psi\rangle = 1$. For two different states, the *overlap* between them is given by the modulus square of the inner product $|\,\langle\psi_1|\psi_2\rangle\,|^2$.

These superpositions are a fundamental part of quantum mechanics. It is *not* the relic of some lack of statistical knowledge on the part of the observer, it is that without observation the state truly lives in this *unknown* sum of different possibilities.

Some statistical lack of knowledge is also possible. The introduction of this *statistical mixture* can be thought of as information about the state either being *lost* or *accessible but unobserved*. In some sense, that information is no longer within the

---

[1] Dirac notation (or bra-ket notation) is a general formulation of expressing a quantum state. This notation offers great flexibility and allows for complicated states and equations to be represented extremely simply. The *ket*, $|\psi\rangle$, describes a state and can generally be represented as a column vector. The *bra*, $\langle\psi|$, is its adjoint, or Hermitian conjugate, denoted as $\langle\psi| \equiv (|\psi\rangle)^\dagger$.

system and is not known by the observer. A more general formalism for the quantum state which allows for this statistical lack of knowledge is the *density matrix*. The relationship between the density matrix and the wavefunction is given by

$$\rho = |\psi\rangle \langle\psi| . \tag{2.2}$$

Note the existence of a wavefunction means a density matrix exists, but the opposite is not necessarily true. The normalisation condition above means that here we need $\mathrm{tr}(\rho) = 1$ where $\mathrm{tr}(\cdot)$ means to take the trace. A state which can be represented as a wavefunction is referred to as a *pure state*, while any state that exists with some statistical mixture is a *mixed state*. A pure state has the property that

$$\mathrm{tr}(\rho^2) = 1 \tag{2.3}$$

and so the density matrix allows us to calculate the purity for the system.

In some circumstances we have two systems, or two parts of the same system, that interact and, by the postulate above, there is a wavefunction that describes everything about the composite system. If the individual systems have states $|\psi_A\rangle$ and $|\psi_B\rangle$ then our composite system can be given by

$$|\psi_{A\otimes B}\rangle = |\psi_A\rangle \otimes |\psi_B\rangle \tag{2.4}$$

where $\otimes$ is the tensor product. $|\psi_{A\otimes B}\rangle$ lives in the composite Hilbert space $\mathcal{H}_A \otimes \mathcal{H}_B$. We can find the state in space $\mathcal{H}_A$ by tracing over $\mathcal{H}_B$.

This decomposition is not necessarily possible, i.e. $|\psi_{A\otimes B}\rangle \neq |\psi_A\rangle \otimes |\psi_B\rangle$. Sometimes tracing out one of the systems leaves the other in a mixed state. This means that we have an *entangled state* with correlations between the systems that *require* a composite description. Information about system B is contained in system A and vice versa. Tracing out one of the systems introduces a statistical mixture to the system because that information has been removed. Two systems are thus entangled if there is more mixture in an individual system than in the composite system

$$\mathrm{tr}(\rho^2_{A\otimes B}) > \mathrm{tr}(\rho^2_{A,B}). \tag{2.5}$$

2.1.2 Operators

Associated to any observation or action on the system is an operator.

Properties of the state are described by operators, $\hat{\mathcal{O}}$. In the linear algebra form these are matrices, while in Dirac notation they are formed by sums over ket-bra pairs. In some orthonormal basis $\{\,\phi_i\,\}$ we express an operator as

$$\hat{\mathcal{O}} = \sum_{ij} c_{ij} \left|\phi_i\right\rangle \left\langle\phi_j\right| \tag{2.6}$$

and its action on a state

$$\begin{aligned} \hat{\mathcal{O}} \left|\psi\right\rangle &= \sum_{ij} c_{ij} \left|\phi_i\right\rangle \left\langle\phi_j\right| \sum_k \alpha_k \left|\phi_k\right\rangle \\ &= \sum_{ik} c_{ik} \alpha_k \left|\phi_i\right\rangle . \end{aligned} \tag{2.7}$$

That is, the action of an operator is to map states in a Hilbert space to other states in the Hilbert space, $\left|\phi_j\right\rangle \to \left|\phi_i\right\rangle$, with some coefficient c_{ij}. The equivalent form for the density matrix is

$$\hat{\mathcal{O}} \left|\psi\right\rangle \to \hat{\mathcal{O}} \rho \hat{\mathcal{O}}^{\dagger} . \tag{2.8}$$

Like any matrix, these operators can have eigenstates and eigenvalues given by

$$\hat{\mathcal{O}} \left|e_i\right\rangle = \xi_i \left|e_i\right\rangle \quad \leftrightarrow \quad \hat{\mathcal{O}} = \sum_i \xi_i \left|e_i\right\rangle \left\langle e_i\right| . \tag{2.9}$$

Physical observables, such as position or momentum, must have real eigenvalues. Therefore, the operators that describe these physical observables must be Hermitian, meaning that they are their own adjoint

$$\hat{\mathcal{O}} = \hat{\mathcal{O}}^{\dagger} . \tag{2.10}$$

Eigenstates of Hermitian operators form a complete orthonormal basis for the system they act upon[2], which in composite systems may only be a part of the system. This means any state in that system can be written in terms of the eigenstates of any physical observable of the system.

Operators that act on the same system can have different eigenstates, allowing for different representations of the state. Whether two operators $\hat{\mathcal{O}}$ and $\hat{\mathcal{P}}$ share eigenstates can be found by considering the *commutator* of the two

$$[\hat{\mathcal{O}}, \hat{\mathcal{P}}] = \hat{\mathcal{O}}\hat{\mathcal{P}} - \hat{\mathcal{P}}\hat{\mathcal{O}} . \tag{2.11}$$

If this is zero then the two operators share eigenstates. If instead it is non-zero, then we note that they have separate eigenstates and the order in which the operators act upon the state is important.

In composite systems, operators may act on all or part of the Hilbert space. If we

---

[2] Non-Hermitian operators need not have real eigenvalues, or even have eigenstates at all and so are not necessarily useful as a basis.

have an operator that acts only on $\mathcal{H}_A$, $\hat{\mathcal{O}}_A$, then we have that

$$\hat{\mathcal{O}}_A(|\psi_A\rangle \otimes |\psi_B\rangle) = (\hat{\mathcal{O}}_A |\psi_A\rangle) \otimes |\psi_B\rangle \tag{2.12}$$

Similarly, any operator that only acts on $\mathcal{H}_B$ allows for $|\psi_A\rangle$ to be factored out. This means if we act with both operators then we have

$$(\hat{\mathcal{O}}_A \otimes \hat{\mathcal{O}}_B)(|\psi_A\rangle \otimes |\psi_B\rangle) = (\hat{\mathcal{O}}_A |\psi_A\rangle) \otimes (\hat{\mathcal{O}}_B |\psi_B\rangle). \tag{2.13}$$

It does not matter which order we write down these operations since they act on different parts of the Hilbert space, and so operators that act on different spaces will *always* commute.

2.1.3 Measurement

Measuring a physical observable collapses the wavefunction to an eigenstate of the operator associated with that measurement.

If we make a measurement with some Hermitian operator $\hat{\mathcal{O}}$ then the only results we can get are the eigenvalues associated with the eigenstates of the operator. We can define operators which collapse the state onto a single eigenstate

$$\hat{P}_i = |e_i\rangle \langle e_i| \tag{2.14}$$

where the sum of the full set of these *projectors* is the identity, $\mathbb{1}$. A measurement of the observable on a wavefunction results in the action of one of the set $\{ \hat{P}_i \}$ on the system with a probability given by

$$p_i = \langle\psi| \hat{P}_i |\psi\rangle . \tag{2.15}$$

If the state can be recreated and measured multiple times, then the statistics of this random collapse can be interrogated. If we were to make infinite measurements, then the mean would be given by the *expectation value*

$$\langle\hat{\mathcal{O}}\rangle = \langle\psi| \hat{\mathcal{O}} |\psi\rangle \quad \leftrightarrow \quad \langle\hat{\mathcal{O}}\rangle = \mathrm{tr}(\rho\hat{\mathcal{O}}). \tag{2.16}$$

These expectation values do not necessarily need to be eigenvalues of the operators and tracking their evolution can give a useful picture of how the system evolves.

The action of two measurements on the same system one after the other is an important concept. If we have an operator $\hat{\mathcal{O}}$ with eigenstates, $|\phi_1\rangle$ and $|\phi_2\rangle$, then a measurement of some superposition gives one of these states. If we have a second operator $\hat{\mathcal{P}}$ which has different eigenstates, i.e. it does not commute with $\hat{\mathcal{O}}$, then a measurement of that observable collapses the state into this new basis, destroying the information gained by the first measurement. Measurement of non-commuting operators cannot be performed simultaneously and full information about both cannot be known at the same time. It is this fact that leads to Heisenberg's famous uncertainty principle. For two operators $\hat{\mathcal{O}}$ and $\hat{\mathcal{P}}$ with commutator relation

$$[\hat{\mathcal{O}}, \hat{\mathcal{P}}] = i\hat{\mathcal{Q}} \tag{2.17}$$

then the product of their standard deviations is bounded by

$$(\Delta\hat{\mathcal{O}})^2(\Delta\hat{\mathcal{P}})^2 \geq \frac{1}{4}\left\langle\hat{\mathcal{Q}}\right\rangle^2 . \tag{2.18}$$

Note that $\hat{\mathcal{Q}}$ is kept as an operator here, but it is a constant in many cases.

A projective measurement, as described above, of $\hat{\mathcal{O}}$ means nothing can be known about $\hat{\mathcal{P}}$ as its variance must become infinite to satisfy the inequality. So-called weak measurements are possible, where the system is coupled to some external system and measurements of that are performed [1]. This gives some information about the desired observable with a comparatively small perturbation of the state. This allows information about both observables to be known at the same time, but with error bars that meet the above equality.

The inequality also describes the statistics of the state itself. When the inequality becomes an equality, we have a minimum uncertainty state, which can have the uncertainty equally split between the two observables, or *squeezed* such that one variable contains more noise than the other. These squeezed states cannot be described by classical physics and so are inherently *quantum*.

2.1.4 Evolution

Between measurements the wavefunction evolves according to the time-dependent Schrödinger equation.

When the system is not being measured it evolves coherently according to the Schrödinger equation. For a wavefunction $|\psi\rangle$ this is

$$i\hbar\frac{\partial}{\partial t}|\psi(t)\rangle = \hat{H}|\psi(t)\rangle \quad \leftrightarrow \quad i\hbar\frac{\partial\rho}{\partial t} = [\hat{H}, \rho] \tag{2.19}$$

where we have introduced the Hamiltonian operator $\hat{H}$ and $\hbar$ is the reduced Planck constant.

We can solve the Schrödinger equation for the wavefunction such that

$$|\psi(t)\rangle = \mathrm{e}^{-i\hat{H}t/\hbar}|\psi(0)\rangle . \tag{2.20}$$

For that process to be reversible, and time-symmetry tells us it must be, then changing $t \rightarrow -t$ must produce the inverse. This is equivalent to saying that $\mathrm{e}^{-i\hat{H}t/\hbar}$ must be unitary - meaning its conjugate transpose is its inverse such that $\hat{U}^\dagger \hat{U} = \mathbb{1}$ - as only these can describe reversible time evolution. For the Hamiltonian we require

$$\mathrm{e}^{it\hat{H}^\dagger/\hbar}\mathrm{e}^{-it\hat{H}/\hbar}\left|\psi(0)\right\rangle = \left|\psi(0)\right\rangle \quad \rightarrow \quad \mathrm{e}^{-it/\hbar(\hat{H}-\hat{H}^\dagger)} = \mathbb{1} \quad \rightarrow \quad \hat{H} = \hat{H}^\dagger. \tag{2.21}$$

The Hamiltionian is Hermitian and that means it represents some physical observable. In fact, this quantum mechanical operator is a direct descendent from classical Hamiltonian mechanics. As there we have that

$$\hat{H} = \hat{T} + \hat{V} \tag{2.22}$$

where $\hat{T}$ is the kinetic energy operator and $\hat{V}$ is the potential operator. Usually, the Hilbert space of the system is restricted to a subset of properties such that this historical picture is not particularly useful. Instead, the idea that the Hamiltonian is the "energy operator" that describes the evolution of the system is more intuitive.

We diverge from classical mechanics because, as a Hermitian operator, the Hamiltonian here has a series of eigenstates and eigenvalues. These eigenvalues tell us about the energy levels of the system, and so the lowest eigenvalue gives us the *ground state* and its energy.

The Hamiltonian can also tell us about the evolution of operators. The expectation value of an observable at some time t is given by

$$\left\langle\hat{\mathcal{O}}\right\rangle_t = \left\langle\psi(0)\right| \mathrm{e}^{i\hat{H}t/\hbar}\hat{\mathcal{O}}\mathrm{e}^{-i\hat{H}t/\hbar}\left|\psi(0)\right\rangle. \tag{2.23}$$

If the operator and the Hamiltonian commute then we can move that operator out of the centre and, cancelling the unitaries to the identity, we find that

$$\left\langle\hat{\mathcal{O}}\right\rangle_t = \left\langle\hat{\mathcal{O}}\right\rangle_0. \tag{2.24}$$

That is, if an operator commutes with the Hamiltonian, then the observable it represents must be conserved. This includes, of course, the Hamiltonian itself and so energy conservation is intrinsically built into this picture.

2.2 Photon statistics

Quantum optics deals with light at the level of single quanta - *photons* - and their interaction with matter. The idea of a quantised light field can be traced back to Planck and his attempts to explain the spectral distribution of thermal light. Further evidence came with Einstein's explanation of the photoelectric effect. What we think of as quantum optics began more earnestly with the experiments of Hanbury Brown and Twiss and their observation of photon bunching in thermal light [2]. A full quantum picture of coherent light fields was then introduced by Glauber and Sudarshan [3–5]. In this Section we discuss that theory and its implications. Many of the details and derivations are left out in exchange for brevity. More comprehensive descriptions can be found in [6], or for a more complete mathematical treatment see [1,7].

2.2.1 Quantisation of the electromagnetic field

We begin with Maxwell's equations, specifically Ampère's circuital law

$$\mu_0 \nabla \times \mathbf{B} = \varepsilon_0 \frac{\partial \mathbf{E}}{\partial t} \tag{2.25}$$

where $\mathbf{B}$ and $\mathbf{E}$ are the magnetic and electric fields, and μ_0 and ε_0 are the permeability and permittivity of free space. The vector potential $\mathbf{A}(\mathbf{r}, t)$ relates the fields as

$$\mathbf{B} = \nabla \times \mathbf{A}, \quad \mathbf{E} = -\frac{\partial \mathbf{A}}{\partial t} \tag{2.26}$$

and we operate in the Coulomb gauge where the vector potential satisfies

$$\nabla \cdot \mathbf{A} = 0 \quad \rightarrow \quad \nabla^2 \mathbf{A} = \frac{1}{c^2} \frac{\partial^2 \mathbf{A}}{\partial t^2} \tag{2.27}$$

where we show that Ampère's circuital law becomes a wave equation for the vector potential and use $c = 1/\sqrt{\mu_0 \varepsilon_0}$ is the speed of light in a vacuum.

We now split the vector potential into two complex terms

$$\mathbf{A}(\mathbf{r}, t) = \mathbf{A}^+(\mathbf{r}, t) + \mathbf{A}^-(\mathbf{r}, t) \tag{2.28}$$

$$\text{where} \quad \mathbf{A}^+(\mathbf{r}, t) = \sum_k C_k \mathbf{u}_k(\mathbf{r}) \mathrm{e}^{-i\omega_k t}, \quad \mathbf{A}^- = (\mathbf{A}^+)^* \tag{2.29}$$

and electromagnetic modes of frequency ω_k have spatial functions $\mathbf{u}_k(\mathbf{r})$. Following on from the gauge condition, $\nabla \cdot \mathbf{u}_k(\mathbf{r}) = 0$, and from the wave equation

$$\left(\nabla^2 + \frac{\omega_k^2}{c^2} \right) \mathbf{u}_k(\mathbf{r}) = 0. \tag{2.30}$$

The form of these spatial modes depends on the boundary conditions of the relevant volume and they form a complete orthonormal set over the space indexed by k which sums over *both* space and polarisation. The vector potential is now given by

$$\mathbf{A}(\mathbf{r}, t) = \sum_k \left(\frac{\hbar}{2\omega_k \varepsilon_0} \right)^{1/2} \left[a_k \mathbf{u}_k(\mathbf{r}) \mathrm{e}^{-i\omega_k t} + a_k^\dagger \mathbf{u}_k^*(\mathbf{r}) \mathrm{e}^{i\omega_k t} \right] \tag{2.31}$$

where we normalise the equation such that the amplitudes a_k are dimensionless and that the energy in the field is commensurate with the Planck-Einstein relation.

The electric field is then given by

$$\mathbf{E}(\mathbf{r}, t) = \sum_k \left(\frac{\hbar \omega_k}{2\varepsilon_0} \right)^{1/2} \left[a_k \mathbf{u}_k(\mathbf{r}) \mathrm{e}^{-i\omega_k t} - a_k^\dagger \mathbf{u}_k^*(\mathbf{r}) \mathrm{e}^{i\omega_k t} \right]. \tag{2.32}$$

In classical electromagnetism these amplitudes a_k are complex numbers. Quantisation of the electromagnetic field is accomplished by designating these as operators. Photons are bosons and so these operators obey

$$[\hat{a}_k, \hat{a}_{k'}] = 0, \quad [\hat{a}_k^\dagger, \hat{a}_{k'}^\dagger] = 0, \quad [\hat{a}_k, \hat{a}_{k'}^\dagger] = \delta_{kk'}. \tag{2.33}$$

This quantisation describes the electric field as a sum of independent harmonic oscillators. Operators for different modes commute because they act on different Hilbert spaces. This lets us consider a relevant set of single modes of the electromagnetic field without considering the full spectrum. For the same mode the operators do not commute meaning they are non-Hermitian.

The Hamiltonian for the electromagnetic field is given by

$$H = \frac{1}{2} \int (\varepsilon_0 \mathbf{E}^2 + \mu_0^{-1} \mathbf{B}^2)\, \mathrm{d}\mathbf{r} \tag{2.34}$$

which by following through the above conditions and expanding out gives

$$\hat{H} = \sum_k \hbar \omega_k \left(\hat{a}_k^\dagger \hat{a}_k + \frac{1}{2} \right). \tag{2.35}$$

$\hat{a}_k^\dagger \hat{a}_k$ is the *number operator* and so the energy of the field is a sum over the energy in each mode: the energy per photon multiplied by the number of photons *plus one half*. This half represents the energy of the vacuum fluctuations in each mode. Since there are infinite modes, this means that with zero photons in all modes we still have infinite energy in the field. This may seem counterintuitive, but experiments measure a change in energy so this infinite background does not influence measurements.

2.2.2 Fock states

For simplicity we now consider a single mode with a specific polarisation and frequency ω. Our Hamiltonian is then

$$\hat{H} = \hbar \omega \left(\hat{a}^\dagger \hat{a} + \frac{1}{2} \right). \tag{2.36}$$

This has obvious eigenstates: exact numbers of photons. These states are called Fock states (or number states) and are written simply as $|n\rangle$. Clearly they are eigenstates of the number operator with eigenvalues n. The ground state is that with zero photons. The action of these operators on the Fock states is

$$\hat{a}\,|n\rangle = \sqrt{n}\,|n-1\rangle\,, \quad \hat{a}^\dagger\,|n\rangle = \sqrt{n+1}\,|n+1\rangle\,, \quad \hat{a}^\dagger\hat{a}\,|n\rangle = n\,|n\rangle\,. \tag{2.37}$$

We can see that $\hat{a}$ and $\hat{a}^\dagger$ are *annihilation* and *creation* operators respectively. That is, their action on a state removes or adds a photon to the state.

The Fock states form a complete basis for the mode. We can define a state

$$|\psi\rangle \equiv n_0\,|0\rangle + n_1\,|1\rangle + n_2\,|2\rangle \cdots = \sum_{i=0}^{\infty} n_i\,|i\rangle \tag{2.38}$$

and write our operators as

$$\hat{a} \equiv |0\rangle\langle 1| + \sqrt{2}\,|1\rangle\langle 2| + \sqrt{3}\,|2\rangle\langle 3| + \cdots = \sum_{i=1}^{\infty} \sqrt{i}\,|i-1\rangle\langle i| \tag{2.39}$$

$$\hat{a}^\dagger \equiv |1\rangle\langle 0| + \sqrt{2}\,|2\rangle\langle 1| + \sqrt{3}\,|3\rangle\langle 2| + \cdots = \sum_{i=0}^{\infty} \sqrt{i+1}\,|i+1\rangle\langle i| \tag{2.40}$$

$$\hat{a}^\dagger\hat{a} \equiv |1\rangle\langle 1| + 2\,|2\rangle\langle 2| + 3\,|3\rangle\langle 3| + \cdots = \sum_{i=0}^{\infty} i\,|i\rangle\langle i|\,. \tag{2.41}$$

This clearly shows that the annihilation and creation operators are not Hermitian and that the number operator is Hermitian with the Fock states as eigenstates.

Fock states make sense from a mathematical perspective and are physically intuitive, but, in experiments, Fock states above a few photons are difficult to produce. Most fields are a superposition or a mixed state of Fock states.

2.2.3 Coherent states

A useful basis for many situations are the coherent states $|\alpha\rangle$. These are eigenstates of the annihilation operator $\hat{a}$ with eigenvalues α

$$\hat{a}\,|\alpha\rangle = \alpha\,|\alpha\rangle\,. \tag{2.42}$$

This means subtracting photons from a coherent state returns the *exact* same state. Since $\hat{a}$ is non-Hermitian these eigenvalues can be complex.

Coherent states can be expressed in Fock states as

$$|\alpha\rangle = \mathrm{e}^{-|\alpha|^2/2} \sum_{n=0}^{\infty} \frac{\alpha^n}{\sqrt{n!}}\,|n\rangle \quad \rightarrow \quad p(n) = \frac{|\alpha|^{2n}\mathrm{e}^{|\alpha|^2}}{n!}. \tag{2.43}$$

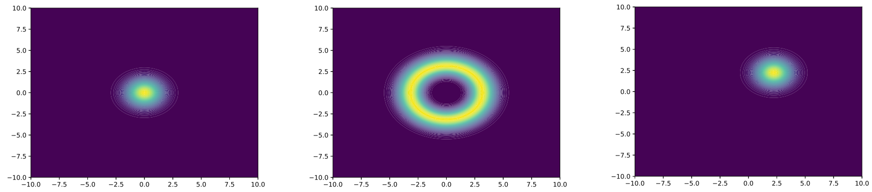

(a) Vacuum **(b)** $|n=5\rangle$ **(c)** $|\alpha=\sqrt{5}\mathrm{e}^{i\pi/4}\rangle$

Figure 2.1: Q-function plots for different states of light.

where $p(n)$ is the probability distribution of the photon number. This distribution is Poissonian and the expectation value is $\langle\hat{a}^\dagger\hat{a}\rangle=|\alpha|^2$. Coherent states can be thought of as a shift on the vacuum, formed by acting with the displacement operator

$$\hat{D}(\alpha)=\mathrm{e}^{(\alpha\hat{a}^\dagger-\alpha^*\hat{a})}. \tag{2.44}$$

A pair of coherent states are not necessarily orthogonal. Whilst they can form a basis for the states, they are *overcomplete*. This means that any state of the field can be represented in multiple different combinations of coherent states. This allows us to construct a useful visual representation for an electromagnetic field state: the Q-function. This is given by

$$Q(\alpha)=\frac{\langle\alpha|\,\rho\,|\alpha\rangle}{\pi}. \tag{2.45}$$

Figure 2.1 shows Q-function plots of states discussed so far.

Defining the position and momentum operators for the harmonic oscillator as

$$\hat{q}=\sqrt{\frac{\hbar}{2\omega}}\left(\hat{a}+\hat{a}^\dagger\right),\quad \hat{p}=i\sqrt{\frac{\hbar\omega}{2}}\left(\hat{a}-\hat{a}^\dagger\right), \tag{2.46}$$

we calculate variances on the coherent states as

$$(\Delta\hat{q})^2=\frac{\hbar}{2\omega},\quad (\Delta\hat{p})^2=\frac{\hbar\omega}{2}. \tag{2.47}$$

The product of the standard deviations is then $\hbar/2$, showing that coherent states are minimum uncertainty states.

2.2.4 Squeezed states

If we take a coherent state and redistribute noise between two orthogonal axes, we can create squeezed states. This is done with the squeezing operator

$$\hat{S}(\xi)=\mathrm{e}^{(\xi^*\hat{a}^2-\xi\hat{a}^{\dagger 2})/2} \tag{2.48}$$

where ξ is a complex number. The squeezing takes the form of correlated pairs of photons being added to and removed from the mode. A squeezed vacuum thus only has contributions from even photon numbers. The magnitude and phase of ξ tell us about the degree to which noise is redistributed and the axis about which it is squeezed, as shown in Figure 2.2.

Two-mode squeezed states are formed by the alternate operator

$$\hat{S}(\xi) = \mathrm{e}^{(\xi^* \hat{a}_1 \hat{a}_2 - \xi \hat{a}_1^\dagger \hat{a}_2^\dagger)/2} \tag{2.49}$$

where instead of pairs of photons correlated in a single mode, the pair is split between two modes. The quantum correlations are thus between two modes rather than between the populations of a single mode.

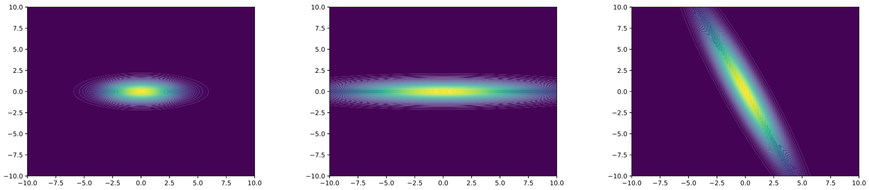

(a) $\hat{S}(\xi = 1\mathrm{e}^{i\pi})\,|0\rangle$ **(b)** $\hat{S}(\xi = 2\mathrm{e}^{i\pi})\,|0\rangle$ **(c)** $\hat{S}(\xi = 2\mathrm{e}^{i\pi/4})\,|0\rangle$

Figure 2.2: Q-function plots for different squeezed vacuum states of light.

2.2.5 Thermal states

Another class of states that are important to consider are thermal states. These are states that do not satisfy the minimum-uncertainty relation. Instead, their population statistics follow the Bose-Einstein distribution

$$p(n) = \frac{1}{\bar{n}+1}\left(\frac{\bar{n}}{\bar{n}+1}\right)^n \tag{2.50}$$

where $\bar{n}$ is the expectation value of the number operator and, for a temperature T and mode of frequency ω, is given by

$$\bar{n} = \frac{1}{\exp(\hbar\omega/k_B T) - 1}. \tag{2.51}$$

where k_B is the Boltzmann constant.

For cold enough temperatures and large enough frequencies then this is approximately the vacuum. For lower frequencies or higher temperatures, these thermal photons must be taken into account.

It is possible to create thermal coherent and squeezed states simply by applying the displacement or squeezing operator to this thermal state instead of the vacuum.

Figure 2.3 shows that, instead of displacing the state, larger thermal states simply enlarge the uncertainties. For any $\bar{n}$, the most probable photon number is still zero, but the average photon number increases as the size of the spread increases. Note that there is no phase information associated with the thermal state.

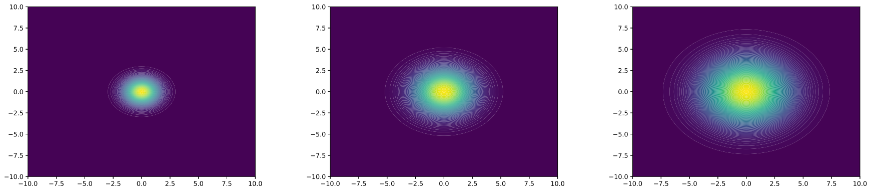

(a) $\bar{n} = 0$ **(b)** $\bar{n} = 2$ **(c)** $\bar{n} = 5$

Figure 2.3: Q-function plots for different thermal states of light.

2.2.6 Photon counting statistics

Important information about the state can be gained by looking at the counting statistics. For light incident on a photon detector, we can measure the times of arrival of the photons and so the correlations in these times can be studied. We can do this with photon correlation measurements. We define the second-order correlation function

$$G^{(2)}(\tau) = \langle \hat{a}^\dagger(t+\tau)\hat{a}^\dagger(t)\hat{a}(t+\tau)\hat{a}(t)\rangle \,. \tag{2.52}$$

Intuitively, this is the probability of measuring a photon at a time $t+\tau$ conditioned on having measured a photon at time t. Often this is normalised by the probability of measuring that first photon,

$$g^{(2)}(\tau) = \frac{\langle \hat{a}^\dagger(t+\tau)\hat{a}^\dagger(t)\hat{a}(t+\tau)\hat{a}(t)\rangle}{\langle \hat{a}^\dagger(t)\hat{a}(t)\rangle^2} \,. \tag{2.53}$$

For the rest of this analysis we will focus on $g^{(2)}(0)$, i.e. the probability of measuring two photons simultaneously relative to the probability of measuring one photon squared. This can be written in the forms

$$g^{(2)}(0) = \frac{\langle \hat{a}^\dagger\hat{a}^\dagger\hat{a}\hat{a}\rangle}{\langle \hat{a}^\dagger\hat{a}\rangle^2} \tag{2.54}$$

$$= 1 + \frac{(\Delta\hat{n})^2 - \langle\hat{n}\rangle}{\langle\hat{n}\rangle^2} \,. \tag{2.55}$$

The easiest case to decipher is that of coherent states. The statistics of Poissonian distributions, such as the photon number probability distribution of a coherent state, intrinsically apply to random processes. If a coherent beam or source produces photons at random intervals, there cannot be correlation between the photon measurements. A coherent state has $\Delta\hat{n} = \sqrt{\langle\hat{n}\rangle}$ which clearly leads to $g^{(2)}(0) = 1$. There are no correlations between photon counts since the probability of measuring a second photon is the same as measuring the first. Remembering that coherent states are eigenstates of the annihilation operator, this makes perfect sense. The measurement of the first photon does not impact the statistics of measuring a second photon because the annihilation operator *does not change a coherent state*.

Thermal light produces what is known as super-Poissonian light. The variance of a thermal state follows the relation $\Delta n > \sqrt{\langle\hat{n}\rangle}$ and so $g^{(2)}(0) > 1$ and so there the measurement of one photon makes it more likely to have a second. This is often called *bunched* light as photons will tend to come closer together with longer pauses between those "bunches". As $\bar{n}$ increases, the average population of the thermal state increases and so the bunching effect becomes stronger.

A Fock state $|n\rangle$ gives the result

$$g^{(2)}(0) = 1 - \frac{1}{n}. \tag{2.56}$$

For a single photon this is zero, which makes sense given that measuring one photon negates any possibility of measuring a second. For higher photon numbers then $g^{(2)}(0)$ tends towards unity but is *always* less. Measuring a photon makes it less likely to measure a second photon and so we have an example of something we call *anti-bunched* light. Bunching and random statistics can both be perfectly explained with classical statistics, but anti-bunching is a distinctly quantum phenomenon. This means any state with $g^{(2)}(0) < 1$, or equivalently $\Delta n < \sqrt{\langle\hat{n}\rangle}$ is inherently quantum.

2.3 Open system evolution

A problem with simulating quantum systems is that the system in which we are interested in is always coupled in some way to the environment around it. That interaction thus needs to be included in the simulation, but including the environment in the simulation makes the Hilbert space far too large. Of course, the environment also has its own interactions with its environment and so on. Instead, we need to trace out the environment in some way. In this Section, I discuss methods of doing this in quantum optics that will be used in the rest of the thesis. Much of the mathematical detail here is skipped over since it is covered in much more detail elsewhere. Each case has relevant references to where those details can be found.

2.3.1 Master equation

The first method to discuss is the quantum optical master equation [7–9]. Here, we take a total Hamiltonian

$$\hat{H} = \hat{H}_S + \hat{H}_E + \hat{H}_{SE} \tag{2.57}$$

where S stands for system, E for environment and SE for the system-environment interaction. The density matrix P for both the system and environment follows the equation

$$\dot{\mathrm{P}} = -\frac{i}{\hbar}[\hat{H}, \mathrm{P}]. \tag{2.58}$$

What we want is

$$\rho(t) = \mathrm{tr}_E\left(\mathrm{P}(t)\right). \tag{2.59}$$

We transform to the interaction picture such that

$$\mathrm{P}'(t) = \mathrm{e}^{i(\hat{H}_S+\hat{H}_E)t/\hbar}\mathrm{P}(t)\mathrm{e}^{-i(\hat{H}_S+\hat{H}_E)t/\hbar} \quad \text{and} \quad \hat{H}'_{SE}(t) = \mathrm{e}^{i(\hat{H}_S+\hat{H}_E)t/\hbar}\hat{H}_{SE}(t)\mathrm{e}^{-i(\hat{H}_S+\hat{H}_E)t/\hbar}. \tag{2.60}$$

This gives us an evolution equation

$$\dot{\mathrm{P}}' = -\frac{i}{\hbar}\left[\hat{H}'_{SE}, \mathrm{P}'\right]. \tag{2.61}$$

We can integrate this and substitute that result in to give

$$\dot{\mathrm{P}}' = \frac{1}{i\hbar}\left[\hat{H}'_{SE}(t), \mathrm{P}'(0)\right] - \frac{1}{\hbar^2}\int_0^t \mathrm{d}t'\left[\hat{H}'_{SE}(t), \left[\hat{H}'_{SE}(t'), \mathrm{P}'(t')\right]\right]. \tag{2.62}$$

At this stage no assumptions have been made and so the form is exact.

The first assumption is that at $t = 0$ there is no correlation between the system and its environment. This means that $\mathrm{P}'(0) = \rho(0)E(0)$ where we introduce E as the environment density matrix.

The second assumption is that the environment is very large and weakly coupled to the system such that it remains virtually unaffected by that coupling. We then make a Born approximation, neglecting all terms to more than second order in $\hat{H}_{SE}$ and so, after both assumptions, we have

$$\rho'(t) = -\frac{1}{\hbar^2}\int_0^t \mathrm{d}t'\ \mathrm{tr}_E\left(\left[\hat{H}'_{SE}(t), \left[\hat{H}'_{SE}(t'), \rho'(t')E(0)\right]\right]\right). \tag{2.63}$$

This equation is interesting because the evolution of $\rho'(t)$ is related to its own past since we integrate over $\rho'(t')$. This means that two identical system states may evolve differently depending on the path they took to that state. This makes the system *non-Markovian*.

Throughout this work, we assume that this is not the case. This Markovian approximation states that the evolution of the state *cannot* be affected by the past state. This is equivalent to saying that any information sent into the environment is lost. This makes sense for most systems, where the environment is very large and thermal such that changes in it would be washed away quickly.

We make the assumption that the environment is composed of a set of electromagnetic modes $\{\hat{r}_j\}$. The system interacts with the environment through an exchange of energy between some system operator $\hat{J}$, which we later refer to as the jump or loss operator, and those modes[3]

$$\hat{H}_E = \sum_j \hbar\omega_j \hat{r}_j^\dagger \hat{r}, \qquad \hat{H}_{SE} = \sum_j \hbar \left(\kappa_j^* \hat{J}\hat{r}_j^\dagger + \kappa_j \hat{J}^\dagger \hat{r}_j \right). \tag{2.64}$$

The density matrix for the environment is then taken as in thermal equilibrium at temperature T as the product of thermal states in each of the set of modes. We then expand out the master equation given in Equation 2.62 under these approximations and calculate the correlations within the environment. A full treatment of this is given in [8]. Here, we summarise the key aspects. Each of the modes is assumed to have no correlations to other modes. Environment operators for each mode are related to themselves at other times with a correlation function that decays much faster than the timescale associated with the evolution of the system operator. By then integrating over the environment to account for the summation of modes and moving back out of the interaction picture we arrive at the quantum optical master equation ($\hbar = 1$)

$$\dot{\rho} = -i\left[\hat{H}, \rho\right] + \frac{\gamma}{2}\left(2\hat{J}\rho\hat{J}^\dagger - \hat{J}^\dagger\hat{J}\rho - \rho\hat{J}^\dagger\hat{J}\right) + \gamma\bar{n}\left(\hat{J}\rho\hat{J}^\dagger + \hat{J}^\dagger\rho\hat{J} - \hat{J}^\dagger\hat{J}\rho - \rho\hat{J}\hat{J}^\dagger\right) \tag{2.65}$$

where

$$\gamma = 2\pi g(\omega_0)|\kappa(\omega_0)|^2 \tag{2.66}$$

and $g(\omega_0)$ and $\kappa(\omega_0)$ are, respectively, the density of states in the environment and the coupling between environment and system to each of those states at the frequency of the emission ω_0. In essence, γ tells us about the rate of excitations being exchanged between the system and its environment. If $\bar{n}$ is non-zero, then excitations can enter the system at rate $\gamma\bar{n}$ and leave at an enhanced rate $\gamma(\bar{n}+1)$. If the environment is very cold relative to the energy of the photons, then $\bar{n}$ can be assumed as zero, as it will be throughout this thesis, and that exchange is one-sided - excitations can leave the system but no excitations will enter - and happens at a rate γ. The master

---

[3] Of course, the same derivation is valid for any form of environment that can be expressed in terms of harmonic oscillators. Moreover, the specific form of the environment is not actually necessary [8]. However, for the purposes of much of quantum optics, and certainly for this thesis, this is a suitable picture and it provides more intuition than a more general derivation.

equation used throughout these thesis will then be[4]

$$\dot{\rho} = -i\left[\hat{H}, \rho\right] + \sum_i \frac{\gamma_i}{2}\left(2\hat{J}_i\rho\hat{J}_i^\dagger - \hat{J}_i^\dagger\hat{J}_i\rho - \rho\hat{J}_i^\dagger\hat{J}_i\right) \equiv \mathcal{L}\rho \tag{2.67}$$

where $\mathcal{L}$ is a set of operations on the state known as a superoperator. Note that these dissipative terms in the sum will generally be referred to using a superoperator defined by

$$\mathcal{D}[\hat{J}_i]\rho \equiv \left(2\hat{J}_i\rho\hat{J}_i^\dagger - \hat{J}_i^\dagger\hat{J}_i\rho - \rho\hat{J}_i^\dagger\hat{J}_i\right). \tag{2.68}$$

The density matrix evolves according to Equation 2.67, and so at each time step we have a mixture of coherent Hamiltonian evolution and scattering to the environment. That scattering to the environment *entangles* it with the system. Information about the system is held within that scattering record. That record is traced over when we trace out the environment, and so the information is lost. Defining a state conditioned on a particular scattering record as $|\psi_{\text{REC}}\rangle$ then the master equation result is

$$\rho(t) = \sum_{\text{REC}} p_{\text{REC}} \left|\psi_{\text{REC}}(t)\right\rangle \left\langle\psi_{\text{REC}}(t)\right| \tag{2.69}$$

where we sum over every single possible scattering record.

2.3.2 Quantum trajectories

The master equation produces a mixed state of all the possible paths of loss and no loss that the initial state can take as it evolves in the system. An alternative method is to stochastically choose a single path: a Monte-Carlo quantum trajectory. We choose to *either* evolve the system dissipatively or coherently at each time step rather than the mixture of both prescribed by the master equation. The physical interpretation for this is the placing of a detector outside the system that measures whether or not there is a loss event. Such a move provides information about the environment and so the mixture caused by the information lost to the environment in the master equation is removed. The measurement *disentangles* the system from its environment, and so returns a pure state. Each trajectory has a unique record of times (and locations) of each loss measurement and the average of all possible trajectories returns the master equation result, as shown in Figure 2.4.

A strict and thorough mathematical description of trajectories and how they relate to the master equation is given in [10]. Here, I briefly discuss the key points of such

---

[4] It should be noted that this master equation assumes that the loss processes are all completely independent. This is an assumption that, while it does hold for the work considered in this thesis, is not necessarily always true. When it is not, the master equation cannot be written in this simple form and instead γ is a matrix.

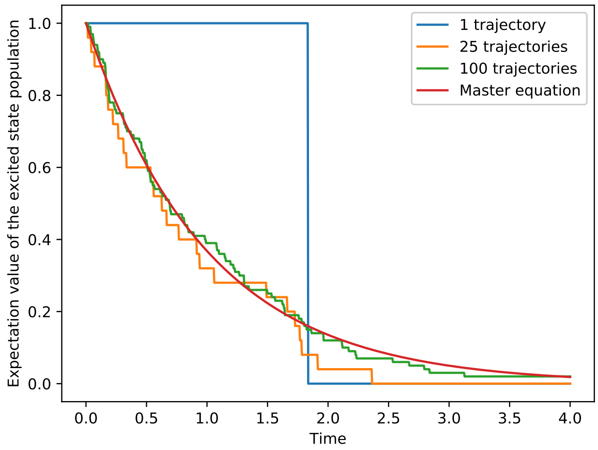

Figure 2.4: A comparison of quantum trajectories and the master equation for spontaneous emission from a single atom (see Section 3.2.2 for more details). The master equation result is an exponential decay, while individual trajectories instead "jump" to the ground state at a particular time. Averaging over those times returns an exponential decay.

a derivation. We take our master equation and split $\mathcal{L}$ into two parts[5]

$$\dot{\rho} = (\mathcal{L}_C + \mathcal{L}_S)\,\rho \tag{2.70}$$

$$\mathcal{L}_C\rho = -i[\hat{H},\rho] - \frac{1}{2}\left(\hat{J}^\dagger\hat{J}\rho + \rho\hat{J}^\dagger\hat{J}\right), \qquad \mathcal{L}_J\rho = \hat{J}\rho\hat{J}^\dagger. \tag{2.71}$$

The first of these superoperators, $\mathcal{L}_C$, represents coherent evolution. We can write its action on the density matrix in the form

$$\mathcal{L}_C\rho = -i\left(\hat{H}_C\left|\psi\right\rangle\left\langle\psi\right| - \left|\psi\right\rangle\left\langle\psi\right|\hat{H}_C^\dagger\right) \quad \text{where} \quad \hat{H}_C = \hat{H} - i\hat{J}^\dagger\hat{J}. \tag{2.72}$$

The state evolves according to a Schrödinger equation ($\hbar = 1$)

$$\frac{\mathrm{d}\left|\psi(t)\right\rangle}{\mathrm{d}t} = -i\hat{H}_C\left|\psi(t)\right\rangle \quad \rightarrow \quad \left|\psi(t)\right\rangle = \left(\mathrm{e}^{-i\hat{H}/t}\mathrm{e}^{-\hat{J}^\dagger\hat{J}t}\right)\left|\psi(0)\right\rangle. \tag{2.73}$$

The fact the Hamiltonian is now *non-Hermitian* means that states with non-zero values for $\langle\hat{J}^\dagger\hat{J}\rangle$ will "decay". This subtlety can be of great importance, and creates a distinctly different evolution to the usual unitary Schrödinger equation.

Let us consider a state such that $\hat{H}\left|\psi\right\rangle \propto \left|\psi\right\rangle$ and $\left\langle\psi\right|\hat{J}^\dagger\hat{J}\left|\psi\right\rangle = 0$. These states do not decay and, as eigenstates of the Hamiltonian, they do not evolve beyond a global phase rotation. This means such states are *decoupled* from the evolution.

---

[5] For the sake of simplicity in this derivation we consider one jump operator, but the treatment is easily generalised to any number.

The backaction of the null measurement in the photon emission channel *projects* the system into such a state, since the measurement of no photons over long times is not commensurate with the system being anywhere else. Due to this absence of emission, they are called *dark states*. Multiple dark states can exist for the same system. In that case, the scattering record before the emergence of the dark state might signal which dark state has been reached.

If the system has several dark states or a dark state and a stable "bright" state, the master equation gives us a statistical mixture of the various solutions. If those dark states are not obvious or are obscured by bright states, then it is often ambiguous what the underlying physics is. The ambiguity is broken by considering Monte-Carlo trajectories where a single trajectory shows a single specific attractor.

The action of $\mathcal{L}_J$ is even simpler to consider

$$\mathcal{L}_J \rho \to \hat{J} \left| \psi \right\rangle . \tag{2.74}$$

We act with the jump operator on the state.

For an initial pure state, this means that both superoperators in Equation 2.70 can be replaced by regular operators acting on a pure state. Our stochastic choice of which operator to apply thus leads us through the time evolution *with a pure state*. Herein lies the practical benefit of using quantum trajectories. For a Hilbert space of size M then a pure state formalism involves a differential equation for a vector of M complex numbers. The master equation approach requires the density matrix, for which the differential equation is now for a matrix of M^2 complex numbers. Evolving the master equation thus takes M times more computational time than a trajectory. Therefore, running a large number of trajectories[6] is still substantially faster than one master equation integration for large systems.

The Monte-Carlo algorithm to move from $|\psi(t)\rangle \to |\psi(t) + \delta t\rangle$ is as follows:

1. Generate a uniformly distributed random number between zero and one, R.

2. Calculate the probability that the jump operator occurs in the time step

$$p(\hat{J}) = \langle \psi(t) | \hat{J}^{\dagger} \hat{J} | \psi(t) \rangle \, \delta t. \tag{2.75}$$

3. (a) If $p(\hat{J}) \geq R$ then

$$|\psi(t + \delta t)\rangle = \hat{J} \left| \psi(t) \right\rangle . \tag{2.76}$$

---

[6] It should also be noted that trajectories are trivially parallelised since each trajectory is completely separate. This parallelisation allows for a trajectory to be run on each CPU *simultaneously*, and so as many trajectories as the computer has CPUs can be run at once. This means that trajectories can offer a greatly improved speed at finding evolution even when it is the master equation result that is desired.

(b) If $p(\hat{J}) < R$ then

$$|\psi(t+\delta t)\rangle = \left(1 + \delta t \frac{1}{i\hbar}\hat{H}\right)|\psi(t)\rangle . \tag{2.77}$$

4. Normalise the state.

By iterating this process we can go from some initial state through to some final state $|\psi_{\text{REC}}\rangle$ uniquely defined by the record of when (a) and (b) were chosen[7]. Remembering that the master equation returns a weighted average over all possible records, it is intuitive from this picture to see how a sample average of trajectories returns an approximation of the master equation result.

2.3.3 Other stochastic methods

The quantum trajectory theory has limitations. One of the more obvious relates to the measurement of the systems output. Perfect photon detection, as described by the formalism above, is not currently feasible. Instead, excitations are lost that are never measured. In a lot of cases, the intuition gained from trajectories is enough to predict what would happen with a realistic detector. However, there are also methods of adapting quantum trajectories to allow for a true mathematical picture. These methods are not used explicitly in this thesis, and so the discussion of them is kept brief and is included solely to illustrate how the assumptions made above can be worked around. For a detailed mathematical approach to such methods see [9].

Firstly, we continue to assume detection of single quanta that escape the system but that measurement is done with efficiency η. This means that η of those quanta are measured and $1-\eta$ are not. This means that we can run the Monte-Carlo algorithm above with a simple tweak: we now have two jump operators $\sqrt{\eta}\hat{J}$ and $\sqrt{1-\eta}\hat{J}$. The first of these is measured so still performs stochastic jumps on the system. The second is not and so, in between jumps, a *master equation* must be used instead of coherent evolution. These stochastic master equations therefore unravel *some* of the system-environment entanglement but not all of it.

Alternative measurement schemes are also possible. For photon fields, measuring signals mixed with a strong coherent field is often advantageous for practical reasons. Even with a perfect detection scheme, the noise associated with that coherent field needs to be modelled on top of the measurement. This leads to *stochastic Schrödinger equations* where coherent evolution exists in parallel with noise elements. Of course, such systems can be modelled with imperfect schemes as well, where we return to a form of stochastic master equation.

---

[7] For systems with multiple jump operators then this set of steps is followed for each operator at each time step.

Chapter 3

Atomic physics

To study quantum mechanics, we need quantum systems that can be contained and controlled. One of the more obvious options, and most conceptually simple, is that of single atoms - in particular, the outermost electron of a single alkali atom. That electron lives in particular orbits around the nucleus, giving us a set of quantum states for the electron to live in. In this Chapter, I describe the structure of those electronic levels, and how through interaction with modes of the electromagnetic field the electron can move between them. I then discuss the cooling of the atoms down to temperatures where their motion is restricted, enabling more control over those interactions. Finally I discuss the algebra of two-level systems and integer spins, how to describe ensembles of atoms and the idea of squeezing in a finite size ensemble.

3.1 Atomic level structure

Manipulating the state of atoms is a key component of the work in this thesis, and so it is necessary to explain what those states are. I start from the traditional place - the single hydrogen atom - and go through the corrections and field shifts that provide the rich structure of states used by atomic physicists. These explanations draw from [11] and that is an excellent place to seek further details.

3.1.1 Gross structure

The Hamiltonian eigenvalue equation for the spatial wavefunction, $\psi(\mathbf{r})$, of the electron in a hydrogen atom is

$$\left(-\frac{\hbar^2}{2m_e}\nabla^2 - \frac{e^2}{4\pi\epsilon_0 r}\right)|\psi\rangle = E\psi(\mathbf{r}) \tag{3.1}$$

where the electron is assumed to be in a Coulomb potential created by the nucleus and we introduce the mass and charge of the electron as m_e and $-e$ respectively.

We cast to spherical coordinates $\{\, r, \theta, \varphi \,\}$, in which the solution must be separable, $\psi(\mathbf{r}) = R(r)Y(\theta, \varphi)$, due to the spherically symmetric potential. We have

$$\frac{1}{R}\frac{\partial}{\partial r}\left(r^2\frac{\partial R}{\partial r}\right) - \frac{2m_e r^2}{\hbar^2}(V(r) - E) = \frac{1}{Y}\hat{\mathbf{l}}^2 Y \quad \rightarrow \quad \hat{\mathbf{l}}^2 Y = CY \tag{3.2}$$

where we have simplified the angular dependence to the orbital angular momentum squared, $\hbar^2\hat{\mathbf{l}}^2$, and used that each side now depends on different variables and so both equal the same constant, C.

For the φ component, $\Phi(\varphi)$, the result is somewhat trivial

$$-\frac{\partial^2\Phi}{\partial\varphi^2} \propto \Phi \quad \rightarrow \quad \Phi = Ae^{im\varphi} + Be^{-im\varphi}. \tag{3.3}$$

Physical solutions require $\psi(\mathbf{r})$, and thus Φ, to be continuous in space and so $\Phi(\phi + 2\pi) = \Phi(\phi)$. This means that m must be an *integer*. We can now introduce the operator $\hat{l}_z$. This operator is the projection of the orbital angular momentum onto the z-axis and is given by

$$\hbar\hat{l}_z = -i\hbar\frac{\partial}{\partial\varphi}. \tag{3.4}$$

Clearly this operator has eigenvalues m with $\Phi = e^{im\varphi}$ the eigenfunctions.

The θ dependence, $\Theta(\theta)$ is more complicated. One method to find these solutions makes use of the ladder operators, which increase or decrease m, defined by

$$\hat{l}_\pm = \hat{l}_x \pm i\hat{l}_y, \qquad \hat{l}_\pm = e^{\pm i\varphi}\left(\pm\frac{\partial}{\partial\theta} + i\cot\theta\frac{\partial}{\partial\varphi}\right). \tag{3.5}$$

Repeated application of the raising or lowering operator does not continue indefinitely. The maximum value that can be achieved is $\pm m$ and action to move the state beyond that gives zero. Making use of this and defining that maximum m as l

$$\hat{l}_{+} Y = 0 \quad \rightarrow \quad Y \propto \sin^{l} \theta \mathrm{e}^{il\varphi}. \tag{3.6}$$

To find an arbitrary combination of l and m, we can then use the lowering operator[8]

$$Y_{l,m} \propto \left(\hat{l}_{-}\right)^{l-m} \sin^{l} \theta \mathrm{e}^{il\varphi}. \tag{3.7}$$

$Y_{l,m}$ gives us the value of the constant: $C = l(l+1)$. This gives us two quantum numbers by which to categorise the angular dependence of the state: l is the *angular momentum quantum number* and m is the *magnetic quantum number*.

We can now consider the radial component of the distribution. We make the substitution $P(r) = rR(r)$ to simplify the equation and use the constant from above

$$-\frac{\hbar^2}{2m_e}\frac{\mathrm{d}^2 P}{\mathrm{d}r^2} + \left[\frac{\hbar^2}{2m_e}\frac{l(l+1)}{r^2} - \frac{e^2}{4\pi\epsilon_0 r} - E\right] P = 0. \tag{3.8}$$

We can make the equation dimensionless using the substitution

$$\rho^2 = \frac{2m_e|E|r^2}{\hbar^2} \quad \rightarrow \quad \frac{\mathrm{d}^2 P}{\mathrm{d}\rho^2} + \left[-\frac{l(l+1)}{\rho^2} + \frac{\lambda}{\rho} - 1\right] P = 0 \tag{3.9}$$

where we define a constant λ that characterises the Coulomb interaction strength as

$$\lambda = \frac{e^2}{4\pi\epsilon_0}\sqrt{\frac{2m_e}{\hbar^2|E|}}. \tag{3.10}$$

The solution to such an equation requires finite term polynomials[9] and it is found that these converge when $\lambda = 2n$. This gives energies

$$E_n = -\frac{m_e e^4}{16\pi^2\epsilon_0^2\hbar^2}\frac{1}{n^2}. \tag{3.11}$$

Here we have defined another quantum number - n - the *principal quantum number*. This energy is independent of l and m making those states degenerate. The polynomial defining the radial state *does* depend on l and so limits $0 \leq l < n$.

We can thus describe the positional state of the electron of a hydrogen atom with three quantum numbers: $|n, l, m\rangle = R_{n,l}(r) Y_{l,m}(\theta, \varphi)$.

---

[8] The resultant functions are actually well known functions called spherical harmonics. They form a complete orthogonal set for states living on a sphere.

[9] These polynomials are Laguerre polynomials. They form an orthogonal set for the radial component of the electron's wavefunction. This means that between these polynomials and the spherical harmonics we have an orthogonal set to describe the state in 3D.

3.1.2 Fine structure

The electron itself has its own intrinsic angular momentum: *spin*[10]. This means that our hydrogen electron needs two more quantum numbers $|n, l, m_l, s, m_s\rangle$ where s is the spin and m_s its z-axis projection. For an electron, s is 1/2 and so m_s can be $+1/2 \equiv\uparrow$ or $-1/2 \equiv\downarrow$.

Electrons moving around the nucleus create magnetic fields. The electron spin provides an intrinsic magnetic moment and so the electron responds to the magnetic field created by its own motion. This phenomenon is referred to as *spin-orbit coupling*. This extra term in the Hamiltonian gives an energy shift proportional to $\langle \hat{\mathbf{s}} \cdot \hat{\mathbf{l}} \rangle$. We can calculate this by considering the total angular momentum of the electron

$$\hat{\mathbf{j}} = \hat{\mathbf{l}} + \hat{\mathbf{s}} \quad \rightarrow \quad 2\langle \hat{\mathbf{s}} \cdot \hat{\mathbf{l}} \rangle = \langle \hat{\mathbf{j}}^2 \rangle - \langle \hat{\mathbf{l}}^2 \rangle - \langle \hat{\mathbf{s}}^2 \rangle = j(j+1) - l(l+1) - s(s+1). \tag{3.12}$$

The sum is either $j = l \pm 1/2$. We thus break the degeneracy of the different l states and we might think we split those l states into two j states too. However, due to relativistic considerations, a full calculation actually recreates degeneracy between states with the same n and j. This degeneracy is slightly broken by the Lamb shift which includes vacuum fluctuations of the electromagnetic field. These shifts are on the order of a tenth of the fine structure splitting. For the alkali atoms, which we focus on in this thesis, the different l states are split by another effect.

3.1.3 Hyperfine structure

The above work all assumes the nucleus is a fixed charge that can be treated completely classically. However, protons and neutrons also have spin and so the nucleus has its own spin[11]. This means that the nucleus spin, $\hat{\mathbf{I}}$, is also affected by the magnetic field produced by the moving electron. This *hyperfine splitting* is proportional to $\langle \hat{\mathbf{I}} \cdot \hat{\mathbf{j}} \rangle$. Defining a total angular momentum of the atom

$$\hat{\mathbf{F}} = \hat{\mathbf{j}} + \hat{\mathbf{I}} \quad \rightarrow \quad 2\langle \hat{\mathbf{I}} \cdot \hat{\mathbf{j}} \rangle = \langle \hat{\mathbf{F}}^2 \rangle - \langle \hat{\mathbf{I}}^2 \rangle - \langle \hat{\mathbf{j}}^2 \rangle = F(F+1) - I(I+1) - j(j+1). \tag{3.13}$$

That means that different vector sums of I and j are split. For the hydrogen atom (assuming the common isotope with zero neutrons) then $I = 1/2$ and so for each level we have a split into two hyperfine levels. For atoms with higher values of I then we have $|I - j| \leq F \leq I + j$ where we also satisfy $F = |I - j| + n$ with n an integer.

---

[10] All elementary particles have spin angular momentum. Protons, neutrons and electrons are all spin-1/2 particles, also called fermions. This means they have an intrinsic spin of $\hbar/2$. Pauli's exclusion principle states that no two fermions can have the same wavefunction. Photons are bosons or spin-1 particles. They have an intrinsic spin of $\hbar$ and no exclusion principle. A physical intuition to spin is difficult to obtain since these elementary particles are points and therefore cannot really be thought of as literally spinning. Instead, this intrinsic angular momentum needs to be taken as mathematical and experimental fact.

[11] Summing over the spin of many nucleons can give a variety of total nuclear spin. However, one of these total spins is generally the most stable and so for each isotope there is a fixed nuclear spin value.

3.1.4 Zeeman & light shifts

In the presence of a low strength external magnetic field, the energy of the levels shift proportional to $\hat{\mathbf{F}} \cdot \hat{\mathbf{B}}$. If we define the z-axis along the magnetic field then the shift is proportional to Bm_F, where m_F is the magnetic quantum number of the total angular momentum. The magnetic field splits states with different magnetic numbers, removing the last layer of degeneracy. This effect is linear and so the shifts on $|F, \pm m_F\rangle$ are equal in magnitude and opposite in sign and so the gaps between neighbouring states are the same. For higher fields a second effect becomes relevant due to the coupling between the spin and orbital angular momentum that results in a shift proportional to the square of the previous shift. This shift is called the quadratic Zeeman effect and it shifts states $|F, \pm m_F\rangle$ the same amount with the *same* sign.

An electromagnetic field also shifts the levels. These *light shifts* are most relevant to this work in the limit where the field is strongly detuned from the transition. In that case the light shift is given by $\Omega^2/4\Delta$, where Δ is the detuning and Ω is the Rabi frequency introduced in Section 3.2.1.

3.1.5 Full structure

We now have states uniquely identified by the quantum numbers $|n, l, j, F, m_F\rangle$. Generally states are not written in this format. In chemistry the spin effects are not generally important and so states are written with the first two quantum numbers

$$nl \tag{3.14}$$

where l is generally represented by letters. For example, $l = 0$ is the S orbital and $l = 1$ is the P orbital. With fine structure and hyperfine structure we will write

$$nl_j \left|F, m_F\right\rangle . \tag{3.15}$$

3.1.6 Electronic structure of alkali atoms

Everything above is for the hydrogen atom, and all other atoms have multiple electrons. These electrons interact and so performing analysis like above becomes very difficult. The majority of this thesis considers alkali atoms - primarily ^{87}Rb. Rubidium has 37 electrons. We can express the first 36 electrons in ground state as

$$1\mathrm{S}^2 2\mathrm{S}^2 2\mathrm{P}^6 3\mathrm{S}^2 3\mathrm{P}^6 3\mathrm{D}^{10} 4\mathrm{S}^2 4\mathrm{P}^6 \tag{3.16}$$

where the superscripts are the number of electrons in that level. This means that the electrons fill all the levels *except* for one spare electron; the same holds for all other alkali atoms. A surprisingly powerful picture is to then think of the atom as a single electron outside of a core - which includes the nucleus and the other 36 electrons - of charge $+e$. This core creates a Coulomb potential with the same charge, though a different mass, to the hydrogenic case.

There are other differences to take into account. The orbitals are probability distributions with different shapes, so for different l orbitals the amount of the distribution contained within the core is different. The lower l orbitals penetrate the core more and so the approximation of a hydrogenic potential is less accurate. This means that they, on average, see a deeper potential than they would in hydrogen, and so those orbitals are shifted to lower energies. For higher l the orbitals are closer to the hydrogenic forms. This means that the different l orbitals are shifted away from each other; in fact, the shift is substantial enough that for rubidium the 5S level has a lower energy than the 4D level, and so it is filled first. The second key difference is that, due to more nucleons being added, the nuclear spin is not necessarily 1/2 any more. This can lead to much richer structure than the hydrogen atom.

It is this picture which will be used in much of this thesis. There is an inner core of electrons and the nucleus, and a single electron that is manipulated. ^{87}Rb has a nuclear spin of 3/2 and so the ground state 5S is split into two hyperfine levels $5^2\mathrm{S}_{1/2}\,|F=1, m_F\rangle$ and $5^2\mathrm{S}_{1/2}\,|F=2, m_F\rangle$, where the superscript is $2s+1$. The relevant excited states are then those with $l=1$, which we separate into two sets of states due to the fine structure splitting: the D_1 line $5^2\mathrm{P}_{1/2}$ and the D_2 line $5^2\mathrm{P}_{3/2}$. The fine structure splitting is large enough that these lines can be considered separately. The hyperfine splitting, which allows for $F=1,2$ in the D_1 line and $F=0,1,2,3$ in the D_2 line, is considerably smaller and so it is often necessary to consider the full structure of the line for the work in this thesis.

3.2 Interactions of atoms & light

I now introduce a key concept for this thesis: how light can be used to manipulate the state of the outer electron of an alkali atom.

3.2.1 Rabi oscillations

Let us consider a single atom exposed to a single-mode oscillating electric field at frequency ω, for example, a single-mode laser. We assume that the frequency and polarisation match such that the field acts on *a single transition*. This means that we can consider the atom as a two-level system with a ground and an excited state, which we label as $|0\rangle$ and $|1\rangle$ respectively, as shown in Figure 3.1. This gives us a Hamiltonian ($\hbar = 1$)

$$\hat{H} = \omega_g\,|0\rangle\langle 0| + \omega_e\,|1\rangle\langle 1|\,. \tag{3.17}$$

The atom has an electric dipole $-e\hat{\mathbf{r}}$ and so the interaction with the field gives an extra Hamiltonian term

$$\hat{H}(t) = \omega_0 \left|1\right\rangle \left\langle 1\right| + e\hat{\mathbf{r}} \cdot \hat{\mathbf{E}}_0 \cos(\omega t) \tag{3.18}$$

where we have moved to a reference frame where $\omega_g = 0$ and $\omega_0 = \omega_e - \omega_g$ is the transition frequency between the two-levels.

Our wavefunction for the atom lives in some state

$$\left|\psi(t)\right\rangle = c_g(t)\left|0\right\rangle + c_e(t)\left|1\right\rangle \tag{3.19}$$

and the Hamiltonian's action upon that state gives us

$$\dot{c}_g = -i\frac{\Omega}{2}\mathrm{e}^{i\Delta t}c_e, \quad \dot{c}_e = -i\frac{\Omega^*}{2}\mathrm{e}^{-i\Delta t}c_g \tag{3.20}$$

where we have moved to a rotating frame, defined the detuning $\Delta = \omega - \omega_0$ and the *Rabi frequency*

$$\Omega = \left\langle 0\right| e\hat{\mathbf{r}} \cdot \hat{\mathbf{E}}_0 \left|1\right\rangle . \tag{3.21}$$

Combining these coupled differential equations gives a second order equation for c_e

$$\frac{\mathrm{d}^2 c_e}{\mathrm{d}t^2} + i\Delta\frac{\mathrm{d}c_e}{\mathrm{d}t} + \frac{|\Omega|^2}{2}c_e = 0. \tag{3.22}$$

Taking $c_g(0) = 1$ then the population in the excited state oscillates

$$|c_e(t)|^2 = \frac{\Omega^2}{W^2}\sin^2\left(\frac{Wt}{2}\right) \quad \text{where} \quad W^2 = \Omega^2 + \Delta^2. \tag{3.23}$$

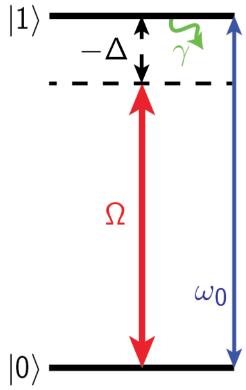

Figure 3.1: Diagram of a two-level system driven between $\left|0\right\rangle \leftrightarrow \left|1\right\rangle$ by a coherent field at Rabi frequency Ω and with detuning Δ.

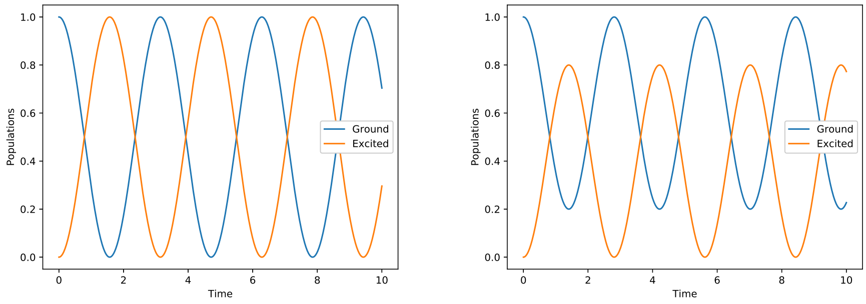

(a) Resonant **(b)** Detuned

Figure 3.2: Populations in the ground and excited states of a two-level atom driven with coherent radiation with Rabi frequency Ω with time in units Ω^{-1}.

At resonance, $\Delta = 0$, these *Rabi oscillations* reduce to

$$|c_e(t)|^2 = \sin^2\left(\frac{\Omega t}{2}\right) \quad \rightarrow \quad |c_g(t)|^2 = \cos^2\left(\frac{\Omega t}{2}\right). \tag{3.24}$$

Quite simply the atom oscillates completely between the two states with the Rabi frequency. This allows us to prepare specific superpositions of the two states. Allowing $\Omega t = \pi$ prepares the atom entirely in the excited state, while $\Omega t = \pi/2$ prepares an equal superposition of the two. These are called π- and $\pi/2$-pulses respectively.

Figure 3.2 shows this resonant behaviour. We also see that with a non-zero detuning then we still have oscillations but some population always remains in the ground state and the oscillations occur on a faster timescale.

3.2.2 Spontaneous emission

Rabi oscillations imply entirely coherent interactions between the field and the atom. This ignores an important fact: *spontaneous emission*. The excited state is by nature unstable and so decays back to the ground state by emitting a photon. This happens on a time-scale defined by the spontaneous emission rate [11]

$$\gamma = \frac{2e^2\omega_0^3}{3\varepsilon_0 hc^3}\,|\langle g|\,\hat{\mathbf{r}}\,|e\rangle|^2. \tag{3.25}$$

We can include this in a master equation for the Rabi oscillation picture

$$\dot{\rho} = -i[\hat{H}, \rho] + \frac{\gamma}{2}\mathcal{D}[|g\rangle\langle e|]\rho. \tag{3.26}$$

Figure 3.3 shows that spontaneous emission damps the oscillations. When $\gamma \gg \Omega$ then this emission process dominates and there are no oscillations and we reach a steady state quickly. This steady state is the balance of how much population is on

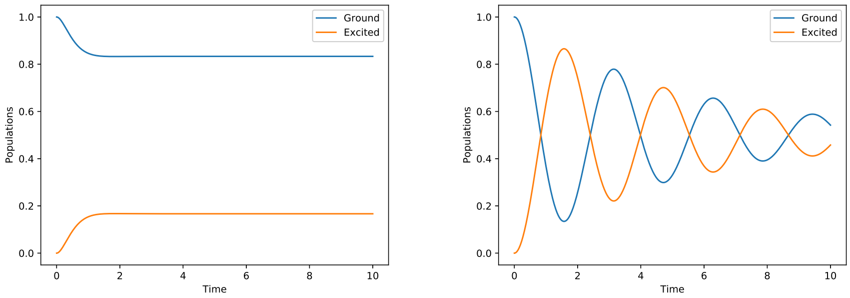

(a) $\gamma = 3\Omega$ **(b)** $\gamma = \Omega$ (master equation)

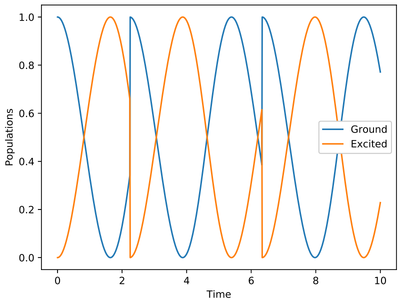

(c) $\gamma = \Omega$ (single trajectory)

Figure 3.3: Populations in the ground and excited states of a two-level atom with spontaneous emission rate γ driven with resonant coherent radiation at Rabi frequency Ω with time in units Ω^{-1}.

average excited before an emission. Thus for high γ, that steady state is primarily the ground state. With $\gamma \lesssim \Omega$ and zero detuning, then we see decaying oscillations to some steady state much closer to an even split between the states.

Mapping to the trajectory picture shows that the oscillations are still present and continue indefinitely. The difference is that the spontaneous emission events *reset* the oscillations. This means the master equation, which is the *average* over all possible trajectories, is the average of oscillations with different phases. After a timescale allowing for a few events, then the phase of the oscillations is evenly distributed. This means that a single trajectory may show oscillations, but the average will completely destructively interfere, producing a steady state.

3.2.3 Selection rules

So far we have considered just two states and for both the coherent and dissipative cases we have to evaluate quantities related to the electric dipole moment

$$\langle g | \hat{\mathbf{r}} | e \rangle . \tag{3.27}$$

For real atoms these quantities can be non-zero or zero, i.e. *allowed* and *forbidden* transitions. Due to the symmetries of the systems, the parity of the state must change. We also have to conserve angular momentum. This gives us the following set of rules [6]:

- $\Delta l = \pm 1$. The parity of the azimuthal wavefunction is given by $(-1)^l$ and so this must change by one to flip parity. This forbids, for example, $S \leftrightarrow S$ or $S \leftrightarrow D$ transitions.

- Δm depends on the polarisation of the light. For linear z- or, as it will called henceforth, π-polarised light $\Delta m = 0$. For σ_+- and σ_--polarised light then $\Delta m = +1, -1$ respectively. For $x-$ or $y-$polarised light, we can think of them as a combination of both $\sigma_\pm$ and so $\Delta m = \pm 1$.

- $\Delta s = 0$. Light does not interact with the spin of the electron and so this cannot change. This limits the change of angular momentum to either zero or ±1.

Remembering the relevant set of levels for a ^{87}Rb atom this means that the two lower hyperfine levels, $5^2\mathrm{S}_{1/2}\left|F = 1, 2\right\rangle$ cannot be coupled because they have the same l and so the $\left|F = 2\right\rangle$ state does not decay[12]. Those ground states can be coupled to the states in the D_1 or D_2 line provided that $\Delta F = 0, \pm 1$ and, making use of the correct light polarisations, $\Delta m_F = 0, \pm 1$.

3.2.4 Raman transitions

A key component for the work in this thesis is that of Raman transitions. We couple our ground and excited states $\left|0\right\rangle$ and $\left|1\right\rangle$ via some intermediary state $\left|m\right\rangle$, as shown in Figure 3.4. These could be driven by the same laser, or by two separate lasers. In the latter case, either the frequency of the drives, the polarisation of the drives, or both might be different. Moving to the interaction picture, we have a Hamiltonian

$$\hat{H} = \frac{\Omega_0}{2}\mathrm{e}^{i\Delta_0 t}\left|m\right\rangle\left\langle 0\right| + \frac{\Omega_1}{2}\mathrm{e}^{i\Delta_1 t}\left|m\right\rangle\left\langle 1\right| + \text{h.c.} \tag{3.28}$$

where h.c. means Hermitian conjugate and therefore provides the reverse processes and $\Omega_{0,1}$ and $\Delta_{0,1}$ are the Rabi frequencies and detunings for the two transitions. From the form of the Hamiltonian, it can be seen that there is no direct coupling between $\left|0\right\rangle \leftrightarrow \left|1\right\rangle$.

If both drives are resonant and we start in the ground state, as in Figure 3.5, then we can see that the population moves through $\left|m\right\rangle$ to $\left|1\right\rangle$ and back. Oscillations

---

[12] In reality, there are other types of transitions possible. Magnetic-dipole and electric-quadrupole transitions do not need to change the parity and so the $F = 2$ states can decay via those processes. However, such transitions generally occur on much longer timescales than electric-dipole transitions and so we can consider the $F = 2$ level as a metastable "ground state" over the timescales considered in this thesis.

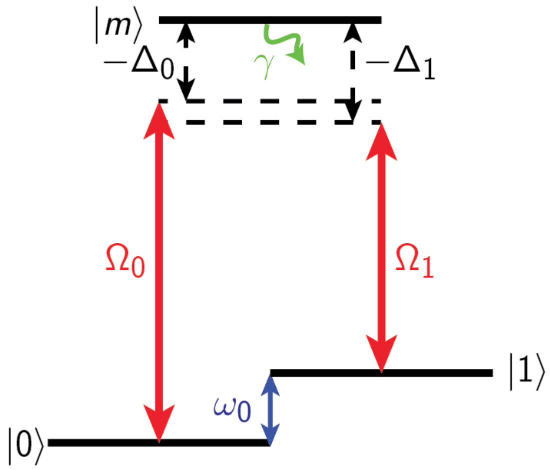

Figure 3.4: Diagram of a Raman transition between $|0\rangle \leftrightarrow |1\rangle$ formed via Rabi oscillations between an intermediary state $|m\rangle$ and both states. The driving fields have Rabi frequencies $\Omega_{0,1}$ and detunings $\Delta_{0,1}$.

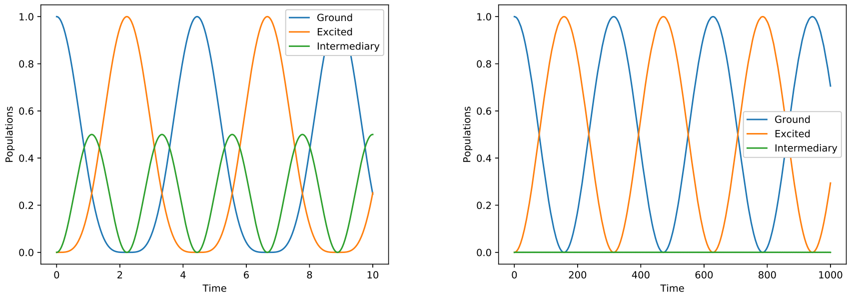

(a) $\Delta = 0$

(b) $\Delta = 100\Omega$

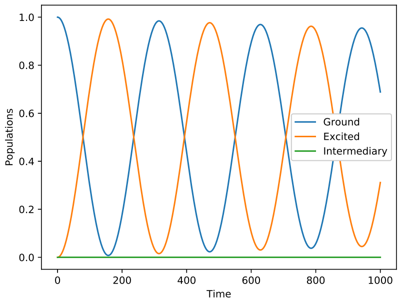

(c) $\Delta = 100\Omega,\ \gamma = \Omega$

Figure 3.5: Populations in the ground, excited and intermediary states of an atom undergoing Raman transitions. Both driving fields have Rabi frequency Ω with time in units of Ω^{-1}.

between the ground state and the excited state are complete, though they are not sinusoidal due to the intermediary step.

However, if the detunings are instead large then the same process happens but with significantly lower population in the intermediary level and on a much slower timescale. The intermediary state is only slightly excited by the process, yet the full population is transferred to the excited state. What we have looks a lot like Rabi oscillations between the ground and excited state, yet there is no direct coupling between the two. Instead, we have two-photon transitions where a photon is absorbed from the first mode and emitted into the second via a *virtual excitation* of the intermediary state.

Since the intermediary state is only virtually excited we can *adiabatically eliminate* the state from the Hamiltonian, i.e. since there is almost no population there, we can trace it out. The Hamiltonian for the remaining two-level system then effectively describes Rabi oscillations between those states where the rate is dependent on the true Rabi frequencies and detunings as well as the mismatch between the two light fields.

Of course we can also get Rabi oscillations between two states directly, so why is this technique useful? Raman transitions allow us to couple two states between which a direct transition is forbidden. This means that both are stable, and there is no spontaneous emission from $|1\rangle \rightarrow |0\rangle$ (or vice versa). This allows us to produce systems without dephasing due to spontaneous emission events as the only dephasing in this system comes from spontaneous emission from the intermediary state. Remaining in the three state system we can include spontaneous emission from that intermediary state. Figure 3.5c shows that the effective Rabi oscillations dephase after a significantly larger number of oscillations than if we used an excited state. For most of this thesis we operate in a hierarchy of scales $\Delta \gg \Omega \gg \gamma$ and so the rate of spontaneous emission is so small that we can disregard it.

3.3 Cold atoms & Bose-Einstein condensates

To be able to manipulate and monitor the internal states of these atoms requires them to be "contained". This cannot happen if the atom is moving around. This means the atoms need to be cooled and held in some sort of trap. In this Section, I give a brief explanation of these processes. More detail can be found in [6,11].

3.3.1 Laser cooling

Much of laser cooling relies on the recoil force of an atom scattering photons. A photon carries momentum $\hbar\mathbf{k}$, where $|\mathbf{k}| = 2\pi/\lambda$ is the wavevector and λ is the wavelength of the photon. Momentum is conserved and so, if an atom absorbs a photon with momentum $\hbar\mathbf{k}$ then the atom gains $\hbar\mathbf{k}$ momentum. Equivalently, spontaneous emission carries away momentum. Spontaneous emission is randomly distributed, so this momentum "kick" is randomly distributed.

Initially, we consider a beam of atoms travelling in a single specific direction which takes them *into* a laser beam. Atoms travelling into the laser beam thus absorb photons travelling in the opposite direction to them which slows them down. They then emit and are able to absorb again. Absorbing multiple photons eventually means this process should slow the photons down to velocities limited by the random walk process induced by the spontaneous emission.

However, the atoms are travelling and so they see a Doppler shifted version of the light. This means that light resonant for the atom initially, once it has been slowed and sees a different Doppler shifted frequency, is no longer resonant for that atom. There are two methods to deal with this: a Zeeman slower and chirp cooling. The Zeeman slower is a tapered solenoid that, due to the changing magnetic field, Zeeman shifts the relevant states to compensate for the slowing. Chirp cooling involves changing the frequency of the laser to compensate instead.

In three dimensions, a similar technique known as optical molasses is used. This involves three pairs of counter-propagating laser beams at the same frequency. The frequency is chosen with negative detuning, $\Delta = \omega - \omega_0$, such that the Doppler shift causes the atom to see the laser beam it is travelling into to be closer to the resonant frequency than its pair. The momentum is on average reduced rather than increased as the atom preferentially interacts with the field of direction opposite to its direction.

The heating caused by the random spontaneous emission can be balanced against the cooling to find the limit of such a technique. For a spontaneous emission rate γ the optimal detuning is $\Delta = -\gamma/2$ and the Doppler cooling limit is

$$T_D = \frac{\hbar\gamma}{2k_B}. \tag{3.29}$$

This is not the ultimate limit of laser cooling. The two counter-propagating lasers interfere to produce a standing wave. If they have orthogonal polarisations then the standing wave has a modulated polarisation pattern. This polarisation gradient means that different magnetic states of the atom see a different modulated light shift and therefore a different potential.

Consider an atom travelling through that potential; it must convert potential energy to and from kinetic energy. An atom at its largest potential will have its lowest kinetic energy and vice versa. The laser can be tuned such that the atom is most likely to absorb a photon at this point of highest potential. It can then emit a photon with polarisation such that it leaves the atom in a different magnetic state. This state sees a different modulation to the potential and so it is not at its maximum potential energy. This means that the spontaneously emitted photon has to have carried off some of that potential energy. This process means that the most likely outcome is for the atom to climb a potential hill and then lose some (or all) of the potential energy it has gained and start back over again at low potential. This repeated climbing of hills only to lose the gained energy has lead to this process being given the rather poetic name of *Sisyphus cooling*.

This process works until the energy of the atoms is such that the kinetic energy is lower than the potential barrier. This means that, up to some limit, the smaller that barrier can be made, i.e. large detuning, the colder the atoms become. The limit is actually still set by the random recoils from the spontaneous emission events, but in this case it is set by a single recoil rather than the random walk process and so the limit is much lower

$$T_R = \frac{\hbar^2 |\mathbf{k}|^2}{k_B M} \tag{3.30}$$

where M is the mass of the atom.

To cool atoms down to temperatures useful for quantum optics experiments the following procedure might be followed:

1. Create a beam of atoms and pass that beam through a Zeeman slower into an optical molasses[13] with detuning $\Delta = -\gamma/2$.

2. Detuning is held long enough for the ensemble to approach the Doppler limit.

3. Greatly increase the detuning and reduce the intensity such that Sisyphus cooling takes over.

3.3.2 Trapping

Our discussion of Sisyphus cooling already implies the concept behind trapping: reducing the velocity in a potential such that the atoms do not have the kinetic energy to move out of the potential dip. The first type of trap to discuss is a magneto-optical trap (MOT). This uses optical molasses with a magnetic field gradient. The field is zero at the centre and linearly increases in all directions. This field is not what directly traps the atoms[14]; the field creates Zeeman shifts on the levels providing an imbalance in the scattering forces that encourages the atom to move back towards the centre. Often a MOT will be overlapped with the optical molasses at the time of collection from the slowed beam, then turned off once the atoms have accumulated to allow them to be further cooled.

---

[13] For those atoms not suitably slowed by the Zeeman slower, their velocity will simply be too large to be "captured" by the optical molasses and they will be lost. Overlapping a trap over the optical molasses, as discussed in Section 3.3.2, allows us to increase that capture velocity.

[14] Magnetic trapping, where the atoms are directly trapped by the field, is also possible. Here the magnetic dipole provides a force on the atom $\propto -m_F \mathrm{d}B/\mathrm{d}z$. For cold atoms it is possible for these trajectories to bend round to form closed loops, localising the atoms. This of course only works for one sign of magnetic state m_F and so cannot be used for the sorts of experiments described in this thesis.

A second type of trap uses the other force exerted by light on atoms: the dipole force. The energy of a dipole in an electric field is

$$U = \frac{1}{2} e\mathbf{r} \cdot \mathbf{E} \quad \rightarrow \quad F_z = -\frac{\partial U}{\partial z} \propto E \frac{\partial E}{\partial z}. \tag{3.31}$$

If the radiation propagates along that axis we have a force

$$F_z = -ex \left[\frac{\partial E_0}{\partial z} \cos(\omega t - kz) + kE_0 \sin(\omega t - kz) \right]. \tag{3.32}$$

Taking time averages of these two terms and following the derivation through gives us that the second term is related to the scattering force that we discussed with laser cooling [11]. The first term is the dipole force and is important when the field gradient is strong. The dipole force for large detuning can be shown to be equal to the derivative of the light shift. This means that if we have a gradient on the light shift, then the potential follows that gradient as

$$U_{\text{dipole}} \approx \frac{\hbar \Omega^2}{4\Delta}. \tag{3.33}$$

If the detuning is negative then this potential is at a minimum at points of high intensity and the atoms are attracted to the points of highest intensity.

An extension of this dipole force is that it can form a lattice potential. Forming a standing wave with counter-propagating lasers creates a pattern of maximum intensity and zero intensity. The gradient is high since that change happens over half a wavelength and so forms a pattern of potential wells for an ensemble of atoms in 1D, 2D, or 3D. If the potential is deep then the atoms will be strongly localised to one site, while if the filling factor for the lattice - i.e. the average occupation per site - is low then the atoms should be spatially separated. This means that the atoms should not interact with each other or move around too much, allowing manipulations of the internal states with light without concern for the external states of the atoms[15].

3.3.3 Bose-Einstein condensation

When the temperature of the atoms is reduced to extremely low temperatures then a different type of physics appears. At some critical temperature, Bose-Einstein

---

[15] This is the limit useful for the work in this thesis, but it should be noted that optical lattices are much more than a tool to isolate atoms. Indeed, atoms in optical lattices are an interesting enough field for books (or at least one book) to have been written about them [12]. They can be described by a rich Hamiltonian that allows atoms to hop between sites and includes a wide variety of possible ways the atoms can interact with one another. Those interactions might be, for example, that two atoms cannot be on the same site, or perhaps that atoms prefer to be sat next to atoms with the opposite spin. The evolution of the system depends on the strengths and forms of those terms, as well as the filling factor and the shape and dimensions of the lattice. This interplay can produce complex dynamics and a wide range of ground states, offering a fascinating window into fundamental many-body quantum mechanical behaviour.

condensation takes place. In a Bose-Einstein condensate (BEC), the vast majority of atoms occupy the same ground state and have to be thought of as a single macroscopic fluid. This is because the de Broglie wavelength, defined as,

$$\lambda = \frac{h}{p} \tag{3.34}$$

increases considerably as the velocity is reduced. At some velocity this delocalisation of the atoms is on a similar scale to the spacing between atoms in the gas. At this point, thinking of the gas as an ensemble of localised individual atoms is not accurate; there is a global wavefunction that governs the entire fluid and follows a non-linear Schrödinger equation called the Gross-Pitaevskii equation.

Reaching the temperatures needed for Bose-Einstein condensation requires an extra form of cooling: evaporative cooling. Much simpler in concept than laser cooling, evaporative cooling involves trapping and cooling atoms and then reducing the depth of that trap sharply. The atoms with high velocities then escape taking their energy with them. The rest of the gas assumes a new Maxwell-Boltzmann distribution with a lower average energy and therefore a *lower velocity*. Repeated changes of the trap depth cool the atoms further, but it is necessary for the atoms to be laser cooled first to leave significant population after evaporative cooling. In such a way, this acts as an extra step to the cooling process described in Section 3.3.1

BECs have been at the forefront of atomic physics since they were first produced in 1995 and many of those experiments have considered a problem that this thesis focuses on - many-body dynamics in atomic gases. The proposals discussed in this thesis do not require BECs. However, many of them were inspired by BEC experiments and many of them could be implemented in a BEC. Discussions on the most important BEC experiments to this work are found in Sections 4.4.3 and 9.1.

3.4 Atomic state representations

We now know the full set of states available to the atoms and that they can be cooled and trapped. This is the toolbox necessary for experiments on alkali atoms. We now need a mathematical framework to deal with them algebraically and computationally. The atoms are complex sets of many levels, but to treat them that way is generally infeasible. Instead, we want to approximate their wavefunction to discrete subsets of those levels. I have discussed how to carefully control excitations with light fields and so restrict the atom to a subset to very good approximation. In this Section, I introduce a formalism to describe the states of single atoms in such subsets as well as ensemble of atoms.

3.4.1 Two-level systems

For a single atom, the simplest possible system is to isolate two states, making the atom a pseudo spin-1/2. Our basis is then just two states: $|0\rangle$ and $|1\rangle$ (alternatively these states can be labelled $|\downarrow\rangle, |\uparrow\rangle$) and our atomic wavefunction then lives in some superposition

$$|\psi\rangle = \alpha\,|0\rangle + \beta\,|1\rangle = \begin{pmatrix} \alpha \\ \beta \end{pmatrix} \tag{3.35}$$

where α, β are complex numbers that satisfy $\alpha^2 + \beta^2 = 1$. More generally, it exists in some density matrix

$$\rho = \begin{pmatrix} c_{00} & c_{01} \\ c_{10} & c_{11} \end{pmatrix} \tag{3.36}$$

where for the pure state above we have

$$\rho = |\psi\rangle\langle\psi| = \begin{pmatrix} \alpha \\ \beta \end{pmatrix} \begin{pmatrix} \alpha^* & \beta^* \end{pmatrix} = \begin{pmatrix} |\alpha^2| & \alpha\beta^* \\ \beta\alpha^* & |\beta^2| \end{pmatrix}. \tag{3.37}$$

For a spin-1/2 particle any operator acting on the state can be described by some combination of the Pauli operators (and the identity)

$$\hat{\sigma}_x = |0\rangle\langle 1| + |1\rangle\langle 0| = \begin{pmatrix} 0 & 1 \\ 1 & 0 \end{pmatrix} \tag{3.38}$$

$$\hat{\sigma}_y = i(|0\rangle\langle 1| - |1\rangle\langle 0|) = \begin{pmatrix} 0 & i \\ -i & 0 \end{pmatrix} \tag{3.39}$$

$$\hat{\sigma}_z = |1\rangle\langle 1| - |0\rangle\langle 0| = \begin{pmatrix} -1 & 0 \\ 0 & 1 \end{pmatrix}. \tag{3.40}$$

Note that the ladder operators introduced in Section 3.1.1 can be formed as they were there: $\hat{\sigma}_\pm = \hat{\sigma}_x \pm i\hat{\sigma}_y$.

These matrices each have two eigenstates with eigenvalues ± 1. These are

$$|x_\pm\rangle = \frac{1}{\sqrt{2}}(|0\rangle \pm |1\rangle) \tag{3.41}$$

$$|y_\pm\rangle = \frac{1}{\sqrt{2}}(|0\rangle \mp i\,|1\rangle) \tag{3.42}$$

$$|z_-\rangle = |0\rangle,\ |z_+\rangle = |1\rangle. \tag{3.43}$$

In the same way that the Pauli operators span the operator space, any of these eigenstate pairs span the state space. The three pairs, and thus the state, can also be mapped to the axes of a sphere of unit radius. Our state on the sphere is given simply by solving

$$|\psi\rangle = \sin\left(\frac{\theta}{2}\right)|0\rangle + \mathrm{e}^{i\varphi}\cos\left(\frac{\theta}{2}\right)|1\rangle \tag{3.44}$$

where θ and φ define spherical coordinates in the usual way. This is the Bloch sphere and the state described in this way is the Bloch vector.

3.4.2 Spinor systems

Let us now consider a three level, or spin-1, atom. Our basis now has three states: $|-1\rangle$, $|0\rangle$ and $|+1\rangle$. Our wavefunction lies in some superposition

$$|\psi\rangle = \alpha\,|-1\rangle + \beta\,|0\rangle + \gamma\,|+1\rangle = \begin{pmatrix}\alpha\\ \beta\\ \gamma\end{pmatrix} \tag{3.45}$$

with the more general density matrix for such a state obtained in the usual way.

We can define spin operators for these spin-1 atoms just like the Pauli matrices described the two-level systems

$$\hat{\sigma}_x = \frac{1}{\sqrt{2}}\left(|0\rangle\langle+1| + |-1\rangle\langle 0| + |+1\rangle\langle 0| + |0\rangle\langle -1|\right) = \frac{1}{\sqrt{2}}\begin{pmatrix}0 & 1 & 0\\ 1 & 0 & 1\\ 0 & 1 & 0\end{pmatrix} \tag{3.46}$$

$$\hat{\sigma}_y = \frac{i}{\sqrt{2}}\left(|0\rangle\langle+1| + |-1\rangle\langle 0| - |+1\rangle\langle 0| - |0\rangle\langle -1|\right) = \frac{i}{\sqrt{2}}\begin{pmatrix}0 & 1 & 0\\ -1 & 0 & 1\\ 0 & -1 & 0\end{pmatrix} \tag{3.47}$$

$$\hat{\sigma}_z = |1\rangle\langle 1| - |-1\rangle\langle -1| = \begin{pmatrix}-1 & 0 & 0\\ 0 & 0 & 0\\ 0 & 0 & 1\end{pmatrix}. \tag{3.48}$$

Generally speaking the ladder operators will be used more frequently in this thesis and these are defined as

$$\hat{\sigma}_- = \sqrt{2}\left(|0\rangle\langle+1| + |-1\rangle\langle 0|\right) = \begin{pmatrix}0 & 0 & 0\\ \sqrt{2} & 0 & 0\\ 0 & \sqrt{2} & 0\end{pmatrix} \tag{3.49}$$

$$\hat{\sigma}_+ = \sqrt{2}\left(|0\rangle\langle-1| + |+1\rangle\langle 0|\right) = \begin{pmatrix}0 & \sqrt{2} & 0\\ 0 & 0 & \sqrt{2}\\ 0 & 0 & 0\end{pmatrix}. \tag{3.50}$$

The form of the ladder operators is reminiscent of the annihilation and creation operators for the electromagnetic field. Both feature off diagonal terms that move populations one rung of a ladder up or down. $\hat{\sigma}_z$ plays the role of the number operator in this picture, in that it is proportional to the number of "excitations" in the system. The key difference of course is that these atomic operators act on a finite Hilbert space, whereas there is no bound to the number of photons in a field.

Unlike the spin-1/2 case these do not form a complete set of operators. For example, the operator for the population in the $|0\rangle$ state, $|0\rangle\langle 0|$, cannot be formed from these operators. The third degree of freedom in the state means we require more operators to describe action upon the states. A full set can be formed with the three operators above, the identity and the following [13]

$$\hat{q}_{xy} = i\begin{pmatrix} 0 & 0 & 1 \\ 0 & 0 & 0 \\ -1 & 0 & 0 \end{pmatrix} \tag{3.51}$$

$$\hat{q}_{yz} = \frac{i}{\sqrt{2}}\begin{pmatrix} 0 & 1 & 0 \\ -1 & 0 & -1 \\ 0 & 1 & 0 \end{pmatrix} \tag{3.52}$$

$$\hat{q}_{zx} = \frac{1}{\sqrt{2}}\begin{pmatrix} 0 & 1 & 0 \\ 1 & 0 & -1 \\ 0 & -1 & 0 \end{pmatrix} \tag{3.53}$$

$$\hat{D}_{xy} = \begin{pmatrix} 0 & 0 & 1 \\ 0 & 0 & 0 \\ 1 & 0 & 0 \end{pmatrix} = \frac{1}{2}\left(\hat{q}_{xx} - \hat{q}_{yy}\right) \tag{3.54}$$

$$\hat{Y} = \frac{1}{\sqrt{3}}\begin{pmatrix} 1 & 0 & 0 \\ 0 & -2 & 0 \\ 0 & 0 & 1 \end{pmatrix} = \frac{1}{2\sqrt{3}}\left(2\hat{q}_{zz} - \hat{q}_{xx} - \hat{q}_{yy}\right) \tag{3.55}$$

where we have defined the nematic tensor $\hat{\mathbf{q}}$ with elements [13–15]

$$\hat{q}_{ij} = \hat{\sigma}_i\hat{\sigma}_j + \hat{\sigma}_j\hat{\sigma}_i - \frac{4}{3}\delta_{ij}. \tag{3.56}$$

For higher spin particles the number of degrees of freedom for the state increases and so the number of operators required increases too. In the few cases in this thesis that spin-2 or higher particles are considered, the states are confined in such a way that these extra operators are not necessary.

3.4.3 Dicke states

This thesis generally concerns ensembles of atoms and so a collective basis is needed. Let us consider an ensemble of N atoms each in some state $|\psi_i\rangle$. The collective wavefunction is then the product state $|\Psi\rangle = |\psi_1\rangle \otimes |\psi_2\rangle \otimes |\psi_3\rangle \otimes \cdots \otimes |\psi_N\rangle$. The basis size to properly describe such a state for N two-level atoms scales like $\sim 2^N$ which limits us to very small numbers of atoms. A more restricted subset of the possibilities is necessary.

In the vast majority of this work, we rely on the fact that these atoms are indistinguishable[16]. This is equivalent to saying that the global spin state is symmetric under particle exchange[17], or more simply, the state does not change if the labels of any two atoms are switched.

This insistence on symmetric states reduces the Hilbert space to a set of states known as Dicke states. These are collective states with a known collective angular momentum length S and $z-$projection m: $|S, m\rangle$. This means that, for a fixed spin length S, we reduce our basis size to $2S + 1$.

Let us consider N two-level atoms all in the same state $|0\rangle$. Remembering that a two-level system is mathematically equivalent to a spin-1/2 particle, $|0\rangle = |S = 1/2, m = -1/2\rangle$. The wavefunction for the ensemble in the collective picture is then $|\Psi\rangle = |1/2, -1/2\rangle^{\otimes N}$ which is equivalent to the Dicke state $|S = N/2, m = -N/2\rangle$. This is a definite total spin of $N/2$ with a definite z-projection $-N/2$.

This picture lets us consider an ensemble of atoms as equivalent to a single large spin. A single large spin has its own ladder operators $\hat{S}_\pm$ which add and subtract one to the magnetic quantum number. Let us consider the action of $\hat{S}_+$ on the Dicke state $|S = N/2, m = -N/2\rangle$,

$$\hat{S}_+ |S = N/2, m = -N/2\rangle \propto |S = N/2, m = -N/2 + 1\rangle \, . \tag{3.57}$$

The total magnetic quantum number has increased by one. This is interesting when we move back to the picture of individual spins, where, since the atoms are indistinguishable and thus equally likely to have been excited, the wavefunction is now a balanced superposition of all possible combinations of exactly one atomic excitation in the ensemble

$$|N/2, -N/2 + 1\rangle = \frac{1}{\sqrt{N}} \left(|1\rangle \otimes |0\rangle \otimes |0\rangle \otimes \cdots + |0\rangle \otimes |1\rangle \otimes |0\rangle \cdots + \cdots \right) . \tag{3.58}$$

Instead of raising a single atom, we have spread the excitation throughout the ensemble. Note that this is *not* the same as the product of each atom being partially

---

[16] In theory, the atoms are held at different points of a lattice such that they could be distinguished. However, we consider them to be identically coupled to the fields that drive them such that to those fields they are indistinguishable. Where we consider processes that can break that indistinguishability, we do not operate in a Dicke state basis.

[17] Of course, this is not strictly true. For fermions, the total wavefunction should in fact be anti-symmetric under particle exchange due to Pauli's exclusion principle. For the purposes of this thesis, we assume the global spin wavefunctions to be symmetric, and that the anti-symmetry is instead in the spatial degree of freedom that we do not consider.

excited as the state insists on *exactly* one excitation. The state for each atom is

$$\rho_i = \frac{N-1}{N} \left|0\right\rangle \left\langle 0\right| + \frac{1}{N} \left|1\right\rangle \left\langle 1\right| . \tag{3.59}$$

Note that this is a density matrix whilst the collective state was a pure state. This is because the Dicke states, excluding $\left|N/2, \pm N/2\right\rangle$, are entangled. They feature an exact number of excitations, and so, like the Fock states, are inherently non-classical. As with Fock states, they are a useful basis for calculation but are not trivial to produce in the laboratory. This is the motivation behind our work on producing Dicke states for an atomic ensemble found in Chapter 6.

3.4.4 Collective spin operators

The Dicke states allow us to consider the ensemble as a large spin of length S with associated operators $\hat{S}_\pm$ and $\hat{S}_z$. These operators are formed by summing over the individual spin operators, for example,

$$\hat{S}_z = \sum_{i=0}^{N} \sigma_z^{(i)}. \tag{3.60}$$

More useful is the form of these in the basis of Dicke states where

$$\hat{S}_z = \sum_{m=-S}^{S} m \left|S, m\right\rangle \left\langle S, m\right| \tag{3.61}$$

$$\hat{S}_\pm = \sum_{m=-S}^{S} \sqrt{S(S+1) - m(m \pm 1)} \left|S, m \pm 1\right\rangle \left\langle S, m\right| . \tag{3.62}$$

Note that $\hat{S}_\pm \left|S, \pm S\right\rangle = 0$ and so the boundary conditions are met. This equation shows that the ladder operators act strongest on states with m close to zero, with coefficients $\sim S$, and weakest on those that are near fully polarised, with coefficients $\sim \sqrt{S}$. This effect is thus more pronounced for larger spins, or, in the case of an ensemble, more spins.

3.4.5 Coherent spin states

It is also useful to consider unentangled pure states of the ensemble: a *coherent spin state* (CSS). Let us take the product state

$$\left|\psi\right\rangle = \left[\sin\left(\frac{\theta}{2}\right) \left|0\right\rangle + \mathrm{e}^{i\varphi} \cos\left(\frac{\theta}{2}\right) \left|1\right\rangle\right]^{\otimes N} . \tag{3.63}$$

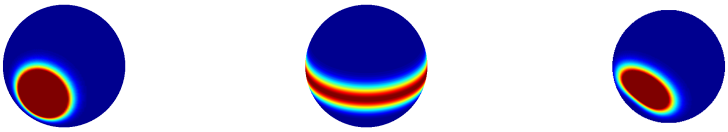

(a) Coherent spin state **(b)** Dicke state **(c)** One-axis twisted state

Figure 3.6: Atomic Q-function plots of different atomic ensemble states.

Clearly such a state is also symmetric to particle exchange and so can describe a state in our indistinguishable system. We can calculate this state in the basis of Dicke states as [16,17]

$$|\theta,\varphi\rangle = \sum_{m=-N/2}^{N/2} \begin{pmatrix} N \\ N/2+m \end{pmatrix}^{1/2} \cos\left(\frac{\theta}{2}\right)^{N/2+m} \sin\left(\frac{\theta}{2}\right)^{N/2-m} e^{i(N/2+m)\varphi}\,|N/2,m\rangle$$
$$|\eta = e^{i\varphi}\tan(\theta/2)\rangle = \frac{1}{(1+|\eta|^2)^{N/2}} \sum_{m=-N/2}^{N/2} \begin{pmatrix} N \\ N/2+m \end{pmatrix}^{1/2} \eta^{N/2-m}\,|N/2+m\rangle\,. \quad (3.64)$$

where we have used that the statistics of the product states will follow a binomial distribution with probabilities given by the superposition of the single atom. Note that, as with the vacuum, the Dicke states $|S,\pm S\rangle$ are also CSSs with $\theta = 0,\pi$.

These states are defined by two angles and a definite length, meaning that they can be mapped to a sphere. Like coherent states of light, CSSs are not orthogonal and so we can define an atomic Q-function. This atomic Q-function lives on a sphere rather than the plane and is formed by the overlap with CSSs [17,18]

$$Q(\eta) = \langle\eta|\,\rho\,|\eta\rangle\,. \quad (3.65)$$

Examples of this are given in Figure 3.6. CSSs appear as circles, like their light analogy, while Dicke states appear as rings similarly to the circles of the Fock states.

3.4.6 Spin squeezing

A sequence of N uncorrelated measurements of some property gives a sample mean and an associated sample variance that scales as $1/N$. Simultaneous measurement of N uncorrelated particles thus gives a variance with ideal scaling $1/N$, called the standard quantum limit (SQL)[18]. A measurement of N correlated particles is not

---

[18] The standard quantum limit is just that, a limit, rather than the scaling of any ensemble measurement. Other sources of noise associated with the ensemble, the experiment or the measurement may increase with N such that the scaling is actually worse than $1/N$.

constricted by the same bound but instead by the Heisenberg limit $1/N^2$. This means that the precision available to quantum states exceeds that for classical states.

If there is some property that we wish to measure precisely, we can couple that property to a quantum system such that the property imprints a phase proportional to its magnitude on the quantum state. This phase is then measured so as to estimate the magnitude of the desired property. For this reason, often the metrological precision available is referred to as the phase sensitivity. Here I discuss how to characterise the metrological properties of an ensemble of spins.

To think about spin squeezing we need to consider the commutator relations for the angular momentum components

$$[\hat{S}_x, \hat{S}_y] = i\hat{S}_z, \quad [\hat{S}_y, \hat{S}_z] = i\hat{S}_x \quad \text{and} \quad [\hat{S}_z, \hat{S}_x] = i\hat{S}_y. \tag{3.66}$$

A squeezing parameter based solely on these relations does not correctly capture the physics because of the fact there are three dimensions. Instead of noise being hidden in a different component, it can simply be that the vector points more along one of the two axes than the other.

A more useful spin squeezing parameter is defined around the mean-spin direction. Here, we use the Heisenberg relation above, but for a set of axes defined by the mean-spin direction and two vectors perpendicular to that direction and each other. Introduced by Kitagawa and Ueda, the spin squeezing parameter is [19, 20]

$$\xi_S^2 = \frac{\min\left(\Delta\hat{S}_\perp^2\right)}{S/2}. \tag{3.67}$$

A state is spin squeezed if, along some axis perpendicular to the mean spin direction, the variance on the spin is smaller than the length of the spin. It can be shown that for a CSS $\xi_S^2 = 1$. If $\xi_S^2 < 1$ then the state is entangled.

A subtly different term, first proposed by Wineland et al [21], is given as

$$\xi_R^2 = \frac{N \min\left(\Delta\hat{S}_\perp^2\right)}{|\langle\hat{\mathbf{S}}\rangle|^2}. \tag{3.68}$$

Whilst the differences to ξ_S^2 are subtle, it offers a distinct advantage. Instead of considering the variances in relation to the uncertainty principle, this parameter tells us directly about the improved phase sensitivity of the state over a CSS for a particular type of phase measurement called Ramsey interferometry. While ξ_S^2 is a witness to entanglement, ξ_R^2 is a witness to useful metrological improvement over a classical state. In many cases, including for the indistinguishable ensemble considered above, the length of the spin is given by S and so the two are equivalent.

Kitagawa and Ueda [19] also introduced a commonly used method to spin squeeze.

The first of these is one-axis twisting, which has been produced in various systems [20, 22]. This involves operating upon the Dicke state $|S, -S\rangle$ with the Hamiltonian

$$\hat{H} = \chi \hat{S}_x^2 = \frac{\chi}{4}(\hat{S}_+^2 + \hat{S}_-^2 + \hat{S}_+\hat{S}_- + \hat{S}_-\hat{S}_+). \tag{3.69}$$

It is clear from the form on the right hand side that this Hamiltonian creates and annihilates pairs of excitations, analogously to the squeezing operator. However, due to the finite size of the Hilbert space, the squeezing is limited to a variance $1/N^{2/3}$ improved over a CSS. Kitagawa and Ueda also introduced two-axis twisted squeezed states [19], which offer Heisenberg limited precision but are yet to be realised experimentally.

There are lots of other methods used to produce spin squeezed states. These include, but are certainly not limited to, the transfer of squeezed light onto an ensemble, quantum non-demolition measurements and adiabatic state preparation of ground states [20, 22].

For the specific case of the Dicke states we run into an issue using either of these spin squeezing parameters as they require a mean-spin direction. The Dicke states have a definite $\hat{S}_z$ and so, by the uncertainty principle, cannot have any information in either of the other coordinates. Considering the atomic Q-function plot in Figure 3.6b we see that the Dicke state is a ring. The mean point of a ring is the centre of it, which has no direction and length of zero. Instead, for Dicke states and entangled states in the vicinity of such states we can use the Dicke squeezing parameter [23]

$$\xi_D^2 = N\frac{(\Delta\hat{S}_z)^2 + 1/4}{\langle \hat{S}_x^2 + \hat{S}_y^2\rangle}. \tag{3.70}$$

For a pure Dicke state $|S, m\rangle$ this is

$$\xi_D^2 = \frac{1}{N + 2 - 4m^2/N} \tag{3.71}$$

and so for $m \sim 0$ and large N offers significant squeezing. This parameter gives us access to the metrological sensitivity equivalently to the Wineland parameter, given in Equation 3.68, and so those central Dicke states offer Heisenberg limited metrology. This parameter also gives access to a minimum bound to the entanglement depth of the system $\lceil \xi_D^{-1} - 2\rceil$ [24]. The entanglement depth quantifies the minimum size of a subset of atoms that are genuinely entangled between all members of the subset.

Another complication arises if we consider an ensemble of spinor particles. As discussed in Section 3.4.7, such an ensemble does not necessarily have maximal spin or live on the surface of the collective Bloch sphere. In such cases, other measures of the phase sensitivity can be used, as in Chapter 8, or a different set of axes can be found to define a sphere that the state does live on, as in Chapter 10.

3.4.7 Bosonic mode picture

For collective spinor states initialised into a fully polarised state - i.e. $|\pm 1\rangle^{\otimes N}$ - then the Dicke model picture above works fine[19]. However, for states involving the zero mode this picture is not suitable. The issue is that two bosons in the $|0\rangle$ state do not have a set collective spin. Instead

$$|1,0\rangle \otimes |1,0\rangle = \sqrt{\frac{2}{3}}\,|2,0\rangle - \sqrt{\frac{1}{3}}\,|0,0\rangle\,. \tag{3.72}$$

This means that, for any product state of indistinguishable spinor atoms with any population in the zero mode, there will be a spread of different angular momentum length states and so a Dicke state representation does not simplify the basis in the same way. The full properties of such superpositions of angular momentum are encountered in many sections of this thesis, and exploiting them is the basis of the proposal in Chapter 8.

Instead of tracking the spin length and polarisation, we track the populations in each state. Simply, each state of our spin-1 atom, $|m\rangle$, has an annihilation operator $\hat{b}_m$ and creation operator $\hat{b}_m^\dagger$. These have exactly the same form and statistics as the photon annihilation and creation operators and so, for example, the number operator in each case is given by $\hat{b}_m^\dagger \hat{b}_m$. Using a basis of Fock states in each state, our wavefunction for N atoms is then given by the superposition

$$|\psi\rangle = \sum_{m,n,o} c_{mno}\,|m\rangle_{-1} \otimes |n\rangle_0 \otimes |o\rangle_{+1} \quad \forall \;\; m,n,o \;\; \text{s.t.} \;\; m+n+o = N. \tag{3.73}$$

Our operators need to be recast in terms of angular momentum operators

$$\hat{S}_i = \begin{pmatrix} \hat{b}_{-1}^\dagger & \hat{b}_0^\dagger & \hat{b}_{-1}^\dagger \end{pmatrix} \hat{\sigma}_i \begin{pmatrix} \hat{b}_{-1} \\ \hat{b}_0 \\ \hat{b}_{-1} \end{pmatrix} \tag{3.74}$$

where $\hat{S}_i$ is the collective equivalent of the single-atom operator $\hat{\sigma}_i$. Note that replacing $\hat{\sigma}_i$ with $\hat{q}_{ij}$ produces the elements of the collective nematic tensor.

---

[19] From the work that follows, it should be stated that this treatment is valid if neither the Hamiltonian nor the dissipation couples different angular momentum length states. In that case then the bosonic mode representation described in the following text would also be needed.

Chapter 4

Cavity quantum electrodynamics

The interaction of an electron and the electromagnetic field in free space is inherently very weak. Using light to manipulate the atoms in the ways we desire requires a much stronger interaction. We can do this by using very strong fields or by increasing the strength of the interaction. The simplest method is to use high quality optical resonators. These confine the light into very small volumes, such that an atom placed inside that space has a greatly enhanced interaction with the confined light. I will discuss this as well as briefly discussing less obvious architectures that produce equivalent systems. I then discuss the simplest model of a single atom interacting with a single mode of the electromagnetic field: the Jaynes-Cummings model. For an ensemble of atoms, such a model can be generalised to the Tavis-Cummings model. In a somewhat different limit, that interaction can be described by the Dicke model. I include a discussion of the historical origins of that model, as well as much more recent attempts to recreate the model in a Bose-Einstein condensate.

4.1 Optical cavities

The Rabi oscillations and Raman transitions described in Section 3.2 considered single modes of the electromagnetic field coupled strongly to single atoms. However, photons interact very weakly with such small dipoles. When thinking of lasers, we have interactions between the atom and *lots* of indistinguishable photons building up to be substantial. When thinking of cavities, we can think of a *single photon* that is reflected back and forth lots of times and so interacts multiple times to build up the substantial interaction.

4.1.1 Cavity modes

The simplest form of an optical cavity is a planar, or *Fabry-Pérot*, cavity and involves two very highly reflective mirrors with a spacing L. If light of wavelength λ is introduced to the cavity then, after one round trip, the light accumulates phase

$$\phi = \frac{4\pi L}{\lambda} \tag{4.1}$$

where we assume the refractive index of the intracavity medium is unity. A second round trip doubles that accumulated phase. With light bouncing back and forth in the cavity, these different phase shifts will interfere. If $\phi = 2\pi j$, where j is an integer, then that interference will be constructive. These are resonant modes of the cavity. For any other frequency, it will destructively interfere after some number of trips. If the cavity has some transmission, then the confined light does not perform infinite round trips and so wavelengths with $\phi \approx 2\pi j$ will have interference that is not completely destructive. This gives the cavity resonances a linewidth which translates to a deviation of the accepted round trip phase shift with full width at half

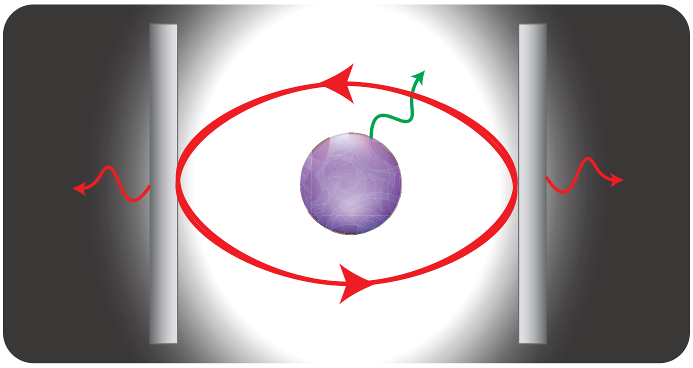

Figure 4.1: An atom contained within a planar cavity. Light is confined between two mirrors and an atom is placed inside. The atom is coupled to the cavity light, and both the atom and cavity can emit excitations into free space.

maximum [6]

$$\Delta\phi = 2\pi/\mathfrak{F} \quad \text{where} \quad \mathfrak{F} = \frac{\pi(R_1R_2)^{1/4}}{1-\sqrt{R_1R_2}} \tag{4.2}$$

and we have defined the cavity finesse $\mathfrak{F}$ and the reflectivity of the two mirrors $R_{1,2}$. If the finesse is high enough, then we have isolated a series of single frequencies

$$\omega_m = m\frac{\pi c}{L} \quad \text{with spectral width} \quad \Delta\omega = \frac{\pi c}{\mathfrak{F}L}. \tag{4.3}$$

A high finesse leads to sharp lines while a small cavity length is important to create well separated lines.

If we have a single photon in the cavity then after a round trip there is a $1-\sqrt{R_1R_2}$ chance of the photon remaining. This allows us to construct an average timescale a photon would be expected to remain in the cavity

$$\tau = \frac{L}{c(1-\sqrt{R_1R_2})} \quad \rightarrow \quad \kappa = \frac{1}{\tau} \tag{4.4}$$

where we have defined κ as the decay rate for the cavity. Comparison of this to the spectral width of the line shows that, if $R_{1,2} \approx 1$, then

$$\Delta\omega_m = 2\tilde{\kappa} \tag{4.5}$$

where we now define $\tilde{\kappa} = \kappa/2$ as the half width of the cavity. This value will be used henceforth and will just be called κ.

This means that the cavity has just two important characteristics: its finesse and its frequencies. For a more general system, where defining reflectivity is not necessarily simple, the finesse is replaced with the quality factor [11]

$$Q = \frac{\omega}{\Delta\omega} = \frac{\omega}{2\kappa}. \tag{4.6}$$

It means we can also create a master equation formulation for the cavity as

$$\dot{\rho} = -i[\hat{H}, \rho] + \kappa\mathcal{D}[\hat{a}]\rho. \tag{4.7}$$

4.1.2 Cavity enhanced interactions

We now introduce an atom into the cavity. There are now three important rates: the decay rates of the atom and cavity governed by γ and κ, as well as the coupling between the two of them, g. We have no external field and so the interaction strength is the energy of the interaction between the cavity vacuum mode and the electric dipole, $-e\hat{\mathbf{r}}$, of the atom

$$\hbar g = |\mu_{12}\mathcal{E}| \tag{4.8}$$

where $\mu_{12} = -e \langle 1 | \hat{\mathbf{r}} | 2 \rangle$ and $\mathcal{E}$ is the vacuum field strength [6]

$$\mathcal{E} = \left(\frac{\hbar\omega}{2\epsilon_0 V} \right)^{1/2} \quad \rightarrow \quad g = \left(\frac{\mu_{12}^2 \omega}{2\epsilon_0 \hbar V} \right)^{1/2}. \tag{4.9}$$

where V is the mode volume.

For the types of experiments we consider in this thesis, we want the coupling strength g to be larger than the decay rates κ and γ. The first requirement means we want a quality factor

$$Q \gg \left(\frac{\epsilon_0 \hbar \omega V}{2\mu_{12}^2} \right)^{1/2}. \tag{4.10}$$

A high quality factor is required, but the requirement can be relaxed somewhat by an increased vacuum field strength. This can be done by choosing transitions with high μ_{12}, though that also raises the spontaneous emission rate, or by confining the light in a very small mode volume[20].

One method of enhancing the coupling is simply to use more atoms. For N atoms initiated in the collective Dicke state $|N/2, -N/2\rangle$ the coupling is enhanced by $\sqrt{N}$ over a single atom $|1/2, -1/2\rangle$. This can be trivially seen by the form of $\hat{S}_+$ in Equation 3.62. This then allows us to have strong coupling for the ensemble even when the cavity does not have strong coupling for a single atom. This is particularly useful for the work described in this thesis as we need to overcome the reduction in effective coupling strength caused by operating at high detunings.

4.1.3 Alternative architectures

There are alternative architectures that can help increase the coupling to losses ratio. An example would be a cavity embedded into a tapered optical fibre [25, 26]. In sub-wavelength diameter fibres the majority of the electromagnetic field travels *outside* the fibre as an evanescent wave. Evanescent fields decay exponentially with distance from the surface and so the majority of the field is close to that surface and thus has a very small mode volume. Trapping atoms near such a surface thus allows very strong interactions. Other systems that use an enhancement via such evanescent fields include micro-resonators [27, 28] and photonic crystal waveguides [29, 30].

Using a different medium as the two-level system "atoms" is also a possibility. Those systems might be atomic defects in crystal structures, such as rare earth ion dopants [31] or nitrogen-vacancy centres in diamond [32]. There are also macroscopic sized objects that have quantised degrees of freedom that can be used. Superconducting circuits have energy levels that are quantised elements of the circuit [33].

---

[20] Of course, in lots of architectures, the mode volume is the volume of the cavity and so decreasing the volume and the length come hand in hand. If all we do is decrease the cavity length, L, then the coupling increases as $\sim L^{-1/2}$ while the cavity decay rate increases as $\sim L^{-1}$ and so the ratio of g/κ will decrease. If we need to reduce the volume, we require a more clever manner than making the cavity smaller.

Often these levels have a strong non-linearity and so it is easy to isolate a two-level system that can be coupled to microwave resonators. Dots of semiconductor material, of a size on the order of nanometres, have levels defined by the band structure of the semiconductor. These can be grown on, for example, a photonic crystal waveguide structure allowing for a single fully integrated "cavity QED" system.

All of these architectures have their benefits and flaws and so are suitable for different purposes. In this thesis, we focus on a traditional cavity QED system with a large ensemble of atoms. However, some of our proposals could be implemented in other architectures. Making use of the different advantages of alternative systems, there are a range of other possibilities building on the methods we introduce here. A brief discussion of some of these ideas is given in Section 12.3.

4.2 The Jaynes-Cummings model

The simplest model of a single atom in a cavity is the Jaynes-Cummings model [34,35]. A two-level system is coupled to a cavity mode with a Hamiltonian

$$\hat{H} = \omega \hat{a}^\dagger \hat{a} + \omega_0 \hat{\sigma}_z + g(\hat{a} + \hat{a}^\dagger)(\hat{\sigma}_- + \hat{\sigma}_+). \tag{4.11}$$

The first two terms are simply the energy associated with photons in the field and the state of the atom. The interaction term involves the exchange of excitations between the field and the atom. Transforming the Hamiltonian to the interaction picture gives

$$\hat{H}' = g\left(\mathrm{e}^{-i(\omega+\omega_0)t}\hat{a}\hat{\sigma}_- + \mathrm{e}^{-i(\omega-\omega_0)t}\hat{a}\hat{\sigma}_+ + \mathrm{e}^{i(\omega-\omega_0)t}\hat{a}^\dagger\hat{\sigma}_- + \mathrm{e}^{i(\omega+\omega_0)t}\hat{a}^\dagger\hat{\sigma}_+\right). \tag{4.12}$$

Two of these terms rotate at $\pm(\omega + \omega_0)$ and two at $\pm(\omega - \omega_0)$. If $\omega \sim \omega_0$ then those second terms are close to resonant and the first terms rotate at an extremely high frequency and so are strongly suppressed [7]. This allows us to make the *rotating wave approximation* and so, coming out of the interaction picture, we have

$$\hat{H} = \omega \hat{a}^\dagger \hat{a} + \omega_0 \hat{\sigma}_z + g(\hat{a}\hat{\sigma}_+ + \hat{a}^\dagger \hat{\sigma}_-). \tag{4.13}$$

The interaction has been simplified to those that *conserve* the number of excitations. An atomic excitation turns into a field excitation and vice versa.

The obvious states to consider are Fock states coupled to the bare levels, $|0\rangle$ and $|1\rangle$, of the two-level system. If we take these states, with notation $|n\rangle \otimes |0\rangle \equiv |n, 0\rangle$ and $|n\rangle \otimes |1\rangle \equiv |n, 1\rangle$, then the action of the Hamiltonian (where we transform $\hat{\sigma}_z \to |1\rangle\langle 1|$ for simplicity) is

$$\hat{H}|n, 0\rangle = n\omega|n, 0\rangle + \sqrt{n}g|n - 1, 1\rangle \tag{4.14}$$

$$\hat{H}\left|n-1,1\right\rangle = ((n-1)\omega+\omega_0)\left|n-1,1\right\rangle + \sqrt{n}g\left|n,0\right\rangle \tag{4.15}$$

and so we have a closed set. Of course, this should be expected, due to the excitation conservation of the Hamiltonian. This means that we can form eigenstates which have n excitations split between the field and the atom

$$\left|\psi\right\rangle = A\left|n,0\right\rangle + B\left|n-1,1\right\rangle \tag{4.16}$$

upon which the action of the Hamiltonian, defining $\Delta = \omega - \omega_0$, gives us

$$\hat{H}\left|\psi\right\rangle = \left[A\omega n + Bg\sqrt{n}\right]\left|n,0\right\rangle + \left[B(\omega n - \Delta) + Ag\sqrt{n}\right]\left|n-1,1\right\rangle \tag{4.17}$$

If $\omega = \omega_0$ then the eigenstates are

$$\left|\psi_{\pm n}\right\rangle = \sqrt{\frac{1}{2}}\left(\left|n,0\right\rangle \pm \left|n-1,1\right\rangle\right) \quad \text{with} \quad E_{\pm n} = n\omega \pm g\sqrt{n}. \tag{4.18}$$

Without the coupling, $\left|n,0\right\rangle$ and $\left|n-1,1\right\rangle$ are both eigenstates and are degenerate. The coupling creates two new *dressed states* which have an energy difference of $2g\sqrt{n}$. Note that the energy gap between the pair of dressed states increases with the number of excitations in the system[21].

If $\omega \neq \omega_0$ then, defining $\Delta = \omega - \omega_0$, the eigenvalues are

$$E_{\pm n} = n\omega - \frac{\Delta}{2} \pm \sqrt{\left(\frac{\Delta}{2}\right)^2 + g^2 n} \tag{4.19}$$

and the eigenstates are now imbalanced superpositions of the states. The split between the dressed states is now even larger, which makes sense since the bare cavity and atomic excitations are now at different frequencies as well. If Δ is positive then there is less energy in the atomic excitation, and so the lower energy dressed state has *more* of the atomic excitation in it. For negative Δ the opposite is obviously true. As Δ, and thus the split, increases, the eigenstates become focussed more and more to one side. In the large detuning limit, $\Delta \gg g\sqrt{n}$, the eigenvalue equation shows that the two "dressed" states have gone back to the undressed picture. We thus require near resonance between the cavity and atom frequencies to notice the splitting caused by the interaction.

If we initiate the system with an excited atom, as in Figure 4.2a, then the excitation

---

[21] This fact can be used to generate single photons. If we drive the system in its ground state with light at a frequency $\omega + g$ then we excite the upper of those dressed states. The next pair of excited states has its upper level $\omega + (1-\sqrt{2})g$ above this first rung, meaning it is out of resonance. As such, if the driving is weak, the system cannot gain more than one excitation. This so-called *photon blockade* [36,37] thus produces one photon as it drops back to the ground state and then has a dead time while the driving re-excites the system. This means that a weakly driven Jaynes-Cummings system - higher driving does break the blockade [38] - can produce only single photons separated by at least the time taken to re-excite the system following emission.

oscillates between the two components. With a detuning, that oscillation exists but not for the entire population. Adding dissipation to the system makes $|0, 0\rangle$ the only stable state as the excitations leave via the losses and so we have oscillations until the excitation decays. This is reminiscent of the Rabi oscillations discussed in Section 3.2.1, except with an interesting difference: these Rabi oscillations are *self-driven*. The only excitation in the system is the original excitation of the atom.

We can prepare the system in different levels of the ladder. Figure 4.2b shows that the oscillations are at higher frequencies at higher rungs. Comparing to Rabi oscillations from a coherent drive, we see that, for n excitations, $\Omega = \sqrt{n}g$. If we start the cavity mode in a coherent state, then the oscillations induced by different photon numbers will become out of phase and destructively interfere. Figure 4.2c shows that this is exactly what happens, except with the curious feature that after some time the oscillations *come back*. This *collapse and revival* is because the important contributions have come back around to being in phase again and is a distinct feature of discrete systems.

If we prepare the cavity in its vacuum and a ground-state atom, $|0, 0\rangle$, and then

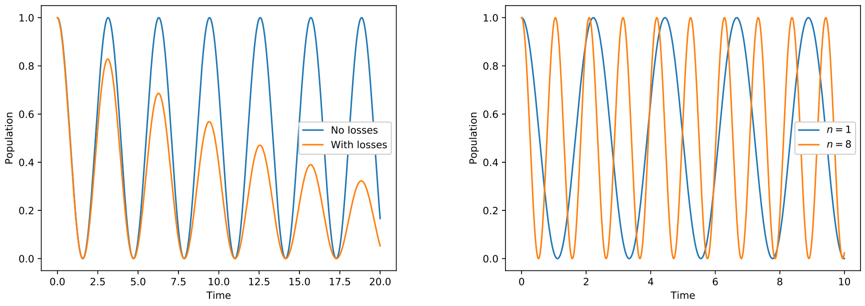

(a) Initial state $|0\rangle \otimes |1\rangle$ with and without losses.

(b) Initial state $|n\rangle \otimes |1\rangle$ and no losses.

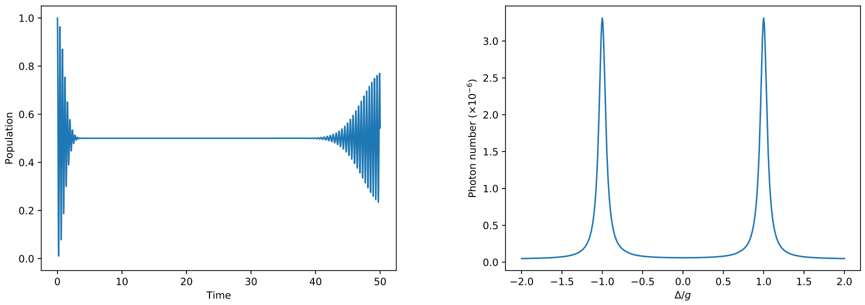

(c) Initial state $|\alpha = 8.0\rangle \otimes |1\rangle$ and no losses.

(d) Drive detuning Δ and strength $\Xi = 0.01g$.

Figure 4.2: Plots of different phenomena in the Jaynes-Cummings model. In all cases the atom and field are considered resonant. (a,b,c) show the population in the excited state over time in units g^{-1}, (d) shows the steady-state photon number. Where used, losses are $\gamma = \kappa = 0.04g$.

drive the system with a laser field of strength Ξ with frequency near the first pair of states, then we can directly measure the splitting. We consider the Hamiltonian in the interaction picture of this driving, assuming resonance between the atom and mode

$$\hat{H} = \Delta \hat{a}^\dagger \hat{a} + g(\hat{a}\hat{\sigma}_+ + \hat{a}^\dagger \hat{\sigma}_-) + \Xi(\hat{a} + \hat{a}^\dagger) \tag{4.20}$$

defining $\Delta = \omega - \omega_d$ with ω_d the drive frequency. Figure 4.2d shows the response of the system. The presence of losses does give the two resonances a finite width and so $g > \kappa, \gamma$ is required to observe the splitting. Observations of this splitting have been performed for a single atom falling through a cavity [39] and later for a single atom trapped in a cavity [40]. Observations have since been made for all sorts of other architectures including Rydberg atoms[22] in microwave resonators [41], superconducting qubits [42] and quantum dots [43].

4.3 The Tavis-Cummings model

The Hamiltonian for N atoms under the rotating wave approximation is

$$\hat{H} = \omega \hat{a}^\dagger \hat{a} + \omega_0 \hat{S}_z + g(\hat{a}\hat{S}_+ + \hat{a}^\dagger \hat{S}_-), \tag{4.21}$$

where we have replaced the two-level operators with collective operators. Due to the presence of these collective operators, the coupling is enhanced by $\sqrt{N}$ and this enhancement can be used to observe an enhanced vacuum Rabi splitting of $2g\sqrt{N}$. This makes the splitting much larger, and so was observed before the single-atom case [44]. This splitting can actually be used to determine either g or N if one is known. Indeed, in the experiments described in Chapters 5 and 7, the vacuum Rabi splitting was used to quantify the effective coupling rate for a given laser power.

For higher ladder levels the n excitations can be distributed in the field mode and the ensemble in a variety of ways. Figure 4.3a shows how an initially empty cavity and an ensemble of excited atoms evolves. The evolution shows complicated oscillations of excitations and the field. This is because of the different frequencies that different numbers of excitations in each state exchange energy. We can see that, in the absence of losses, these oscillations continue indefinitely, conserve the total number of excitations and are *never* complete.

As above, dissipation makes an empty cavity and a fully polarised ensemble the only ground state. However, the complicated structure above that ground state leads to interesting transient behaviour. Taking that excited ensemble and allowing it to decay means that excitations leave the system. The way in which they do is extremely

---

[22] Rydberg atoms are atoms where the outer electron has an extremely high principal quantum number. In [41] the two-level system is between the principal quantum numbers $n = 50 \leftrightarrow 51$. For these orbits, the difference in energy is much smaller and so the relevant frequencies of light are in the microwave regime.

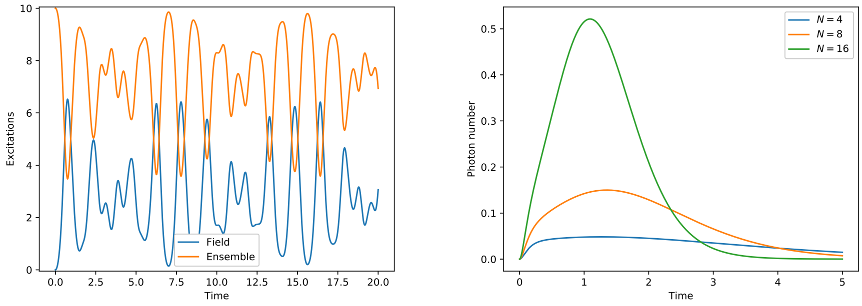

(a)

(b)

Figure 4.3: Plots of different phenomena in the Tavis-Cummings model. (a) Excitations in the ensemble and field from an initial state $|0\rangle \otimes |e\rangle^{\otimes N}$ and no losses and (b) photon number in the field from an initial state $|0\rangle \otimes |e\rangle^{\otimes N}$ with $\kappa = 5g$. In both cases the atoms and field are considered resonant and time is in units of g^{-1}.

interesting. We consider the so-called "bad-cavity" limit, where $\kappa \gg g, \gamma$.

Let us first consider an ensemble of atoms that are not strongly coupled to a shared mode; the atoms emit into free space and so each undergoes a simple exponential decay. The sum over the ensemble thus gives a collective exponential decay, i.e. the master equation would give an expectation value for the remaining excitations of $N\exp(\gamma t)$ and the average peak emission will be at $t = 0$ and will be γN.

Strongly coupling the atoms to a mode means the atoms will exchange their excitations with that shared mode. Since we are in the bad-cavity limit, the excitations will generally leave via the cavity decay. Figure 4.3b shows this cavity-mediated decay process. Instead of an exponential decay, we have an increase in the cavity mode population, which we note is directly proportional to the cavity output flux. This increase continues until, at some non-zero time, it reaches a peak $\sim N^2$. The presence of a shared mode allows the atoms to decay collectively, with a greatly enhanced rate. This *superradiance* was first introduced by Dicke in 1954 [45].

This can be explained by a chain reaction caused by the combination of the two operators that form the important interaction: $\hat{a}^\dagger \hat{S}_-$. Both of these act with increasing strength as we populate the field. If we consider the form of the creation operator we can see that the impact of the operator is enhanced for higher photon states by a factor $\sqrt{n+1}$. This means as the field builds up, the interaction term $\hat{a}^\dagger \hat{S}_-$ *increases* in effective "strength". Essentially, the production of photons in the cavity mode enhances the rate of producing *more* photons. Similarly, the ladder operators for the ensemble, $\hat{S}_\pm$, have higher coefficients for states away from the polarised states. The ensemble losing excitations thus also *increases* the power of the interaction term and the rate at which the cavity mode is populated. Of course, after passing through the central point, this rate decreases until the cavity decay becomes a faster process and the field depopulates instead.

4.4 The Dicke model

We have so far assumed that we operate in a situation close to resonance - $\omega \approx \omega_0$ - where we can make the rotating wave approximation. If we are far from resonance, or if the coupling is extremely strong, then that approximation does not necessarily hold. For an ensemble of atoms that means we have the Dicke model Hamiltonian

$$\hat{H} = \omega \hat{a}^\dagger \hat{a} + \omega_0 \hat{S}_z + \frac{\lambda}{\sqrt{N}} \left(\hat{a} + \hat{a}^\dagger \right) \left(\hat{S}_- + \hat{S}_+ \right) \tag{4.22}$$

where $\lambda = \sqrt{N} g$ and the factor of $1/\sqrt{N}$ is introduced as a normalising factor that is useful for analysis of the equation. This model, and variations of it, form the basis for much of the work in this thesis and so a brief history is provided.

4.4.1 Steady-state superradiance

This equation is fundamentally different to the Tavis-Cummings model because it does not conserve the number of excitations. There are two terms, $\hat{a}\hat{S}_-$ and its conjugate, that respectively destroy and create an excitation in *both* the field and the ensemble. This means our states are not limited to the ladder we found in the Tavis-Cummings model; states can now be spread between different levels and energy can be created or destroyed by the Hamiltonian.

We can look at the ground state of the system by splitting the Hamiltonian into two parts: one that describes the energy of the system and the other the interaction terms. With small $\lambda \ll \omega, \omega_0$, the energy part dominates. Our ground state is then the ground state for those terms, which is the same as for the Tavis-Cummings model: a fully polarised state with the entire ensemble in the lower energy level and an empty cavity mode. For very high $\lambda \gg \omega, \omega_0$, then instead the ground state should be decided by the interaction part. The interaction part is symmetric for the two energy levels of the atoms and so it does not have a preferred “direction” to move the ensemble. As such, it should be that the ground state there is halfway between the two atomic levels. This is where the collective operator acts strongest and so amounts to *steady-state superradiance* [46–51].

Between these two phases is a second order phase transition [46–48] that has generated a lot of interest ever since it was first proposed[23]. As λ increases, the

---

[23] It should be noted that the first predictions of steady-state superradiance were for the Tavis-Cummings model at non-zero temperatures. The critical point was thus dependent on the coupling strength and the temperature. It was not until [49,50] that the counter-rotating terms were included in the calculations. There are subtle differences to the physics around the transition depending on whether it is a thermodynamic or quantum, that is zero temperature, transition. This is excellently summarised in [51].

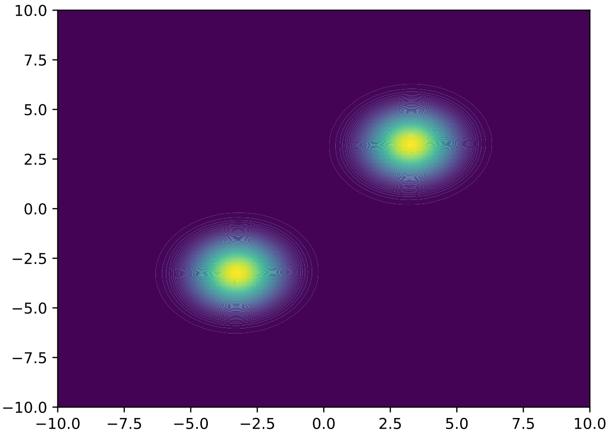

Figure 4.4: *Q*-function of the cavity field for a typical state of the Dicke model above threshold.

system undergoes a distinct change. In the thermodynamic limit[24], this happens at a critical point

$$\lambda_c = \frac{1}{2}\sqrt{\omega_0 \omega}. \tag{4.23}$$

Above this threshold the atoms cohere via the cavity mode.

If we move to an open system for the cavity mode, ignoring spontaneous emission, we have the Dicke model master equation

$$\rho = -i[\hat{H}, \rho] + \kappa \mathcal{D}[\hat{a}]\rho \quad \rightarrow \quad \lambda_c = \frac{1}{2}\sqrt{\omega_0 \frac{\omega^2 + \kappa^2}{\omega}}. \tag{4.24}$$

The presence of losses from the cavity mode changes the threshold equation. A physical intuition is that the formation of the coherence between the atoms becomes more difficult because the channel by which that process occurs is now lossy. Above this threshold, we still have steady-state superradiance.

Figure 4.4 shows a typical state of the field above threshold. The field is a mixed state of two coherent states of the same magnitude and opposite phase, $|\alpha\rangle$ and $|-\alpha\rangle$. Associated to each of these coherent states are coherent spin states of equal magnitude and opposite phase, $|\eta\rangle$ and $|-\eta\rangle$. The steady-state wavefunction is then an entangled superposition of these correlated coherent field and spin states[25].

---

[24] The thermodynamic limit is a term used in this thesis, and quantum optics more broadly, to mean that the size of the system is infinite. This allows us to ignore quantum fluctuations in our treatment of the system. In this thesis, the thermodynamic limit means to assume an infinite sized ensemble, though the quantum results often approach the thermodynamic limit for surprisingly small N.

[25] It can actually be shown at small superradiant state amplitudes that there is Einstein-Podolsky-Rosen entanglement between the atoms and field [52, 53].

Again, coherences between the atoms are formed *through* the cavity mode.

Both the master equation and quantum trajectory pictures produce the entangled superposition described above. Since the two terms have the same photon number, observing the photon output flux is not enough to break the superposition. If instead the cavity is monitored with a phase sensitive detection system, such as a homodyne detector, we can collapse the state according to the phase of the field. This random choice of phase following the transition is referred to as *symmetry breaking*. The system undergoes a *bifurcation*, moving from a single ground state to two degenerate ground states.

4.4.2 An important correction

This picture should have alarm bells ringing. What was a fundamental description of the interaction between an ensemble of emitters and an electromagnetic mode resulted in self-sustaining superradiance in the presence of losses. At zero temperature, we predict an ensemble will produce photons into the environment *in perpetuity*. The system has no energy put into it and yet creates energy indefinitely. This would seem to break a lot of rules of thermodynamics.

In fact, this problem is something that is still debated in quantum optics literature. An initial resolution was presented by Rzążewski et al [54]. There, it was explained that the approximation of the dipole interaction is too simple to capture this system. Essentially, there is a second order term that, at least in the case of atoms, blocks the steady-state superradiance described above. A second treatment provided an alternative proof of the lack of a superradiant threshold [55]. However, in more recent years, alternative models for the electromagnetic field, or in some cases alternative architectures, have questioned or confirmed those results [56–61].

Much of this discussion does not treat an open system, or considers very particular configurations and architectures. One thing that does seem certain is that we should not simply put atoms in a cavity and expect superradiance. Luckily, to study the Dicke model we can bypass these fundamental questions with a little creativity.

4.4.3 Implementation in a Bose-Einstein condensate

Self-organisation is a process where atoms coupled to a cavity mode arrange themselves spatially so as to maximise their collective emission into the cavity [62–65]. The mapping of a self-organisation process to an effective Dicke model was proposed [66] and then performed with a Bose-Einstein condensate in a cavity [67–70]. These experiments used detuned Raman transitions between different momentum states of the BEC. The ground state of the atoms is the momentum ground state, while the excited state is a symmetric superposition of one quanta of momentum in the $x-$ and $z-$direction. The Raman transitions are via the states with a quanta of momentum in either of those directions, providing the two paths which can be mapped to the quanta conserving and non-conserving terms.

In this case, superradiance happens if the atoms are spatially arranged such that their emission into the cavity happens with the same phase. The atoms *self-organise* to this pattern through the cavity mode. This process feeds back on itself. The field creates a square lattice that the atoms sit in, while the enhanced scattering of atoms in that pattern feed the field. The atoms sit in a two-dimensional square lattice in a chequerboard pattern where no two atoms sit next to each other. This chequerboard pattern has two possibilities: the black squares or the white squares. Instead of the correlations between coherent field and atomic states, we have correlations between a particular spatial pattern for the atoms and the phase of the coherent field. Measurement of the photon number shows the distinct phase transition [67] while the use of a homodyne detector shows the spontaneous symmetry breaking at the transition [68].

An effective Dicke model can also be produced using spin states of a dilute gas of cold atoms [71,72], as discussed in Chapters 5 and 7 of this thesis. Combining these ideas such that the atoms self-organise in both the spatial and spin components is also possible [73,74]. One interesting extension to these models is to use multiple modes of the cavity such that the position of the atomic cloud impacts the critical threshold [75]. An alternative extension is the addition of a second cavity, such that the atoms will self-organise with respect to one cavity or the other or some arbitrary superposition of the two [76,77].

Chapter 5

Engineering the Dicke model in a cavity QED setup

The Dicke model is one of the simplest examples of how light and matter can interact, and yet it describes a peculiar trait that many-body systems can self-organise and offer amplified behaviour. Interest in its implementation is thus driven by a fundamental interest in light-matter interactions, quantum phase transitions and many-body physics. In this Chapter, I discuss a method used to study the Dicke model at the Centre for Quantum Technologies in Singapore. The first section of this Chapter discusses the theoretical origins of this work over a decade ago. The second section describes the specific setup and results of the Dicke model experiment carried out by Zhiqiang Zhang, Chern Hui Lee, Ravi Kumar, Kyle Arnold and Murray Barrett. The third section describes my theoretical modelling of the experiment performed under the supervision of Scott Parkins. Some of the work in this section was actually performed in response to the experiment described in Chapter 7, but discussion is included here as the results are relevant to both cases. The final section describes a treatment of the experiment allowing for atomic motion performed in collaboration with Murray Barrett, Zhiqiang Zhang and Scott Parkins.

5.1 The Dicke model via cavity-assisted Raman transitions

In Section 4.4.3, we discussed experiments that simulated the Dicke model using the momentum states of atoms in a BEC as the two-level systems. The Dicke model can also be realised using cavity-assisted Raman transitions between atomic *spin states*. Dimer et al [53] proposed confining an ensemble of atoms within a circular cavity, also known as a ring cavity.

Figure 5.1 shows that such a scheme requires four states of the atoms: two ground states $|0\rangle$ and $|1\rangle$, which become the two-level systems, and two excited states $|e\rangle$ and $|f\rangle$, via which Raman transitions are driven. These states are chosen such that $|0\rangle \leftrightarrow |e\rangle$ and $|1\rangle \leftrightarrow |f\rangle$ are driven by a cavity mode, while $|0\rangle \leftrightarrow |f\rangle$ and $|1\rangle \leftrightarrow |e\rangle$ are driven by different laser fields respectively. By matching the frequencies correctly, we can drive Raman transitions between $|0\rangle \leftrightarrow |1\rangle$.

In the limit that the transitions are significantly detuned, then the excited states can be adiabatically eliminated. We are left with the exchange of photons between a cavity mode and two laser fields driving the atoms between $|0\rangle$ and $|1\rangle$. If certain selection rules are met, there are two different routes between the two states. One laser drives from $|0\rangle \rightarrow |1\rangle$ depositing a photon into the cavity mode, but requires a photon to be taken from the cavity mode to drive from $|1\rangle \rightarrow |0\rangle$. The other laser has the opposite effect. Thus, one of the Raman transitions produces the rotating terms, $\hat{a}^\dagger \hat{S}_-$ and $\hat{a}\hat{S}_+$, and the other the counter-rotating terms, $\hat{a}^\dagger \hat{S}_+$ and $\hat{a}\hat{S}_-$.

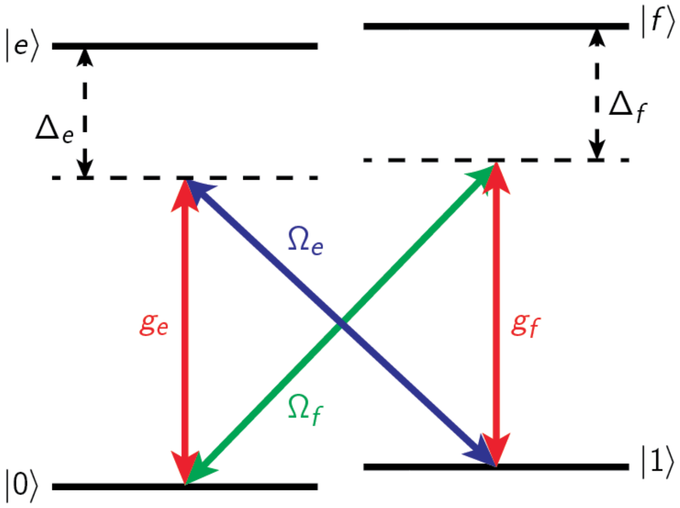

Figure 5.1: Level diagram to produce the Dicke model via the Dimer et al proposal [53]. Two ground-state levels, $|0\rangle$ and $|1\rangle$ have Raman transitions driven between them via two excited states $|e\rangle$ and $|f\rangle$ using a cavity mode (red arrow) and two laser modes (blue, green).

For a single atom the system in Figure 5.1 can be written in the Hamiltonian form

$$\begin{aligned}\hat{H} =&\omega_c \hat{a}^\dagger \hat{a} + \omega_1 |1\rangle\langle 1| + \omega_E |e\rangle\langle e| + \omega_F |f\rangle\langle f| \\ &+ \frac{\Omega_f}{2} \mathrm{e}^{-i\omega_f t} |f\rangle\langle 0| + \frac{\Omega_e}{2} \mathrm{e}^{-i\omega_e t} |e\rangle\langle 1| + g_e |e\rangle\langle 0| \hat{a} + g_f |f\rangle\langle 1| \hat{a} + \text{h.c.} \qquad (5.1)\end{aligned}$$

where h.c. means Hermitian conjugate and applies to all the transition terms. Here ω_c is the cavity mode frequency, and so the first term describes the cavity mode occupation energy. $\omega_{1,E,F}$ are the frequencies of the levels $|1\rangle, |e\rangle, |f\rangle$ respectively and the frequency of $|0\rangle$ is assumed to be zero. These terms therefore describe the atomic energy. $\omega_{e,f}, \Omega_{e,f}$ are the bare frequencies and Rabi frequencies respectively of the two lasers and so these terms describe the atom's stimulated absorption and emission into the laser modes. $g_{e,f}$ are the single-atom coupling strengths normalised on their transitions and so these terms describe the exchange of quanta between the atom and cavity mode. Adiabatic elimination of the excited states and summation over the ensemble then leads to the master equation [53]

$$\dot{\rho} = -i[\hat{H}, \rho] + \kappa \mathcal{D}[\hat{a}]\rho \qquad (5.2)$$

with a Hamiltonian

$$\hat{H} = \omega \hat{a}^\dagger \hat{a} + \omega_0 \hat{S}_z + \frac{\lambda_e}{\sqrt{N}} (\hat{S}_+ \hat{a} + \hat{S}_- \hat{a}^\dagger) + \frac{\lambda_f}{\sqrt{N}} (\hat{S}_- \hat{a} + \hat{S}_+ \hat{a}^\dagger) + \frac{U}{N} \hat{S}_z \hat{a}^\dagger \hat{a} \qquad (5.3)$$

and parameters given by

$$\begin{aligned}\omega &= \omega_c - \left(\frac{\omega_f + \omega_e}{2} \right) + \frac{N}{2} \left(\frac{g_e^2}{\Delta_e} + \frac{g_f^2}{\Delta_f} \right) && (5.4) \\ \omega_0 &= \omega_1 - \left(\frac{\omega_f - \omega_e}{2} \right) + \frac{1}{4} \left(\frac{\Omega_e^2}{\Delta_e} - \frac{\Omega_f^2}{\Delta_f} \right) && (5.5) \\ \lambda_{e,f} &= \frac{\sqrt{N} g_{e,f} \Omega_{e,f}}{2\Delta_{e,f}} && (5.6) \\ U &= \frac{g_e^2}{\Delta_e} - \frac{g_f^2}{\Delta_f}. && (5.7)\end{aligned}$$

One can see that if $\lambda_- = \lambda_+$ and $U = 0$ then the effective system represents a Dicke model as discussed in Section 4.4. Whilst removing the dispersive term (i.e. $U = 0$) is possible through manipulation of the microscopic parameters, it is not strictly necessary. Provided it is small in comparison to ω, ω_0 (most relevantly $< 2\omega$) then its impact on the phase transition point is well understood [78–81]. The derivation of the superradiant phase transition in the presence of this non-linearity is given in Section 5.1.2.

5.1.1 Semi-classical equations

In the thermodynamic limit, we can neglect quantum fluctuations and factorise operator products (e.g. $\langle \hat{S}_- \hat{a} \rangle \rightarrow \langle \hat{S}_- \rangle \langle \hat{a} \rangle$) giving the semi-classical equations [53,78,79]

$$\dot{\alpha} = -\kappa\alpha - i\omega\alpha - iU\alpha\gamma - i\lambda_+\beta - i\lambda_-\beta^* \tag{5.8}$$

$$\dot{\beta} = -i\omega_0\beta - iU|\alpha|^2\beta + 2i\lambda_+\alpha\gamma + 2i\lambda_-\alpha^*\gamma \tag{5.9}$$

$$\dot{\gamma} = i\lambda_+(\alpha^*\beta - \alpha\beta^*) + i\lambda_-(\alpha\beta - \alpha^*\beta^*) \tag{5.10}$$

where

$$\alpha = \frac{\langle \hat{a} \rangle}{\sqrt{N}}, \quad \beta = \frac{\langle \hat{S}_- \rangle}{N}, \quad \gamma = \frac{\langle \hat{S}_z \rangle}{N}, \quad |\beta|^2 + \gamma^2 = 0.25. \tag{5.11}$$

These equations offer two trivial solutions: $\alpha = \beta = 0$ and $\gamma = \pm 0.5$. This means an empty cavity and all spins in one state, i.e. the collective spin aligned along the z-axis of the Bloch sphere. $\gamma = -0.5$ is the normal phase, while $\gamma = 0.5$ is the inverted phase. These trivial solutions represent the sub-threshold ground states with positive (normal) and negative (inverted) ω_0.

Outside of these two solutions, the behaviour of these equations is extremely rich and complex, something explored in much detail in [79] and in the specific case of imbalanced coupling in Section 7.3 and [82].

5.1.2 Superradiant phase transition

We now consider the specific case of the Dicke model and so $\lambda_- = \lambda_+ \equiv \lambda$. This reduces the above equations to

$$\dot{\alpha} = -\kappa\alpha - i\omega\alpha - iU\alpha\gamma - i\lambda(\beta + \beta^*) \tag{5.12}$$

$$\dot{\beta} = -i\omega_0\beta - iU|\alpha|^2\beta + 2i\lambda(\alpha\gamma + \alpha^*\gamma) \tag{5.13}$$

$$\dot{\gamma} = i\lambda(\alpha^*\beta - \alpha\beta^* + \alpha\beta - \alpha^*\beta^*). \tag{5.14}$$

We are interested in the steady-state solutions to these equations so the left hand side is set to zero. The third equation reduces to a form that means that either the real part of α or the imaginary part of β, which corresponds to $\beta_y = \langle \hat{S}_y \rangle / N$, must be zero. It also follows from the second equation that it be β_y since there is no imaginary part on the right hand side.

We can then combine and solve those two equations for γ to give [78,79]

$$\gamma = -\frac{\omega}{U} \pm \sqrt{\frac{\lambda^2(4\omega^2 - U^2) - \omega_0 U\kappa^2}{U^2(\omega_0 U + 4\lambda^2)}}. \tag{5.15}$$

We can find the real part of β from the normalisation condition and then α follows from the form of the ensemble.

The threshold occurs when the equation above allows for physical solutions, i.e. $|\gamma| \leq 0.5$ and real. Setting $\gamma = -0.5$ should thus give the boundary between the normal state and the onset of superradiance[26]. This gives the critical coupling as

$$\lambda_c = \frac{1}{2}\sqrt{\omega_0 \frac{(\omega - U/2)^2 + \kappa^2}{\omega - U/2}}. \tag{5.16}$$

Below this point the system is fully polarised in $|0\rangle$ (or $|1\rangle$ if ω_0 is negative), and above it the atoms self-organise their spin degree of freedom through the cavity mode and the system becomes superradiant. At the transition, from a dynamical system perspective, the system goes through a supercritical pitchfork bifurcation [82]; one solution splits into three, with the original solution becoming unstable and two new stable solutions emerging. In this case, these two new solutions differ through a choice of sign in β and of the cavity field, highlighting the broken symmetry. Dynamic simulations of these equations have to choose one of these superradiant solutions, as this semiclassical picture does not allow for the quantum result of a superposition of the two solutions nor the ensuing entanglement between the atoms and cavity field.

If we return to the original Dicke model, where $U = 0$, the above threshold reduces to

$$\lambda_c = \frac{1}{2}\sqrt{\omega_0 \frac{\omega^2 + \kappa^2}{\omega}}. \tag{5.17}$$

If instead $|U| > 2\omega$ then the above treatment is not accurate. This has been studied in [79–81] and the limit of very large U is explored in Chapter 6 of this thesis.

5.2 Experimental implementation

5.2.1 Switch to a Fabry-Pérot cavity

The original proposal of Dimer et al [53] makes use of a circular cavity, but the same model can be implemented in a Fabry-Pérot cavity. Here the laser fields are perpendicular to the cavity mode, with the only complication that the laser fields must be counter-propagating, i.e. the two lasers must illuminate the atoms from opposite directions, as shown in Figure 5.2. With co-propagating lasers, a phase factor is introduced that, averaged over the spatial distribution of the entire ensemble, removes the presence of the phase transition and any superradiant behaviour [72]. This is discussed in Section 5.2.4.

---

[26] $\gamma = +0.5$ will give the boundary between the inverted and superradiant states if that is the ground state. This means that for negative ω_0 the threshold equations still produce a real critical coupling.

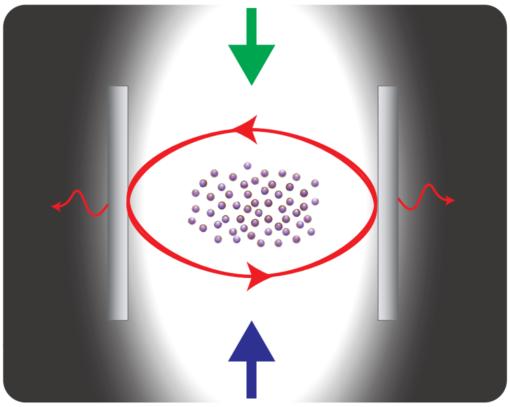

Figure 5.2: Experimental setup to produce the Dicke model in a Fabry-Pérot cavity. Here we have two counter-propagating lasers illuminating an ensemble of ^{87}Rb atoms confined within the cavity.

5.2.2 Choice of levels in ^{87}Rb

Here, we consider ^{87}Rb, choosing the specific hyperfine states $|0\rangle = |F = 1, m_F = 1\rangle$ and $|1\rangle = |F = 2, m_F = 2\rangle$ as the two-level systems [81] (see Figure 5.3). Selection rules allow for two separate Raman transitions made of a $\pi-$polarised cavity mode and a $\sigma_\pm$-polarised laser field. These can then be driven on either the D_1 or D_2 lines, though here we consider the D_2 line. As such $|f\rangle = |F' = 2, m_{F'} = 2\rangle$ and $|e\rangle$ is actually the pair of states $|F' = 2, m_{F'} = 1\rangle$ and $|F' = 1, m_{F'} = 1\rangle$ which we take

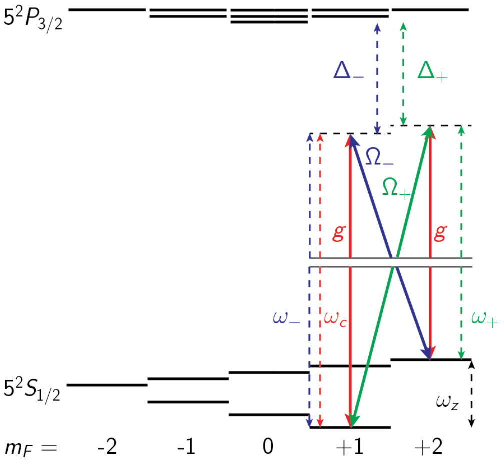

Figure 5.3: Level diagram to produce the Dicke model using hyperfine states in ^{87}Rb. The two-level systems are made from the states $|F = 1, m_F = 1\rangle$ and $|F = 2, m_F = 2\rangle$ with detuned Raman transitions driven between them via the D_2 line made from a cavity mode (red arrows) and σ_+-polarised (green) and σ_--polarised (blue) lasers. For the experiment the relevant scales are $\omega_z \sim 7 \times 2\pi$ GHz, $\Delta_\pm \sim 100 \times 2\pi$ GHz and $\omega_{c,\pm} \sim 50 \times 2\pi$ THz. Note also that both lasers drive both states, which produces a light shift on the levels and that the diagram is not to scale.

to be at the same energy due to the large detuning. There are also other relevant excited states, such as $|F' = 0, m_{F'} = 0\rangle$, which are coupled to only one active state and so result in a light shift on the active state.

5.2.3 Full model

Using these levels and notation such that $|F = 1, m_F = 1\rangle \equiv |0\rangle$, $|F = 2, m_F = 2\rangle \equiv |1\rangle$ and $|F' = i, m_{F'} = j\rangle \equiv |i, j\rangle$, we have a full Hamiltonian

$$\begin{aligned}\hat{H} =& \omega_c \hat{a}^\dagger \hat{a} + \omega_z |1\rangle\langle 1| + \sum_{\mathrm{e}} \omega_e |e\rangle\langle e| + \frac{\Omega_+}{2} \mathrm{e}^{i\omega_+ t} \left(\sqrt{\frac{1}{4}} |0\rangle\langle 2,2| + \sqrt{\frac{1}{2}} |1\rangle\langle 3,3| \right) \\ &+ \frac{\Omega_-}{2} \mathrm{e}^{i\omega_- t} \left(\sqrt{\frac{1}{6}} |0\rangle\langle 0,0| - \sqrt{\frac{5}{24}} |0\rangle\langle 1,0| + \sqrt{\frac{1}{24}} |0\rangle\langle 2,0| \right) \\ &+ \frac{\Omega_-}{2} \mathrm{e}^{i\omega_- t} \left(\sqrt{\frac{1}{20}} |1\rangle\langle 1,1| - \sqrt{\frac{1}{12}} |1\rangle\langle 2,1| + \sqrt{\frac{1}{30}} |1\rangle\langle 3,1| \right) \\ &+ g\hat{a}^\dagger \left(\sqrt{\frac{5}{24}} |0\rangle\langle 1,1| - \sqrt{\frac{1}{8}} |0\rangle\langle 2,1| + \sqrt{\frac{1}{6}} |1\rangle\langle 2,2| - \sqrt{\frac{1}{6}} |1\rangle\langle 3,2| \right) + \text{h.c.}\end{aligned} \tag{5.18}$$

where h.c. means Hermitian conjugate and is meant for all the transition terms. In this equation ω_c is the cavity frequency, ω_z is the splitting between the two active states, $\sum_{\mathrm{e}}$ sums over the excited manifold with ω_e being their frequency relative to the energy of $|1, 1\rangle$ which is taken to be zero. $\omega_\pm, \Omega_\pm$ are, respectively, the bare frequencies and Rabi frequencies of the $\sigma_\pm$-polarised lasers and g is the single-atom coupling strength normalised on the D_2 cycling transition. The coefficients on each of the interaction terms are the dipole-matrix coefficients for the transitions [83].

Adiabatic elimination of the excited states (an example of how this can be done is given in Section 7.1.1) gives a master equation

$$\dot{\rho} = -i[\hat{H}, \rho] + \kappa\mathcal{D}[\hat{a}]\rho \tag{5.19}$$

with an effective Hamiltonian summed over N atoms

$$\hat{H} = \omega \hat{a}^\dagger \hat{a} + \omega_0 \hat{S}_z + \frac{\lambda_-}{\sqrt{N}}(\hat{S}_+ \hat{a} + \hat{S}_- \hat{a}^\dagger) + \frac{\lambda_+}{\sqrt{N}}(\hat{S}_- \hat{a} + \hat{S}_+ \hat{a}^\dagger) + \frac{U}{N}\hat{S}_z \hat{a}^\dagger \hat{a} \tag{5.20}$$

and parameters given by [72]

$$\omega = \omega_c - \frac{1}{2}(\omega_+ + \omega_-) + \frac{N}{3}\left(\frac{g^2}{\Delta_+} + \frac{g^2}{\Delta_-} \right) \tag{5.21}$$

$$\omega_0 = \omega_z - \frac{1}{2}(\omega_+ - \omega_-) + \frac{1}{6}\left(\frac{\Omega_-^2}{\Delta_-} - \frac{\Omega_+^2}{\Delta_+} \right) \tag{5.22}$$

$$\lambda_{\pm} = \frac{\sqrt{3N}\Omega_{\pm} g}{12\Delta_{\pm}} \tag{5.23}$$

$$U = \frac{2N}{3}\left(\frac{g^2}{\Delta_+} - \frac{g^2}{\Delta_-}\right) \tag{5.24}$$

where $\Delta_{\pm}$ are the detunings from the excited states of the $\sigma_{\pm}$ lasers.

5.2.4 Co-propagating vs. counter-propagating lasers

The Hamiltonian given in Equation 5.18 omits a phase factor to the laser coupling terms introduced by the positional spread of the atoms. Following the derivation with such a phase factor left in for a single atom gives us coupling terms [72]

$$\mathrm{e}^{-i(\mathbf{k}_-\cdot\mathbf{r})}\hat{\sigma}_+\hat{a} + \mathrm{e}^{i(\mathbf{k}_-\cdot\mathbf{r})}\hat{\sigma}_-\hat{a}^\dagger + \mathrm{e}^{i(\mathbf{k}_+\cdot\mathbf{r})}\hat{\sigma}_+\hat{a}^\dagger + \mathrm{e}^{-i(\mathbf{k}_+\cdot\mathbf{r})}\hat{\sigma}_-\hat{a} \tag{5.25}$$

where $\mathbf{k}_{\pm}$ is the wavevector of the $\sigma_{\pm}$-polarised laser fields and $\mathbf{r}$ is the position of the atom. If the driving laser fields are counter-propogating then $\mathbf{k}_- \approx -\mathbf{k}_+ = \mathbf{k}$ and we can make the rotation $\hat{\sigma}_+ \rightarrow \hat{\sigma}_+\mathrm{e}^{i(\mathbf{k}\cdot\mathbf{r})}$ to remove this atom-by-atom phase factor. If instead the lasers are co-propagating then $\mathbf{k}_- \approx \mathbf{k}_+$ and no such rotation is possible. In that case, once we sum over the entire ensemble and its uniform distribution in that phase, we do not have a superradiant threshold.

5.2.5 Experimental procedure & results

The experiment at the Centre for Quantum Technologies [72] used this method to measure the transition threshold, λ_c, as a function of various parameters. Their experiment involved ^{87}Rb atoms in a cavity with parameters $\{g, \kappa, \gamma\} = 2\pi \times \{1.1, 0.1, 3\}$ MHz and a detuning of $-2\pi \times 127$ GHz from the D_2 transition line. The atoms are cooled and around 5×10^6 are loaded into a one-dimensional optical lattice within the cavity. This lattice is created by a laser driving along the cavity axis at twice the wavelength of the cavity resonance used in the Raman transition scheme. This pins the atoms to positions such that they have identical coupling to the cavity mode.

Once loaded, the atoms are allowed to evaporate until a specific number of atoms, fixed from run to run, are left in the cavity, achieved by a non-destructive measurement of the dispersive shift on the cavity frequency, which is proportional to the atom number. The experimental sequence is triggered once the desired number of atoms is inferred. This sequence involves slow ramping[27] of the coupling lasers until the output from the cavity field, measured by a single-photon counting module (SPCM), is deemed to show that the transition has been crossed. This is done simply by comparing the output photon flux to some threshold. By varying parameters in the

---

[27] This is done for reasons of practicality. Further discussion of this ramp is presented in Section 5.3.2.

Hamiltonian in Equation 5.20 it is thus possible to compare the behaviour of the measured threshold with Equation 5.16.

The results of the experiment show that there is a range of ω_0 for which the threshold predicted in Equation 5.16 is accurate, as shown in Figure 5.4 reproduced from [72]. However, there are also significant regions where this is not true. In particular, Equation 5.16 predicts a critical coupling of zero for $\omega_0 = 0$ but in reality the threshold tends to infinity as $\omega_0 \to 0$.

This could be due to effects such as spontaneous emission, collisions and evaporation. All of these things decay the length of the collective spin, either by breaking the indistinguishability or literally by removing atoms. The impact of such an effect has been considered in [84,85] where their methods lead to a new transition point of

$$\lambda_c = \frac{1}{2}\sqrt{\frac{\omega_0^2 + \gamma^2}{-2\left\langle \hat{\sigma}_z \right\rangle \omega_0} \frac{(\omega - U/2)^2 + \kappa^2}{\omega - U/2}} \tag{5.26}$$

where γ quantifies the decay of the collective spin and $\left\langle \hat{\sigma}_z \right\rangle = \left\langle \hat{S}_z \right\rangle / N$ is the expectation value of an individual spin initially, allowing for imperfect initial state preparation which will also decrease the spin length.

Qualitatively, such a formula can be explained in the same way that the introduction of cavity decay was explained. Introducing an atomic decay means that there is something *more* for the atomic ensemble to overcome to self-organise. Such a formula can be fitted, by varying γ, to the data. However, the value of γ needed for that fit is much larger than any estimated rate of the cause of such a collective spin decay, i.e. the rates of evaporation, spontaneous emissions or collisions. Moreover, the length of the pulses emitted by the experiment gives their own indication of the decay of the spin length. These pulse lengths indicate that the spin length decay rate is on the order of the spontaneous emission and collision processes, supporting the estimated

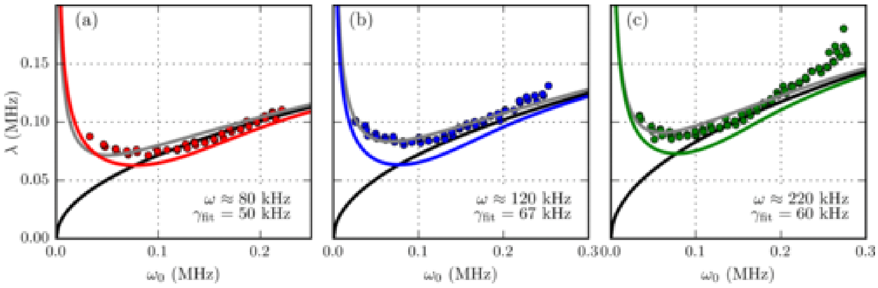

Figure 5.4: Figure reproduced from [72]. Measured threshold for varying ω_0 for different fixed values of ω. Comparison to theoretical fits from the traditional threshold of Equation 5.16 (black line), the threshold including spin length decay given by Equation 5.26 with fitted γ and $\left\langle \hat{\sigma}_z \right\rangle = -0.5$ (grey) and the derived threshold including motion given in Equation 5.40 (solid coloured lines). For the experimental data, the trap depth is 219 μK giving a Doppler broadening $\gamma_d = k\bar{v} = 2\pi \times 59$kHz for the motional threshold.

rates of those processes. This implies that there is something else going on, which delays the onset of superradiance *without* decaying the spin length or altering the length of the output pulses.

Our interpretation was that the differences were actually caused by the motion of the atoms. Since the atoms are thermal, rather than in a condensate, the atoms have residual thermal motion. This motion produces a Doppler shift to the frequency and so, since the atoms move at different velocities, ω_0 varies between atoms, causing a blurring of the phase transition point for different atoms. The subsequent delay in the onset of superradiance can be explained qualitatively by this *inhomogeneous broadening* meaning that the atoms want to self-organise *differently*, again acting as an extra barrier for the system to overcome to become superradiant. We believe that this is why the predicted threshold is less accurate for small ω_0, where this Doppler broadening is comparatively larger[28]. A mathematical approach to this problem is given in Section 5.4.

5.3 Theoretical modelling of the experiment

5.3.1 Comparison of quantum & semi-classical simulations

Much of this Section, and the earlier derivation of the phase transition point, relies on integration of the semi-classical equations discussed earlier in Section 5.1.1. These equations rely on two key assumptions: operator product factorisation and infinite atom number. Of course, no experiment can have an infinite atom number, but at what point does this become a reasonable approximation? Given the entanglement between the field and the atomic ensemble, can we simply factorise those operator products without losing information?

Figure 5.5 shows a comparison between a quantum treatment of the system and a semi-classical approximation of the dynamics. The quantum side of the comparison is presented in two ways: a single trajectory and an ensemble average of 100 trajectories. We can see that for a single trajectory, the photon measurement record introduces a significant amount of noise on the photon number in the cavity. However, this noise clearly is centred on some photon number. An ensemble of trajectories thus shows a rise to some final photon number. The semi-classical equations are integrated from an initial state slightly perturbed from the normal phase (i.e. $\{\alpha, \beta, \gamma\} = \{0.001, 0.0, -0.5\}$) and multiplied by N for comparison. They also show a rise to a steady photon number. The approximation is clearly better for higher atom number. Indeed, for $N = 80$ atoms the master equation estimate even appears

---

[28] Note also that, perhaps coincidentally, the fitted parameter for the decaying spin length threshold is remarkably close to the Doppler broadening. This is also true for the lower trap depth for which measurements were made. This could be argued to be extra evidence that indeed it is the inhomogeneous Doppler broadening that shifts the threshold.

to have decaying oscillations of around the same frequency that the semi-classical method predicts. Therefore, for the system above threshold the semi-classical model accurately predicts the dynamics and the steady state, even for quite small atom numbers. For the large numbers of atoms used in the experiments, $\sim 10^5$ atoms, this would be an excellent approximation.

Below threshold is a somewhat different situation. Figure 5.6 shows two examples of below threshold behaviour. Clearly the perfect normal phase one would expect is not present. Instead, noise creates population in the cavity mode, and by considering $g^2(0)$ we can see that this field is thermal in nature. The size of the ensemble does not seem to change either the average photon number of the thermal state nor its $g^2(0)$ value (which should characterise the size of the thermal fluctuations). This implies that again, noise on the system below threshold tends towards zero photons (and thus atomic excitations) *per atom* as the atom number increases, bringing it in line with the semi-classical predictions.

We now turn our attention to the focus of much of the experimental study of this system: the phase transition. The semi-classical prediction is that below threshold there is no cavity field and above we have a sudden increase in the photon number.

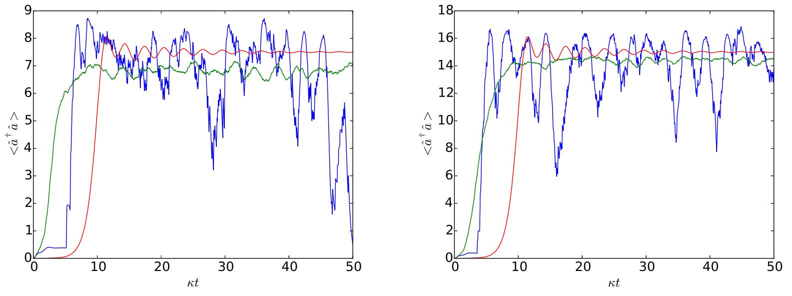

(a) $N = 20$ **(b)** $N = 40$

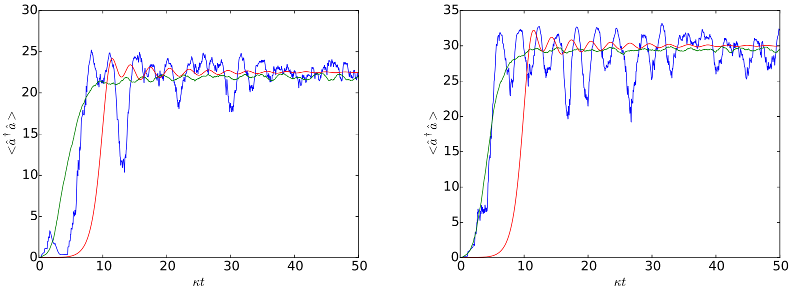

(c) $N = 60$ **(d)** $N = 80$

Figure 5.5: Comparisons between a single quantum trajectory (blue), an ensemble average of 100 quantum trajectories (green) and the semi-classical result (red) for the Dicke model above threshold with different size atomic ensembles. In each case the parameters are $\{\,\omega, \omega_0, \lambda, U\,\}/\kappa = \{\,1.0, 1.0, 1.0, 0.0\,\}$.

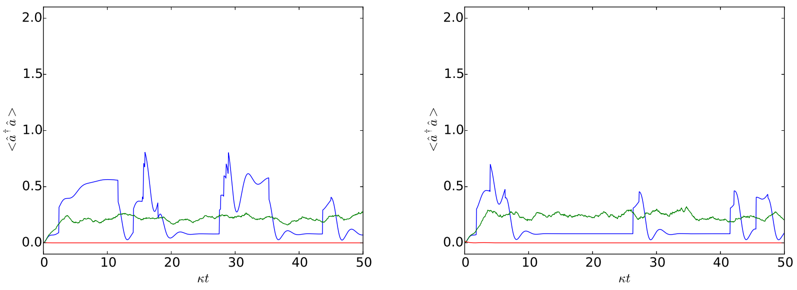

(a) $N = 20$ **(b)** $N = 160$

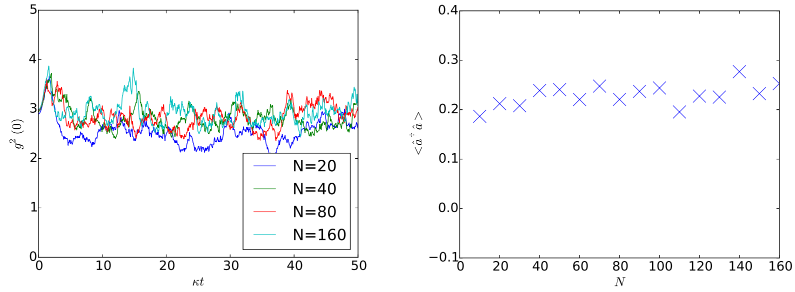

(c) Ensemble average $g^2(0)$ **(d)** Mean thermal state size

Figure 5.6: (a,b) Comparisons between a single quantum trajectory (blue), an ensemble average of 100 quantum trajectories (green) and the semi-classical result (red) for the Dicke model above threshold with different size atomic ensembles. (c) Average of 100 trajectories $g^2(0)$ for different atomic ensemble size. (d) Average photon number over a single long trajectory (average over $\kappa t = 100 \rightarrow 1000$) and its scaling with atomic ensemble size. In all cases the parameters are $\{\,\omega, \omega_0, \lambda, U\,\}/\kappa = \{\,1.0, 1.0, 0.5, 0.0\,\}$.

In reality, we know this cannot be exactly true for the quantum treatment as below threshold we have a small thermal state rather than a vacuum. Any transition in the semi-classical picture also requires some "fluctuation" away from the normal state, which is still a solution above threshold, albeit an unstable one.

This is an area in which the semi-classical picture fundamentally cannot tell us what is going on. In reality, those fluctuations could be quantum in nature. The experimental results for the BEC formulation of the Dicke model support the idea of quantum density fluctuations seeding the transition [67–70]. In our system, the temperature is high enough that vacuum fluctuations may seed the cavity mode with enough photons to drive the transition. What drives this transition is actually of some importance to our understanding of what happens in the experiment. In particular, the source of the fluctuations, characterised by a realistic set of initial conditions for the semi-classical integration, has a significant impact on the rise time once the system crosses the threshold. Due to the way the lasers are ramped up until the threshold is deemed to have been crossed, any delay in self-organisation leads to an overestimate of the critical coupling.

Figure 5.7 shows the photon number around the threshold for a variety of atom numbers. We can see that with a small atomic ensemble size the transition is smoothed out quite considerably, but as we increase the atom number we see sharper behaviour. This again indicates that for the atom numbers considered in the experiment, the shape of the transition is accurately predicted by the semi-classical equations.

5.3.2 Ramping the laser powers

The experimental sequence involves a slow ramp of the laser powers until the cavity output indicates the transition has been crossed. Why? It can be argued that this slow ramp provides time for atoms to undergo collisions, spontaneous emission or evaporate, and thus decay the spin length and delay the threshold. This delay would be higher for higher thresholds and so create an exaggerated profile for the transition. Why is it not a better idea to simply quench the system to different values of λ and make the judgement on whether the state is superradiant or not at each point? The simple answer is one of experimental practicality: the experiment works better if ramped [86]. We aim to explain why this ramp is preferred by considering the reaction of the semi-classical equations.

For the semi-classical approach, we begin at the theoretical transition and turn on the ramp. Starting at zero would allow the initial perturbation on the state to decay such that at threshold the perturbation would vary depending on the ramp speed. Regardless of the source of this perturbation in the experiment, it should not

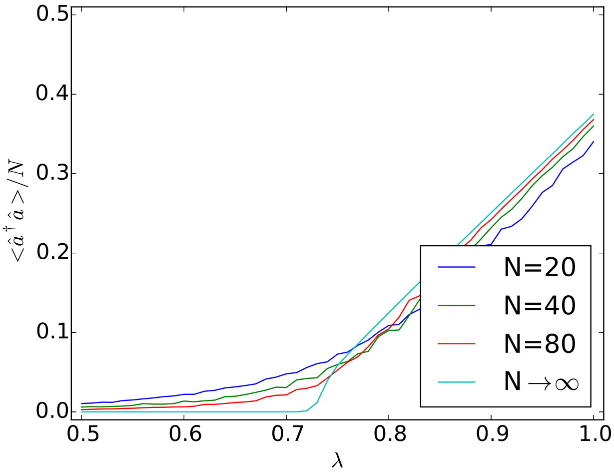

Figure 5.7: Average photon number over a single long trajectory for different atomic ensemble sizes. In all cases the parameters are $\{\omega, \omega_0, U\}/\kappa = \{1.0, 1.0, 0.0\}$

be dependent on the ramp, and so we choose initial conditions such that we ensure that the state is the same as it crosses the threshold in each case.

Figure 5.8 shows the response of the system given an abrupt switch, or *quench*, to a value above threshold, and the same response with a slow ramp to that value. We see that the response in the case of the ramp is significantly smoother. We believe that it is this smoother reaction that creates a more stable experiment. Given that the system starts with near vacuum in the cavity mode and a fully polarised atomic ensemble, it seems fair to state that in the initial spike of population, the predominant active term is $\hat{a}^\dagger \hat{S}_+$. Thus that initial reaction to an imbalance in population is scattering predominantly from one Raman beam. Each event produces a momentum kick on the atom due to the absorption and emission of photons, and so, if most are from one beam, most of them give a momentum kick in the same direction. The expectation value of $\hat{S}_z$ of the atomic ensemble therefore tells us how much momentum is being put into the system and its derivative can tell us the rate[29].

If that initial imbalance between the steady state and current state is large, as it is when a quench is performed, then a large momentum kick is given to the ensemble. The plot shows that this adjustment happens in a very short period of time (the first transfer of population takes around $\kappa t \approx 5$, or 8μs with $\kappa = 100 \times 2\pi$ kHz). Further than that, we can see that the initial reaction to a quench is an overcompensation followed by an overcorrection, followed by another smaller overcompensation and another smaller overcorrection, etc.. This means the state oscillates around the steady state with a decaying amplitude and so the large initial kick is larger than is even necessary and is followed by a sequence of smaller kicks. Momentum is transferred in a very short period of time, such that lots of kinetic energy is put into the system without much opportunity for dissipation of that energy.

If instead the system is reacting to very small changes in the steady state, as it does when following a ramp, then those momentum kicks are much fewer, and the level of response is more in line with the imbalance. It can clearly be seen that there is some initial period whereby the system adjusts to the threshold being crossed, but that it does so much more gradually than with the quench. Even for the fastest ramp considered here the peak of the derivative of $\langle \hat{S}_z \rangle$ is an order of magnitude lower than for the quench. Once the system has adjusted to the steady state it follows it reasonably closely, with a constant derivative for the atomic response, until it is turned off. This means that the momentum put into the experiment is much more spread out and so the introduced kinetic energy is smaller. We believe that this

---

[29] The other term that produces atomic excitations is $\hat{a}\hat{S}_+$ which is operated by the other Raman beam. However, if we consider the origin of the actual term it relates to the conversion of a cavity photon into a σ_- photon in that laser mode. The predominant term, $\hat{S}_+\hat{a}^\dagger$, relates to the conversion of a σ_+ laser photon into a cavity photon. This means that both processes give the atoms a momentum kick in the same direction if the lasers are counter-propagating. Similarly, both $\hat{S}_-$ terms give the atoms a kick in the opposite direction. Therefore, the time derivative of $\langle \hat{S}_z \rangle$ is directly proportional to the time derivative of the momentum delivered into the system along the axis of laser propagation.

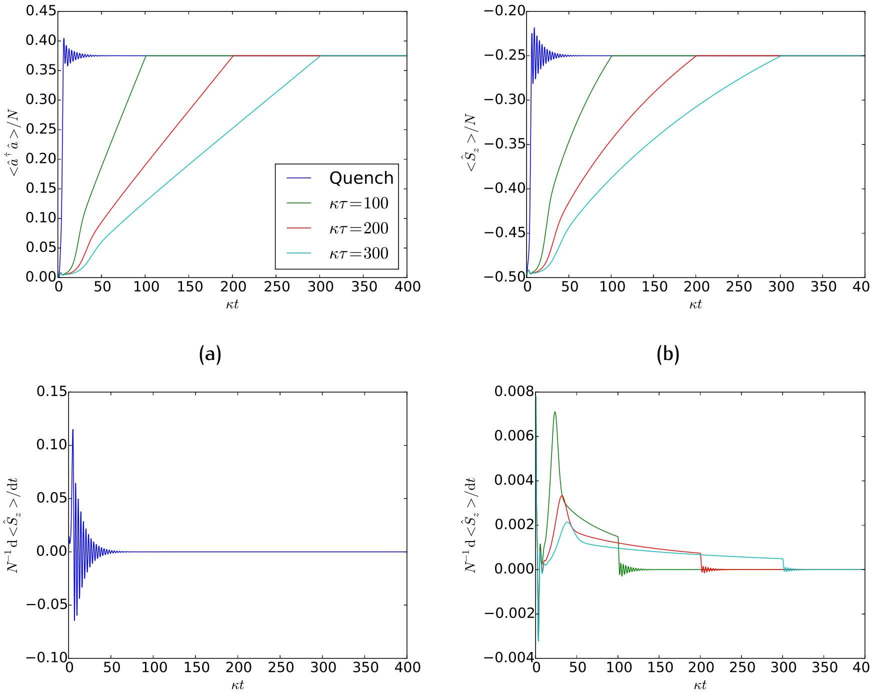

(a) (b)

(c) (d)

Figure 5.8: Semi-classical simulations for the Dicke model with parameters $\{\omega, \omega_0, U\}/\kappa = \{1.0, 1.0, 0.0\}$ beginning with $\lambda/\kappa = 1/\sqrt{2}$ and ending at $\lambda/\kappa = 1.0$ either by quench or by a linear ramp categorised by a total ramp time $\kappa\tau$. Plotted are (a) the average photon number per atom, (b) the population inversion per atom and (c,d) its derivative.

is why the ramp provides a more stable response. Essentially the quench puts too much momentum into the system in too short a period of time for it to respond and this leads to significant increases in collisions and evaporation and therefore a much shorter and less reproducible output pulse.

5.3.3 Impact of single-atom effects

The Dicke model derivation above assumes all atoms are coupled indistinguishably to the cavity mode, allowing us to treat the atomic ensemble as one large collective spin. This is true only if there is nothing that affects single atoms. A true treatment of the experimental system must therefore include single-atom events, either through evaporation or atoms being scattered into non-contributing states by collisions or spontaneous emission events. This can be accounted for reasonably simply in the semi-classical model by simply putting a decay on all components of the spin. At some point, the number of atoms is too small to support a superradiant state, and the remaining atoms return to the normal phase.

This collective spin treatment cannot be modified to account for spontaneous emission events, which break the indistinguishability criterion. These events can either decay or increase the spin length (of course not above $N/2$), and as described in [84, 85], increase the value of the critical coupling. Here we discuss the impact of these spontaneous emission events on a small ensemble, and, using this insight, discuss the idea of using a laser to repump atoms scattered into other states back into the active states.

We consider a simplified model to deal with spontaneous emission. Since we consider the system around threshold and as it self-organises, we assume the majority of the population is in $|0\rangle \equiv |F = 1, m_F = 1\rangle$ and the cavity mode is near unpopulated. This means that the only source of spontaneous emission events is the σ_+ laser driving off-resonant Rabi oscillations with $|F' = 2, m_{F'} = 2\rangle$[30]. That state can undergo three emission processes: decay to $|F = 2, m_F = 2\rangle$ ($|1\rangle$), $|F = 2, m_F = 1\rangle$ ($|s\rangle$) and $|F = 1, m_F = 1\rangle$ ($|0\rangle$). In our effective system where the excited states have been eliminated the three processes can be represented as follows: the first is $|1\rangle\langle 0| = \hat{\sigma}_+$, the second shelves[31] the atom outside of the Dicke model scheme which we will call $\hat{\sigma}_s$ and the third is a dephasing process $|0\rangle\langle 0|$ which we call $\hat{\sigma}_1$. The rates for these are in a fixed ratio given by the Clebsch-Gordan coefficients for the relevant levels [83]. The rate at which these happen can be stated in terms of the Raman transition rates, detuning and the cavity co-operativity [71].

The Hamiltonian in this treatment is unchanged, but the master equation now features these three loss terms on each atom,

$$\dot{\rho} = -i[\hat{H}, \rho] + \kappa\mathcal{D}[\hat{a}]\rho + \sum_{i=0}^{N}\left(\frac{\gamma_+}{2}\mathcal{D}[\hat{\sigma}_+^{(i)}]\rho + \frac{\gamma_1}{2}\mathcal{D}[\hat{\sigma}_1^{(i)}]\rho + \frac{\gamma_s}{2}\mathcal{D}[\hat{\sigma}_s^{(i)}]\rho\right), \qquad (5.27)$$

where we assume that each process can be distinguished.

The impact of the shelving process is the easiest to consider, as its impact is the same as atoms leaving the trap. As above, this simply puts an exponential decay on the spin length and so any superradiance achieved will be temporary. Clearly a state with all atoms in the inactive state $|s\rangle$ is uncoupled from the Hamiltonian and so with that term active the only possible steady state is all atoms in this dark state. Figure 5.9 shows this clearly. A superradiant state is formed, and then slowly decays until there are not enough atoms in the active states to support superradiance.

For the six atoms considered here, then, with coupling $\lambda/\kappa = 1.0$, a state of spin

---

[30] Of course spontaneous emission from the other Raman process is also possible. These events would add extra shelving processes, as well as a dephasing process for $|2, 2\rangle$ and a traditional spontaneous emission term $|1, 1\rangle\langle 2, 2|$. The impact of such terms would be much the same as for their equivalent processes discussed in the text and so they are omitted for the sake of simplicity.

[31] The atom being "shelved" means that the atom has been put into an inactive state, in this case $|F = 2, m_F = 1\rangle$, from which there are no active Raman transitions.

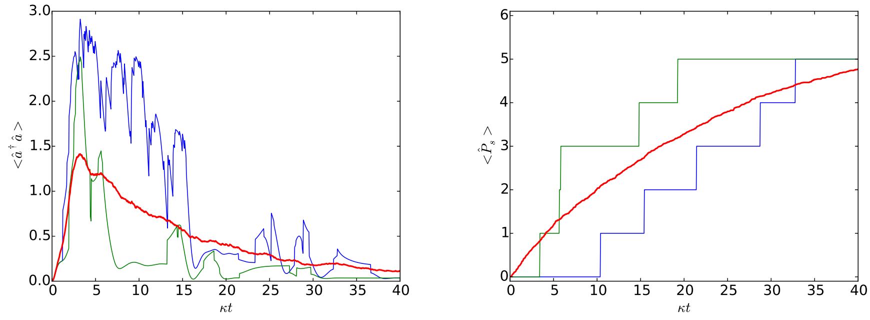

(a)

(b)

Figure 5.9: Dicke model simulation for six atoms with $\{\,\omega, \omega_0, \lambda, U\,\}/\kappa = \{\,1.0, 1.0, 1.0, 0.0\,\}$ where for each atom a spontaneous emission term is simulated by a loss term $\hat{\sigma}_s$ at a rate $\gamma_s/\kappa = 0.05$. Shown are two individual trajectories (blue, green) and an ensemble average of 200 trajectories (red). Plotted are (a) the photon number in the cavity mode while (b) shows the expectation value of a projector into the shelved state $|s\rangle$. The atomic jumps in the individual trajectories can be seen by jumps in the population of the shelved state, with the system expected to be below threshold once the number of shelved atoms is greater than half of the total number of atoms.

length $S = 3/2$ would be at exactly the semi-classical threshold[32]. All states with larger spin length than that would support a superradiant state, with the maximal spin length meaning the largest magnitude of superradiant state. States with spin length below $S = 3/2$ will be below threshold, which for six atoms means thermal fluctuations about the normal phase. The lower the spin length the smaller these fluctuations, with zero spin length leading to no movement at all. Therefore, as the spin length decays, so does the magnitude of the cavity field occupation leading to a measured output of a pulse of finite length. This is what is seen in the experiments, though of course other causes of spin length decay in the experiment will also contribute to this.

The impact of the other two spontaneous emission processes is more complex. Figure 5.10 shows that the response of the system is a decay of the spin length to some non-zero steady state. However, an individual trajectory shows that individual events do not necessarily lower the spin length. Some events decrease the spin length, some do not alter it and some even increase it. In fact, the spin length can be reduced to below superradiance but then another event can seemingly bring the superradiance back. In the experiments, this is not seen. This is because other processes, including the shelving processes shown above, also decay the spin length irreversibly. This means that any "resuscitation" comes too late. However, the reason why this can happen when those processes are ignored gives a fundamental insight into the impact of these single-atom effects.

The change in the collective spin length happens because of the way different

---

[32] An explanation of this and a more in-depth consideration of the impact of the spin length on the response of the system is given in Section 7.2.

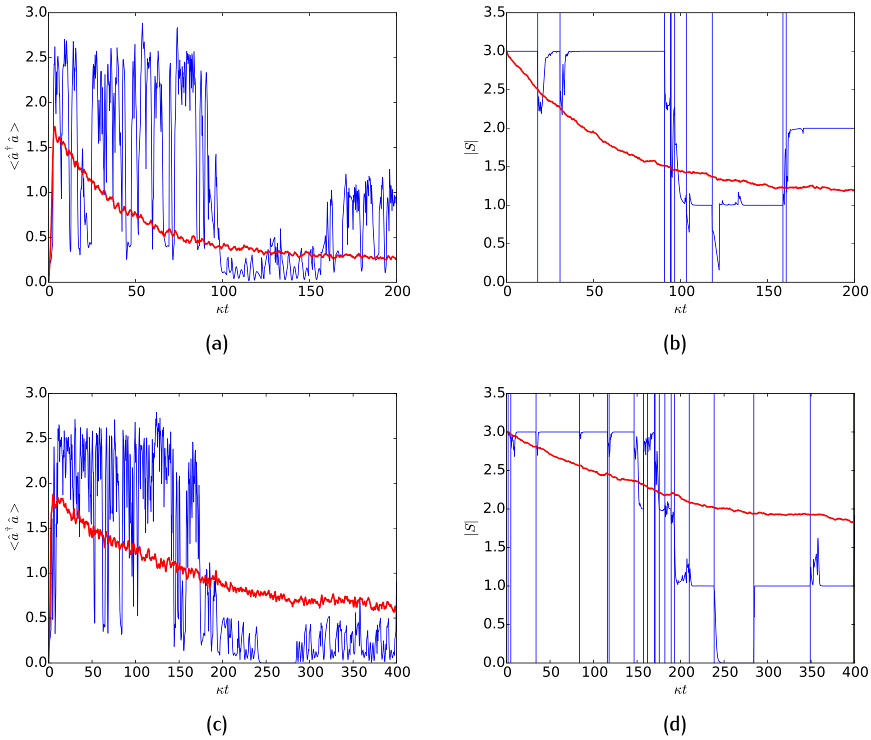

(a) (b)

(c) (d)

Figure 5.10: Dicke model simulation for six atoms with $\{\,\omega, \omega_0, \lambda, U\,\}/\kappa = \{\,1.0, 1.0, 1.0, 0.0\,\}$ where for each atom a spontaneous emission term is simulated by a loss term (a,b) $\hat{\sigma}_+$ or (c,d) $\hat{\sigma}_1$, at rates $\gamma_i/\kappa = 0.01$. Shown is an individual trajectory (blue) and its jumps (blue vertical lines) and an ensemble average of 200 trajectories (red). Plotted are (a,c) the photon number in the cavity mode while (b,d) shows the magnitude of the spin vector $\hat{\mathbf{S}}$ found by calculating $\langle \hat{S}_x^2 + \hat{S}_y^2 + \hat{S}_z^2 \rangle = S(S+1)$ and solving for S. The system is expected to be below threshold when the spin length is below 3/2.

spin states combine to form a collective spin, whereby the length of some product $S_1 \otimes S_2$ is not necessarily the sum $S_1 + S_2$. The state after, for example, the first $\hat{\sigma}_+$ event is something of the form $\rho = \rho_{N-1} \otimes |1\rangle$ where ρ_{N-1} represents $N-1$ indistinguishable atoms in some collective state. The length of ρ_{N-1}, due to this being the first event, is $(N-1)/2$, and the length of $|1\rangle$ (in this basis) is $1/2$. This means that the length of ρ is some *superposition* of $S = (N-1)/2 \pm 1/2$ with the coefficients decided by the particular states occupied by the atoms.

The cavity output field is different for each of these spin length contributions, and so, in a quantum trajectory picture, one of them is projected out by the cavity output measurement. Thus, the first event can cause the spin length to drop or stay maximal. If a drop has occurred, and the spin length now sits at some sub-maximal length S_{N-1}, then the subtraction and re-addition of the spin-1/2 particle add separately. This gives the length of the total spin as some superposition $S = S_{N-1} \pm 1/2 \pm 1/2$ (where the two ± are independent). This means the event can cause the spin to jump up one, jump down one or stay the same.

The jump to a superposition, and the subsequent measurement backaction, occur after every event, and so on an individual trajectory we have a sequence of events, each followed by the spin length being projected into a state below, above or the same as the one it was in before. On average, this trends down to some steady-state value. At this point, the superposition imposed by each event does not *on average* change the spin length because the average of the states in the post-jump superposition is that of the steady state. Of course individual trajectories must choose a specific state of the superposition and so will jump around the steady state. It should be noted that this steady-state spin length is *always* less than maximal. We see that the $\hat{\sigma}_+$ events have a lower steady-state spin length and reach that value faster. This can be explained by the fact that the impact of $\hat{\sigma}_1$ events is lower given that most of the atoms are in that state as it is.

If the loss of atoms by scattering into non-active states, in particular $|s\rangle$ as discussed above, is a major source of the decay in the spin length, then it would seem

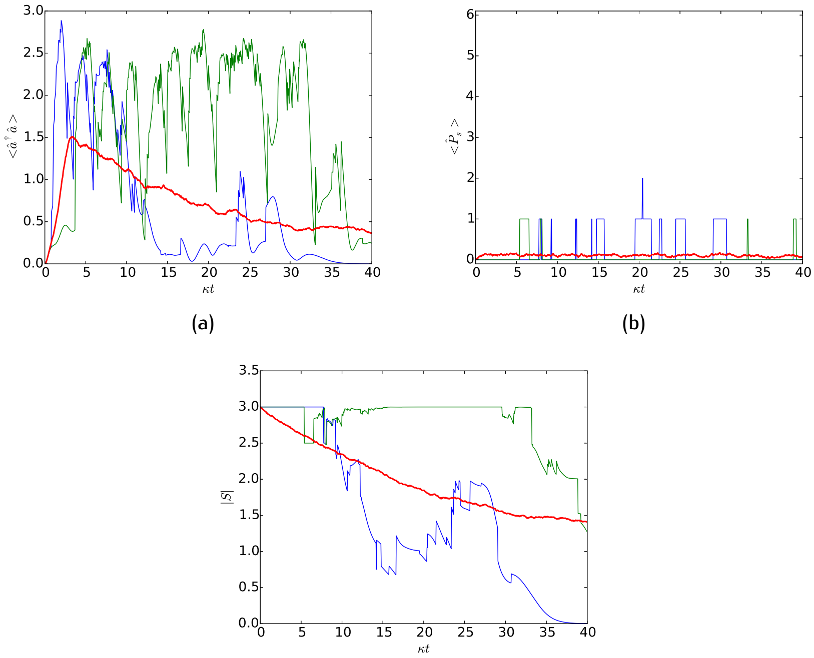

(a)

(b)

(c)

Figure 5.11: Dicke model simulation for six atoms with $\{\,\omega, \omega_0, \lambda, U\,\}/\kappa = \{\,1.0, 1.0, 1.0, 0.0\,\}$ where for each atom a spontaneous emission term is simulated by a loss term $\hat{\sigma}_s$ at a rate $\gamma_s/\kappa = 0.05$ and a repump laser is simulated by the repump terms $|1,1\rangle\langle 2,1|$ at rate $\gamma/\kappa = 10.0$ and $|2,2\rangle\langle 2,1|$ at rate $\sqrt{2/3}\gamma$. Shown are two individual trajectories (blue, green) and an average of 200 trajectories (red). Plotted are (a) the photon number in the cavity mode while (b) shows the expectation value of a projector into the shelved state $|s\rangle$ and (c) shows the magnitude of the spin vector $\hat{\mathbf{S}}$ found by calculating $\langle \hat{S}_x^2 + \hat{S}_y^2 + \hat{S}_z^2 \rangle = S(S+1)$ and solving for S. For the individual trajectory the jumps into and out of the shelved state can be seen in the value of the shelved state projector. The system is expected to be below threshold for $S < 3/2$.

that repumping from that state into the two active states would help. Essentially, a strong laser can be added to the scheme, driving transitions from $|s\rangle$ to some excited state. The resultant emissions from there will drop the atom down into down into either of the other states (or back to $|s\rangle$ where the process repeats). The excited state could be, for example, $|F'=2, m_{F'}=2\rangle$ in the D_1 line[33]. To simulate this we take Equation 5.27 and add two extra dissipative terms for each atom $|0\rangle\langle s|$ at a rate $\gamma_r \gg \gamma_s$ and $|1\rangle\langle s|$ at a rate $\sqrt{2/3}\gamma_r$.

Figure 5.11 shows that this does not necessarily help. One trajectory is stabilised but the other quickly decays. We can use the insight garnered above to explain this: pumping atoms back into states that do not match the global state does not necessarily replenish the spin length. This is in line with limited results from the experiments [87], where the addition of the repump laser sometimes helped and sometimes did not help and was thus not used in the collection of data for [72].

5.4 Impact of motion on the phase transition

As discussed in 5.2.5, there are discrepancies between the theoretical and experimental results, with particular inaccuracy for low ω_0. Our interpretation of this mismatch is that it is caused by the atomic motion. Different atoms move at different speeds, and so the Doppler shift on ω_0 is a spectrum across the ensemble. This inhomogeneous broadening means that different atoms see different transition points. This means that the self-organisation of the spins, which is required for superradiance, has more to overcome and so the transition is shifted to higher couplings. The following text is adapted from the Appendix of [72].

We assume that the internal atomic and cavity dynamics are much faster than the timescales of the atomic motion, and so treat the position as a classical parameter not tied to the other dynamics. The Hamiltonian, summing over individual atoms, is[34]

$$\hat{H} = \omega\hat{a}^\dagger\hat{a} + \omega_0\sum_{j=1}^{N}\hat{\sigma}_z^{(j)} + \frac{\lambda_-}{\sqrt{N}}\sum_{j=1}^{N}\left(e^{-i\phi_j}\hat{a}\hat{\sigma}_+^{(j)} + e^{i\phi_j}\hat{a}^\dagger\hat{\sigma}_-^{(j)}\right) + \frac{\lambda_+}{\sqrt{N}}\sum_{j=1}^{N}\left(e^{-i\phi_j}\hat{a}^\dagger\hat{\sigma}_+^{(j)} + e^{i\phi_j}\hat{a}\hat{\sigma}_-^{(j)}\right). \tag{5.28}$$

The phases on each atom are given by $\phi_j = \vec{\mathbf{k}}\cdot\vec{\mathbf{r}}_j(t)$ where $\vec{\mathbf{k}}$ is the wavevector of the

---

[33] It is important that this laser is not close in frequency to the Dicke model configuration laser and cavity modes, as otherwise the repump laser would also create Raman transitions and thus impact the active states and the Dicke model configuration. Choosing an excited state in a different hyperfine manifold avoids that issue.

[34] Note that in this derivation U is assumed to be zero for the sake of simplicity, but if it is non-zero, and its magnitude less than 2ω, then it can be easily accounted for. Since we are only interested in the transition point, where $\hat{\sigma}_z = \pm 0.5$ depending on the ground state, then the derivation can be edited such that $\omega \rightarrow \omega \pm U/2$.

laser beam[35] and so the only relevant part of the position, and thus motion, is the single dimension along the path of the lasers and so the dot product becomes $kr_j(t)$.

We make a Holstein-Primakoff approximation $\hat{\sigma}_-^{(j)} \approx \hat{b}_j$, where $\hat{b}_j$ is the annihilation operator for an excitation on atom j. Such an approximation is valid for $\hat{b}_j^\dagger \hat{b}_j \ll 1$, i.e. below threshold where the number of atomic excitations is very low. We can then build quantum Langevin equations

$$\dot{\hat{a}} = -(\kappa + i\omega)\hat{a} - \frac{i\lambda_-}{\sqrt{N}} \sum_{j=1}^{N} \mathrm{e}^{ikr_j(t)} \hat{b}_j - \frac{i\lambda_+}{\sqrt{N}} \sum_{j=1}^{N} \mathrm{e}^{-ikr_j(t)} \hat{b}_j^\dagger + \sqrt{2\kappa}\hat{a}_{\mathrm{in}}(t) \tag{5.29}$$

$$\dot{\hat{b}}_j = -i\omega_0 \hat{b}_j - \frac{i\lambda_-}{\sqrt{N}} \mathrm{e}^{-ikr_j(t)} \hat{a} - \frac{i\lambda_+}{\sqrt{N}} \mathrm{e}^{-ikr_j(t)} \hat{a}^\dagger. \tag{5.30}$$

The formal solution to the second of these is

$$\begin{aligned} \hat{b}_j(t) = \mathrm{e}^{-i\omega_0 t}\hat{b}_j(0) - \frac{i\lambda_-}{\sqrt{N}} \int_0^t \mathrm{e}^{-ikr_j(t')} \mathrm{e}^{-i\omega_0(t-t')} \hat{a}(t') \mathrm{d}t' \\ - \frac{i\lambda_+}{\sqrt{N}} \int_0^t \mathrm{e}^{-ikr_j(t')} \mathrm{e}^{-i\omega_0(t-t')} \hat{a}^\dagger(t') \mathrm{d}t' \end{aligned} \tag{5.31}$$

and this can be substituted into the field annihilation operator equation giving

$$\begin{aligned} \dot{\hat{a}} = -(\kappa + i\omega)\hat{a} &- \frac{i\lambda_-}{\sqrt{N}} \sum_{j=1}^{N} \mathrm{e}^{ikr_j(t)} \mathrm{e}^{-i\omega_0 t} \hat{b}_j(0) - \frac{i\lambda_+}{\sqrt{N}} \sum_{j=1}^{N} \mathrm{e}^{ikr_j(t)+i\omega_0 t} \hat{b}_j^\dagger(0) \\ &+ \sqrt{2\kappa}\hat{a}_{\mathrm{in}}(t) - \frac{\lambda_-^2}{N} \left(\sum_{j=1}^{N} \int_0^t \mathrm{d}t' \mathrm{e}^{ik[r_j(t)-r_j(t')]-i\omega_0(t-t')} \hat{a}(t') \right) \\ &+ \frac{\lambda_+^2}{N} \left(\sum_{j=1}^{N} \int_0^t \mathrm{d}t' \mathrm{e}^{-ik[r_j(t)-r_j(t')]+i\omega_0(t-t')} \hat{a}(t') \right) \\ &- \frac{\lambda_-\lambda_+}{N} \left(\sum_{j=1}^{N} \int_0^t \mathrm{d}t' \mathrm{e}^{ik[r_j(t)-r_j(t')]-i\omega_0(t-t')} \hat{a}^\dagger(t') \right) \\ &+ \frac{\lambda_-\lambda_+}{N} \left(\sum_{j=1}^{N} \int_0^t \mathrm{d}t' \mathrm{e}^{-ik[r_j(t)-r_j(t')]+i\omega_0(t-t')} \hat{a}^\dagger(t') \right). \end{aligned} \tag{5.32}$$

We now consider $r_j(t) \approx r_j + v_j t$, such that r_j is the initial position and the velocity v_j is assumed unchanged through the length of the experiment. This means that the

---

[35] The signs of the phases in the Hamiltonian here take the counter-propagation of the lasers into account. In the co-propagating case the phases in the λ_+ term are switched. This has strong implications, primarily that in two of the integrals introduced in Equation 5.32 the positions no longer cancel. This introduces an integral over the positions which cancels those terms to zero. This reduces the entire problem to something more akin to a single-beam.

initial position dependence drops out of every one of the integrals. The velocities are assumed to follow a one-dimensional Maxwell-Boltzmann distribution such that

$$\frac{1}{N}\sum_{j=1}^{N} f(v_j) = \frac{1}{\sqrt{2\pi\bar{v}^2}}\int\limits_{-\infty}^{\infty} \exp\left(-\frac{v^2}{2\bar{v}^2}\right) \mathrm{d}v \tag{5.33}$$

where $\bar{v}$ is the route-mean-square (rms) velocity. Thus all the above integrals become a variant on the single integral

$$\begin{aligned}\frac{1}{\sqrt{2\pi\bar{v}^2}}\int_{-\infty}^{\infty}\int_{0}^{t} \exp\left(-\frac{v^2}{2\bar{v}^2}\right) \mathrm{e}^{\pm i(\omega_0-kv)(t-t')}\left\langle\hat{\mathcal{O}}(t')\right\rangle \mathrm{d}t'\mathrm{d}v&\\ = \int\limits_{0}^{t}\exp\left[-\frac{k^2\bar{v}^2(t-t')^2}{2}\right]\mathrm{e}^{\pm i\omega_0(t-t')}\left\langle\hat{\mathcal{O}}(t')\right\rangle \mathrm{d}t'&\end{aligned} \tag{5.34}$$

where $\hat{\mathcal{O}}$ represents $\hat{a}$ or $\hat{a}^\dagger$. We then take the Laplace transform

$$\int_0^\infty \mathrm{e}^{-st}\left\{\int\limits_0^t \exp\left[-\frac{k^2\bar{v}^2(t-t')^2}{2}\right]\mathrm{e}^{\pm i\omega_0(t-t')}\left\langle\hat{\mathcal{O}}\right\rangle \mathrm{d}t'\right\}\mathrm{d}t$$

$$= \int\limits_0^\infty\int\limits_{t'}^\infty \exp\left[-\frac{k^2\bar{v}^2(t-t')^2}{2}\right]\mathrm{e}^{-st\pm i\omega_0(t-t')}\left\langle\hat{\mathcal{O}}(t')\right\rangle \mathrm{d}t\mathrm{d}t' \tag{5.35}$$

$$= \int\limits_0^\infty\left\{\int\limits_{t'}^\infty \exp\left[\frac{-k^2\bar{v}^2(t-t')^2}{2}\right]\mathrm{e}^{-(s\mp i\omega_0)(t-t')}\mathrm{d}t\right\}\mathrm{e}^{-st'}\left\langle\hat{\mathcal{O}}(t')\right\rangle \mathrm{d}t' \tag{5.36}$$

$$= \int\limits_0^\infty\left[\int\limits_{0}^\infty \exp\left(-\frac{k^2\bar{v}^2\tau^2}{2}\right)\mathrm{e}^{-(s\mp i\omega_0)\tau}\mathrm{d}\tau\right]\mathrm{e}^{-st'}\left\langle\hat{\mathcal{O}}(t')\right\rangle \mathrm{d}t' \tag{5.37}$$

$$= \frac{1}{k\bar{v}}\sqrt{\frac{\pi}{2}}\exp(z_\mp^2)\mathrm{erfc}(z_\pm)\left\langle\hat{\mathcal{O}}(s)\right\rangle \tag{5.38}$$

where $\langle\hat{\mathcal{O}}(s)\rangle$ is the Laplace transform of $\langle\hat{\mathcal{O}}(t)\rangle$, $z_\pm = (s \pm i\omega_0)/(k\bar{v}\sqrt{2})$ and $\mathrm{erfc}(z)$ is the complementary error function.

Considering initial expectations $\langle\hat{b}_j(0)\rangle = \langle\hat{b}_j^\dagger(0)\rangle = 0$ and noise $\langle\hat{a}_{\mathrm{in}}(t)\rangle = 0$ then the Laplace transform of Equation 5.32 is given by

$$\begin{aligned}(s+\kappa+i\omega)\langle\hat{a}(s)\rangle - \langle\hat{a}(0)\rangle = &-\frac{\lambda_-^2}{k\bar{v}}\sqrt{\frac{\pi}{2}}f(z_+)\langle\hat{a}(s)\rangle + \frac{\lambda_+^2}{k\bar{v}}\sqrt{\frac{\pi}{2}}f(z_-)\langle\hat{a}(s)\rangle\\ &-\frac{\lambda_-\lambda_+}{k\bar{v}}\sqrt{\frac{\pi}{2}}f(z_+)\langle\hat{a}^\dagger(s)\rangle + \frac{\lambda_-\lambda_+}{k\bar{v}}\sqrt{\frac{\pi}{2}}f(z_-)\langle\hat{a}^\dagger(s)\rangle\end{aligned} \tag{5.39}$$

where we have defined $f(z) = \exp(z^2)\mathrm{erfc}(z)$.

For the Dicke model $\lambda_+ = \lambda_- \equiv \lambda$ and so the above can be translated to two coupled equations for $\langle \hat{a}(s) \rangle$ and its conjugate. If any of the poles of $\langle \hat{a}(s) \rangle$ have a positive real part, the solution describes an amplification process[36]. This means that the cavity field becomes non-zero, and so the threshold has been reached. The threshold is thus the smallest value of λ for which a pole crosses the imaginary axis. For these equations, the poles can be found as the roots of the determinant. This gives us the threshold expression

$$\lambda_c = \sqrt{\frac{\sqrt{2}k\bar{v}(\omega^2 + \kappa^2)}{8\omega F\left(\frac{\omega_0}{\sqrt{2}k\bar{v}}\right)}} \tag{5.40}$$

where $F(y)$ is the Dawson function defined by

$$F(y) = \mathrm{e}^{-y^2} \int_0^y \mathrm{e}^{x^2} \mathrm{d}x. \tag{5.41}$$

This method still underestimates the transition, but the shape seems much more accurate in comparison to the traditional threshold given in Equation 5.16. In comparison to Equation 5.26 the fit for this method is perhaps somewhat less convincing. However, given our lack of explanation of the high fitting parameter required for that method to match the data, it would seem like our method is a much more solid explanation.

There are several reasons why our treatment is still not perfect, including the assumption that velocities do not change over the length of the experiment, and that they are not coupled to the cavity field or the spins. The motional fit is also more convincing for the lower trap depth considered in [72]. At lower temperatures, the atomic velocities are smaller, and so perhaps the assumptions made about the velocity distribution are more accurate.

The fact that the fit is also more convincing with a single-beam or co-propagating lasers (as considered in [72]) is also of interest. In those cases the threshold is for a switch in polarisation of the atoms, and so at most one photon can be scattered per atom. In the Dicke model case multiple scattering events can occur from each atom. Coupling between the spin and velocity would be via those scattering events

---

[36] It is interesting to discuss, and a significant part of the original work, what happens for a single beam and for the case of the co-propagating lasers. With $\lambda_- = 0$, the situation is a Tavis-Cummings model and so naïvely we would anticipate a complete switching of the state to the inverted phase for any non-zero λ_+. In reality, the inhomogeneous broadening and spin length decaying processes delay this threshold to a higher value of λ_+. For the co-propagating case then the two cross terms (i.e. those with $\lambda_-\lambda_+$ as the coefficient) are zero and so we are left with two expressions. Similarly to the single beam case this can lead to a transient pulse as the state switches from normal to inverted, and again that threshold is at some non-zero λ. For the particular situation ω_0 is zero, then that threshold becomes infinite. In both of these cases, the match to the experimental data is excellent, and so it is with confidence that we can say that the Doppler broadening plays a significant role in defining transitions. Our understanding is that it is this threshold that was being measured in [88] rather than the Dicke model phase transition as originally thought.

and so it makes sense that our treatment would be more accurate for situations with controlled scattering. There are of course other experimental concerns, not factored into our treatment, that could impact the critical coupling.

Chapter 6

Extreme spin squeezing in the steady state of a generalised Dicke model

Generally, research on cavity engineered Dicke models either wishes to minimise or neglect the dispersive shift, $\hat{S}_z \hat{a}^\dagger \hat{a}$. This non-linearity can somewhat complicate the phase transition behaviour and the dynamics of the system, at the very least being an added parameter of which to keep track. Once it becomes large it completely changes the behaviour of the system. In this Chapter, we consider what happens when that term is allowed to dominate the Hamiltonian. What we find is extremely slow dynamics from any state eventually trending towards a highly entangled atomic state: the central Dicke state $|N/2, 0\rangle$. We propose methods to access this state: a simple heralded probabilistic method and a more complicated protocol involving a time-dependent Hamiltonian. This work is presented in the form of a paper published in Physical Review A. It has been reformatted for this thesis, with added subsection headings, minor changes to some figures and some notation and spelling altered to provide consistency throughout the thesis, but is available in its original form at https://journals.aps.org/pra/abstract/10.1103/PhysRevA.99.023822.

6.1 Introduction

Atom interferometers are useful for making precision measurements of acceleration, time, rotation, and, potentially, even gravitational waves [89]. Interferometers employing uncorrelated states of N atoms have a variance limited by the standard quantum limit (SQL), which scales like $1/N$, but suitably entangled atomic states could potentially reach the Heisenberg limit, where scaling like $1/N^2$ becomes the lower bound for the variance [90, 91]. Spin squeezed states [17, 19–22, 92] are a popular choice to try and make measurements that are below the SQL and potentially approach the Heisenberg limit. Successful spin squeezing experiments have been carried out using atomic collisions in Bose-Einstein condensates [14, 93–100], quantum non-demolition measurements [101–107], and various other methods [108–112]. The best of these experiments have exceeded the SQL by 100-fold [107], but for the large numbers of atoms that were involved, this is still nowhere near the corresponding Heisenberg limit. If this limit could be approached, then the actual number of atoms required for significant gains in precision could in fact be relatively small.

6.1.1 Metrology of Dicke states

A class of idealised states that can potentially reach the Heisenberg limit are the so-called Dicke states [113, 114], which are simultaneous eigenstates of the collective angular momentum operators $\hat{\mathbf{S}}^2$ and $\hat{S}_z$, denoted by $|S, m\rangle$. Here we shall consider only symmetric Dicke states, for which the wavefunction is symmetric under particle exchange.

Dicke states do not lend themselves well to characterisation by conventional spin squeezing measures, which generally rely on a well-defined polarisation of the spin state. Instead, to characterise the squeezing we consider the Dicke squeezing parameter [23],

$$\xi_D = N\frac{(\Delta\hat{S}_z)^2 + 1/4}{\langle\hat{S}_x^2 + \hat{S}_y^2\rangle} \,. \tag{6.1}$$

This parameter gives us access to the metrological sensitivity relative to the SQL. For Mach-Zehnder interferometry, the variance is bounded by $\beta(\xi_D/N)$, where β is a factor of order one [23]. The parameter also provides a lower bound for the entanglement depth of $\lceil\xi_D^{-1} - 2\rceil$ [24], where $\lceil x\rceil$ denotes the minimum integer no less than x. Considering this bound, we can see that the limit for entanglement, and thus metrological gain, is $\xi_D = 1/2$.

For a Dicke state $|N/2, m\rangle$, the Dicke squeezing parameter is given by

$$\xi_D = \frac{1}{N + 2 - \frac{4m^2}{N}} \,. \tag{6.2}$$

This means that the Dicke states offer near Heisenberg limited metrological sensitivity for $N \gg \{2, m\}$. In addition, for $m < \sqrt{N}/2$ the entanglement depth must be the size of the entire atomic ensemble. There have been proposals for schemes to prepare Dicke states of an atomic ensemble (see, e.g., [115–122]), typically based upon conditional or probabilistic processes and possibly also feedback of some sort. Alternatively, schemes using collisions in spin-1 Bose-Einstein condensates are possible and have been implemented [123–125].

6.1.2 Summary of the Chapter

Here we propose an approach that can, in principle, prepare an arbitrary Dicke state as the *steady state* of a cavity QED system with a suitably engineered atom-cavity interaction. In particular, this interaction is described by the so-called generalised Dicke model, which may be engineered, as described in Chapter 5, in an optical cavity QED setting with alkali atoms, via laser- and cavity-driven Raman transitions between ground-state electronic sublevels of the atoms [53,71,72,80,81].

We describe the model and the specific parameter regime in which the desired steady-state behaviour - a near pure Dicke state - is obtained, as well as explaining the mechanism that allows that steady state to exist. We then explain how that same mechanism means that reaching that steady state through natural evolution is an extremely slow process, which leads us to consider modified schemes. The first of these produces the state heralded by the detection of a single photon in the output channel, while the second makes use of time variation of one of the parameters of the model. These methods allow for the preparation of the state on much faster timescales. We conclude with a discussion of a specific realisation in an optical cavity QED system and show that significant squeezing and high fidelity states can be achieved with feasible experimental conditions.

6.2 System & model

We consider a generalised Dicke model for N two-level atoms and a single mode of the electromagnetic field, as described by the master equation [51,53,72,79–81]

$$\dot{\rho} = -i[\hat{H}, \rho] + \kappa\mathcal{D}[\hat{a}]\rho \tag{6.3}$$

with the Hamiltonian

$$\hat{H} = \omega_0 \hat{S}_z + \omega \hat{a}^\dagger \hat{a} + \frac{\lambda}{\sqrt{N}}(\hat{a} + \hat{a}^\dagger)(\hat{S}_+ + \hat{S}_-) + \frac{U}{N}\hat{S}_z \hat{a}^\dagger \hat{a} \tag{6.4}$$

where $\mathcal{D}[\hat{a}]\rho$ represents the superoperator

$$\mathcal{D}[\hat{a}]\rho = 2\hat{a}\rho\hat{a}^\dagger - \hat{a}^\dagger\hat{a}\rho - \rho\hat{a}^\dagger\hat{a}. \tag{6.5}$$

Here $\hat{a}$ ($\hat{a}^\dagger$) is the annihilation (creation) operator for the quantised cavity mode, and $\hat{S}_i$ are collective atomic spin operators satisfying the usual angular momentum commutation relations. The linear atom-field coupling strength is denoted by λ, the non-linear (or dispersive) coupling strength is given by U, ω and ω_0 are the cavity and atomic resonance frequencies, respectively, and κ is the cavity field decay rate.

This system possesses a rich phase diagram, which has been studied both semi-classically [78,79] and quantum mechanically [80]. In [80], it was noticed that as U becomes very large compared to the other parameters, the atomic state can become strongly squeezed in the $\hat{S}_z$ spin component. The present work looks more closely at, and provides an explanation for, this large U behavior.

Before continuing, we note that our Hamiltonian is similar in structure to that put forward in [126], where a method based on time-varying parameters was proposed for preparing Dicke states of donor nuclear spins in silicon. The discrete stepping method we describe in Section 6.6 can be viewed as parallel to the method in [126].

6.3 Steady-state behaviour

6.3.1 Expectation values

We consider the steady-state behaviour of the master equation in Equation 6.3 as we vary U. Figure 6.1a displays various properties of the system as U is varied for several different values of (linear) coupling strength λ. In particular, it plots the steady-state values of the mean intracavity photon number, $\langle\hat{a}^\dagger\hat{a}\rangle$, the collective atomic inversion, $\langle\hat{S}_z\rangle$, and the Dicke squeezing parameter, ξ_D.

For small $|U|$ we see that the properties of the system depend rather sensitively on U and λ. However, for large $|U|$ we observe a simpler, monotonic dependence: the mean photon number reduces steadily, becoming very small, the atomic inversion converges quite rapidly to zero, while the Dicke squeezing parameter approaches the value $1/(N+2)$. This indicates that the system settles predominantly into the Dicke state $|N/2, 0\rangle$, corresponding to genuine multipartite entanglement of the entire ensemble and Heisenberg limited metrological sensitivity. The relative lack of sensitivity to the coupling strength λ is in direct contrast to the traditional and well-known superradiant behaviour of the Dicke model that occurs when U is small or negligible [51,53,71,72,78–81,127]

In Figure 6.1b we plot $\langle\hat{a}^\dagger\hat{a}\rangle$, $\langle\hat{S}_z\rangle$, and ξ_D as a function of U/N for several different values of N and observe that the same general pattern holds. We do note,

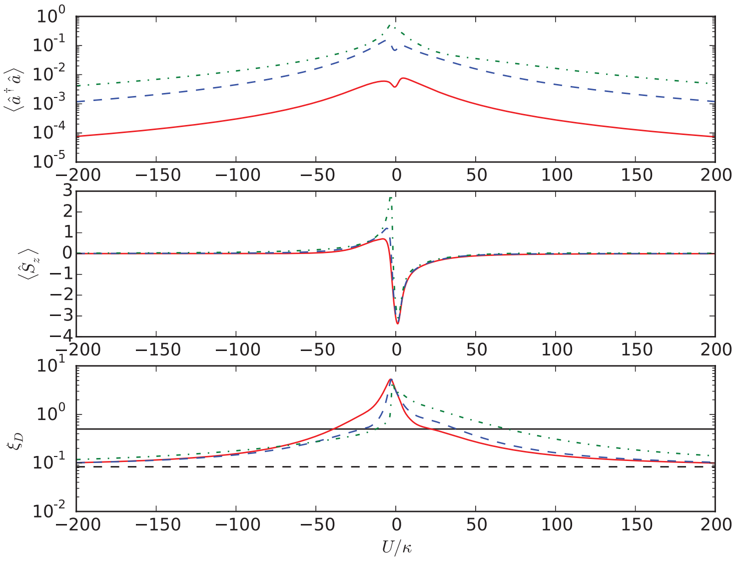

(a)

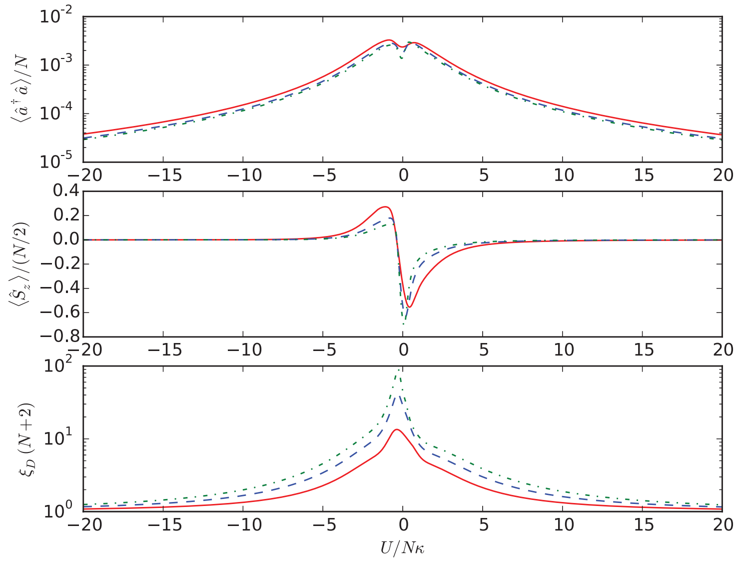

(b)

Figure 6.1: (a) Steady-state expectation values for $\{\,\omega, \omega_0\,\}\,/\kappa = \{\,1.0, 0.2\,\}$ and $N = 10$, with $\lambda/\kappa = 0.05$ (red solid line), $\lambda/\kappa = 0.2$ (blue dashed) and $\lambda/\kappa = 0.4$ (green dash-dotted). The black lines in the plot of ξ_D are the standard quantum limit (solid) and the ideal limit of $1/(N{+}2) = 1/12$ (dashed). (b) Steady-state expectation values for $\{\,\omega, \omega_0, \lambda\,\}\,/\kappa = \{\,1.0, 0.2, 0.1\,\}$ with $N = 4$ (red solid line), $N = 8$ (blue dashed), and $N = 12$ (green dash-dotted). Here the Dicke squeezing parameter, ξ_D, is given in proportion to the ideal limit, $1/(N + 2)$.

though, that for a given (large) value of U/N the Dicke squeezing parameter is closer to its ideal limit of $1/(N+2)$ for smaller N, though it should be noted that the absolute squeezing is still larger for higher N.

6.3.2 Dicke state preparation - $|N/2, 0\rangle$

If we consider the energy level structure of the system in the limit of large $|U|$ (see Figure 6.2), and consider the possible transitions between states as allowed by the atom-cavity coupling Hamiltonian and by cavity photon emission, then it is possible to understand why the steady atomic spin state $|N/2, 0\rangle$ emerges. Let us use the notation $|N/2, m, n\rangle = |N/2, m\rangle \otimes |n\rangle$, where $|n\rangle$ is the n-photon Fock state of the cavity mode.

Now, consider the state $|N/2, m, 0\rangle$ with $m < -1$. The only processes by which a transition from this state may occur are described by the terms $\hat{a}^\dagger \hat{S}_+$ and $\hat{a}^\dagger \hat{S}_-$ in the Hamiltonian. The corresponding transitions are $|N/2, m, 0\rangle \rightarrow |N/2, m+1, 1\rangle$ and $|N/2, m, 0\rangle \rightarrow |N/2, m-1, 1\rangle$, respectively. For large U (i.e., U much larger than any of the other parameters), both of these transitions are off-resonance by $\sim U(m \pm 1)/N$. Whilst both transitions are strongly off-resonant, for negative m, the former is less so by an amount $\sim 2U/N$, and will therefore be favoured, causing a net evolution towards states of larger m (in combination with cavity photon emissions, which cause the transitions $|N/2, m+1, 1\rangle \rightarrow |N/2, m+1, 0\rangle$). Similarly, for $m > 1$, transitions via $\hat{a}^\dagger \hat{S}_-$ will be preferred, causing a net evolution towards states of smaller m.

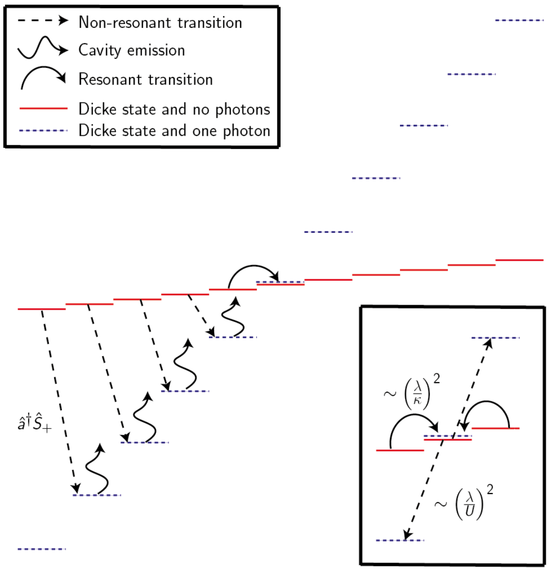

Figure 6.2: Approximate level diagram for large positive $U \gg \omega, \omega_0, \lambda$. The dominant evolution pathway is illustrated.

Hence, whatever its initial state, the system will evolve towards the centre of the spin angular momentum ladder.

On reaching the states $|N/2, \pm 1, 0\rangle$, "inward" transitions to the state $|N/2, 0, 1\rangle$ become approximately resonant (for $\lambda \sim \omega \sim \omega_0$), and, following emission of the cavity photon, the state $|N/2, 0, 0\rangle$ is prepared. Importantly, provided $U/N \gg \{\omega_0, \omega, \lambda, \kappa\}$, transitions out of the state $|N/2, 0, 0\rangle$ to $|N/2, \pm 1, 1\rangle$ (followed by photon emission to $|N/2, \pm 1, 0\rangle$) will be much weaker, due to the much larger energy gap ($\sim U/N$), than the inward transitions. Hence, the system essentially becomes "trapped" in the Dicke state $|N/2, 0, 0\rangle$.

6.3.3 Dicke state preparation - $|N/2, m\rangle$

If we rewrite the Hamiltonian as

$$\hat{H} = \omega_0 \hat{S}_z + \hat{a}^\dagger \hat{a} \left(\omega + \frac{U}{N} \hat{S}_z \right) + \frac{\lambda}{\sqrt{N}} (\hat{a} + \hat{a}^\dagger)(\hat{S}_+ + \hat{S}_-) \tag{6.6}$$

then we see that for $U = -\omega N/m$ (with $\omega \gg \kappa$) the states $|N/2, m, n\rangle$ are degenerate for all n. This means that the transitions $|N/2, m \pm 1, 0\rangle \rightarrow |N/2, m, 1\rangle$ are now the resonant transitions. Following the same arguments as given above, one finds that this shifts the trapped state to $|N/2, m, 0\rangle$. Hence, by tuning parameters, the steady state can be adjusted to an arbitrary Dicke state. Figure 6.3 illlustrates this possibility in the form of Dicke squeezing "resonances" occurring at $U/\omega = -N/m$ ($m = \pm 1, \ldots, \pm 5$) for $N = 10$.

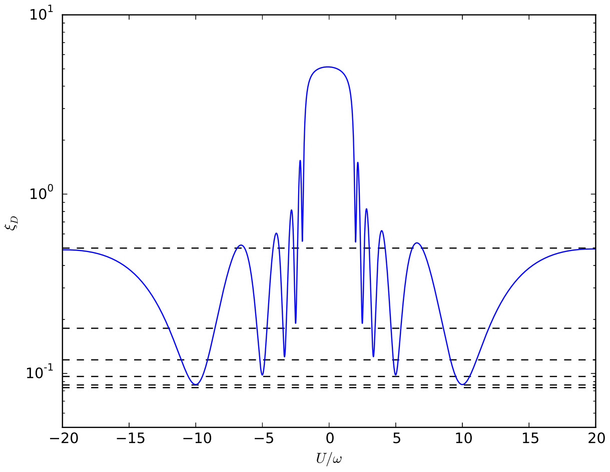

Figure 6.3: Steady-state Dicke squeezing parameter ξ_D as a function of U/ω for $\{\omega, \omega_0, \lambda\}/\kappa = \{100.0, 0.2, 0.2\}$, with $N = 10$. The dashed lines are those predicted by Equation 6.2.

6.4 Dynamic behaviour

A problem with using the above approach to produce Dicke states is the timescale involved with reaching the steady state. To estimate the timescale of some transition $|N/2, m, 0\rangle \rightarrow |N/2, m+1, 0\rangle$, we consider an analytic quantum trajectory approach with a state

$$|\psi(t)\rangle = \alpha(t)\,|N/2, m, 0\rangle + \beta(t)\,|N/2, m-1, 1\rangle + \gamma(t)\,|N/2, m+1, 1\rangle\,, \qquad (6.7)$$

where $\alpha(0) = 1$, $\beta 0 = \gamma(0) = 0$, and we assume that no more than one photon is present in the cavity mode. We then calculate the Schrödinger evolution of the state with an effective Hamiltonian

$$\hat{H}_{\text{eff.}} = \hat{H} - i\kappa\hat{a}^{\dagger}\hat{a} \qquad (6.8)$$

where $\hat{H}$ is the generalised Dicke model given in Equation 6.4. The cavity output flux is proportional to $|\beta(t)|^2 + |\gamma(t)|^2$ and so, taking $U \gg \{\,\omega, \omega_0, \lambda, \kappa\,\}$, the timescale for the transition $|N/2, m, 0\rangle \rightarrow |N/2, m \pm 1, 0\rangle$ (except for $m = \pm 1$) can be calculated approximately as

$$T_m \approx \frac{U^2}{2N\kappa\lambda^2}\frac{(m+1)^2}{N/2(N/2+1) - m(m+1)}\,. \qquad (6.9)$$

The total time will thus scale as U^2 and so be extremely large in the parameter regime considered. For constant U/N, more atoms increases the time due to requiring more steps to reach $m = 0$.

Evolution from the fully polarised states $|N/2, \pm m\rangle$ requires the entire population to undergo every single step to $|N/2, 0\rangle$. However, we could instead use an initial coherent spin state (CSS) [16],

$$|\eta\rangle = (1 + |\eta|^2)^{-j} \sum_{m=-j}^{j} \begin{pmatrix} N \\ j+m \end{pmatrix}^{1/2} \eta^{j+m}\,|j, m\rangle \qquad (6.10)$$

where $\eta = \mathrm{e}^{-\mathrm{i}\varphi}\tan(\theta/2)$ and $\{\theta, \varphi\}$ are spherical coordinates. With a suitable choice of η (e.g., $\eta = 1$), this improves the evolution time because much of the population in this state overlaps with or is close to the steady state, while very little of the state is in or near the fully polarised end states. Such an initial state also immediately shows Dicke squeezing upon evolution, whilst the fully polarised initial state first evolves to an anti-squeezed state before slowly approaching the squeezed steady state.

Whilst the initial coherent spin state improves the short term generation of Dicke squeezing, the time for significant squeezing to appear is still very large even for very small ensembles. Remembering that increased N or U dramatically increases this time, even with an optimised initial state, the evolution to the steady state is likely to be prohibitively slow.

6.5 Probabilistic preparation

One potential method for preparing the steady state in a shorter time span involves using an initial CSS for the atomic ensemble and probabilistic photon detection. A photon detection collapses the state into a superposition weighted by how likely the states in the initial superposition were to have produced a photon. The resultant superposition is dominated by the resonant state, as its neighbours are by far the most likely states to produce photons. Single-photon detection can thus produce extremely high fidelity Dicke states in very short time frames. The production of highly non-classical states via heralded single-photon detection schemes has been proposed and implemented in other systems [128–136].

The probability of creating the steady state $|N/2, m, 0\rangle$ with this method is the sum of the populations in the states $|N/2, m \pm 1, 0\rangle$. For example, if the desired state is $|N/2, 0, 0\rangle$ then a CSS with $\eta = 1$ maximises the overlap and the probability of success is

$$P = 2^{-N}\left[\binom{N}{\frac{N}{2}+1} + \binom{N}{\frac{N}{2}-1}\right]. \tag{6.11}$$

For small atomic ensembles this proves to be a fairly efficient method. The results of trajectory simulations are shown in Table 6.1. Here we see reasonably high success rates that decline with N, and match reasonably with those predicted in Equation 6.11 (e.g., for $N = 10(100)$ the prediction is 41.3% (15.6%)). The fidelity is extremely high and, since the rate of these resonant transitions is independent of U, can be made arbitrarily higher without increasing the time taken or reducing the success probability. We also see very strong squeezing and high levels of multipartite entanglement. For $N = 100$, the squeezing has metrological sensitivity -19.39dB improved over the SQL. This means that this method can produce competitive levels of squeezing with a relatively high success probability in a very short time span for much smaller numbers of atoms than usual spin squeezing techniques.

However, creating significantly better squeezing comes at a cost. To match the ~ 3000 depth multipartite entanglement in [132] would require a Dicke state $|1500, 0\rangle$ with an associated success rate of 2.9%, though we note much stronger entanglement could be created. With 10^6 atoms the probability has become a fractional 0.16%. A potentially useful fact is that the speed at which the transition occurs scales as $1/N$ for central Dicke states. If the CSS could be recreated very quickly then it might be

N	Efficiency	Fidelity	$\bar{\xi}_D$ (E_D)	Within 1%	Within 10%
10	40.3%	99.94%	0.0839 (10)	91.8%	98.7%
20	31.8%	99.91%	0.0460 (20)	81.3%	97.6%
50	20.8%	99.89%	0.0197 (49)	42.0%	95.2%
100	15.5%	99.52%	0.0115 (85)	0.0%	89.2%

Table 6.1: Properties of 5000 trajectories (1000 for $N = 100$) for various N with $\{\omega, \omega_0, \lambda, U/N\}/\kappa = \{1.0, 0.2, 0.1, 100\}$. All properties except the efficiency are only for successful trajectories, i.e., trajectories that have exactly one jump before $\kappa t = 52$. Fidelity is the average fidelity with the Dicke state $|N/2, 0\rangle$, $\bar{\xi}_D$ is the average Dicke squeezing, E_D is the minimum entanglement depth and within 1% (10%) is the percentage of trajectories with squeezing within 1% (10%) of the ideal limit for Dicke squeezing.

possible to do more iterations with higher N, and thus help to account for some of the inefficiency. Alternatively, a spin squeezed state aligned along the equator of the collective Bloch sphere will have enhanced population in the central Dicke states, including $|N/2, \pm 1\rangle$, and so the use of a spin squeezed initial state could enhance the efficiency of this probabilistic scheme.

There is a special case for this method for which the efficiency would be unity. If parameters are set such that the resonant transition is between $|N/2, \pm N/2, 0\rangle \to |N/2, \pm N/2 \mp 1, 1\rangle$ then preparing the initial state in $|N/2, \pm N/2\rangle$ would always mean a jump within a short time frame. These so-called W states [137] (symmetric Dicke states with a single excitation) have numerous applications in quantum information [138–140] and here we have a method that can produce them with close to unit efficiency on a short timescale and in the steady state. The error in the fidelity can be approximated by the probability that two photons have been created which gives an error of

$$\varepsilon \approx \frac{15 g^2 N^2}{4U^2}. \tag{6.12}$$

We can see that the error is kept approximately constant for constant U/N, and, since the transition time here is independent of U and N, this method scales very well to larger atomic ensembles.

6.6 Time dependent parameters

We have shown that, by correct choice of parameters, the steady state can be tuned to a desired Dicke state. We have also shown that if the system is one Dicke state either side of the steady state, then the evolution to that state is very fast. Thus, with complete control of the parameters, it should be possible to step the system from $|N/2, -N/2, 0\rangle \to |N/2, -N/2+1, 0\rangle \to \ldots \to |N/2, 0, 0\rangle$. This requires time dependence in ω.

Successful runs can be postselected based on the number of photons emitted. If that number is equal to the total number of steps necessary then the trajectory is

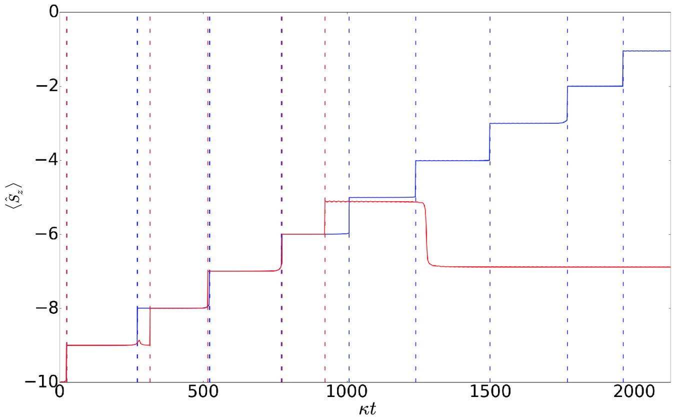

Figure 6.4: The time evolution of $\langle \hat{S}_z \rangle$ with photon detections (vertical lines) for a successful trajectory (blue) and a failure (red), parameters of $\{\, \omega_0, \lambda, U \,\}/\kappa = \{\, 0.2, 0.2, 1000.0 \,\}$, $N = 20$ and ω linearly varied as $\omega(t)/\kappa = 470 - 0.2\kappa t$.

deemed successful, otherwise it is a failure. Experimentally, this would require an extremely efficient single-photon detector. However, it is also possible to differentiate successes and failures by the pattern of the photon emissions. If the state is "dragged" all the way to the middle, then the photons should come at relatively frequent intervals throughout the length of the experiment. This means that if a photon is detected near the end of the trajectory then all the photons that came before can be inferred, as shown in Figure 6.4.

Linear variation of ω, such that the system is initially resonant for creation of the W state, and then ends at zero, such that the final resonant transition is to the

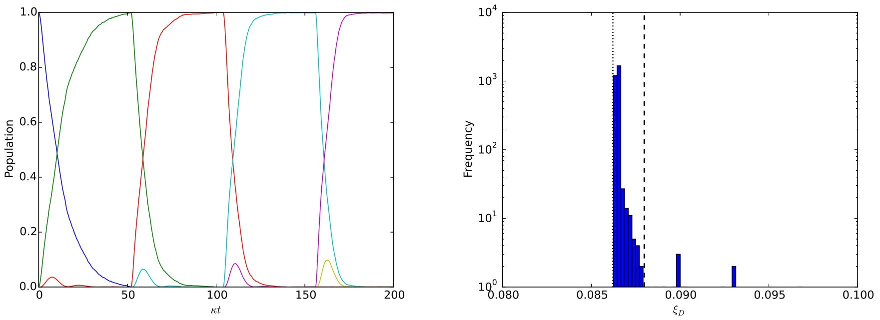

(a) .

(b)

Figure 6.5: For 2958 successful trajectories, parameters of $\{\, \omega_0, \lambda, U \,\}/\kappa = \{\, 0.2, 0.2, 500.0 \,\}$, $N = 10$ and time dependent ω discretely stepped such that it makes each transition from $|0, -5\rangle \rightarrow |0, -1\rangle$ resonant in turn. The system is held at each step for $\kappa t_h = 52$. (a) Time evolution of Dicke state populations with blue, green, red, cyan and pink (or peaks from left to right) denoting $m = -5, -4, -3, -2$, and -1 respectively and (b) histogram of final squeezing. The vertical lines are the ideal limit (dotted) and steady-state squeezing (dashed).

central Dicke state, thus has some probability of producing that central Dicke state with very high fidelity. For ten atoms, an ensemble of quantum trajectories produces a 58.0% success rate, a best squeezing of $\xi_D = 0.086$ and an average squeezing of $\bar{\xi}_D = 0.100$.

More successful, if perhaps more experimentally challenging, is discretely stepping ω, i.e., implementing the time dependence

$$\omega(t) = -\frac{U}{N}\left(-\frac{N}{2} + j\right) \quad \text{for} \quad t_h(j-1) \leq t < t_h j \tag{6.13}$$

where t_h is the time the system is held at each step and j is an integer stepping from $1 \to \Delta m$. We know that the slowest transition is the first one, and so we set t_h such that the first transition will almost certainly have occurred.

The population transfer and squeezing for this discrete stepping approach with $N = 10$ are shown in Figure 6.5. The best squeezing is $\xi_D^{\min} = 0.086$, but with a greatly improved average squeezing of $\bar{\xi}_D = 0.087$. There are also much higher success rates, with 98.6% of 1000 trajectories being successful. This scales well with N as well, with a success rate of 98.5% (83.9%) for $N = 20$ (50).

6.7 Cavity QED realisation

6.7.1 Microscopic parameters

We now consider the optical cavity QED realisation of the Dicke model described in [53, 72, 80] (see Figure 6.6). The necessary Hamiltonian is produced via resonant Raman transitions in an ensemble of ^{87}Rb atoms interacting with a high finesse optical cavity mode. Here the effective parameters are given in terms of the microscopic parameters by [72]

$$\begin{aligned}\omega_0 = {} & \omega_1 - \frac{1}{2}(\omega_s - \omega_r) \\ & + \frac{1}{6}\left(\frac{\Omega_r^2}{\Delta_r} - \frac{\Omega_r^2}{\Delta_r - \omega_1} - \frac{\Omega_s^2}{\Delta_s} + \frac{\Omega_s^2}{\Delta_s + \omega_1}\right)\end{aligned} \tag{6.14}$$

$$\omega = \omega_c - \frac{1}{2}(\omega_r + \omega_s) + \frac{N}{3}\left(\frac{g^2}{\Delta_s} + \frac{g^2}{\Delta_r}\right) \tag{6.15}$$

$$U = \frac{2N}{3}\left(\frac{g^2}{\Delta_s} - \frac{g^2}{\Delta_r}\right) \tag{6.16}$$

$$\lambda_{r,s} = \frac{\sqrt{3N}g\Omega_{r,s}}{12\Delta_{r,s}} \tag{6.17}$$

where $\{\lambda_r, \lambda_s\}$ are the Raman coupling strengths for the rotating and counter-rotating terms, respectively, and ω and ω_0 are the *effective* cavity and atomic frequencies,

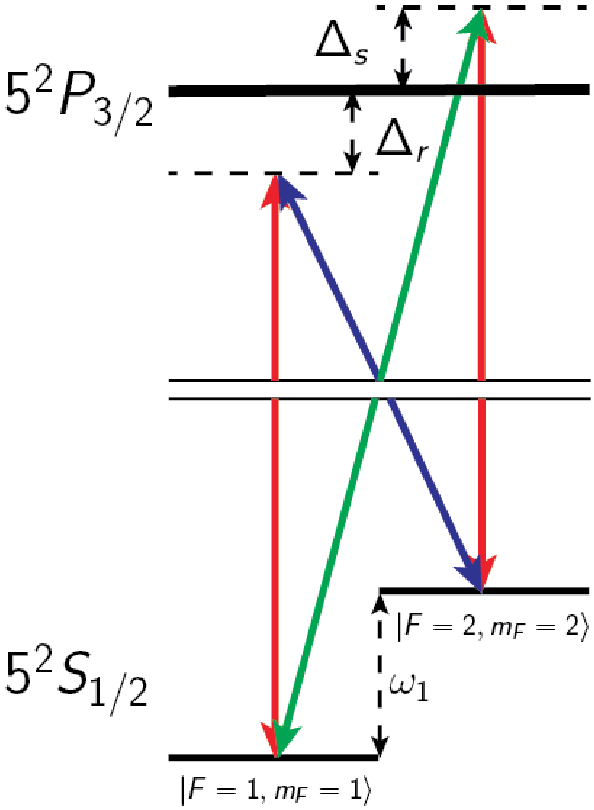

Figure 6.6: Level scheme for the implementation of the generalised Dicke model with ^{87}Rb atoms. Transitions are driven with Raman transitions composed of a cavity mode (red) and σ_+- (green) and σ_-- (blue) polarised laser fields. Raman transitions are detuned on either side of the excited manifold to maximise the non-linear term.

respectively, defined by combinations of detunings and light shifts. Specifically, ω_c is the cavity frequency, ω_1 is the frequency difference between the two active states, g is the single-atom-cavity coupling, and $\omega_{r,s}$ is the frequency of the σ_-— and σ_+—polarised lasers, respectively with $\Delta_{r,s}$ and $\Omega_{r,s}$ being the related detunings and single-atom-laser coupling strengths, respectively. By setting $\Delta_s = -\Delta_r$ we can maximise U and greatly reduce ω. If we choose $g = 20(2\pi)$MHz, $\Omega_{r,s} = 500(2\pi)$kHz, $\kappa = 50(2\pi)$kHz[37], and $|\Delta_{r,s}| = 3.5(2\pi)$GHz and assume full tuneability of the small frequency offsets and magnetic field strength that define ω and ω_0, then we could reach a regime of effective parameters $\{\,\omega, \omega_0, U/N, \lambda/\sqrt{N}\,\}/\kappa = \{\,0.01, 0.01, 3.0, 0.01\,\}$. Whilst this regime does not offer the idealised squeezing above, it does still offer significant metrological gain over a coherent state.

---

[37] See, e.g., [141,142], although we choose a smaller κ than realised in these experiments. However, we note that good squeezing is still possible with larger κ.

6.7.2 Unresolved Dicke squeezing

We use these parameters with the atomic ensemble initiated into a coherent spin state centred on the equator of the Bloch sphere. Here, considering single quantum trajectories, we calculate the squeezing *immediately* after each photon detection. As in the ideal case, the probability of a photon arising from population in the central states is higher than from the outer states, but due to the lower value of U, the difference is much less sharp. This means that the measurement of a photon tightens the distribution around the central state rather than "resolving" a single Dicke state (see Figure 6.7). Due to this, each photon detection shortly afterwards tightens the spread further. In between photon detections, the backaction of the null measurement drains population from the central states and the degree of squeezing worsens. As such, the optimal squeezing is likely to come when a number of photon detections are measured in a short amount of time. This means that a protocol where one waits for a certain number of photon detections in a certain time frame can achieve substantial Dicke squeezing. It should be noted that such a protocol could also work with high efficiency. For 1000 atoms and the parameters described above, 38.9% of trajectories run had 12 or more jumps.

6.8 Conclusion

We have shown the existence of strong spin squeezing and entanglement depth in the steady state of an open generalised Dicke model. We have shown that this arises from the collective atomic state being "pumped" towards the highly entangled Dicke state $|N/2, 0\rangle$, in a manner reminiscent of resolved sideband cooling of atoms trapped in harmonic potentials. By altering the Dicke model parameters, it is also possible to instead pump towards an arbitrary Dicke state $|N/2, m\rangle$. This means that entanglement between every atom in an ensemble could be achieved in steady state, rather than as a transient or probabilistic phenomenon. The steady-state nature of the entanglement, even when accessed via a probabilistic method, means that the produced Dicke state is stable. The possibility of producing such a stable entangled state has obvious benefits for quantum information and quantum computing protocols.

While the timescale involved in preparing these states through natural evolution is very large, we have also shown that it is possible to access the steady state on a much shorter timescale via either a single-photon-heralded, probabilistic scheme or by suitable time variation of a parameter of the model. The squeezing is at the Heisenberg limit for the ideal case, but we show that substantial squeezing is still possible with realistic cavity QED parameters.

This work highlights the stark change in dynamics that can occur with the addition of a non-linear term to the Dicke model. The interplay of the linear terms with a

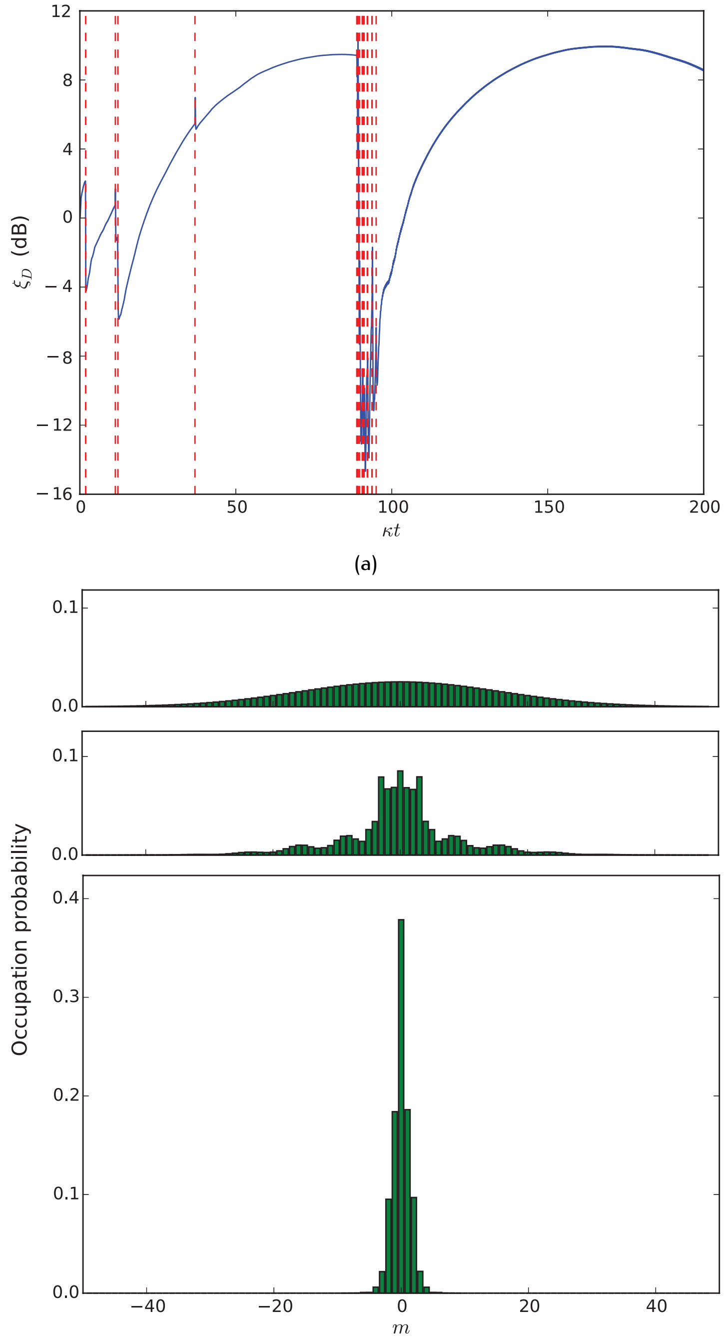

(a)

(b)

Figure 6.7: For a single trajectory with $N = 1000$ and $\{\,\omega, \omega_0, \lambda, U\,\}\,/\kappa = \{\,0.01, 0.01, 0.316, 3000.0\,\}$, (a) squeezing with the times of photon detection events represented by red vertical dashed lines and (b) populations initially (top) and after the first jump (middle) and twelfth jump (bottom).

simple non-linear shift of energy levels has been shown here to give rise to exotic steady states. This raises the question of what other possibilities might arise from similar non-linear terms in, for example, models involving atoms of higher spin as discussed in Chapter 7. In particular, the spin-1 derivation in Chapter 7 introduces a term of the form $\hat{n}_0\hat{a}^\dagger\hat{a}$, where $\hat{n}_0$ is the number operator for the $|m=0\rangle$ state of the spin-1 atoms. If this term is allowed to dominate, then we might expect the ensemble to be pumped to states with no atoms in the $|m=0\rangle$ state; i.e., to a family of states containing completely classical states, such as $|m=\pm1\rangle^{\otimes N}$, as well as highly entangled states such as the Dicke state $|N,0\rangle$ with the atoms exactly split between the two states $|m=\pm1\rangle$.

Chapter 7

Generalisation of the Dicke model to integer-spin particles

The study of the Dicke model as an ensemble of two-level systems is most simply considered in a collective picture of a single large spin. As such, the makeup of that internal spin is not necessarily of importance. This means that it is possible to engineer a Dicke model using an ensemble of spinor particles and it will respond identically to the two-level ensemble case. In the first section of this Chapter, I derive a Dicke model built from alkali atoms isolated to an entire ground-state hyperfine manifold. I initially show the structure of a generic treatment, before more specifically showing how this works for the $F = 1$ manifold in ^{87}Rb. This derivation was performed following a concept conceived in collaboration with Murray Barrett and Scott Parkins. The second section, in somewhat of an aside from the discussion of the experiment, discusses what can happen if the state is initiated such that a single large spin is not a suitable picture. Returning to the single large spin picture, the final section discusses the implementation of this scheme at the Centre for Quantum Technologies, and in particular the use of such a scheme to study phase transitions with imbalanced couplings. This experimental work was carried out by Zhiqiang Zhang, Chern Hui Lee, Ravi Kumar, Kyle Arnold and Murray Barrett. My theoretical modelling, informed by that experiment and carried out under the supervision of Scott Parkins, follows.

7.1 Deriving the Dicke model for integer spins

Here I derive the Dicke model using the same scheme of cavity-assisted Raman transitions used in Chapter 5, except instead of isolating two active states, an entire hyperfine manifold F is used for the active states. This means that each atom is now an effective spin-F particle rather than a spin-1/2 particle. Initially this treatment is kept as general as possible before focussing in on a specific case of the $F = 1$ manifold in ^{87}Rb. It is this treatment that is used in the experiment and in our proposals.

7.1.1 Derivation for a generic integer-spin manifold

We take an arbitrary ground-state hyperfine manifold in an alkali atom. This could be $F = 1$ $\left(\text{available for } ^{87}\text{Rb}\right)$, $F = 2$ $\left(^{87}\text{Rb or } ^{85}\text{Rb}\right)$, $F = 3$ $\left(^{85}\text{Rb or } ^{133}\text{Cs}\right)$ or $F = 4$ $\left(^{133}\text{Cs}\right)$. These are coupled with laser and cavity modes via some excited-state manifold as shown in Figure 7.1. In contrast to the two-level scheme, where each laser-cavity mode pair drives one Raman transition from $|0\rangle \leftrightarrow |1\rangle$, each pair of beams now drives a set of transitions. As in that scheme, the σ_+-polarised laser Raman transition is a raising (or lowering) operator for both the collective spin and the cavity field, meaning it drives the counter-rotating terms in the derived Dicke model. Conversely, the σ_--polarised laser transition drives the rotating terms. In both cases, the generalisation just means that the $\hat{\sigma}_i$ operators are now for spin-F particles rather than the spin-1/2 Pauli matrices.

Denoting the ground states $|F, m_F = j\rangle \equiv |g_j\rangle$ and denoting the excited states $|F' = k, m_{F'} = l\rangle \equiv |e_{k,l}\rangle$ then, for a single atom, the full Hamiltonian can be written

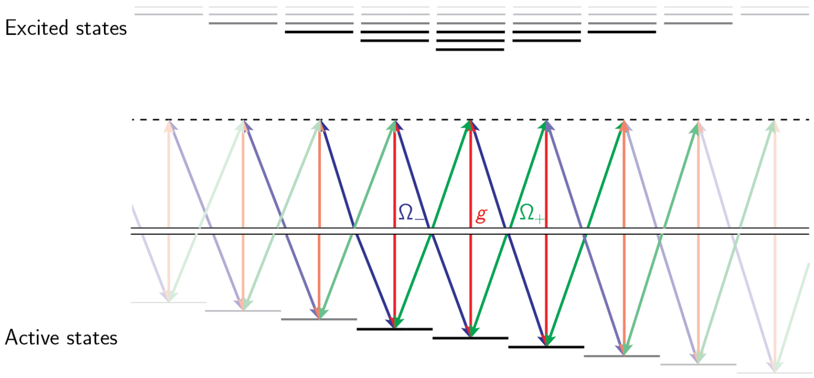

Figure 7.1: Level diagram to produce a spinor Dicke model using an entire hyperfine level as the active levels. The levels form effective spin-F particles with detuned Raman transitions driven between them, via some set of excited states, by a cavity mode (red arrows) and σ_+-polarised (green) and σ_--polarised (blue) lasers. Here each pair of beams operates two or more Raman transitions. Different F levels and the associated schemes of light fields necessary are shown in different intensities.

in the form

$$
\begin{aligned}
\hat{H} = \omega_c \hat{a}^\dagger \hat{a} + \omega_z \sum_{j=-F}^{+F} j \left|g_j\right\rangle \left\langle g_j\right| + \sum_{k=F-1}^{F+1} \sum_{l=-k}^{+k} \omega_k \left|e_{k,l}\right\rangle \left\langle e_{k,l}\right| \\
+ \frac{\Omega_-}{2} \mathrm{e}^{-i\omega_- t} \sum_{j=-F}^{+F} \sum_{k=F}^{F+1} c_{jk}^{(-)} \left|e_{k,j-1}\right\rangle \left\langle g_j\right| + \frac{\Omega_+}{2} \mathrm{e}^{-i\omega_+ t} \sum_{j=-F}^{+F} \sum_{k=F-1}^{F} c_{jk}^{(+)} \left|e_{k,j+1}\right\rangle \left\langle g_j\right| \\
+ g\hat{a} \sum_{j=-F}^{+F} \sum_{k=F-1}^{F+1} c_{jk}^{(\pi)} \left|e_{k,j}\right\rangle \left\langle g_j\right| + \text{h.c.}
\end{aligned}
\tag{7.1}
$$

where h.c. means Hermitian conjugate and is meant for all the transitions terms. In this equation ω_c is the cavity frequency, ω_z is the linear Zeeman splitting of the ground states[38], $|F, 0\rangle$ is chosen as zero energy and ω_k is the energy of the excited-state manifold $F' = k$, where Zeeman splittings within those hyperfine manifolds are ignored. $\omega_\pm, \Omega_\pm$ are the bare frequencies and Rabi frequencies respectively of the two lasers and g is the single-atom coupling strength normalised on some transition. The coefficients $c_{jk}^{(X)}$ are then the dipole matrix elements for transitions between the ground state $|g_j\rangle$ and an excited state in the $F' = k$ manifold for X-polarised radiation normalised on the same transition as g and $\Omega_\pm$.

Even in this extremely generic form it is possible to see the structure of the Hamiltonian. The energy associated with the cavity occupation and the state of the atom appear on the first line. Interactions raising the atom from ground states to excited states are driven by the two lasers and the cavity mode, while interactions lowering the atom from excited states to the ground states are given by the Hermitian conjugates of those terms. Note here that each laser or cavity field now explicitly drives whole sums of transitions.

The elimination of excited states, wherever it appears during this thesis, was performed using the method laid out in [143]. The Hamiltonian is first moved to the interaction frame of the active states and the cavity mode. We build an operator, $\hat{Q}$, which is a sum over transition terms that raise the system to the excited manifold. In this frame we have

$$
\hat{H} = \sum_{\mathrm{e}} \omega_e \left|e\right\rangle \left\langle e\right| + \hat{Q} + \hat{Q}^\dagger. \tag{7.2}
$$

A second operator $\hat{Q}'$, which is the same sum but divided by the detuning of that term (i.e. the frequency of the laser or cavity mode driving the term minus the relevant excited-state frequency), is also constructed. In the limit of large detuning, and thus small excited-state populations, the excited states can be adiabatically eliminated

---

[38] Any quadratic Zeeman shift would survive the elimination process, and so its presence would result in something other than a true effective Dicke model. It is thus assumed to be zero here.

leading to an effective Hamiltonian [143]

$$\hat{H}_{\text{eff}} = \hat{Q}^{\dagger}\hat{Q}'. \tag{7.3}$$

More explicitly, we create operators

$$\begin{aligned}\hat{Q} =& \frac{\Omega_-}{2}\sum_{j=-F}^{+F}\sum_{k=F}^{F+1} c_{jk}^{(-)}\mathrm{e}^{-i(\omega_-+j\omega_z)t}\left|e_{k,j-1}\right\rangle\left\langle g_j\right| \\ &+\frac{\Omega_+}{2}\sum_{j=-F}^{+F}\sum_{k=F-1}^{F} c_{jk}^{(+)}\mathrm{e}^{-i(\omega_+j\omega_z)t}\left|e_{k,j+1}\right\rangle\left\langle g_j\right| \\ &+g\hat{a}\sum_{j=-F}^{+F}\sum_{k=F-1}^{F+1} c_{jk}^{(\pi)}\mathrm{e}^{-i(\omega_c+j\omega_z)t}\left|e_{k,j}\right\rangle\left\langle g_j\right|\end{aligned} \tag{7.4}$$

and

$$\begin{aligned}\hat{Q}' =& \frac{\Omega_-}{2}\sum_{j=-F}^{+F}\sum_{k=F}^{F+1} c_{jk}^{(-)}\frac{\mathrm{e}^{-i(\omega_-+j\omega_z)t}}{\omega_- - \omega_k + j\omega_z}\left|e_{k,j-1}\right\rangle\left\langle g_j\right| \\ &+\frac{\Omega_+}{2}\sum_{j=-F}^{+F}\sum_{k=F-1}^{F} c_{jk}^{(+)}\frac{\mathrm{e}^{-i(\omega_++j\omega_z)t}}{\omega_+ - \omega_k + j\omega_z}\left|e_{k,j+1}\right\rangle\left\langle g_j\right| \\ &+ g\hat{a}\sum_{j=-F}^{+F}\sum_{k=F-1}^{F+1} c_{jk}^{(\pi)}\frac{\mathrm{e}^{-i(\omega_c+j\omega_z)t}}{\omega_c - \omega_k + j\omega_z}\left|e_{k,j}\right\rangle\left\langle g_j\right|.\end{aligned} \tag{7.5}$$

This leads to a time-dependent Hamiltonian with a variety of different terms. A rotation removes the time dependence and grouping of terms into spin-F operators leaves a mixture of expected Dicke model terms and higher spin operator terms. For a specific example of this see Section 7.1.2, where the derivation produces various spin-1 specific terms.

These additional terms offer physics not available to spin-1/2 systems, and so could be of interest for further study. In this Section, a limit where those terms drop out is found, reducing the effective Hamiltonian to a Dicke model. That limit turns out to be that the detunings of the Raman transitions from the excited-state manifolds must be much larger than the internal level splittings of that manifold.

In such a limit, then, for all the species mentioned above, all terms except for those in the Dicke model reduce to zero. Summing over N of these spin-F atoms we are left with the Hamiltonian

$$\hat{H} = \omega\hat{a}^{\dagger}\hat{a} + \omega_0\hat{S}_z + \frac{\lambda_-}{\sqrt{2FN}}(\hat{S}_+\hat{a} + \hat{S}_-\hat{a}^{\dagger}) + \frac{\lambda_+}{\sqrt{2FN}}(\hat{S}_-\hat{a} + \hat{S}_+\hat{a}^{\dagger}) \tag{7.6}$$

where the parameters are determined by Raman transition rates, detunings and light shifts. Note here that, unlike all current cavity-based spin-1/2 formulations for the Dicke model, there is no extra term of the form $\hat{S}_z\hat{a}^\dagger\hat{a}$ [53,66–68,72,78,79,144]. The spin-1 derivation in Section 7.1.2 shows that this shift is actually quadratic in nature for that case, but that it vanishes under the large detuning approximation. This can be reasoned by the fact that the excited-state manifolds do still produce cavity driven light shift but some with different signs to others, such that the sum of the shifts is zero.

7.1.2 Derivation for the $F = 1$ manifold in ^{87}Rb

We now use the specific case of the $F = 1$ manifold in ^{87}Rb with transitions driven via the D_1 line, shown in Figure 7.2. This example is chosen because it is the choice of levels in the derivations for Chapters 8, 10 and 11. Whilst the experiment described in Section 7.3 used the same active levels, Raman transitions were driven via the D_2 line instead. This results in minor changes to some of the final parameters, but is for the most part completely equivalent to this derivation.

We use notation $|m_F\rangle$ for active levels and $|F', m_{F'}\rangle$ for excited states in the F' excited hyperfine level. Our full Hamiltonian is then

$$\begin{aligned}\hat{H} = \hat{H}_0 + \hat{H}_e &+ \frac{g}{\sqrt{12}}\left(\hat{a}\hat{H}_c + \hat{a}^\dagger\hat{H}_c^\dagger\right)\\ &- \frac{\Omega_+}{2\sqrt{12}}\left(e^{-i\omega_+ t}\hat{H}_+ + e^{i\omega_+ t}\hat{H}_+^\dagger\right) + \frac{\Omega_-}{2\sqrt{12}}\left(e^{-i\omega_- t}\hat{H}_- + e^{i\omega_- t}\hat{H}_+\right)\end{aligned} \tag{7.7}$$

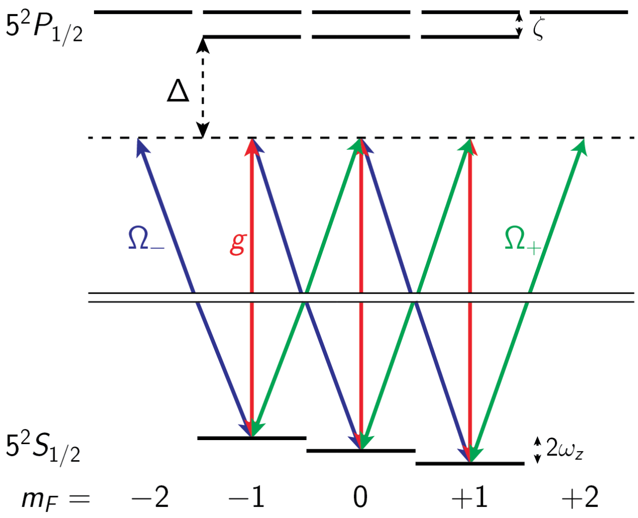

Figure 7.2: Level diagram to produce a spinor Dicke model using hyperfine states in ^{87}Rb. The entire $F = 1$ manifold forms effective spin-1 particles with detuned Raman transitions driven between them via the D_1 line made from a cavity mode (red arrows) and σ_+-polarised (green) and σ_--polarised (blue) lasers.

where

$$\hat{H}_0 = \omega_c \hat{a}^\dagger \hat{a} + \omega_z(|1\rangle\langle 1| - |{-1}\rangle\langle -1|) \tag{7.8}$$

$$\hat{H}_e = \sum_{F'=1,2} \sum_{m_{F'}=-F}^{+F} \omega_{F'} |F', m_{F'}\rangle\langle F', m_{F'}| \tag{7.9}$$

$$\hat{H}_c = |1,-1\rangle\langle -1| + \sqrt{3}\,|2,-1\rangle\langle -1| + 2\,|2,0\rangle\langle 0| - |1,1\rangle\langle 1| + \sqrt{3}\,|2,1\rangle\langle 1| \tag{7.10}$$

$$\hat{H}_+ = |1,0\rangle\langle -1| + |2,0\rangle\langle -1| + |1,1\rangle\langle 0| + \sqrt{3}\,|2,1\rangle\langle 0| + \sqrt{6}\,|2,2\rangle\langle 1| \tag{7.11}$$

$$\hat{H}_- = -\sqrt{6}\,|2,-2\rangle\langle -1| + |1,-1\rangle\langle 0| - \sqrt{3}\,|2,-1\rangle\langle 0| + |1,0\rangle\langle 1| - |2,0\rangle\langle 1|\,. \tag{7.12}$$

Here ω_c is the cavity frequency, ω_z is the Zeeman splitting of the $F = 1$ manifold working around the energy of $|0\rangle$ being zero, and $\omega_{F'}$ is the energy assumed for the entire F' hyperfine manifold. $\omega_\pm, \Omega_\pm$ are the bare frequencies and Rabi frequencies respectively of the two lasers and g is the single-atom coupling strength normalised on the ^{87}Rb D_2 line cycling transition.

$\hat{H}_0$ gives the energy associated with population in the cavity mode and in the ground atomic states. $\hat{H}_e$ gives the energy associated with population in excited atomic states, where we have assumed that the linear Zeeman shifts of those levels can be neglected. $\hat{H}_c$ and $\hat{H}_\pm$ tell us how the cavity and laser fields move the atom between states weighted with the associated Clebsch-Gordan coefficients.

Once again, we move to an interaction picture around $\hat{H}_0$ and build operators in line with the derivation laid out in [143]. The first of these operators is

$$\hat{Q} = \frac{g \mathrm{e}^{-i\omega_c t}}{\sqrt{12}} \hat{a} \hat{Q}_c - \frac{\Omega_+ \mathrm{e}^{-i\omega_+ t}}{2\sqrt{12}} \hat{Q}_+ + \frac{\Omega_- \mathrm{e}^{-i\omega_- t}}{2\sqrt{12}} \hat{Q}_- \tag{7.13}$$

with

$$\begin{aligned}\hat{Q}_c = {} & \mathrm{e}^{i\omega_z t} \Big(|1,-1\rangle\langle -1| + \sqrt{3}\,|2,-1\rangle\langle -1| \Big) + 2\,|2,0\rangle\langle 0| \\ & + \mathrm{e}^{-i\omega_z t} \Big(- |1,1\rangle\langle 1| + \sqrt{3}\,|2,1\rangle\langle 1| \Big)\end{aligned} \tag{7.14}$$

$$\begin{aligned}\hat{Q}_+ = {} & \mathrm{e}^{i\omega_z t} (|1,0\rangle\langle -1| + |2,0\rangle\langle -1|) + |1,1\rangle\langle 0| + \sqrt{3}\,|2,1\rangle\langle 0| \\ & + \mathrm{e}^{-i\omega_z t} \sqrt{3}\,|2,1\rangle\langle 1|\end{aligned} \tag{7.15}$$

$$\begin{aligned}\hat{Q}_- = {} & -\mathrm{e}^{i\omega_z t} \sqrt{6}\,|2,-2\rangle\langle -1| + |1,-1\rangle\langle 0| - \sqrt{3}\,|2,-1\rangle\langle 0| \\ & + \mathrm{e}^{-i\omega_z t} (|1,0\rangle\langle 1| - |2,0\rangle\langle 1|)\,.\end{aligned} \tag{7.16}$$

The second is

$$\hat{Q}' = \frac{g \mathrm{e}^{-i\omega_c t}}{\sqrt{12}} \hat{a} \hat{Q}'_c - \frac{\Omega_+ \mathrm{e}^{-i\omega_+ t}}{2\sqrt{12}} \hat{Q}'_+ + \frac{\Omega_- \mathrm{e}^{-i\omega_- t}}{2\sqrt{12}} \hat{Q}'_- \tag{7.17}$$

with

$$\begin{aligned}\hat{Q}'_c &= \mathrm{e}^{i\omega_z t}\left(\frac{|1,-1\rangle\langle -1|}{\omega_c-\omega_1}+\sqrt{3}\frac{|2,-1\rangle\langle -1|}{\omega_c-\omega_2}\right)+2\frac{|2,0\rangle\langle 0|}{\omega_c-\omega_2}\\ &\qquad + \mathrm{e}^{-i\omega_z t}\left(-\frac{|1,1\rangle\langle 1|}{\omega_c-\omega_1}+\sqrt{3}\frac{|2,1\rangle\langle 1|}{\omega_c-\omega_2}\right) \quad (7.18)\\ \hat{Q}'_+ &= \mathrm{e}^{i\omega_z t}\left(\frac{|1,0\rangle\langle -1|}{\omega_+-\omega_1}+\frac{|2,0\rangle\langle -1|}{\omega_+-\omega_2}\right)+\frac{|1,1\rangle\langle 0|}{\omega_+-\omega_1}+\frac{\sqrt{3}\,|2,1\rangle\langle 0|}{\omega_+-\omega_2}\\ &\qquad + \mathrm{e}^{-i\omega_z t}\sqrt{3}\frac{|2,1\rangle\langle 1|}{\omega_+-\omega_2} \quad (7.19)\\ \hat{Q}'_- &= -\mathrm{e}^{i\omega_z t}\sqrt{6}\frac{|2,-2\rangle\langle -1|}{\omega_--\omega_2}+\frac{|1,-1\rangle\langle 0|}{\omega_--\omega_1}-\sqrt{3}\frac{|2,-1\rangle\langle 0|}{\omega_--\omega_2}\\ &\qquad + \mathrm{e}^{-i\omega_z t}\left(\frac{|1,0\rangle\langle 1|}{\omega_--\omega_1}-\frac{|2,0\rangle\langle 1|}{\omega_--\omega_2}\right). \quad (7.20)\end{aligned}$$

From here our effective Hamiltonian is given by

$$\hat{H}=\hat{Q}^\dagger\hat{Q}'\equiv\sum_{i,j=-1}^{+1}C_{i,j}\,|i\rangle\langle j|\,. \tag{7.21}$$

Introducing a detuning $\Delta_i=\omega_i-\omega_1$ and the excited-state hyperfine splitting as $\zeta=\omega_1-\omega_2$, we have a full set of coefficients

$$C_{-1,-1}=\frac{g^2}{12\Delta_c}\hat{a}^\dagger\hat{a}+\frac{g^2}{4(\Delta_c+\zeta)}\hat{a}^\dagger\hat{a}+\frac{\Omega_+^2}{48\Delta_+}+\frac{\Omega_+^2}{48(\Delta_++\zeta)}+\frac{\Omega_-^2}{8(\Delta_-+\zeta)} \tag{7.22}$$

$$C_{0,0}=\frac{g^2}{3(\Delta_c+\zeta)}\hat{a}^\dagger\hat{a}+\frac{\Omega_+^2}{48\Delta_+}+\frac{\Omega_+^2}{16(\Delta_++\zeta)}+\frac{\Omega_-^2}{48\Delta_-}+\frac{\Omega_-^2}{16(\Delta_-+\zeta)} \tag{7.23}$$

$$C_{+1,+1}=\frac{g^2}{12\Delta_c}\hat{a}^\dagger\hat{a}+\frac{g^2}{4(\Delta_c+\zeta)}\hat{a}^\dagger\hat{a}+\frac{\Omega_+^2}{8(\Delta_++\zeta)}+\frac{\Omega_-^2}{48\Delta_-}+\frac{\Omega_-^2}{48(\Delta_-+\zeta)} \tag{7.24}$$

$$C_{-1,0}=\frac{g\Omega_-\mathrm{e}^{i(\omega_c-\omega_--\omega_z)t}}{24}\left(\frac{1}{\Delta_-}-\frac{3}{\Delta_-+\zeta}\right)\hat{a}^\dagger-\frac{2g\Omega_+\mathrm{e}^{i(\omega_+-\omega_c-\omega_z)t}}{24(\Delta_c+\zeta)}\hat{a} \tag{7.25}$$

$$C_{0,+1}=\frac{g\Omega_+\mathrm{e}^{i(\omega_+-\omega_c-\omega_z)t}}{24}\left(\frac{1}{\Delta_c}-\frac{3}{\Delta_c+\zeta}\right)\hat{a}-\frac{2g\Omega_-\mathrm{e}^{i(\omega_c-\omega_--\omega_z)t}}{24(\Delta_-+\zeta)}\hat{a}^\dagger \tag{7.26}$$

$$C_{0,-1}=\frac{g\Omega_-\mathrm{e}^{i(\omega_--\omega_c+\omega_z)t}}{24}\left(\frac{1}{\Delta_c}-\frac{3}{\Delta_c+\zeta}\right)\hat{a}-\frac{2g\Omega_+\mathrm{e}^{i(\omega_c-\omega_++\omega_z)t}}{24(\Delta_++\zeta)}\hat{a}^\dagger \tag{7.27}$$

$$C_{+1,0}=\frac{g\Omega_+\mathrm{e}^{i(\omega_c-\omega_++\omega_z)t}}{24}\left(\frac{1}{\Delta_+}-\frac{3}{\Delta_++\zeta}\right)\hat{a}^\dagger-\frac{2g\Omega_-\mathrm{e}^{i(\omega_--\omega_c+\omega_z)t}}{24(\Delta_c+\zeta)}\hat{a} \tag{7.28}$$

$$C_{+1,-1}=\frac{\Omega_+\Omega_-\mathrm{e}^{i(\omega_--\omega_++2\omega_z)t}}{48}\left(\frac{1}{\Delta_+}-\frac{1}{\Delta_++\zeta}\right) \tag{7.29}$$

$$C_{-1,+1}=\frac{\Omega_+\Omega_-\mathrm{e}^{i(\omega_+-\omega_--2\omega_z)t}}{48}\left(\frac{1}{\Delta_-}-\frac{1}{\Delta_-+\zeta}\right). \tag{7.30}$$

The first three equations can be simplified using $\hat{\sigma}_z=|1\rangle\langle 1|-|-1\rangle\langle -1|$, $\hat{\sigma}_{zz}=$

$|1\rangle\langle 1| + |-1\rangle\langle -1|$[39] and the identity $\mathbb{1} = |-1\rangle\langle -1| + |0\rangle\langle 0| + |1\rangle\langle 1|$.

Equations 7.25-7.28 require four degrees of freedom, of which the first two are simply $\hat{\sigma}_+ = \sqrt{2}\,(|1\rangle\langle 0| + |0\rangle\langle -1|)$ and $\hat{\sigma}_- = \sqrt{2}(|-1\rangle\langle 0| + |0\rangle\langle +1|)$. The other two are single-atom elements of the nematic tensor operator: $\hat{q}_{xz} = \sqrt{2}(|+1\rangle\langle 0| + |0\rangle\langle +1| - |0\rangle\langle -1| - |-1\rangle\langle 0|)$ and $i\hat{q}_{yz} = \sqrt{2}(|1\rangle\langle 0| - |0\rangle\langle 1| - |0\rangle\langle -1| + |-1\rangle\langle 0|)$.

The last two terms can be very easily simplified using $\hat{\sigma}_-^2 = 2\,|-1\rangle\langle 1|$ and $\hat{\sigma}_+^2 = 2\,|1\rangle\langle -1|$.

Ignoring a shift to the vacuum energy (i.e. terms proportional to $\mathbb{1}$) then the Hamiltonian can be reduced to this simpler form. We first rotate about the axis

$$\hat{R} = \left(-\omega_c + \frac{\omega_+ + \omega_-}{2}\right)\hat{a}^\dagger\hat{a} + \left(-\omega_z + \frac{\omega_+ - \omega_-}{2}\right)\hat{S}_z \tag{7.31}$$

to remove time dependence and we make the assumption that all detunings are similar (i.e. $\Delta_c^{-1} \approx \Delta_\pm^{-1} = \Delta^{-1}$). This leaves us with the Hamiltonian

$$\hat{H} = \omega\hat{a}^\dagger\hat{a} + \omega_0\hat{\sigma}_z + \omega_q\hat{\sigma}_{zz} + \frac{\delta_q}{2}\hat{\sigma}_{zz}\hat{a}^\dagger\hat{a} + \frac{\lambda_1}{\sqrt{2}}(\hat{\sigma}_+\hat{a} + \hat{\sigma}_-\hat{a}^\dagger) + \frac{\lambda_2}{\sqrt{2}}(\hat{\sigma}_-\hat{a} + \hat{\sigma}_+\hat{a}^\dagger) \\ + \xi_1\hat{q}_{xz}(\hat{a} + \hat{a}^\dagger) + i\xi_2\hat{q}_{yz}(\hat{a} - \hat{a}^\dagger) + h(\hat{\sigma}_+^2 + \hat{\sigma}_-^2) \tag{7.32}$$

where we have parameters

$$\omega = \frac{g^2}{3(\Delta+\zeta)} + \omega_c - \frac{\omega_+ + \omega_-}{2} \tag{7.33}$$

$$\omega_0 = \frac{\Omega_+^2 - \Omega_-^2}{96}\left(\frac{5}{\Delta+\zeta} - \frac{1}{\Delta}\right) + \omega_z + \frac{\omega_- - \omega_+}{2} \tag{7.34}$$

$$\omega_q = \frac{\Omega_+^2 + \Omega_-^2}{96}\left(\frac{1}{\Delta+\zeta} - \frac{1}{\Delta}\right) \tag{7.35}$$

$$\delta_q = \frac{g^2}{6}\left(\frac{1}{\Delta} - \frac{1}{\Delta+\zeta}\right) \tag{7.36}$$

$$\lambda_1 = \frac{g\Omega_-}{48}\left(\frac{1}{\Delta} - \frac{5}{\Delta+\zeta}\right) \tag{7.37}$$

$$\lambda_2 = \frac{g\Omega_+}{48}\left(\frac{1}{\Delta} - \frac{5}{\Delta+\zeta}\right) \tag{7.38}$$

$$\xi_1 = \frac{g\Omega_-}{96}\left(\frac{1}{\Delta+\zeta} - \frac{1}{\Delta}\right) + \frac{g\Omega_+}{96}\left(\frac{1}{\Delta} - \frac{1}{\Delta+\zeta}\right) \tag{7.39}$$

$$\xi_2 = \frac{g\Omega_-}{96}\left(\frac{1}{\Delta+\zeta} - \frac{1}{\Delta}\right) + \frac{g\Omega_+}{96}\left(\frac{1}{\Delta+\zeta} - \frac{1}{\Delta}\right) \tag{7.40}$$

$$h = \frac{\Omega_+\Omega_-}{96}\left(\frac{1}{\Delta} - \frac{1}{\Delta+\zeta}\right). \tag{7.41}$$

Clearly this is not exactly equivalent to the spin-1/2 model. There is something akin

---

[39] This is actually $\hat{\sigma}_z^2$ or a shifted version of the element of the nematic tensor $\hat{Q}_{zz}$ for a single atom.

to a quadratic Zeeman shift ($\hat{\sigma}_{zz}$ could be trivially expressed in terms of constants and $\hat{n}_0$), a quadratic version of the dispersive term, and exchange terms where the cavity mode and the atoms exchange excitations in ways that do not exist for spin-1/2 systems. There is also a full flip term whereby atoms can be taken between $|\pm 1\rangle$ with no intervention from the cavity mode.

Some of these terms could lead to interesting physics. For example, in one limit, we can produce a system that switches randomly between superradiance and being completely dark. A discussion of this phenomenon is given in Section 12.2.2. The full potential of these terms is yet to be explored, but is discussed in Section 12.2.1.

For the purposes of this Section, we instead want to get rid of the spin-1 terms. This can be done by taking the limit that $\Delta \gg \zeta$. In that limit all of $\{\, \omega_q, \delta_q, \xi_1, \xi_2, h \,\} \to 0$ and the Hamiltonian reduces to

$$\hat{H} = \omega \hat{a}^\dagger \hat{a} + \omega_0 \hat{\sigma}_z + \frac{\lambda_1}{\sqrt{2}}(\hat{\sigma}_+ \hat{a} + \hat{\sigma}_- \hat{a}^\dagger) + \frac{\lambda_2}{\sqrt{2}}(\hat{\sigma}_- \hat{a} + \hat{\sigma}_+ \hat{a}^\dagger). \tag{7.42}$$

Summing over an ensemble of N atoms yields

$$\begin{aligned} \hat{H} &= \omega \hat{a}^\dagger \hat{a} + \sum_{i=1}^{N} \left\{ \omega_0 \hat{\sigma}_z^{(i)} + \frac{\lambda_1}{\sqrt{2}}(\hat{\sigma}_+^{(i)} \hat{a} + \hat{\sigma}_-^{(i)} \hat{a}^\dagger) + \frac{\lambda_2}{\sqrt{2}}(\hat{\sigma}_-^{(i)} \hat{a} + \hat{\sigma}_+^{(i)} \hat{a}^\dagger) \right\} &(7.43)\\ &= \omega \hat{a}^\dagger \hat{a} + \omega_0 \hat{S}_z + \frac{\lambda_-}{\sqrt{2N}}(\hat{S}_+ \hat{a} + \hat{S}_- \hat{a}^\dagger) + \frac{\lambda_+}{\sqrt{2N}}(\hat{S}_- \hat{a} + \hat{S}_+ \hat{a}^\dagger) &(7.44)\end{aligned}$$

where we have effective parameters

$$\begin{aligned} \omega &= \frac{Ng^2}{3\Delta} + \omega_c - \frac{\omega_+ + \omega_-}{2} &(7.45)\\ \omega_0 &= \frac{\Omega_+^2 - \Omega_-^2}{24\Delta} + \omega_z + \frac{\omega_- - \omega_+}{2} &(7.46)\\ \lambda_- &= -\frac{\sqrt{N} g \Omega_-}{12\Delta} &(7.47)\\ \lambda_+ &= -\frac{\sqrt{N} g \Omega_+}{12\Delta} &(7.48)\end{aligned}$$

and we have defined collective spin operators

$$\hat{S}_z = \sum_{i=1}^{N} \hat{\sigma}_z^{(i)}, \qquad \hat{S}_\pm = \sum_{i=1}^{N} \hat{\sigma}_\pm^{(i)}. \tag{7.49}$$

This is the Dicke model, with no dispersive shift and full independence of the coupling terms. This means that, if the treatment of an ensemble of spin-1 particles (or spin-F particles going back to the general proposal) as a single large spin is valid, this method produces a cleaner version of the Dimer et al proposal [53] with the same flexibility to study the Dicke model that that proposal introduced.

7.1.3 Spin-1 Dicke model simulation

We now simulate the Dicke model in the bosonic mode representation

$$\begin{aligned}\hat{H} = \omega \hat{a}^\dagger \hat{a} + \omega_0 \left(\hat{b}_1^\dagger \hat{b}_1 - \hat{b}_{-1}^\dagger \hat{b}_{-1} \right) \\ + \frac{\lambda_-}{\sqrt{2N}} \left[(\hat{b}_1^\dagger \hat{b}_0 + \hat{b}_0^\dagger \hat{b}_{-1}) \hat{a} + (\hat{b}_{-1}^\dagger \hat{b}_0 + \hat{b}_0^\dagger \hat{b}_1) \hat{a}^\dagger \right] \\ + \frac{\lambda_+}{\sqrt{2N}} \left[(\hat{b}_{-1}^\dagger \hat{b}_0 + \hat{b}_0^\dagger \hat{b}_1) \hat{a} + (\hat{b}_1^\dagger \hat{b}_0 + \hat{b}_0^\dagger \hat{b}_{-1}) \hat{a}^\dagger \right] .\end{aligned} \tag{7.50}$$

We will compare that to the single large spin models of the semi-classical model. To begin with we assume a fully polarised initial state. The initial state, in the bosonic mode representation, is $|N, 0, 0\rangle$ and in the Dicke state basis $|N, -N\rangle$.

Figure 7.3 shows that these two pictures are equivalent. The bosonic mode simulation returns the same results as the Dicke state basis. As expected, this means that our integer-spin Dicke model, if initiated into a fully polarised initial state, is equivalent to a two-level ensemble Dicke model.

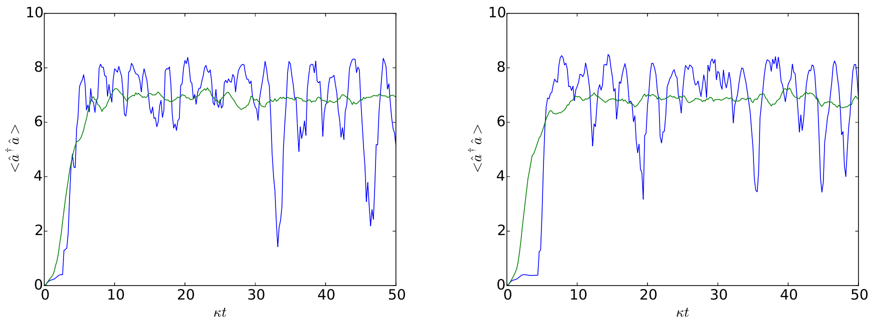

(a) Spinor basis

(b) Dicke state basis

Figure 7.3: Dicke model simulations in two different bases. Spinor basis uses a bosonic mode population picture to describe the atomic state. Dicke state basis uses a long spin picture. In both cases a single trajectory (blue) and an ensemble average (green) are shown. Parameters used were $\{\omega, \omega_0, \lambda\} = \{1.0, 1.0, 1.0\}$ with a spin length equivalent to 20 spin-1 atoms.

7.2 Spin-1 Dicke model without a fixed spin length

A fully polarised initial state will act as a single large spin regardless of what is summed over to produce that large spin. However, if the initial state is not fully polarised, that is not necessarily the case. With two-level systems, there is no product state of N indistinguishable atoms that does not have maximal spin length $N/2$. For a non-polarised state, there is a coherent spin state which still has maximal spin length and still responds to the Dicke model in the same way. For spin-1 atoms, there are options where we still have indistinguishability but the spin length is not maximal; in particular, states where the spin length is in a superposition can exist.

7.2.1 $|0\rangle$ product state

A π-polarised laser operating near the $F = 1 \to F' = 1$ transitions will excite atoms in $|\pm 1\rangle$ but not $|0\rangle$ because selection rules do not allow such a transition. This means that the atoms in $|\pm 1\rangle$ are excited to $|F' = \pm 1, m_{F'} = \pm 1\rangle$, where they can undergo spontaneous emission events that either take them back to $|\pm 1\rangle$ where the process repeats or into $|0\rangle$ where they will stay confined. This optical pumping means that the product state $|0\rangle^{\otimes N}$ can be easily prepared. Such a state is not trivially represented with Dicke states. This is due to the way in which the spins add. Two $|1, 0\rangle$ particles add to a collective sum as

$$|1,0\rangle \otimes |1,0\rangle = \sqrt{\frac{2}{3}}\,|2,0\rangle - \sqrt{\frac{1}{3}}\,|0,0\rangle\,. \tag{7.51}$$

For spin-1 particles we can iterate this process one atom at a time using the *Racah formula*, which tells us how angular momentum states add. For the case of $|J, 0\rangle \otimes |1, 0\rangle$, the Racah formula simplifies very neatly to

$$|J,0\rangle \otimes |1,0\rangle = \sqrt{\frac{J+1}{2J+1}}\,|J+1,0\rangle - \sqrt{\frac{J}{2J+1}}\,|J-1,0\rangle\,. \tag{7.52}$$

If we take our two atom state then we can iterate to a third atom as

$$\begin{aligned}
|1,0\rangle \otimes |1,0\rangle \otimes |1,0\rangle &= \left(\sqrt{\frac{2}{3}}\,|2,0\rangle - \sqrt{\frac{1}{3}}\,|0,0\rangle\right) \otimes |1,0\rangle & (7.53)\\
&= \sqrt{\frac{2}{3}}\,|2,0\rangle \otimes |1,0\rangle - \sqrt{\frac{1}{3}}\,|0,0\rangle \otimes |1,0\rangle & (7.54)\\
&= \sqrt{\frac{2}{3}}\sqrt{\frac{3}{5}}\,|2+1,0\rangle - \sqrt{\frac{2}{3}}\sqrt{\frac{2}{5}}\,|2-1,0\rangle - \sqrt{\frac{1}{3}}\,|0+1,0\rangle\,. & (7.55)
\end{aligned}$$

Since $|2-1, 0\rangle$ and $|0+1, 0\rangle$ are the same collective spin state, but different in the full space, their coefficients add vectorially such that

$$|1,0\rangle \otimes |1,0\rangle \otimes |1,0\rangle = \sqrt{\frac{2}{5}}\,|3,0\rangle - \sqrt{\frac{3}{5}}\,|1,0\rangle\,. \tag{7.56}$$

This process can be iterated for N atoms and gives

$$|1,0\rangle^{\otimes N} = \sum_{k=0}^{\lfloor N/2 \rfloor} c_{N-2k}\,|N-2k,0\rangle \tag{7.57}$$

where $\lfloor N/2 \rfloor$ means to round down if N is odd. The coefficients alternate in sign and are generally not particularly easy to find analytically. However, for any size N, two of the coefficients have obvious analytic forms. Firstly, it is clear from the iteration that

$$|c_N|^2 = \prod_{J=1}^{N} \frac{J+1}{2J+1} \tag{7.58}$$

which for large N will approach 2^{-N} and so high spin length populations become vanishingly small in that limit. Secondly,

$$c_0 = \sqrt{\frac{1}{N+1}} \quad \text{for } N \text{ even}, \qquad c_1 = \sqrt{\frac{3}{N+2}} \quad \text{for } N \text{ odd}. \tag{7.59}$$

These become small for large N but are still much more significant contributions than the large N states.

For 10 atoms the superposition state is

$$\begin{aligned} |1,0\rangle^{\otimes 10} = \sqrt{\frac{256}{46189}}\,|10,0\rangle - \sqrt{\frac{128}{2717}}\,|8,0\rangle + \sqrt{\frac{32}{187}}\,|6,0\rangle \\ - \sqrt{\frac{48}{143}}\,|4,0\rangle + \sqrt{\frac{50}{143}}\,|2,0\rangle - \sqrt{\frac{1}{11}}\,|0,0\rangle\,. \end{aligned} \tag{7.60}$$

We can see that the bulk of the population is in states $|2,0\rangle$, $|4,0\rangle$ and $|6,0\rangle$. Even for this small number of atoms, the population in the maximal spin state is just 0.6%. The populations for 1000 atoms are shown in Figure 7.4. In that case, the vast majority of

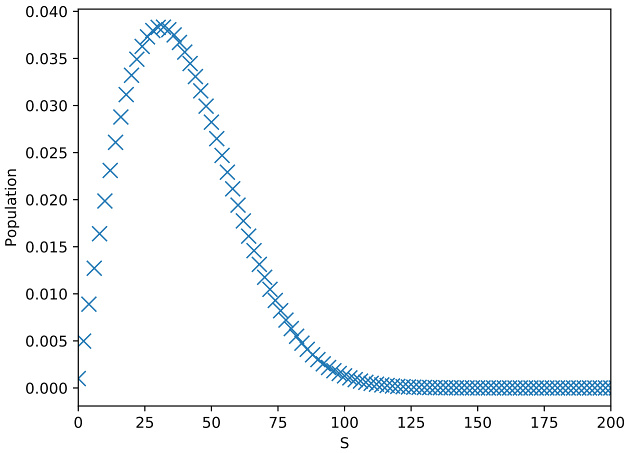

Figure 7.4: Populations $|c_S|^2$ for even S in the collective Dicke states $|S,0\rangle$ for the product state $|m_F = 0\rangle^{\otimes N}$ of $N = 1000$ spin-1 atoms. Populations for states beyond $S = 200$ are not shown as the total sum of these populations is $\sum_{S>200} |c_S|^2 = 1.34 \times 10^{-9}$.

the state is contained at relatively low spin lengths compared to the polarised state. The maximal spin length has a very low population.

7.2.2 Initiation of the Dicke model in the $|0\rangle$ product state

If we think of what these lower states would do under the action of the Dicke model, we can easily identify that, due to the form of the ladder operators for different spin lengths, the response is muted for lower spin lengths. To calculate this we can consult the semi-classical threshold calculation. There, where we normalised the spin per atom to 0.5, we can now take that to be 0.5χ where $\chi = S/N < 1$. Note that we now normalise the semiclassical parameters in Equations 5.12-5.14 by $2N$ rather than N. This shortening of the normalisation condition gives a new critical threshold related to the old one as

$$\lambda_c' = \frac{1}{\sqrt{\chi}}\lambda_c. \tag{7.61}$$

This means that some states in the superposition might be below the threshold when others are above.

The average response is the weighted average of the responses of all the spin lengths. We can calculate this by simulation in different Dicke bases and then taking the weighted average of those results. What we might hope to see is a series of transitions as we increase the coupling as different states become superradiant. Instead, as shown in Figure 7.5a, we see a steady rise with no distinct threshold at all. This is because, for 10 atoms, we do not have a particular sharp transition even if we do start in a polarised state. Sharp transition behaviour requires more atoms.

Figure 7.5b shows 200 atoms around the transition points of the most populated spin lengths and, despite the increased atom number, the weighted average still does

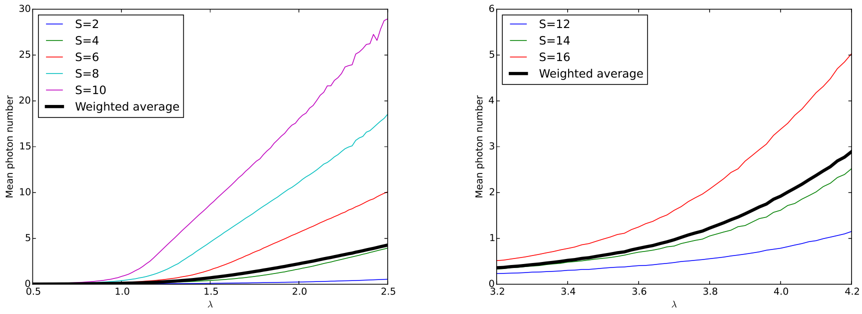

(a) (b)

Figure 7.5: Average photon number over a single long trajectory from the initial atomic state $|S, -S\rangle$ for parameters $\{\omega, \omega_0\}/\kappa = \{\sqrt{3}, \sqrt{3}\}$ with (a) $N = 10$ and (b) $N = 200$ atoms. Parameters are chosen such that for $\chi = S/N$, $\lambda_c/\kappa = 1/\sqrt{\chi}$. In both cases the weighted average is weighted by the initial contributions of those states to the state $|0\rangle^{\otimes N}$.

not feature any sharp transitions. The semi-classical model requires the thermodynamic limit of large N, but more specifically, it requires a large spin length. 200 atoms might be enough for the polarised state to follow the semi-classical model quite closely, but for the $|0\rangle$ product state the peak spin states have spin length $S \sim 10-20$ which certainly do not have such sharp transitions.

We require a number of atoms such that the highest population states have significant spin length. This introduces a new problem. For large numbers of atoms, the transition points for the different spin lengths become closer and closer together. This means that the necessary "sharpness" to be visible in the weighted average becomes higher and higher. The necessary values of λ needed to make $S = 200$ superradiant for 2×10^5 atoms is 31.62 times the usual critical coupling values. For $S = 198$ it is 31.78 times. For the sorts of values used in the experiments, this would mean that there would need to be extraordinary control over the laser powers, and thus λ, and the measurements to be able to see anything. The necessary laser power required to reach those couplings would be extremely large[40].

Our conclusion was that this initial state would not offer particularly interesting results with regards to phase transitions. With a small ensemble the reaction is distinctly outside of the thermodynamic regime where the critical threshold is predicted and so the different spin states' individual "thresholds" overlap significantly. The more atoms we have, the smaller the region in which the transition must occur to avoid overlap, and so those transitions still blur together despite the increased atom number. The required laser power to make such systems work also becomes infeasibly high. If we did use an atom number where the peak spin lengths react semi-classically, then that system would most probably just do nothing since the majority of the population would be so far below threshold for feasible coupling strength λ. What is of much more interest is the individual trajectory case, where the spin length can be projected out by a photon counting measurement. This discovery led to the work in Chapter 8.

7.3 Experimental implementation of imbalanced coupling

The experiment at the CQT used the spinor model to study the Dicke model with imbalanced driving [71]. The setup allows for independent control of the rotating (by altering λ_-) and counter-rotating (by altering λ_+) terms. This is an aspect of these methods where they have an advantage over the BEC method of producing the Dicke

---

[40] Of course there are other parameters that could be altered to improve that coupling. Different atomic species have different Clebsch-Gordan coefficients which can change the numerical factor in the coupling, though not by orders of magnitude. The individual atom-coupling g can be larger than used in the CQT experiments, though again not by several orders of magnitude. The detuning can be reduced, though care would have to be taken that it does not become so small that the excited-state hyperfine splitting becomes a factor. Careful manipulation of those microscopic parameters with the right choice of species might enable the range of possible couplings to increase by an order of magnitude or two.

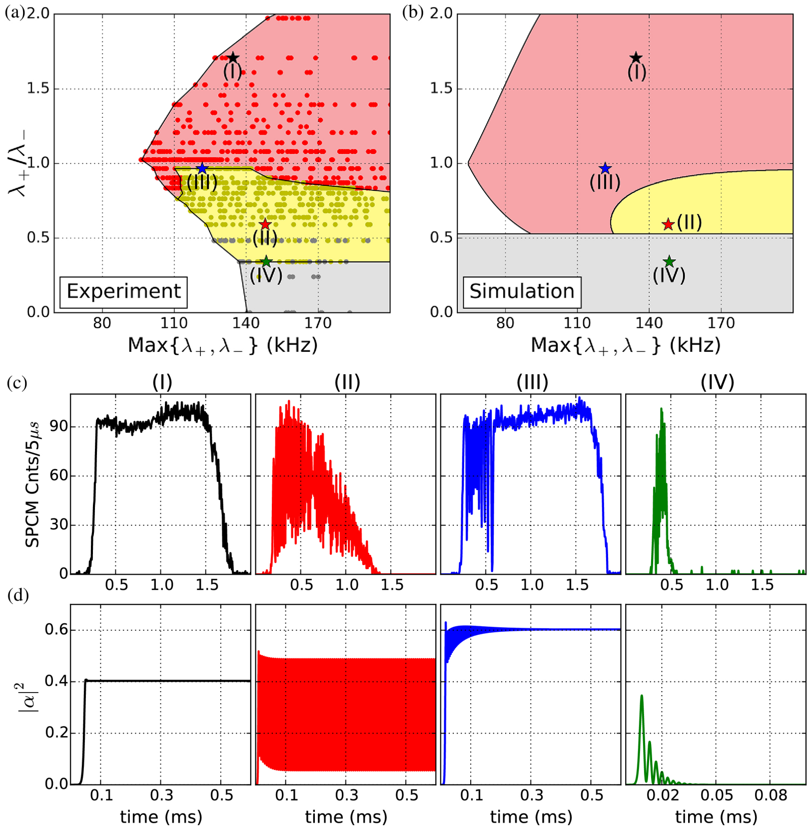

Figure 7.6: Figure reproduced from [71]. Upper plots show (a) experimental and (b) theoretical results for the steady-state phase map of the imbalanced Dicke model. States are as follows: normal (white), inverted (grey), oscillations (yellow) and superradiance (red). Below this are examples of (c) experimental and (d) theoretical runs for particular data points indicated on the phase maps.

model [67–70]. It should be noted that the study of imbalanced driving certainly can be, and in fact was, implemented in the two-level system version.

Much like the experiment described in Section 5.2.5, the experiment involves ^{87}Rb atoms in a cavity with parameters $\{g, \kappa, \gamma\} = \{2\pi\} \times \{1.1, 0.1, 3\}$ MHz and a detuning of $-2\pi \times 127$ GHz from the D_2 transition line. These atoms are cooled and loaded into an optical lattice within the cavity. They are then pumped into the $|F = 1, m_F = 1\rangle$ level, which is given the notation $|-1\rangle$ in this analysis, with approximate fidelity of 94%. Around 2×10^5 atoms are used for each run, with the experimental run triggered once such a value is inferred. As with the Dicke model phase transition investigation, transitions are driven by two counter-propagating lasers which drive the different coupling terms[41]. The two lasers driving

---

[41] In the experiment, both lasers actually contribute both $\sigma_\pm$ laser fields. These are tuned in such a way that only the desired component of the polarisation drives the Raman transitions, though the other part does also produce light shifts. This, and the fact the experiment is performed on a different line to our derivation, is why the form of the parameters given above vary slightly to the parameters in the paper.

the couplings are ramped up with a fixed ratio λ_+/λ_- to some preset value where they remain for 3ms as the dynamics are observed.

The dynamics are categorised as one of four options: superradiance, oscillations, transient pulse and nothing. The transient pulse is characterised by its length being shorter than 250 μs and amounts to when the initial state and steady state are opposite trivial states (i.e. in this experiment, when the steady state is the inverse state). The oscillatory phase is characterised by a peak in the Fourier transform of the output signal, while the superradiant phase is characterised by significant and prolonged cavity output without oscillations. These results were then used to create a phase map for the model, shown in Figure 7.6. Whilst there is qualitative agreement between theory and experiment, significant differences in the onset of each phase and its region in phase space are obvious. These are discussed in Section 7.4.4.

The signal is measured with a single-photon counting module (SPCM) which has a gate time of 5 μs. Theoretically predicted oscillations have a higher frequency than such a gate time would measure and so the measured frequencies are aliased. The SPCM also saturates at $\sim$ 100 counts / gate time, which means that analysis of the photon number is also not possible.

7.4 Theoretical modelling of imbalanced coupling

7.4.1 Semi-classical dynamics

The majority of our theoretical modelling uses the semi-classical model described in Section 5.1.1 with $U = 0$

$$\dot{\alpha} = -\kappa\alpha - i\omega\alpha - i\lambda_+\beta - i\lambda_-\beta^* \tag{7.62}$$

$$\dot{\beta} = -i\omega_0\beta + 2i\lambda_+\alpha\gamma + 2i\lambda_-\alpha^*\gamma \tag{7.63}$$

$$\dot{\gamma} = i\lambda_+(\alpha^*\beta - \alpha\beta^*) + i\lambda_-(\alpha\beta - \alpha^*\beta^*). \tag{7.64}$$

For this treatment, we renormalised for N spin-1 atoms, but they can actually be further generalised to N spin-F particles as

$$\alpha = \frac{\langle\hat{a}\rangle}{\sqrt{2FN}}, \quad \beta = \frac{\langle\hat{S}_-\rangle}{2FN}, \quad \gamma = \frac{\langle\hat{S}_z\rangle}{2FN}, \quad |\beta|^2 + \gamma^2 = 0.25. \tag{7.65}$$

We can see in Figure 7.6 that the four phases reported by the experiment can also be found with the semi-classical equations. The response in the superradiant and trivial phases can be seen to feature decaying oscillations to the relevant steady state, while the oscillatory phase has decaying oscillations to a steady orbit.

In reality, these equations offer an extremely rich phase diagram with a wide variety of phase transitions, broken symmetries and different exotic attractors [82].

7.4.2 Oscillatory phase: analysis of the frequency

Further study of the oscillatory phase shows that all of the semi-classical parameters oscillate, and they do so at some fixed frequency. We can see from Figure 7.7 that this frequency is very cleanly picked out by the Fourier transform, and appears at $\sim 40\ (2\pi)$ kHz for this particular set of experimental parameters. This would give the oscillations a period $\sim 4\ \mu$s, making the gate time slightly more than a period of the oscillations. This puts it outside the resolvable frequencies of the SPCM and so the measurement produces an aliased frequency.

It is possible to predict the behaviour of the oscillations either side of the transition. Figures 7.7c and 7.7d show properties of the system as it passes through the various transitions. The boundary between normal and superradiant phases is marked, as expected, by a rise from zero of the cavity occupation. Perhaps less expected, since it happens as we increase the coupling, is the boundary between superradiant and oscillatory phases. Here, the average photon number actually starts to decrease instead. This boundary is also marked by a change in the frequency of

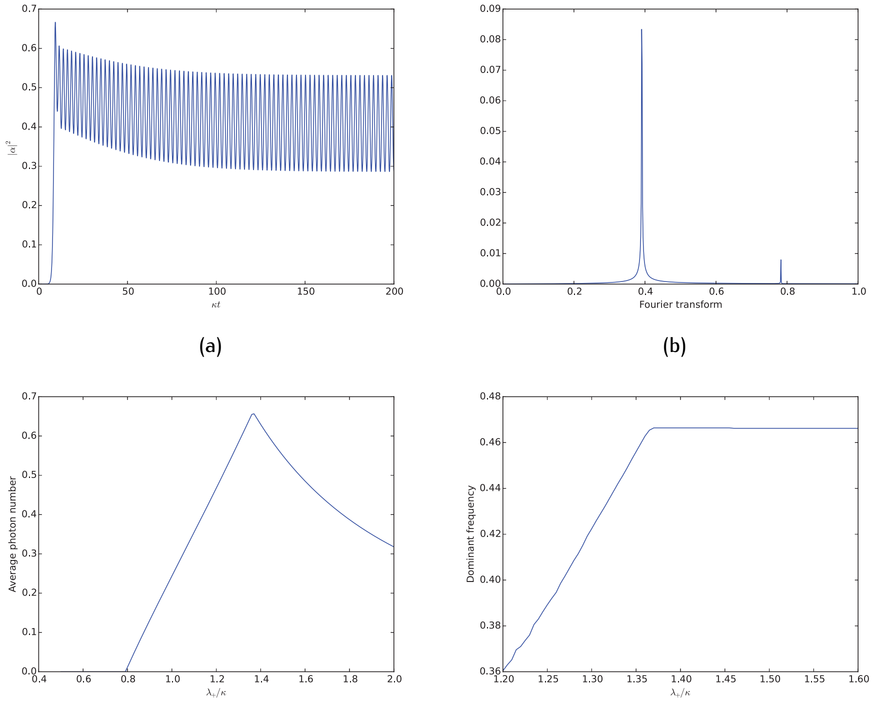

(a) (b)

(c) (d)

Figure 7.7: For semi-classical evolution in the Dicke model with parameters $\{\omega, \omega_0\}/\kappa = \{1.0, 0.7\}$ and (a,b) $\{\lambda_+, \lambda_-\}/\kappa = \{1.5, 1.2\}$ or (c,d) fixed ratio $\lambda_-/\lambda_+ = 0.8$, (a,c) average photon number per atom through the evolution, (b) Fourier transform of the photon number through a long evolution and (d) dominant frequency of a Fourier transform of the photon number. With the Fourier transforms, analysis is of the oscillations around the mean photon number.

the oscillations, which in the superradiant phase are decaying and at increasing frequencies for increasing coupling, but plateau to a specific frequency at the oscillatory boundary.

Unfortunately, it was not possible to study either of these predictions in the experiment due to the saturation and gate time of the SPCM. However, it should be noted that these marked differences between the states do exist. This means that, with a detector with resolution able to measure the amplitude and frequency accurately, these signatures could be searched for to mark the phase boundaries. This would allow the transitions to be mapped out without having to "bin" the results solely according to the photon number, negating some of the issues associated with appropriately deciding which phase the result belongs to, as discussed in Section 7.4.4.

7.4.3 Oscillatory phase: quantum vs. semi-classical

The work above indicates that every aspect of the system oscillates. From a semi-classical standpoint, this can be thought of purely mathematically as the real part of the eigenvalue going to zero, and the system entering a stable orbit. None of that is particularly unusual. However, for the actual system, this would involve the self-organisation of atoms not only into a steady state, but into an evolving steady state that maintains self-organisation. We therefore wish to check that, given the more unusual steady state, the semi-classical assumptions are still valid.

Figure 7.8 shows that a single quantum trajectory in the oscillatory phase not only oscillates, but it does so at the same frequency the semi-classical analysis predicts. Note that the ensemble average does not oscillate, as the starting time of the oscillations will vary due to noise, washing out the oscillations. The quantum

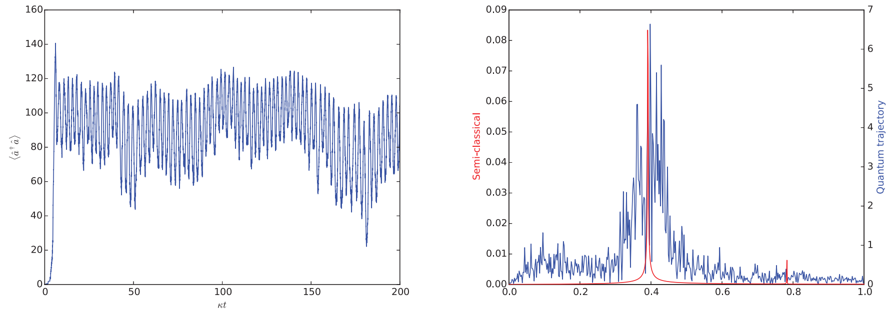

(a)

(b)

Figure 7.8: For quantum trajectory evolution of the Dicke model for 100 atoms with parameters $\{\omega, \omega_0, \lambda_+, \lambda_-\}/\kappa = \{1.0, 0.7, 1.5, 1.2\}$, (a) photon number through the evolution and (b) Fourier transform of the photon number through a long evolution compared to the semi-classical case for the same parameters. With the Fourier transforms, analysis is of the oscillations around a rolling mean.

picture also gives us another interesting insight into the oscillatory phase. Perhaps unsurprisingly, the makeup of the state is a superradiant state. There are two opposite phase solutions that exist in superposition. The oscillatory phase is thus a superradiant state, but one that oscillates in magnitude. As with the Dicke model, measurement with a homodyne detector would pick out a particular phase of the cavity output field and so the system would pick one of the two solutions randomly.

This means that going from the inverted phase into the oscillatory phase means to go through a symmetry breaking bifurcation in exactly the same way as the superradiant phase transition. However, the boundary between the superradiant and oscillatory phases, where the system goes from two stable orbits to two stable points, does not feature symmetry breaking. If the system is in the superradiant phase, and the couplings are changed such that we move towards and into the superradiant state, we have slower decaying orbits until they do not decay and we have stable orbits. In dynamical systems, this phenomenon is known as a *Hopf bifurcation*.

7.4.4 Problems with the phase map

The primary modelling task for this work was to produce a phase map that predicted the regions where the experiment would see the different phases. This involved integrating the semi-classical equations to some large time and then making a judgement on which state had been reached. Given that, with $U = 0$, exact calculation of the superradiant state is possible, direct comparison can be made to all three of the steady-state solutions. Our map, given in Figure 7.6, has some significant differences, which we try to explain in this section.

There are three key areas where the phase map for the experiment differs: the normal to superradiant boundary is shifted to much higher coupling, the oscillatory phase is much larger and the inverted to oscillatory boundary is at a much lower ratio. Our explanation of the first of these is the same as the explanation of why the Dicke model transition is at higher coupling than originally predicted. single-atom effects, and in particular inhomogeneous Doppler broadening due to atomic motion, push the phase transition away from the semi-classical prediction.

We believe that the other two differences, where the oscillatory phase is exaggerated and appears at lower coupling ratio, can be explained by the same reason. In the oscillatory phase the eigenvalues are purely imaginary. This means that in the vicinity of the boundary with the oscillatory phase, the real component of the eigenvalues must tend towards zero. This means that the decay of the oscillations, induced by that real part, is a very slow process. Figure 7.9 shows that in each case, the output looks like stable oscillations for different sets of parameters near the transition even at times on the order of $\kappa t = 1000$, which is ≈ 1.6 μs for the experiment. This value is on the order of the length of the pulse emitted by the

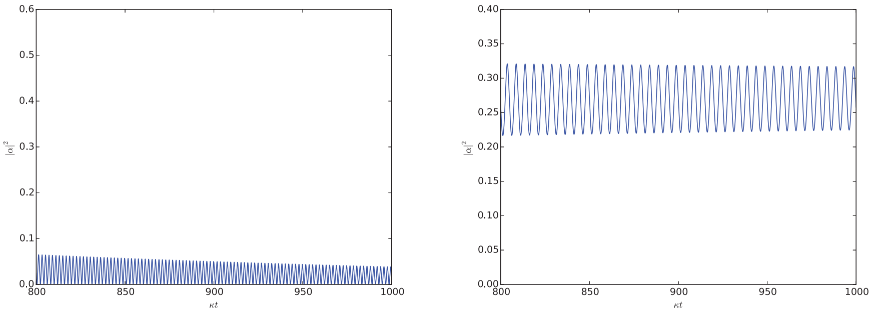

(a) $\lambda_+/\kappa = 1.8$, $\lambda_-/\lambda_+ = 0.528$ **(b)** $\lambda_+/\kappa = 1.16$, $\lambda_-/\lambda_+ = 0.55$

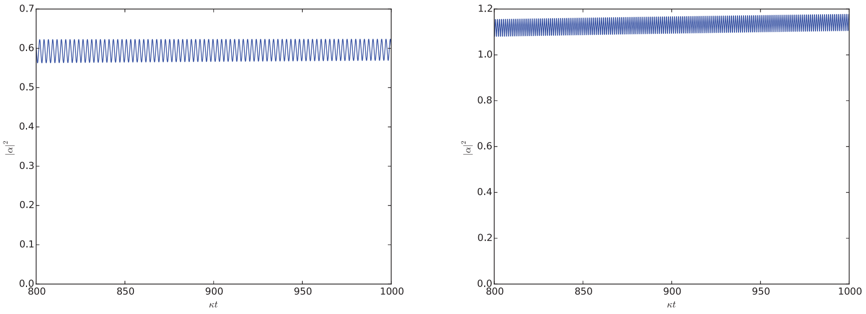

(c) $\lambda_+/\kappa = 1.27$, $\lambda_-/\lambda_+ = 0.82$ **(d)** $\lambda_+/\kappa = 1.85$, $\lambda_-/\lambda_+ = 0.96$

Figure 7.9: Photon number per atom for semi-classical evolution of the Dicke model with parameters $\{\omega, \omega_0\}/\kappa = \{1.0, 0.7\}$ and couplings as shown for each plot.

experiment and so the decaying oscillations give a frequency peak in the Fourier transform and the state is deemed oscillatory. Throwing in experimental noise and the SPCM saturation on top of this means that we would not expect the clean peaks of the semi-classical Fourier transforms in any case, and so separating out a peak in amongst noise due to decaying or actual noise is incredibly difficult. Theoretically, we simulate out to much larger times such that the true steady state emerges. We believe that this difficulty in correctly making judgements on the output measurement explains the exaggeration of the oscillatory phase area.

This explanation raises a further question. The experiments show the superradiant state area happening for lower and lower ratios as the coupling strength increases. This seems contrary to the previous argument. The reason for this is in the saturation threshold for the SPCM. Any oscillations at these high coupling values still happen at high photon numbers, with the troughs still being too high to be seen by the SPCM.

Chapter 8

Rapid production of many-body entanglement in spin-1 atoms via cavity output photon counting

A perfect Dicke model made of integer spins bears no differences to an ensemble of two-level systems *only if* initiated in a maximal spin length state, most obviously the normal or inverted phase. If instead the system is initiated in a superposition of different spin lengths then the response is markedly different and the cavity output is expected to vary significantly from shot to shot. Whilst any study of the Dicke model becomes difficult in these limits, there are still interesting possibilities. The cavity output projects the atomic state into a particular spin length, which, unless the spin length is maximal, means the atoms are entangled. In this particular work, we focussed on a Tavis-Cummings model. In that case an exact photon number is expected for different spin lengths. We showed that with perfect photon detection efficiency, the resultant states offer Heisenberg scaling in the quantum Fisher information. With imperfect photon detection it is still possible to generate metrological sensitivity beyond the standard quantum limit, and we showed how repeated measurements could further refine the knowledge of the spin length and approach the Heisenberg limit. This work is presented in the form of a Letter published in Physical Review Letters. It has been reformatted for this thesis, with the Letter separated into sections, some notation and spelling altered to provide consistency throughout the thesis, and parts of the supplemental material included in the text, but is available in its original form at https://journals.aps.org/prl/abstract/10.1103/PhysRevLett.122.103601.

8.1 Introduction

Entanglement is a fundamental property of quantum mechanics. Two-body or two-mode entanglement is now readily producible and well studied, but study of many-body entangled systems and routine production of large many-body entangled ensembles are still open problems. The generation of such states is of interest not only to fundamental science, but for the use of such states as a resource for quantum information tasks and quantum metrology. In this latter context, there has been significant progress in the production of spin squeezing [20, 22]. For N particles in a non-correlated ensemble, the variance on measurements is limited by the standard quantum limit (SQL), which scales like $1/N$. In spin squeezing, entanglement is induced in an ensemble of atomic spins such that measurements of classical properties can be done more precisely. The fundamental limit on measurements with an ensemble *allowing for entanglement* is the Heisenberg limit with minimum variance scaling like $1/N^2$.

A wide variety of spin squeezing techniques have been used to show sub-SQL variances. A common method involves the "one-axis twisting" mechanism [19, 93, 94, 96, 97, 103]. Other procedures have produced up to a 100-fold reduction in the spin variance compared to classical states [107]. These states have also been used for proof-of-principle, quantum-enhanced implementations of atomic clocks [100,145] and magnetometers [97,105], and to measure microwave fields [96]. Other proposals, such as the two-axis counter-twisting scheme [19], offer a route to achieving Heisenberg limited metrological sensitivity, but these are yet to be implemented experimentally.

The present work concerns entanglement in an ensemble of spin-1 atoms, which, compared with spin-1/2 atoms, clearly require more degrees of freedom to describe, but concomitantly offer more degrees of freedom to entangle [146–148]. Indeed, proposals [15, 149–153] including the work in Chapter 10, and experiments [14, 95, 99, 100, 124, 154–160] with spinor Bose-Einstein condensates (BECs) predict or have produced entanglement either on the Bloch sphere (e.g., squeezing in one of $\hat{S}_x$, $\hat{S}_y$, or $\hat{S}_z$, where $\hat{S}_i$ is the i-component of the collective atomic spin operator) or in the additional spinor degrees of freedom.

8.1.1 Quantum Fisher information

The metrological sensitivity of a quantum state can be captured by the quantum Fisher information (QFI). The variance of a measured phase θ imprinted by a classical parameter is bounded by $(\Delta\theta)^2 \geq \mathcal{F}^{-1}$ where $\mathcal{F}$ is the QFI. As such, the SQL states that for an optimal classical state the QFI scales as N while the Heisenberg limit is signified by a QFI that scales like N^2. For pure states, the QFI over some generator

$\hat{G}$ is

$$\mathcal{F} = 4(\Delta\hat{G})^2. \tag{8.1}$$

More generally, for a density matrix ρ, decomposed into eigenstates as

$$\rho = \sum_i \xi_i \left|e_i\right\rangle \left\langle e_i\right| \tag{8.2}$$

the QFI is given by

$$\mathcal{F} = 2\sum_{i,j} \frac{(\xi_i - \xi_j)^2}{\xi_i + \xi_j} |\left\langle e_i\right| \hat{G} \left|e_j\right\rangle|^2. \tag{8.3}$$

Typically these quantities would be maximised over a set of generators to find the best possible QFI. In this work, given that the state generation protocol we propose produces varying, heralded states, we choose a single generator to consider: $\hat{Q}_{xx} - \hat{Q}_{yy}$. Here, $\hat{\mathbf{Q}}$ is the nematic tensor operator and [14,15]

$$\hat{Q}_{ij} = \sum_{n=1}^{N} \hat{\sigma}_i^{(n)}\hat{\sigma}_j^{(n)} + \hat{\sigma}_j^{(n)}\hat{\sigma}_i^{(n)} - (4/3)\delta_{ij} \tag{8.4}$$

where $i, j \in \{ x, y, z \}$, $\hat{\sigma}_i^{(n)}$ are spin-1 angular momentum operators for a single atom, and δ_{ij} is the Kronecker delta function. This generator, in a bosonic mode operator picture where $\hat{b}_i(\hat{b}_i^\dagger)$ is the annihilation (creation) operator for a particle in state $|m_F = i\rangle$, is given by

$$\hat{G} = 2(\hat{b}_{+1}^\dagger \hat{b}_{-1} + \hat{b}_{-1}^\dagger \hat{b}_{+1}) \tag{8.5}$$

and so involves a transfer of atoms between the $|m_F = \pm 1\rangle$ states. If we were to consider only these two states, reducing the atoms to effective two-level systems, then the algebra would give this as $2\hat{S}_x$ [42].

8.1.2 Summary of the Chapter

In this Chapter, we propose a new method to produce entanglement in an ensemble of spin-1 atoms. We use interactions mediated by cavity-assisted Raman transitions, building on previous work for generating such interactions with two-level (spin-1/2) atoms [53,72,161,162]. This approach has previously been followed to produce an effective Dicke model, as described in Chapters 7 and 10, and spin-exchange interactions, as discussed in [163,164] and Chapters 10 and 11, for spinor (spin ≥ 1) atoms. Here, we engineer instead an effective Tavis-Cummings (TC) model for an ensemble of spin-1 atoms, which, as we show, can be used to herald, via a photon counting measurement on the cavity output field, the production of one of a family of highly

---

[42] It should be noted that this factor of 2 means that the maximum QFI of the system is $16N^2$ rather than the $4N^2$ usually available to N spin-1 atoms [22].

entangled, many-body quantum states. We show further that the average result of this procedure, for ideal photon detection, in fact gives Heisenberg scaling of the QFI, while for non-ideal photon detection, the method still retains metrological sensitivity beyond the SQL and with scaling significantly better than linear. We also show that by alternating between TC and anti-Tavis-Cummings (anti-TC) interactions, so as to produce a sequence of cavity output pulses and corresponding photon counting measurements, it is in principle possible to regain Heisenberg scaling even with finite detection efficiency.

8.2 Methods

8.2.1 Model

For a specific system, we consider N ^{87}Rb atoms confined tightly within an optical cavity and pumped into the $F = 1$ ground hyperfine level[43]. As shown in Figure 8.1, we use a scheme of cavity-assisted Raman transitions on the D_1 line to introduce effective interactions between the atoms and the cavity mode. With both lasers on and detuning Δ much larger than the width of the excited-state hyperfine structure, the model of the system reduces to an effective, dissipative Dicke model for the cavity mode and an atomic spin-1 ensemble ($\hbar = 1$),

$$\dot{\rho} = -i[\hat{H}, \rho] + \kappa(2\hat{a}\rho\hat{a}^\dagger - \hat{a}^\dagger\hat{a}\rho - \rho\hat{a}^\dagger\hat{a}) \tag{8.6}$$

where ρ is the density matrix for the composite atom-cavity system, κ is the cavity field decay rate, $\hat{a}$ is the cavity mode annihilation operator, and

$$\hat{H} = \omega\hat{a}^\dagger\hat{a} + \omega_0\hat{S}_z + \lambda_-(\hat{a}\hat{S}_+ + \hat{a}^\dagger\hat{S}_-) + \lambda_+(\hat{a}\hat{S}_- + \hat{a}^\dagger\hat{S}_+) \tag{8.7}$$

where we have introduced collective spin operators $\hat{S}_{z,\pm}$, which are sums of N spin-1 operators. The coefficients in Equation 8.7 are given by

$$\omega = \omega_c - \frac{\omega_- + \omega_+}{2} + \frac{Ng^2}{3\Delta} \tag{8.8}$$

$$\omega_0 = \omega_z - \frac{\omega_- - \omega_+}{2} + \frac{\Omega_+^2 - \Omega_-^2}{24\Delta} \tag{8.9}$$

$$\lambda_\pm = \frac{g\Omega_\pm}{12\sqrt{2}\Delta}. \tag{8.10}$$

Here ω_c is the frequency of the cavity mode, $\omega_\pm$ and $\Omega_\pm$ are the bare and Rabi frequencies, respectively, of the $\sigma_\pm$-polarised laser fields, ω_z is the Zeeman splitting

---

[43] We note that the scheme works equally well with pumping into the $F = 2$ level, in which case we realise an ensemble of spin-2 atoms. With, e.g., caesium, one could similarly realise the scheme with spin-3 or spin-4 atoms, as discussed in Chapter 7.

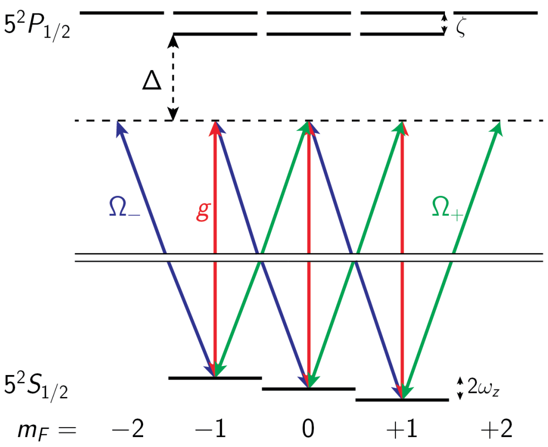

Figure 8.1: Implementation of an effective Dicke model using the $F = 1$ ground state of ^{87}Rb. Interactions are mediated by detuned Raman transitions on the D_1 line mediated by a cavity mode (red) and σ_-- (blue) and σ_+- (green) polarised lasers.

of the $F = 1$ levels, g is the single-atom-cavity coupling strength (for the ^{87}Rb D_2 line cycling transition), and Δ is the detuning of the fields from the atomic resonance.

8.2.2 Initial state

We consider this system with an initial atomic state $|m_F = 0\rangle^{\otimes N}$. This state does not have a certain spin length. Rather, it is given by a superposition of states of different spin lengths, which, in a representation of Dicke states $|S, 0\rangle$, can be written

$$|m_F = 0\rangle^{\otimes N} = \sum_{S=0}^{N} c_S \, |S, 0\rangle \,. \tag{8.11}$$

For even numbers of atoms, $c_S = 0$ for all odd S. Odd numbers of atoms instead have $c_S = 0$ for even S.

We build this superposition by using the Racah formula, which for $|S, 0\rangle \otimes |1, 0\rangle$ reduces to

$$|S, 0\rangle \otimes |1, 0\rangle = \sqrt{\frac{S+1}{2S+1}} \, |S+1, 0\rangle - \sqrt{\frac{S}{2S+1}} \, |S-1, 0\rangle \,. \tag{8.12}$$

We calculate the coefficients $\{c_S\}$ of the superposition in Equation 8.11 by iterating this formula $N - 1$ times. An example of the resulting distribution of $|c_S|^2$ values is shown in Figure 8.2 for $N = 1000$. One sees that the dominant constituents of the state actually have much shorter spin length than the maximum possible value of $S = N$, with the peak of the distribution centered at $S \simeq \sqrt{N}$.

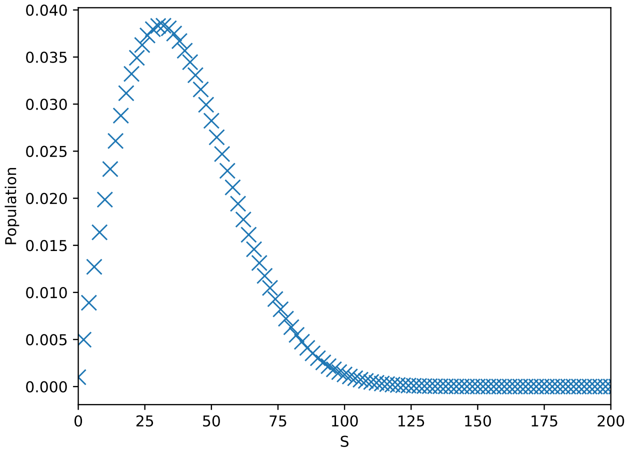

Figure 8.2: Populations $|c_S|^2$ for even S in the collective Dicke states $|S, 0\rangle$ for the product state $|m_F = 0\rangle^{\otimes N}$ of $N = 1000$ spin-1 atoms. Populations for states beyond $S = 200$ are not shown as the total sum of these populations is $\sum_{S>200} |c_S|^2 = 1.34 \times 10^{-9}$.

8.3 Production of entanglement

8.3.1 Entanglement of Dicke states

The states of the atomic ensemble that result from this measurement are Dicke states. We consider the entanglement witness from [148],

$$(\Delta \hat{S}_x)^2 + (\Delta \hat{S}_y)^2 + (\Delta \hat{S}_z)^2 \geq N. \tag{8.13}$$

Any state that breaks this inequality *must* be entangled. This can be rearranged to

$$\langle \hat{\mathbf{S}}^2 \rangle - \langle \hat{S}_x \rangle^2 - \langle \hat{S}_y \rangle^2 - \langle \hat{S}_z \rangle^2 \geq N. \tag{8.14}$$

For any state with definite spin length S, this inequality reduces to

$$S(S+1) - S^2 = S \geq N. \tag{8.15}$$

This is clearly broken for all except the maximal spin length, i.e., $S = N$. This means that the individual elements of the initial superposition given by Equation 8.11 are *on their own* entangled, though the superposition of them is not. Our proposal is thus to project out one element of the superposition and so generate entanglement in the ensemble. For reasonably large N, $|c_N|^2 \approx 2^{-N}$ becomes negligible, and so, with *essentially unit efficiency*, the atomic ensemble would be projected into a many-body entangled state.

8.3.2 Generation of entanglement between the ensemble and the output

The Hamiltonian conserves excitations, while cavity decay removes excitations, so the steady state of the system is trivially calculated: no excitation in either the field or the ensemble. So, if we consider a state of definite spin length S, then the final state must be $|S,-S\rangle \otimes |0\rangle_{\text{cav}}$, where $|n\rangle_{\text{cav}}$ represents a Fock state of n photons in the cavity mode.

If we have an initial state $|S,0\rangle \otimes |0\rangle_{\text{cav}}$, then evolution under the open TC model leads to the final state $|S,-S\rangle \otimes |0\rangle_{\text{cav}}$. This means that the S excitations in the atomic ensemble must have left the system via the cavity decay, meaning that we can write the state as $|S,-S\rangle \otimes |0\rangle_{\text{cav}} \otimes |S\rangle_{\text{out}}$, where $|n\rangle_{\text{out}}$ represents the state with n photons in the cavity output channel. This is shown in Fig. 8.3, where we plot the output photon flux from the cavity, $2\kappa\langle \hat{a}^\dagger \hat{a}\rangle$, versus time, as well as the cumulative, mean output photon number, $2\kappa \int_0^t \langle \hat{a}^\dagger \hat{a}\rangle_t \, dt$. Different initial states $|S,0\rangle$ produce pulses of *precisely* S photons in the cavity output channel.

By considering the steady states above, the initial state given in Equation 8.11 will evolve to a final state (where we omit the empty cavity)

$$|m_F = 0\rangle^{\otimes N} \rightarrow \sum_{S=0}^{N} c_S \, |S,-S\rangle \otimes |S\rangle_{\text{out}} \, . \tag{8.16}$$

The open TC model thus *entangles* the state of the ensemble with the state of the cavity output channel.

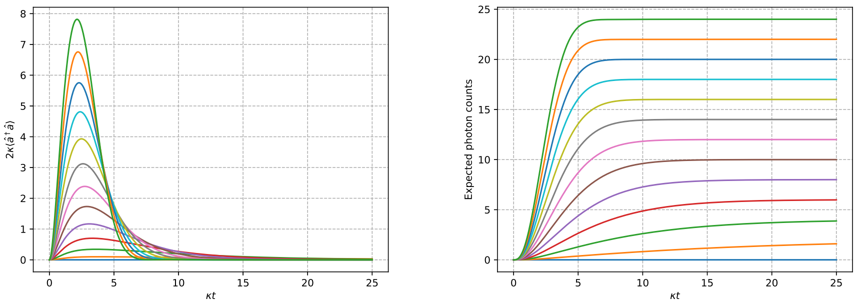

(a)

(b)

Figure 8.3: Master equation simulations of the open Tavis-Cummings model from initial states $|S,0\rangle \otimes |0\rangle_{\text{cav}}$ with S equal to even numbers from 0 to 24 (ranging from $S = 24$ as the highest curve on both plots to $S = 0$ at the bottom) with parameters $\{\omega, \omega_0, \lambda\}/\kappa = \{0.0, 0.0, 0.1\}$. Results show the output photon flux (a) over time and (b) cumulatively.

8.3.3 Collapsing the superposition

A measurement of the number of photons in the output channel, which gives a result of S photons with probability $|c_S|^2$, will collapse the state of the atomic ensemble to $|S, -S\rangle$.

A few examples of this are shown in Fig. 8.4. We use quantum Monte-Carlo trajectories [165] to simulate a monitored cavity output, with (non-Hermitian) effective Hamiltonian

$$\hat{H}_{\text{eff}} = \omega\hat{a}^\dagger\hat{a} + \omega_0\hat{S}_z + \lambda(\hat{a}\hat{S}_+ + \hat{a}^\dagger\hat{S}_-) - i\kappa\hat{a}^\dagger\hat{a}, \tag{8.17}$$

and a jump operator $\sqrt{2\kappa}\hat{a}$, corresponding to photon detection in the cavity output.

We see that a certain number of "jumps" simulated by the trajectory, corresponding to that number of photons counted in the output channel, produces a state with *definite* spin length. In the three examples shown for $N = 24$ spin-1 atoms initially prepared in the $|m_F = 0\rangle$ state, the final atomic states produced are $|12, -12\rangle$, $|8, -8\rangle$, and $|6, -6\rangle$, each of which is a highly entangled atomic state ($S \ll N$).

It is important to note that it is the measurement that produces the entanglement

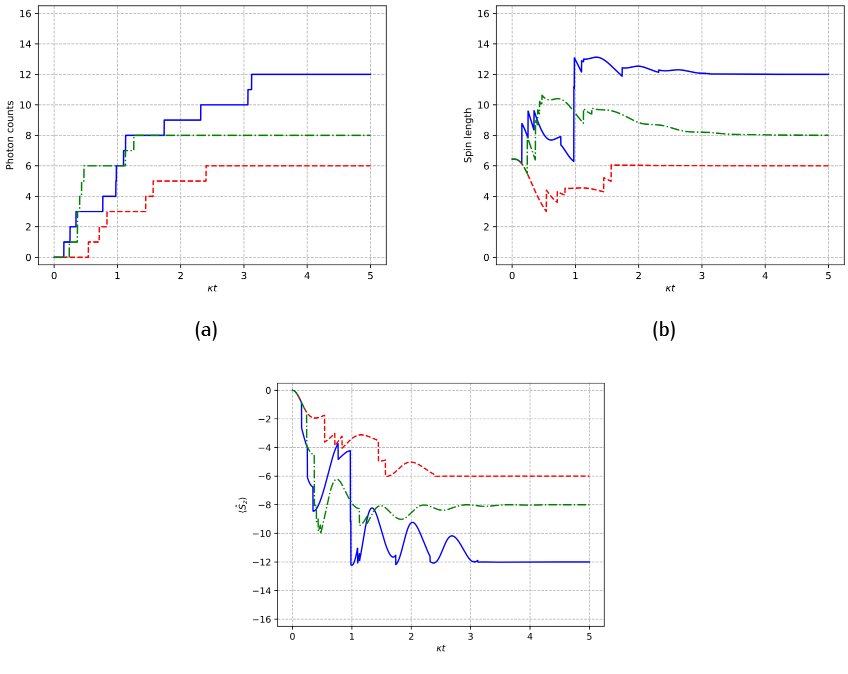

(a)

(b)

(c)

Figure 8.4: Three individual quantum Monte-Carlo trajectory simulations of the open Tavis-Cummings model for $N = 24$ spin-1 atoms initiated in the $|m_F = 0\rangle$ state with parameters $\{\omega, \omega_0, \lambda\}/\kappa = \{0.0, 0.0, 1.0\}$. Results show (a) the number of photon counts, (b) the spin length (found by taking $\langle\hat{\mathbf{S}}^2\rangle = S(S+1)$ and solving for S) and (c) $\langle\hat{S}_z\rangle$.

in the atomic ensemble rather than the interaction. The interaction instead produces entanglement between the output field and the atomic ensemble. This entanglement means that the output field contains information about the state of the atoms which our protocol accesses. The protocol is thus an example of metrological enhancement in an atomic ensemble through the measurement of an auxiliary optical system [166–170].

For $\sqrt{S}\lambda_- \lesssim \kappa/2$, the duration of this pulse is $t_{\text{pulse}} \simeq (S\lambda_-^2/\kappa)^{-1}$, while for $\sqrt{S}\lambda_- > \kappa/2$ the timescale is set simply by κ (i.e., a few times $1/\kappa$). Given the negligible initial population in the state $|N, -N\rangle$, the probability of not producing a state, $1 - |c_N|^2$, is also negligible. This protocol thus provides a simple and efficient method of producing entangled atomic states.

8.4 Metrological sensitivity of the states

8.4.1 Ideal photon counting

To calculate the average entanglement this process introduces in the ensemble, we consider the average QFI of a single run. For a perfect photodetector this is simply

$$\bar{\mathcal{F}} = \sum_{S=0}^{N} |c_S|^2 \mathcal{F}(|S, -S\rangle) \tag{8.18}$$

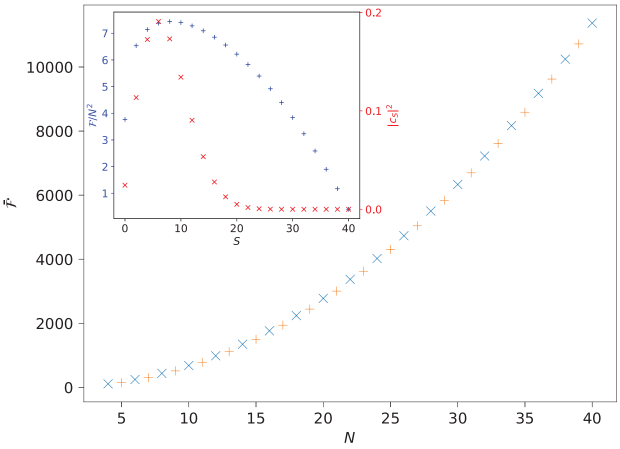

Figure 8.5: Average QFI on the generator $\hat{Q}_{xx} - \hat{Q}_{yy}$ of states $|S, -S\rangle$ weighted by initial populations $|c_S|^2$ of the states $|S, 0\rangle$ in Equation 8.11. Even and odd numbers are represented differently due to their slightly different dependence on N. The inset shows the populations and QFI of the individual states $|S, -S\rangle$ for $N = 40$.

where $\mathcal{F}(|S,-S\rangle)$ is the QFI of state $|S,-S\rangle$ with respect to the generator $\hat{Q}_{xx}-\hat{Q}_{yy}$. Figure 8.5 shows that this quantity increases with N in a quadratic fashion. For even N, a fit of the data gives the average QFI as $\bar{\mathcal{F}} = 6.52N^{2.02}$. For odd N we find $\bar{\mathcal{F}} = 5.17N^{2.09}$. The fits imply a slightly better than quadratic scaling, but we believe that this is due to the contributions of lower order terms; for sufficiently large N these should be negligible and the scaling should return to being purely quadratic. So, we find that our heralded state has optimal scaling for quantum metrology on the generator $\hat{Q}_{xx} - \hat{Q}_{yy}$. In fact, there are a range of generators for which we can show quadratic scaling. These generators are all higher order operators than the angular momentum operators, showing that this entanglement is a distinctly spinor phenomenon.

8.4.2 Realistic photon counting

Now consider the more realistic case in which we have a detector of finite photon detection efficiency η. The state resulting from our measurement scheme can then be modelled as a mixed state, i.e., given the photodetector records n photons in a single run, the resultant state can be written as

$$\rho_n = \sum_{S\geq n}^{N} p(S|n)\,|S,-S\rangle\,\langle S,-S| \tag{8.19}$$

$$\text{with} \quad p(S|n) = \frac{|c_S|^2 \begin{pmatrix} S \\ n \end{pmatrix} \eta^n(1-\eta)^{S-n}}{\sum\limits_{k\geq n}^{N} |c_k|^2 \begin{pmatrix} k \\ n \end{pmatrix} \eta^n(1-\eta)^{k-n}} \tag{8.20}$$

where the sum is only over states that can produce n or more photons.

Actually, this is somewhat of a simplification, as the times at which the photons are detected could in principle provide extra information related to the likelihood of each state. We choose to ignore this aspect of the detection process, but note that, since this information would improve knowledge of the state, using it would only enhance our scheme. We also ignore a possible dark count rate for the photodetector. However, this could be included by assigning a finite probability to the possibility of detection events being the result of dark counts.

The states given by Equation 8.19 are not perfect projections, but they do have a reduced width in S and, for $N \gg 1$, are entangled with virtual certainty, as only the state $|N,-N\rangle$ does not feature entanglement and $|c_N|^2 \sim 2^{-N} \simeq 0$. In other words, even with finite photodetector efficiency, entanglement is still produced with essentially unit efficiency.

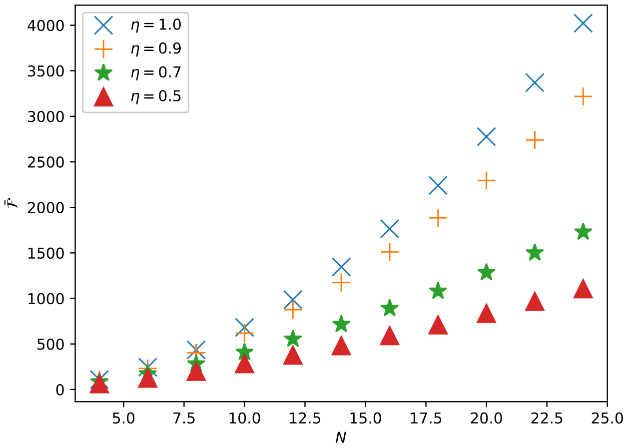

Figure 8.6: Average QFI on the generator $\hat{Q}_{xx} - \hat{Q}_{yy}$ of states ρ_n weighted by the probability $p(n)$ of measuring n photons, as given by Equations 8.21 and 8.22, for various photodetector efficiencies η.

As with the perfect detector, we can consider an average QFI where now

$$\bar{\mathcal{F}} = \sum_{n=0}^{N} p(n)\mathcal{F}(\rho_n) \tag{8.21}$$

$$\text{with} \quad p(n) = \sum_{S\geq n}^{N} |c_S|^2 \begin{pmatrix} S \\ n \end{pmatrix} \eta^n (1-\eta)^{S-n}. \tag{8.22}$$

This average is shown in Figure 8.6. The scaling of the QFI is still better than linear, but it is no longer quadratic. Nevertheless, for $\eta = 0.9$ the data is fitted by $\bar{\mathcal{F}} = 7.56N^{1.91}$, while for $\eta = 0.5$ the scaling is still $\sim N^{1.58}$.

8.4.3 Producing multiple pulses

Significantly, using an imperfect detector does not in fact rule out the possibility of Heisenberg scaling. The flexibility of our engineered atom-cavity interaction offers a straightforward means of improving our knowledge of the spin length. Following the first output pulse of photons resulting from the effective TC interaction, one can switch the polarisation of the laser field such that, in the model given in Equation 8.7, one now has $\lambda_- = 0$ and $\lambda_+ \neq 0$, corresponding to an anti-TC model. The steady states are now $|S, +S\rangle \otimes |0\rangle_{\text{cav}}$, and the resulting transfer $|S, -S\rangle \rightarrow |S, +S\rangle$ will produce an output pulse of $2S$ photons. Detection of this pulse provides a second measurement and subsequent, further narrowing of the distribution in S.

In fact, we can consider a sequence of alternating TC and anti-TC interactions, producing a corresponding sequence of pulses and measurements $\{n\} = \{n, n_1, n_2, ..., n_{i-1}\}$. The density matrix conditioned upon a further measurement of n_i photons can be written

$$\rho_{\{\,n\,\},n_i} = \sum_{S \geq S_{\text{min}}}^{N} p(S|\,\{\,n\,\}\,, n_i)\, |S, \pm S\rangle \langle S, \pm S| \tag{8.23}$$

with probabilities

$$p(S|\,\{\,n\,\}\,, n_i) = \frac{p(S|\,\{\,n\,\})\binom{2S}{n_i}\eta^{n_i}(1-\eta)^{S-n_i}}{\sum\limits_{k \geq S_{\text{min}}}^{N} p(S|\,\{\,n\,\})\binom{2k}{n_i}\eta^{n_i}(1-\eta)^{k-n_i}} \tag{8.24}$$

where S_{min} is the largest value in the set $\{\,n, n_1/2, \ldots, n_i/2\,\}$. That is, we iteratively produce a state conditioned on a sequence of binomially-distributed photon numbers.

A numerical example of such a sequence is shown in Figure 8.7 and it clearly illustrates that with each measurement we gain more knowledge about the state, narrowing the distribution in S. After enough polarisation switches and output pulses we have, with almost certainty, projected out a state of definite spin length.

Taking a sampling approach, Figure 8.8 shows that for lower efficiency more switches and their associated output pulses are necessary. However, eventually, a

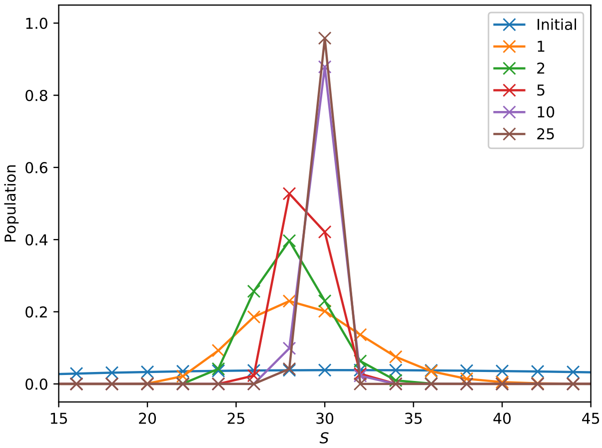

Figure 8.7: Population as a function of spin length S for a varying total number of output (multiphoton) pulses generated by a sequence of TC and anti-TC interactions. Each pulse is simulated with a binomially-distributed registered photon number using a detection efficiency of $\eta = 0.7$ and an assumed actual photon number based on a spin length $S = 30$.

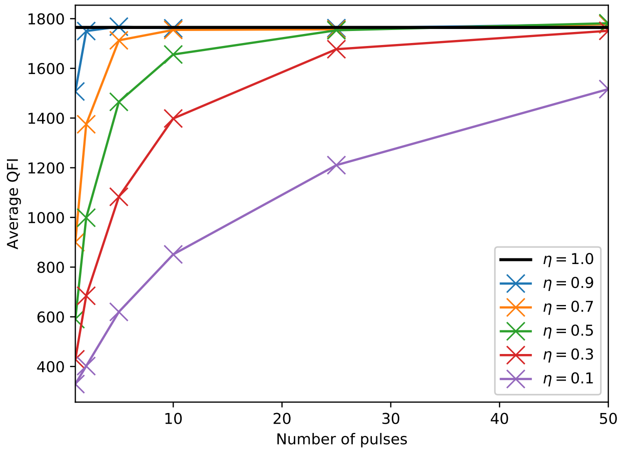

Figure 8.8: Sample mean QFI on generator $\hat{Q}_{xx} - \hat{Q}_{yy}$, for $N = 16$, of 1000 states produced by randomly selecting a spin length S and a sequence of binomially-distributed measured photons given the initial state and a photon detection efficiency η respectively.

state of definite spin length is always generated, and so the average QFI simply reduces to the result for an ideal detector. This means that, in principle, we can achieve Heisenberg level scaling for the metrological sensitivity in spite of finite photodetector efficiency.

For our scheme, we note also that if both lasers are on ($\lambda_+ = \lambda_- > 0$), then we realise an effective Dicke model, in which case the different S states are heralded by the output photon *flux*. This flux could be sensitively measured through heterodyne detection, with longer averaging times providing the mechanism for narrowing the distribution in S.

8.4.4 Potential experimental parameters

Finally, we consider briefly some potential experimental parameters and timescales. Given, e.g., cavity QED parameters $\{g, \kappa, \gamma\}/(2\pi) = \{10, 0.2, 6\}$ MHz and $N = 10^4$ atoms, one finds $t_{\text{pulse}} \simeq (S\lambda_-^2/\kappa)^{-1} \simeq 10\,\mu$s with the choice $\Omega_-/\Delta = 0.01$, and setting $S = \sqrt{N}$ (which corresponds to the most probable spin length in the initial atomic state). Hence, the timescale for preparation of the entangled state is potentially very fast, and, indeed, orders of magnitude shorter than the characteristic timescales associated with the generation of entangled spin states via collisional dynamics or adiabatic ground-state transformations in spin-1 BECs.

Chapter 9

Engineering spinor physics in a cavity QED system

Spinor physics - the study of particles with integer spin - has received relatively little attention in quantum optics. However, there is a rich recent history of extraordinary experiments within the Bose-Einstein condensate (BEC) community. The collisional dynamics inherent to such experiments offer a wide range of fascinating physics involving the interaction of spinor particles. The aim was to combine this area of atomic physics with quantum optics. We did this by derivation of engineered "collisional" dynamics using cavity-assisted Raman transitions. The methods begin with the work of Chapter 7. Taking these engineered integer-spin Dicke models and eliminating the cavity mode produces a Hamiltonian which mimics collisional dynamics. The interactions are now mediated by the exchange of photons with laser and cavity fields rather than collisions of the atoms and so offer higher energy scales, greater flexibility and the option to extend these methods well beyond what is possible with Bose-Einstein condensates. The first section of this Chapter deals with a brief introduction to the specifics of spinor Bose-Einstein condensates relevant to our proposals. The second shows the derivation of similar dynamics in a cavity QED setup, and is reworked from the Supplementary Material of [171].

9.1 Introduction to spinor Bose-Einstein condensates

Bose-Einstein condensates were briefly introduced in Section 3.3.3. Here I discuss the case where multiple magnetic sub-levels of the atom are condensed simultaneously. This gives a quantum fluid with both spatial and spin degrees of freedom. There is the possibility of using such systems to study the evolution of a spinor many-body gas, as I focus on here, but also of the coupling between the spinor and spatial degrees of freedom. The description here is kept fairly brief and focuses on the relevant limit for the rest of the thesis; for reviews see [172, 173].

9.1.1 Spinor collisions

We consider the Hamiltonian for a system of trapped spin-1 atoms

$$\begin{aligned}\hat{H} = \sum_{\alpha} \int d^3\mathbf{r} \hat{\Psi}^{\dagger}_{\alpha}(\mathbf{r}) \left(-\frac{\nabla^2}{2M} + \hat{V}(\mathbf{r}) \right) \hat{\Psi}_{\alpha}(\mathbf{r}) \\ + \sum_{\alpha,\beta,\mu,\nu} \Omega_{\alpha,\beta,\mu,\nu} \int d^3\mathbf{r} \hat{\Psi}^{\dagger}_{\alpha}(\mathbf{r}) \hat{\Psi}^{\dagger}_{\beta}(\mathbf{r}) \hat{\Psi}_{\mu}(\mathbf{r}) \hat{\Psi}_{\nu}(\mathbf{r})\end{aligned} \tag{9.1}$$

where $\hat{\Psi}_{\alpha}(\mathbf{r})$ is the annihilation operator for an atom in spin state α at a position $\mathbf{r}$, M is the mass of a single atom, $\hat{V}(\mathbf{r})$ contains the trapping potential and the magnetic fields and $\Omega_{\alpha,\beta,\mu,\nu}$ is the collisional interaction between spins.

The first term is the non-interacting part which is identical for all the spin state species. Interactions can generally be reduced to s-wave scattering collisions. These happen for atoms at the same point in space with a coupling constant to the spin-F channel of

$$g_F = \frac{4\pi\hbar^2}{M} a_F \tag{9.2}$$

where a_F is the scattering length for that channel. These scattering lengths can be manipulated making use of Feshbach resonances [172].

This interaction can be split into two types of terms: energy shifts and exchange interactions. Energy shifts are the result of collisions between the atom changing the energy of each state without changing the state of the atoms. At some point in space, a particle in state α collides with a particle in state β and one particle leaves in α and the other in β. Note that due to the exchange symmetry of indistinguishable bosons it is equivalent, and unknowable, if the particles have remained unchanged or swapped their spins. This has the effect of changing the potentials for the states, shifting their energies. Exchange interactions involve two particles colliding and changing their spin states. A particle in state α collides with a particle in state β and the particles leave in other states μ and ν.

Using the s-wave scattering conditions to calculate the coefficients for these terms, it is possible to expand out the Hamiltonian above for different spins. Defining

$$\lambda_s = \frac{g_0 + 2g_2}{3} \tag{9.3}$$

$$\lambda_a = \frac{g_2 - g_0}{3} \tag{9.4}$$

then, for spin-1 atoms, we can give form to the interactions expanding the Hamiltonian to give [174,175]

$$\begin{aligned}
\hat{H} = \sum_{\alpha} \int \hat{\Psi}^{\dagger}_{\alpha}(\mathbf{r}) \left(-\frac{\nabla^2}{2M} + \hat{V}(\mathbf{r}) \right) \hat{\Psi}_{\alpha}(\mathbf{r}) \mathrm{d}^3\mathbf{r} &+ \frac{\lambda_s}{2} \sum_{\alpha,\beta} \int \hat{\Psi}^{\dagger}_{\alpha} \hat{\Psi}^{\dagger}_{\beta} \hat{\Psi}_{\alpha} \hat{\Psi}_{\beta} \mathrm{d}^3\mathbf{r} \\
&+ \frac{\lambda_a}{2} \int \hat{\Psi}^{\dagger}_{1}(\mathbf{r}) \hat{\Psi}^{\dagger}_{1}(\mathbf{r}) \hat{\Psi}_{1}(\mathbf{r}) \hat{\Psi}_{1}(\mathbf{r}) + \hat{\Psi}^{\dagger}_{-1}(\mathbf{r}) \hat{\Psi}^{\dagger}_{-1}(\mathbf{r}) \hat{\Psi}_{-1}(\mathbf{r}) \hat{\Psi}_{-1}(\mathbf{r}) \\
&+ 2\hat{\Psi}^{\dagger}_{1}(\mathbf{r}) \hat{\Psi}^{\dagger}_{0}(\mathbf{r}) \hat{\Psi}_{1}(\mathbf{r}) \hat{\Psi}_{0}(\mathbf{r}) + 2\hat{\Psi}^{\dagger}_{-1}(\mathbf{r}) \hat{\Psi}^{\dagger}_{0}(\mathbf{r}) \hat{\Psi}_{-1}(\mathbf{r}) \hat{\Psi}_{0}(\mathbf{r}) \\
&- 2\hat{\Psi}^{\dagger}_{1}(\mathbf{r}) \hat{\Psi}^{\dagger}_{-1}(\mathbf{r}) \hat{\Psi}_{1}(\mathbf{r}) \hat{\Psi}_{-1}(\mathbf{r}) + 2\hat{\Psi}^{\dagger}_{0}(\mathbf{r}) \hat{\Psi}^{\dagger}_{0}(\mathbf{r}) \hat{\Psi}_{1}(\mathbf{r}) \hat{\Psi}_{-1}(\mathbf{r}) \\
&+ 2\hat{\Psi}^{\dagger}_{1}(\mathbf{r}) \hat{\Psi}^{\dagger}_{-1}(\mathbf{r}) \hat{\Psi}_{0}(\mathbf{r}) \hat{\Psi}_{0}(\mathbf{r}) \mathrm{d}^3\mathbf{r}.
\end{aligned} \tag{9.5}$$

The first line is symmetric under interchange of the spin component indices while the other is anti-symmetric. This means we have two parts to the Hamiltonian. The first of these treats all spins identically and so does not change the spin degree of freedom. The other deals with interactions where the form of the spin is important and thus contains all non-global shifts to the energy levels and spin-changing interactions.

9.1.2 Single-mode approximation

In many species, $g_2 \sim g_0$ and so $\lambda_s \gg \lambda_a$. In others, the scattering lengths can be manipulated to meet that criterion. In those cases, the system is primarily ambivalent as to the spin degree of freedom as the Hamiltonian is dominated by the symmetric part. This means we can assume that the spatial degree of freedom is defined solely by the symmetric part of the wavefunction, and so is the same for all modes. This means it decouples from the spin degree of freedom [175]. This is called the *single-mode approximation*. Mathematically, we show this as

$$\hat{\Psi}_{\alpha}(\mathbf{r}) \rightarrow \hat{b}_{\alpha} \phi(\mathbf{r}). \tag{9.6}$$

We make substitutions

$$\hat{n}_{\alpha} = \hat{b}^{\dagger}_{\alpha} \hat{b}_{\alpha} \quad \text{and} \quad \hat{N} = \sum_{\alpha} \hat{n}_{\alpha} \tag{9.7}$$

and use the angular momentum operators instead of the bosonic mode operators using the relations described in Section 3.4.7. The symmetric part of the Hamiltonian for the spin degree of freedom

$$\hat{H}_s = \mu\hat{N} - \lambda_s\hat{N}(\hat{N}-1) \tag{9.8}$$

where we have introduced the chemical potential

$$\mu\phi \equiv \left(-\frac{\nabla^2}{2M} + \hat{V} + \lambda_s' N|\phi|^2\right)\phi \tag{9.9}$$

and the collisional spinor interaction energy per particle integrated over the condensate

$$\lambda_i' \equiv \frac{\lambda_i}{2}\int \mathrm{d}^3\mathbf{r}|\phi(\mathbf{r})|^4. \tag{9.10}$$

The anti-symmetric part is now

$$\hat{H}_a = \lambda_a'\left(\hat{\mathbf{S}}^2 - 2\hat{N}\right). \tag{9.11}$$

If we take the particle number to be conserved, then we can drop the operator notation such that $\hat{N} \to N$ and so terms related to the particle number reduce to shifts to the vacuum energy. The full Hamiltonian can then be written

$$\hat{H} = \lambda_a'\left(\hat{S}_x^2 + \hat{S}_y^2 + \hat{S}_z^2\right). \tag{9.12}$$

Under the single-mode approximation, the complicated dynamics of the spatial and spin degrees of freedom reduces to an extremely simple form.

The presence of a magnetic field adds linear and quadratic Zeeman shifts

$$\hat{H} = \lambda_a'\left(\hat{S}_x^2 + \hat{S}_y^2 + \hat{S}_z^2\right) + \omega_z\hat{S}_z + q\hat{n}_0. \tag{9.13}$$

The interplay of the various parameters leads to a rich variety of ground states [124, 150–152, 159], which we take advantage of for our proposal in Chapter 11. It is also worth noting that this Hamiltonian conserves $\hat{S}_z$ and so both $\langle\hat{S}_z^2\rangle$ and $\langle\hat{S}_z\rangle$ must be constants of the motion. This means we can omit them from the Hamiltonian giving us

$$\hat{H} = \lambda_a'\left(\hat{S}_x^2 + \hat{S}_y^2\right) + q\hat{n}_0. \tag{9.14}$$

This Hamiltonian describes the evolution of a spinor Bose-Einstein condensate in a magnetic field under the single-mode approximation.

Our aim was to emulate this system by engineering an effective Hamiltonian which acts in the same way. However, instead of collisions, in our proposal spin-exchange interactions are mediated by photons.

9.2 Cavity engineering of the collisional Hamiltonian

To emulate the spinor collisional Hamiltonian, we start with the spin-F Dicke model Hamiltonian we derived in Section 7.1.1

$$\hat{H} = \omega \hat{a}^\dagger \hat{a} + \omega_0 \hat{S}_z + \frac{\lambda_-}{\sqrt{2FN}}(\hat{S}_+ \hat{a} + \hat{S}_- \hat{a}^\dagger) + \frac{\lambda_+}{\sqrt{2FN}}(\hat{S}_- \hat{a} + \hat{S}_+ \hat{a}^\dagger). \tag{9.15}$$

We want to move to a limit where the cavity can be adiabatically eliminated. This could be because the energy of creating a single photon is prohibitively high - comparatively large ω - or that the photons leave the cavity immediately - comparatively large κ - or more specifically the limit $\sqrt{\omega^2 + \kappa^2} \gg \omega_0, \lambda_\pm$.

We split our Hamiltonian into two parts $\hat{H} = \hat{H}_0 + \hat{H}_i$ where

$$\hat{H}_0 = \omega \hat{a}^\dagger \hat{a} + \omega_0 \hat{S}_z \tag{9.16}$$

$$\hat{H}_i = \frac{\lambda_-}{\sqrt{2FN}}(\hat{S}_+ \hat{a} + \hat{S}_- \hat{a}^\dagger) + \frac{\lambda_+}{\sqrt{2FN}}(\hat{S}_- \hat{a} + \hat{S}_+ \hat{a}^\dagger) \tag{9.17}$$

and move to the interaction picture defined by

$$\rho'(t) = \mathrm{e}^{i\hat{H}_0 t} \rho(t) \mathrm{e}^{-i\hat{H}_0 t}. \tag{9.18}$$

It follows that

$$\frac{\partial \rho'}{\partial t} = -i[\hat{H}_i', \rho'] + \mathcal{L}_c \rho'(t) \tag{9.19}$$

where

$$\mathcal{L}_c \rho \equiv \kappa \left(2\hat{a}\rho\hat{a}^\dagger - \hat{a}^\dagger \hat{a} \rho - \rho \hat{a}^\dagger \hat{a} \right) \tag{9.20}$$

and our interaction Hamiltonian is

$$\begin{aligned} \hat{H}_i' &= \mathrm{e}^{i\hat{H}_0 t} H_i \mathrm{e}^{-i\hat{H}_0 t} \\ &= \frac{1}{\sqrt{2FN}} \left[\hat{a} \mathrm{e}^{-i\omega t} (\lambda_- \hat{S}_+ \mathrm{e}^{i\omega_0 t} + \lambda_+ \hat{S}_- \mathrm{e}^{-i\omega_0 t}) + \hat{a}^\dagger \mathrm{e}^{i\omega t} (\lambda_- \hat{S}_- \mathrm{e}^{-i\omega_0 t} + \lambda_+ \hat{S}_+ \mathrm{e}^{i\omega_0 t}) \right] \\ &= \hat{a} \mathrm{e}^{-i\omega t} \hat{X}(t) + \hat{a}^\dagger \mathrm{e}^{i\omega t} \hat{X}^\dagger(t) \end{aligned} \tag{9.21}$$

where

$$\hat{X}(t) = \frac{\lambda_-}{\sqrt{2FN}} \hat{S}_- \mathrm{e}^{-i\omega_0 t} + \frac{\lambda_+}{\sqrt{2FN}} \hat{S}_+ \mathrm{e}^{i\omega_0 t}. \tag{9.22}$$

We want $\rho_s' = \mathrm{tr}_c\{\rho'\}$, and so, in the second-order Born-Markov approximation, we have that

$$\frac{\partial \rho_s'}{\partial t} = -\int_0^t \mathrm{d}t' \mathrm{tr}_c \left\{ \left[\hat{H}_i', \mathrm{e}^{\mathcal{L}_c(t-t')} [\hat{H}_i'(t'), \rho_s'(t') \otimes \rho_c'(t')] \right] \right\}. \tag{9.23}$$

Expanding this out, neglecting terms with $\hat{a}\hat{a}$ and $\hat{a}^\dagger\hat{a}^\dagger$ due to the unlikeliness of two photons in the cavity mode, gives

$$\begin{aligned}\frac{\partial \rho_s'}{\partial t} = -\int_0^t \mathrm{d}t'\mathrm{tr}_c\{ &+ \hat{a}\mathrm{e}^{-i\omega t}\hat{X}^\dagger(t)\mathrm{e}^{\mathcal{L}_c(t-t')}\hat{a}^\dagger\mathrm{e}^{i\omega t'}\hat{X}(t')\rho_s'(t')\otimes\rho_c'(t') \\ &- \hat{a}\mathrm{e}^{-i\omega t}\hat{X}^\dagger(t)\mathrm{e}^{\mathcal{L}_c(t-t')}\rho_s'(t')\otimes\rho_c'(t')\hat{a}^\dagger\mathrm{e}^{i\omega t'}\hat{X}(t') \\ &- \mathrm{e}^{\mathcal{L}_c(t-t')}\hat{a}^\dagger\mathrm{e}^{i\omega t'}\hat{X}(t')\rho_s'(t')\otimes\rho_c'(t')\hat{a}\mathrm{e}^{-i\omega t}\hat{X}(t) \\ &+ \mathrm{e}^{\mathcal{L}_c(t-t')}\rho_s'(t')\otimes\rho_c'(t')\hat{a}^\dagger\mathrm{e}^{i\omega t'}\hat{X}(t')\hat{a}\mathrm{e}^{-i\omega t}\hat{X}^\dagger(t) \\ &+ \hat{a}^\dagger\mathrm{e}^{i\omega t}\hat{X}(t)\mathrm{e}^{\mathcal{L}_c(t-t')}\hat{a}\mathrm{e}^{-i\omega t'}\hat{X}^\dagger(t')\rho_s'(t')\otimes\rho_c'(t') \\ &- \hat{a}^\dagger\mathrm{e}^{i\omega t}\hat{X}(t)\mathrm{e}^{\mathcal{L}_c(t-t')}\rho_s'(t')\otimes\rho_c'(t')\hat{a}\mathrm{e}^{-i\omega t'}\hat{X}^\dagger(t') \\ &- \mathrm{e}^{\mathcal{L}_c(t-t')}\hat{a}\mathrm{e}^{-i\omega t'}\hat{X}^\dagger(t')\rho_s'(t')\otimes\rho_c'(t')\hat{a}^\dagger\mathrm{e}^{i\omega t}\hat{X}(t) \\ &+ \mathrm{e}^{\mathcal{L}_c(t-t')}\rho_s'(t')\otimes\rho_c'(t')\hat{a}\mathrm{e}^{-i\omega t'}\hat{X}^\dagger(t')\hat{a}^\dagger\mathrm{e}^{i\omega t}\hat{X}(t)\}. \end{aligned} \tag{9.24}$$

We can then draw several terms out of the trace and, using the cyclical definition of the trace (i.e. $\mathrm{tr}(ABC) \equiv \mathrm{tr}(BCA)$), rearrange to

$$\begin{aligned}\frac{\partial \rho_s'}{\partial t} = -\int_0^t \mathrm{d}t' &\hat{X}^\dagger(t)\hat{X}(t')\rho_s'(t')\mathrm{tr}_c\{\hat{a}\mathrm{e}^{\mathcal{L}_c(t-t')}\hat{a}^\dagger\rho_c'(t')\}\mathrm{e}^{-i\omega(t-t')} \\ &-\hat{X}^\dagger(t)\rho_s'(t')\hat{X}(t')\mathrm{tr}_c\{\hat{a}\mathrm{e}^{\mathcal{L}_c(t-t')}\rho_c'(t')\hat{a}^\dagger\}\mathrm{e}^{-i\omega(t-t')} \\ &-\hat{X}(t')\rho_s'(t')\hat{X}^\dagger(t)\mathrm{tr}_c\{\hat{a}\mathrm{e}^{\mathcal{L}_c(t-t')}\hat{a}^\dagger\rho_c'(t')\}\mathrm{e}^{-i\omega(t-t')} \\ &+\rho_s'(t')\hat{X}(t')\hat{X}^\dagger(t)\mathrm{tr}_c\{\hat{a}\mathrm{e}^{\mathcal{L}_c(t-t')}\rho_c'(t')\hat{a}^\dagger\}\mathrm{e}^{-i\omega(t-t')} \\ &+\hat{X}(t)\hat{X}^\dagger(t')\rho_s'(t')\mathrm{tr}_c\{\hat{a}^\dagger\mathrm{e}^{\mathcal{L}_c(t-t')}\hat{a}\rho_c'(t')\}\mathrm{e}^{i\omega(t-t')} \\ &-\hat{X}(t)\rho_s'(t')\hat{X}^\dagger(t')\mathrm{tr}_c\{\hat{a}^\dagger\mathrm{e}^{\mathcal{L}_c(t-t')}\rho_c'(t')\hat{a}\}\mathrm{e}^{i\omega(t-t')} \\ &-\hat{X}^\dagger(t')\rho_s'(t')\hat{X}(t)\mathrm{tr}_c\{\hat{a}^\dagger\mathrm{e}^{\mathcal{L}_c(t-t')}\hat{a}\rho_c'(t')\}\mathrm{e}^{i\omega(t-t')} \\ &+\rho_s'(t')\hat{X}^\dagger(t')\hat{X}(t)\mathrm{tr}_c\{\hat{a}^\dagger\mathrm{e}^{\mathcal{L}_c(t-t')}\rho_c'(t')\hat{a}\}\mathrm{e}^{i\omega(t-t')}. \end{aligned} \tag{9.25}$$

We can then use

$$\mathrm{tr}_c\{\hat{a}\mathrm{e}^{\mathcal{L}_c(t-t')}\hat{a}^\dagger\rho_c'(t')\} = \langle\hat{a}(t)\hat{a}^\dagger(t')\rangle = \mathrm{e}^{-\kappa(t-t')} \tag{9.26}$$

$$\mathrm{tr}_c\{\hat{a}\mathrm{e}^{\mathcal{L}_c(t-t')}\rho_c'(t')\hat{a}^\dagger\} = \langle\hat{a}^\dagger(t')\hat{a}(t)\rangle = 0 \tag{9.27}$$

$$\mathrm{tr}_c\{\hat{a}^\dagger\mathrm{e}^{\mathcal{L}_c(t-t')}\hat{a}\rho_c'(t')\} = \langle\hat{a}^\dagger(t)\hat{a}(t')\rangle = 0 \tag{9.28}$$

$$\mathrm{tr}_c\{\hat{a}^\dagger\mathrm{e}^{\mathcal{L}_c(t-t')}\rho_c'(t')\hat{a}\} = \langle\hat{a}(t')\hat{a}^\dagger(t)\rangle = \mathrm{e}^{-\kappa(t-t')} \tag{9.29}$$

to simplify the integral, where we assume that the cavity mode is essentially in the vacuum state.

We further assume that we can set $\hat{X}(t') \approx \hat{X}(t)$ and $\rho_s'(t') \approx \rho_s'(t)$, so that it only remains to evaluate

$$\int_0^t \mathrm{d}t' \mathrm{e}^{-(\kappa+i\omega)(t-t')} = \frac{1}{\kappa+i\omega}\left(1-\mathrm{e}^{-(\kappa+i\omega)t}\right) \rightarrow \frac{1}{\kappa+i\omega}, \tag{9.30}$$

where we assume t is large enough to neglect the exponential. Thus, we have

$$\begin{aligned}\frac{\partial\rho_s'}{\partial t} =& -\frac{1}{\kappa+i\omega}\hat{X}^\dagger(t)\hat{X}(t)\rho_s'(t) + \frac{1}{\kappa+i\omega}\hat{X}(t)\rho_s'(t)\hat{X}^\dagger(t) \\ &\qquad + \frac{1}{\kappa-i\omega}\hat{X}(t)\rho_s'(t)\hat{X}^\dagger(t) - \frac{1}{\kappa-i\omega}\rho_s'(t)\hat{X}^\dagger(t)\hat{X}(t) \\ =& \frac{2\kappa}{\kappa^2+\omega^2}\hat{X}(t)\rho_s'(t)\hat{X}^\dagger(t) - \frac{\kappa-i\omega}{\kappa^2+\omega^2}\hat{X}^\dagger(t)\hat{X}(t)\rho_s'(t) - \frac{\kappa+i\omega}{\kappa^2+\omega^2}\rho_s'(t)\hat{X}^\dagger(t)\hat{X}(t) \\ =& i[\frac{\omega}{\kappa^2+\omega^2}\hat{X}^\dagger(t)\hat{X}(t), \rho_s'(t)] \\ &+ \frac{\kappa}{\kappa^2+\omega^2}\left(2\hat{X}(t)\rho_s'(t)\hat{X}^\dagger(t) - \hat{X}^\dagger(t)\hat{X}(t)\rho_s'(t) - \rho_s'(t)\hat{X}^\dagger(t)\hat{X}(t)\right). \end{aligned} \tag{9.31}$$

We rotate back out of the interaction picture to give

$$\frac{\partial\rho_s}{\partial t} = -i[\hat{H},\rho_s] + \frac{\kappa}{\kappa^2+\omega^2}(2\hat{X}\rho_s\hat{X}^\dagger - \hat{X}^\dagger\hat{X}\rho_s - \rho_s\hat{X}^\dagger\hat{X}) \tag{9.32}$$

where

$$\hat{H} = \omega_0\hat{S}_z - \frac{\omega}{\kappa^2+\omega^2}\hat{X}^\dagger\hat{X}, \qquad \hat{X} = \frac{\lambda_-}{\sqrt{2FN}}\hat{S}_- + \frac{\lambda_+}{\sqrt{2FN}}\hat{S}_+. \tag{9.33}$$

Substituting in $\hat{X}$, assuming $\lambda_\pm$ are real, we have the Hamiltonian

$$\begin{aligned}\hat{H} &= \omega_0\hat{S}_z - \frac{\omega}{2FN(\kappa^2+\omega^2)}(\lambda_-\hat{S}_+ + \lambda_+\hat{S}_-)(\lambda_-\hat{S}_- + \lambda_+\hat{S}_+) \\ &= \omega_0\hat{S}_z - \frac{\omega}{2FN(\kappa^2+\omega^2)}\left[(\lambda_- + \lambda_+)^2\hat{S}_x^2 + (\lambda_- - \lambda_+)^2\hat{S}_y^2 + (\lambda_-^2 - \lambda_+^2)\hat{S}_z\right]. \end{aligned} \tag{9.34}$$

If we take $\lambda_+ = 0$ then we have a master equation

$$\frac{\partial\rho_s}{\partial t} = -i[\hat{H},\rho_s] + \frac{\kappa\lambda_-^2}{2FN(\kappa^2+\omega^2)}(2\hat{S}_-\rho_s\hat{S}_+ - \hat{S}_+\hat{S}_-\rho_s - \rho_s\hat{S}_+\hat{S}_-) \tag{9.35}$$

with an effective Hamiltonian that emulates the spinor collisional Hamiltonian

$$\hat{H} = \omega_0'\hat{S}_z + \frac{\Lambda}{2FN}(\hat{S}_x^2 + \hat{S}_y^2) \tag{9.36}$$

with parameters

$$\Lambda = -\frac{\omega\lambda_-^2}{\omega^2+\kappa^2}, \quad \omega_0' = \omega_0 + \frac{\Lambda}{2FN}, \quad \Gamma = -\frac{\kappa}{\omega}\Lambda. \tag{9.37}$$

For spin-1 atoms, we can add an effective quadratic Zeeman shift to this Hamiltonian with the addition of a weak $\pi-$polarised laser field acting near the $F' = 1$ line. The transition $|F = 1, m_F = 0\rangle \leftrightarrow |F' = 1, m'_F = 0\rangle$ is forbidden and so such a field does not shift $|0\rangle$ but does add light shifts to $|\pm1\rangle$. Due to the symmetry of the dipole operator, the light shifts added to $|\pm1\rangle$ are equal in magnitude and sign, exactly like a quadratic Zeeman shift. This means that we can emulate the full range of the collisional Hamiltonian in a magnetic field for a spinor BEC under the single-mode approximation.

Chapter 10

Spin-nematic squeezing via cavity-assisted Raman transitions

Spin squeezing is a generic term for introducing certain types of quantum correlations between an atoms in an ensemble. Numerous experiments have been carried out showing that these spin squeezed states feature entanglement and properties useful for quantum metrology. While these experiments have initially focussed on two-level systems confined to the surface of the Bloch sphere, there are viable alternatives using spinor systems that have no such limitations. This Chapter discusses our proposal to produce one such type of squeezing: spin-nematic squeezing. Following experiments in spinor Bose-Einstein condensates, our proposal details how we can emulate such experiments on much faster timescales. This work is presented in the form of a Letter published in Physical Review Letters. It has been reformatted for this thesis, with the Letter separated into sections, minor changes to some figures and notation and spelling altered to provide consistency throughout the thesis, and parts of the supplemental material relevant to the spin-nematic squeezing included in the text, but is available in its original form at https://journals.aps.org/prl/abstract/10.1103/PhysRevLett.119.213601.

10.1 Introduction

Gases of ultracold Bose atoms possessing internal spin degrees of freedom - spinor Bose gases - offer a remarkable variety of possibilities for the investigation of quantum fluids, in contexts that include, for example, magnetism, superfluidity, and many-body quantum dynamics [172,173]. In this latter context, tremendous experimental progress has occurred in recent years based upon collision-induced spin-mixing dynamics in spinor Bose-Einstein condensates (BECs) [14,95,99,100,124,154–159,176–186]. Such systems have allowed for the generation of quantum spin squeezing and entangled states [14,99,100,124,154–158,160,187] following a range of proposals [146,149–151, 188,189] as well as the study of quantum phase transitions [124,159,180–182,186] and the parametric amplification of quantum spin fluctuations [158,183–185,190].

10.1.1 Spinor Bose-Einstein condensates

Spinor BECs in which atoms in all magnetic sublevels of a single hyperfine ground state (e.g., the $F = 1$ ground state of ^{87}Rb) are condensed correspond to ensembles of integer-spin particles. For small, tightly confined condensates, one may assume that the different atomic states have the same spatial wavefunction - the single-mode approximation - after which one can show that the collisional spin dynamics is described by a Hamiltonian of the form $\lambda\hat{\mathbf{S}}^2$ where $\hat{\mathbf{S}} = (\hat{S}_x, \hat{S}_y, \hat{S}_z)$ is the total spin vector (operator) and λ is the collisional spin interaction energy per particle integrated over the condensate [174,175]. The spinor dynamical rate is $c = 2N\lambda$, where N is the number of atoms, and is typically on the order of 10 Hz for 40,000 ^{87}Rb atoms [14]. If the longitudinal magnetisation $\langle\hat{S}_z\rangle$ is a constant of the motion (e.g., zero), then this Hamiltonian can be reduced further to $\lambda(\hat{S}_x^2 + \hat{S}_y^2)$. With the addition of a magnetic field, the Hamiltonian gains a linear Zeeman shift $p\hat{S}_z$ (which can also be assumed to be a constant of the motion) and a quadratic Zeeman shift $q\hat{N}_0$, where $\hat{N}_0$ is the population in the $m = 0$ state. The ratio q/c describes a rich phase diagram, with highly entangled ground states in several limits [124,150,151,159]. In particular, if $|q| \ll c > 0$, the ground state is the spin singlet state[44], which has fundamental interest due to its high entanglement but also applications ranging from precision measurements [191] to no-classical solution quantum information processing [192]. In addition, the transitions between these different phases are of interest with respect to the Kibble-Zurek mechanism [186,193,194].

10.1.2 Summary of the Chapter

In this Chapter, we propose an alternative scheme to producing spin-mixing dynamics in a gas of integer-spin atoms that uses cavity-mediated Raman transitions to

---

[44] A proposal to make use of our schemes to produce the spin singlet makes up Chapter 11 of this thesis.

engineer the required spinor dynamics. Our proposal borrows from earlier schemes for engineering effective Dicke models of collective two-level-atom ensembles coupled strongly to a quantised cavity mode [53, 161, 162] but considers an arguably simpler configuration and limit, which yields a Dicke model for integer-spin (alkali) atoms. This approach has in fact been demonstrated very recently in a study of non-equilibrium phase transitions in this model [71]. In the dispersive limit of this model, where the cavity mode is only virtually excited, the resulting Hamiltonian mimics collisional interactions in a spinor BEC.

10.2 Model

We consider an ensemble of alkali atoms tightly confined (e.g., by a three-dimensional optical lattice) inside a high-finesse optical cavity. The atomic ensemble is considered dilute enough to exclude direct atom-atom interactions, while the atoms are coupled uniformly to cavity and laser fields. As illustrated in Figure 10.1, we consider a scheme of cavity-assisted Raman transitions in which the fields are very far detuned from the relevant excited-state manifold. Here, instead of isolating effective spin-1/2 systems [81], we consider transitions within a complete hyperfine ground state, in this instance, the $F = 1$ ground state of ^{87}Rb. Adiabatic elimination of the atomic excited states then creates an effective model for an ensemble of spin-1 atoms coupled to a cavity mode (see Section 7.1.2 for the full derivation).

In the limit that the detunings of the fields are very large - in particular, much larger than the energy separations of the excited-state hyperfine levels (e.g., as

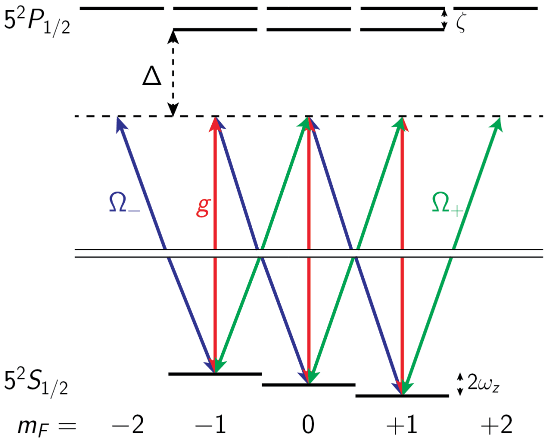

Figure 10.1: Level diagram for the implementation of an effective Dicke model using the $F = 1$ ground state of ^{87}Rb. Interactions are engineered via Raman transitions on the D_1 line mediated by a cavity mode (blue dashed line) and σ_+- (green dotted line) or σ_-- (red dot-dashed line) polarised laser fields.

in [71], where the detuning is 127 GHz) - then the internal structure of the excited-state manifold becomes unimportant, and symmetries in the dipole operator cause the effective Hamiltonian to simplify greatly. Considering an open quantum system, with the cavity field decay rate given by κ (but atomic spontaneous emission neglected due to the large detuning), this model is described by the master equation for the atom-field density operator ρ:

$$\dot{\rho} = -i[\hat{H}, \rho] + \kappa \mathcal{D}[\hat{a}]\rho, \tag{10.1}$$

where $\hat{a}$ is the cavity mode annihilation operator, $\mathcal{D}[\hat{a}]\rho = 2\hat{a}\rho\hat{a}^\dagger - \rho\hat{a}^\dagger\hat{a} - \hat{a}^\dagger\hat{a}\rho$, and

$$\hat{H} = \omega\hat{a}^\dagger\hat{a} + \omega_0\hat{S}_z + \frac{\lambda_-}{\sqrt{2N}}(\hat{a}\hat{S}_+ + \hat{a}^\dagger\hat{S}_-) + \frac{\lambda_+}{\sqrt{2N}}(\hat{a}\hat{S}_- + \hat{a}^\dagger\hat{S}_+). \tag{10.2}$$

Here, $\hat{S}_\pm$ are the spin-1 collective raising and lowering operators, while the coefficients of the various terms (for the $F = 1$ manifold in ^{87}Rb coupled via the D_1 line) are given by

$$\omega = \omega_c - \frac{\omega_- + \omega_+}{2} + \frac{Ng^2}{3\Delta} \tag{10.3}$$

$$\omega_0 = \omega_z - \frac{\omega_- - \omega_+}{2} + \frac{\Omega_+^2 - \Omega_-^2}{24\Delta} \tag{10.4}$$

$$\lambda_\pm = \frac{\sqrt{N}g\Omega_\pm}{12\Delta}. \tag{10.5}$$

Here ω_c is the frequency of the cavity mode, $\omega_\pm$ ($\Omega_\pm$) are the bare frequencies (Rabi frequencies) of the $\sigma_\pm$-polarised laser fields, ω_z is the Zeeman splitting of the $F = 1$ levels (due to an applied magnetic field, if present), g is the single-atom-cavity coupling strength (for the ^{87}Rb D_2 line cycling transition), and Δ is the detuning of the fields from the atomic resonance.

This configuration provides a "clean" and tuneable system with which to study the Dicke model, as demonstrated in [71]. In particular, it has the independence of couplings $\lambda_\pm$ not present in BEC formulations of the Dicke model [67–70, 76], while it also avoids a non-linear coupling term of the form $\hat{S}_z\hat{a}^\dagger\hat{a}$ that features in all the current spin-1/2 versions of the Dicke model [53, 66–68, 78, 79, 81, 144]. We note that it can also be applied to other hyperfine ground states in alkali atoms, enabling, e.g., tuneable interactions for ensembles of effective spin-2 (^{87}Rb or ^{85}Rb), -3 (^{85}Rb, ^{133}Cs), or -4 (^{133}Cs) atoms.

While most previous work has considered many-body cavity QED with two-level systems [65, 195], the generalisation to integer-spin ensembles offers a range of interesting physics not available to spin-1/2 systems. Integer spins have more degrees of freedom, which means that there are different ways to manipulate excitations and constrain the state. In particular, a coherent ensemble of integer spins is not limited to the surface of the angular momentum Bloch sphere. This allows for novel entangled states such as the spin singlet, two-mode squeezed spin states or, as discussed in more detail below, the redistribution of quantum noise into degrees of freedom that are simply not present in two-level systems [147,148,196].

10.3 Tracing out the cavity mode

We now consider the dispersive limit in which the Raman transitions are themselves off-resonant, i.e., $\omega \gg \omega_0, \lambda_\pm$, in which case we can also adiabatically eliminate the cavity mode to yield the reduced master equation

$$\dot{\rho} = -i[\hat{H}, \rho] + \frac{\kappa}{2N(\omega^2 + \kappa^2)} \mathcal{D}[\lambda_- \hat{S}_- + \lambda_+ \hat{S}_+]\rho \tag{10.6}$$

with

$$\hat{H} = \left[\omega_0 - \frac{\omega(\lambda_-^2 - \lambda_+^2)}{2N(\omega^2 + \kappa^2)}\right] \hat{S}_z - \frac{\omega}{2N(\omega^2 + \kappa^2)} \left[(\lambda_- + \lambda_+)^2 \hat{S}_x^2 + (\lambda_- - \lambda_+)^2 \hat{S}_y^2\right]. \tag{10.7}$$

If we set $\lambda_+ = 0$ and $\lambda_- = \lambda$ then Equation 10.6 becomes

$$\dot{\rho} = -i[\hat{H}, \rho] + \frac{\Gamma}{2N} \mathcal{D}[\hat{S}_-]\rho \tag{10.8}$$

where

$$\hat{H} = \omega_0' \hat{S}_z + \frac{\Lambda}{2N}(\hat{S}_x^2 + \hat{S}_y^2) \tag{10.9}$$

with parameters given by

$$\omega_0' = \omega_0 + \frac{\Lambda}{2N}, \quad \Lambda = -\frac{\omega \lambda^2}{\omega^2 + \kappa^2}, \quad \Gamma = -\frac{\kappa}{\omega}\Lambda. \tag{10.10}$$

Note that, by choosing the sign of ω, it is possible to produce ferromagnetic or anti-ferromagnetic behaviour with the same atomic species. An artificial quadratic Zeeman shift could also be added to the system by, for example, a weak π-polarised laser field acting near the $F' = 1$ line in the excited manifold. Then, in the limit that $\Gamma/\Lambda \ll 1$, the atoms will undergo spin-mixing interactions with dynamics of the sort found in spinor BECs. However, here the relevant dynamical rate is set by Raman transition rates, light shifts, and detunings and can therefore be orders of magnitude larger than in spinor BECs. Consider, e.g., the feasible experimental parameters $\{g, \kappa, \gamma\}/2(\pi) = \{10, 0.2, 6\}$ MHz (see, e.g., [71,141,142]), where γ is the atomic spontaneous emission linewidth. With $N = 10^4$ atoms, values of $\lambda/(2\pi) \approx 200$ kHz are then readily achievable, which, with $\omega/(2\pi) \approx 4$ MHz, lead to $\Lambda/(2\pi) \approx 10$ kHz and $\Gamma = 0.05\Lambda$. This means that such a system can emulate the dynamics of a spinor BEC but orders of magnitude faster.

This Hamiltonian gives the opportunity to study a range of models, such as the Lipkin-Meshkov-Glick model, where, unlike in the spin-1/2 case, the spin-1 case features quantum chaotic behaviour [197]. Similar studies have shown that spin-2 models can offer very different dynamics again [198].

The methods described above are not limited to emulations of spinor BEC physics. Since this is an open system, there is also flexibility to deliberately engineer a particular dissipative evolution or monitor the cavity output to gain information about the evolution without destroying the spinor gas[45].

It is also possible to produce Hamiltonians which do not naturally arise in spinor BECs. For example, by setting $\lambda_- = \lambda_+$ we obtain a Hamiltonian $\sim \hat{S}_x^2$, which produces squeezing via one-axis twisting in two-level systems [19, 93, 94, 96, 97, 103]. By adding more cavity and laser modes, an even wider range of Hamiltonians is possible [162,199], with, for example, the possibility of a two-axis twisting Hamiltonian $\sim \hat{S}_x^2 - \hat{S}_y^2$ [19], which can offer Heisenberg limited metrology, but has yet to be implemented experimentally. Such systems with spin-1 (or higher) particles offer the same squeezing possibilities but should also allow further novel, many-body ground states and dynamical phenomena.

The principle behind our scheme could also be applied to the emerging field of quantum simulation with cold atoms coupled to a photonic crystal waveguide [200]. Atoms coupled to the waveguide, but with the atomic resonance frequency located within a photonic band gap, enable localised excitations at the atom trapping sites, while the tunnelling of excitations between neighbouring sites produces effective atom-atom interactions. While work to date has focussed on spin-1/2 systems, the application of our approach should enable the generalisation of this work to integer-spin lattice models with engineered interactions that could be tuned in form, strength, and range, allowing, for example, the exploration of Haldane physics [201].

10.4 Generation of spin-nematic squeezing

Now, we consider an example of how our scheme can be used to emulate spinor BEC physics. In particular, we consider the model given by Equation 10.8 and the preparation of "spin-nematic squeezing" in an ensemble of spin-1 atoms that are initially prepared in the $m = 0$ sublevel [14,15]. With a suitable choice of microscopic parameters, it is possible to set $\omega_0' = 0$ (or at least approximately so). We note, however, that initially $\langle \hat{S}_z \rangle = 0$, and since $\hat{S}_z$ is conserved by the Hamiltonian, this term should not have any significant impact on the evolution, provided that the cavity-

---

[45] Chapter 8 looks at using the cavity output from a spin-1 many-body cavity QED system to herald entanglement within the ensemble.

mediated damping of the spin (which does not conserve $\hat{S}_z$) is weak, i.e., $\kappa \ll \omega$, which means $\Gamma \ll \Lambda$. With this condition met, the Hamiltonian is an active generator of spin-nematic squeezing.

Spin squeezing is a well-established method to produce a metrological enhancement (for reviews, see [20, 22]). In particular, atom interferometers can be used for precision measurements of acceleration, time, rotation, and, potentially, even gravitational waves [89]. If the input states to these interferometers are uncorrelated states of N atoms, then the precision of the measurement is limited by the standard quantum limit, which scales as $1/\sqrt{N}$. However, by generating suitable entanglement within the atomic ensemble, it is possible to exceed this and approach the Heisenberg limit, which scales like $1/N$.

Considering ensembles of N two-level, or spin-1/2, atoms with internal spin degrees of freedom, spin squeezing involves a redistribution of quantum noise on the angular momentum Bloch sphere in such a way as to produce reduced quantum fluctuations along one coordinate axis. Integer-spin systems possess additional degrees of freedom associated with the quadrupole or nematic tensor operator

$$\hat{Q}_{ij} = \sum_{n=1}^{N} \hat{\sigma}_i^{(n)} \hat{\sigma}_j^{(n)} + \hat{\sigma}_j^{(n)} \hat{\sigma}_i^{(n)} - \frac{4}{3}\delta_{ij} \tag{10.11}$$

where $\{ i, j \} \in \{ x, y, z \}$, $\hat{\sigma}_i^{(n)}$ are spin-1 angular momentum operators for a single atom, and δ_{ij} is the Kronecker delta function. Spin-nematic squeezing involves the redistribution of quantum noise in the subspaces $\{ \hat{S}_x, \hat{Q}_{yz}, \hat{Q}_{zz} - \hat{Q}_{yy} \}$ and $\{ \hat{S}_y, \hat{Q}_{xz}, \hat{Q}_{zz} - \hat{Q}_{xx} \}$ [14]. Focussing on the first of these subspaces, the degree of spin-nematic squeezing can be characterised by a parameter ξ_x, which gives the metrological precision relative to the standard quantum limit for Ramsey interferometry and is calculated by minimising the following expression over the angle θ:

$$\xi_x^2 = \frac{2\,\langle [\Delta(\hat{S}_x \cos\theta + \hat{Q}_{yz} \sin\theta)]^2 \rangle}{|\,\langle \hat{Q}_{zz} - \hat{Q}_{yy} \rangle\,|} \tag{10.12}$$

with $\xi_x^2 < 1$ indicating spin-nematic squeezing.

10.4.1 Finite sized ensemble

Figure 10.2 shows the development of spin-nematic squeezing with and without damping for an ensemble of $N = 120$ atoms. These results are obtained from quantum trajectory simulations of Equation 10.8, in which we make use of a representation in terms of bosonic mode operators, $\hat{b}_m$, for the three Zeeman states $m = 0, \pm 1$. In particular, $\hat{b}_m(\hat{b}_m^\dagger)$ annihilates (creates) an atom in state m, and, e.g.,

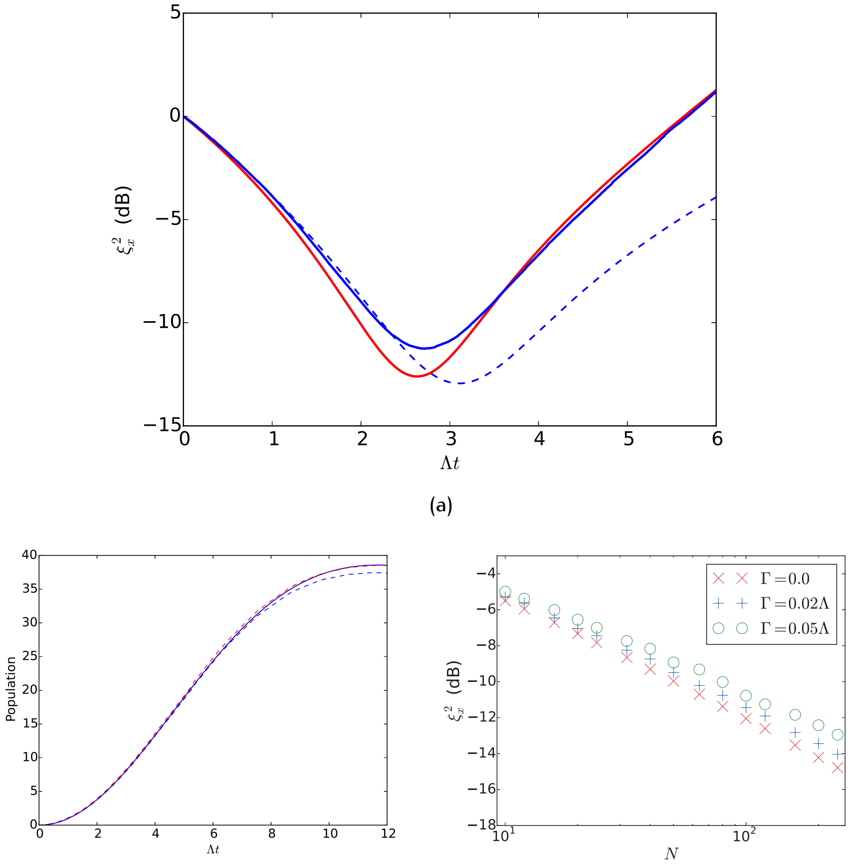

(a)

(b) (c)

Figure 10.2: (a) Time evolution of the spin-nematic squeezing for $N = 120$ atoms without damping (red line) and, with damping rate $\Gamma = 0.05\Lambda$, an ensemble average of 1000 trajectories (dark blue) and a single trajectory in which no jumps occur (dashed dark blue). The phase angle in each case is just below $\theta = 170°$. (b) Populations in each of the states $m = \pm 1$ for $\Gamma = 0$ (solid line) and $\Gamma = 0.05\Lambda$ (dashed lines). (c) Optimised squeezing scaling with atom number with and without damping. With damping, ensemble averages of 1000 trajectories were used to estimate the master equation result.

$\hat{S}_- = \sqrt{2}(\hat{b}_0^\dagger \hat{b}_1 + \hat{b}_{-1}^\dagger \hat{b}_0)$. This allows the Hamiltonian to be rewritten in the form

$$\hat{H} = \frac{\Lambda}{2N}\left(2\hat{b}_1^\dagger \hat{b}_{-1}^\dagger \hat{b}_0 \hat{b}_0 + 2\hat{b}_0^\dagger \hat{b}_0^\dagger \hat{b}_{-1} \hat{b}_1 + \hat{b}_0^\dagger \hat{b}_0 (1 + 2\hat{b}_1^\dagger \hat{b}_1 + 2\hat{b}_{-1}^\dagger \hat{b}_{-1})\right). \qquad (10.13)$$

We start our simulations with an initial state in which the entire population is in the $m = 0$ state and use a Monte-Carlo wavefunction method to simulate the system. An average over an ensemble of trajectories is used to estimate the master equation result for the various moments required to calculate ξ_x^2. The presence of the term $\hat{b}_1^\dagger \hat{b}_{-1}^\dagger \hat{b}_0 \hat{b}_0 + \hat{b}_0^\dagger \hat{b}_0^\dagger \hat{b}_{-1} \hat{b}_1$ highlights explicitly the link to squeezing via four-wave mixing in light [14,15].

With $\Gamma = 0$ the system simply follows the Hamiltonian evolution, and we see significant squeezing generated on a timescale $(\Lambda/2)^{-1}$. After this time, squeezing reduces and ultimately turns into anti-squeezing. This turnaround correlates with a growing number of atoms in the $m = \pm 1$ states, resulting in a reduction in $|\hat{Q}_{zz} - \hat{Q}_{yy}|$.

With the addition of a small rate of damping, which causes (infrequent) quantum jumps with $\hat{S}_-$, we find that the trajectories can be split into two categories. First are those that reach the point of peak squeezing without a jump having occurred. Interestingly, these have squeezing at a slightly higher level than with $\Gamma = 0$, meaning that the null measurement backaction (which essentially adds an imaginary element to the spin-nematic squeezing generator) actually improves the squeezing. Second, when there is a jump before that point, the squeezing is substantially reduced, and so, on average, the presence of damping does decrease the degree of squeezing. However, for sufficiently small κ/ω, such jumps should be rare. In addition, since these jumps are mediated by the cavity mode (i.e., they correspond to the emission of a photon from the cavity mode), then, by monitoring that output and postselecting based on the absence of a photon measurement, it would be possible to remove some of the runs with non-optimal squeezing (allowing for finite detection efficiency).

Figure 10.2 also illustrates more clearly how the best achievable squeezing varies with the number of atoms, with results obtained from trajectory simulations of Equation 10.8. For $\Gamma = 0$, we find that $\xi_x^2 \sim N^{-0.673}$ in the range of atom numbers that we consider. This indicates that this spin-nematic squeezing scales very similarly to one-axis twisting (where the squeezing scales at best as $N^{-2/3}$). Note that we have also considered spin-nematic squeezing in spin-2 particles, as would be relevant to the situation in which the present scheme is applied to the $F = 2$ ground states in either ^{85}Rb or ^{87}Rb, and find similar results.

10.4.2 Visualising the atomic state

We describe squeezing that takes place on a sphere with axes $\{\hat{S}_x, \hat{Q}_{yz}, \hat{Q}_{zz} - \hat{Q}_{yy}\}$ (or equivalently $\{\hat{S}_y, \hat{Q}_{xz}, \hat{Q}_{xx} - \hat{Q}_{zz}\}$, with an equivalent derivation to here). With spin squeezing, it is useful to be able to visualise the state with the atomic Q-function. Analogously to the Q-function for electromagnetic modes, an overlap is taken with coherent states over the space of interest. Since we consider squeezing on the SU(2) sphere $\{\hat{S}_x, \hat{Q}_{yz}, \hat{Q}_{zz} - \hat{Q}_{yy}\}$, we build coherent states of that space. We build these in the same way as coherent spin states of spin-1/2 particles: a binomial distribution across the eigenstates of the z-axis [16,17], which in this case is $\hat{Q}_{zz} - \hat{Q}_{yy}$. In terms of the bosonic annihilation and creation operators, this is

$$\hat{Q}_{zz} - \hat{Q}_{yy} = -2\hat{b}_0^\dagger \hat{b}_0 + \hat{b}_{+1}^\dagger \hat{b}_{+1} + \hat{b}_{-1}^\dagger \hat{b}_{-1} + \hat{b}_{+1}^\dagger \hat{b}_{-1} + \hat{b}_{-1}^\dagger \hat{b}_{+1}. \tag{10.14}$$

It is easy to see that the initial state $|0, N, 0\rangle$ is an eigenstate of this operator with eigenvalue $-2N$. We define this lowest energy eigenstate as the South Pole of our sphere and notate it as $|0\rangle$. To generate the other eigenstates we use the ladder operators

$$\hat{\mathcal{S}}_{\pm} = \hat{S}_x \pm i\hat{Q}_{yz} = 2\sqrt{2}\hat{b}_0(\hat{b}^{\dagger}_{+1} + \hat{b}^{\dagger}_{-1}). \tag{10.15}$$

Applying this operator to our lowest energy eigenstate gives us the rest of the eigenstates, and we can then build coherent states as

$$|M\rangle = (\hat{\mathcal{S}}_{+})^M |0\rangle\,, \tag{10.16}$$

where we have omitted a normalisation factor. We then build coherent states as

$$|\eta = \mathrm{e}^{i\phi}\tan(\theta/2)\rangle = \sum_{M=0}^{N} \begin{pmatrix} N \\ M \end{pmatrix}^{1/2} \eta^M |M\rangle \tag{10.17}$$

where we again omit the normalisation factor. Our atomic Q-function is described by

$$Q(\eta) = \langle\eta|\,\rho\,|\eta\rangle \tag{10.18}$$

and (θ, ϕ) are mapped as the polar and azimuthal angles onto the surface of a sphere.

As discussed above, our squeezing generator is analogous to that in four-wave mixing. Correlated pairs of atoms in the $m = \pm1$ states are created from a reservoir of atoms in the $m = 0$ state. Unlike in the optical analogy, here the reservoir has a finite number of atoms in it, and so the squeezing takes place on a sphere instead of a plane. As pairs are created, $|\langle\hat{Q}_{zz} - \hat{Q}_{yy}\rangle|$ begins to reduce. In terms of the atomic Q-function plots this can be seen as the ends of the state travelling up the sphere. At some point this effect reduces $|\langle\hat{Q}_{zz} - \hat{Q}_{yy}\rangle|$ at a faster rate than the squeezing generator is reducing the variance, and so the squeezing parameter begins to increase. We also see a slight "twist" developing in the state where the extreme ends are at slightly exaggerated angles.

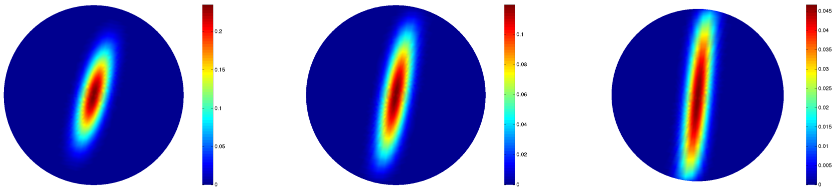

(a) $\Lambda t = 1.8$ **(b)** $\Lambda t = 2.7$ **(c)** $\Lambda t = 4.5$

Figure 10.3: Atomic Q-functions on the space $\{\hat{S}_x, \hat{Q}_{yz}, \hat{Q}_{zz} - \hat{Q}_{yy}\}$ looking from the South Pole, for 120 atoms with $\Gamma = 0$.

10.4.3 Large ensemble limit

In Figure 10.4, we plot the squeezing parameter as a function of both the time and phase angle θ for $N = 120$ atoms and in the limit of large N. For that limit we assume that the $m = 0$ state is essentially undepleted and $\hat{b}_0$ can be replaced by $\sqrt{N}$, so that the Hamiltonian becomes

$$\hat{H} = \frac{\Lambda}{2}\left(2\hat{b}^\dagger_{+1}\hat{b}^\dagger_{-1} + 2\hat{b}_{+1}\hat{b}_{-1} + 1 + 2\hat{b}^\dagger_{+1}\hat{b}_{+1} + 2\hat{b}^\dagger_{-1}\hat{b}_{-1}\right) \tag{10.19}$$

while in the damping term

$$\hat{S}_- \to \sqrt{2N}(\hat{a}^\dagger_{-1} + \hat{a}_{+1}) \quad \text{and} \quad \hat{S}_+ \to \sqrt{2N}(\hat{a}_{-1} + \hat{a}^\dagger_{+1}). \tag{10.20}$$

Equations of motion for the various moments required to compute ξ_x^2 can be deduced from the master equation, but we choose to work instead with the equivalent quantum Langevin equations for $\hat{b}_{\pm 1}$, which, defining a vacuum noise operator $\hat{b}_{\text{in}}(t)$ that satisfies $[\hat{b}_{\text{in}}(t), \hat{b}^\dagger_{\text{in}}(t')] = \delta(t - t')$, take the simple linear forms

$$\frac{\mathrm{d}\hat{b}_{+1}}{\mathrm{d}t} = -(\Gamma + i\Lambda)(\hat{b}_{+1} + \hat{b}^\dagger_{-1}) - \sqrt{2\Gamma}\hat{b}_{\text{in}}(t) \tag{10.21}$$

$$\frac{\mathrm{d}\hat{b}_{-1}}{\mathrm{d}t} = (\Gamma - i\Lambda)(\hat{b}_{-1} + \hat{b}^\dagger_{+1}) + \sqrt{2\Gamma}\hat{b}^\dagger_{\text{in}}(t). \tag{10.22}$$

To calculate the squeezing parameter ξ_x^2 we require two combinations of these: $\hat{A} = \hat{b}_{+1} + \hat{b}^\dagger_{-1}$ and $\hat{B} = \hat{b}_{+1} - \hat{b}^\dagger_{-1}$. These have Langevin equations

$$\frac{\mathrm{d}\hat{A}}{\mathrm{d}t} = 0 \tag{10.23}$$

$$\frac{\mathrm{d}\hat{B}}{\mathrm{d}t} = -2(\Gamma + i\Lambda)\hat{A} - 2\sqrt{2\Gamma}\hat{b}_{\text{in}}(t) \tag{10.24}$$

which are readily integrated to give

$$\hat{A}(t) = \hat{A}(0) \tag{10.25}$$

$$\hat{B}(t) = \hat{B}(0) - 2(\Gamma + i\Lambda)\hat{A}(0)t - 2\sqrt{2\Gamma}\int_0^t \mathrm{d}t'\,\hat{b}_{\text{in}}(t'). \tag{10.26}$$

The specific operators of interest are given by

$$\hat{S}_x(t) = \sqrt{\frac{N}{2}}(\hat{A}(t) + \hat{A}^\dagger(t)), \quad \hat{Q}_{yz}(t) = i\sqrt{\frac{N}{2}}(\hat{B}(t) - \hat{B}^\dagger(t)) \tag{10.27}$$

and using the results for $\hat{A}(t)$ and $\hat{B}(t)$ (and assuming that we can set $\hat{Q}_{zz} - \hat{Q}_{yy} =$

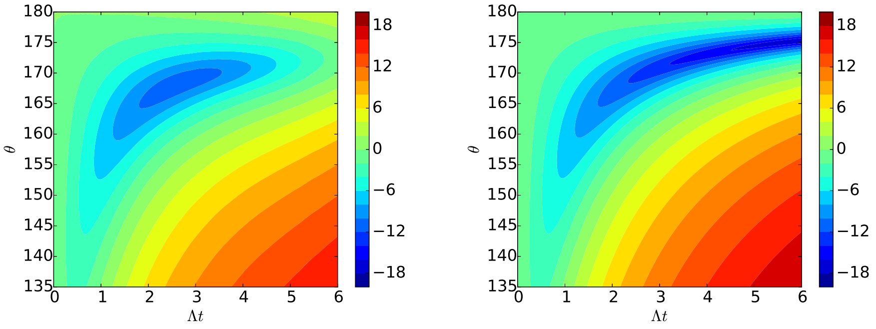

(a) (b)

Figure 10.4: Values of ξ_x^2 (in dB) as a function of time and phase angle for $\Gamma/\Lambda = 0.05$ with (a) $N = 120$ atoms and (b) in the undepleted mode approximation ($N \to \infty$) given by Equation 10.28.

$-2N$) we obtain

$$\xi_x^2 = (\cos\theta + 2\Lambda t \sin\theta)^2 + (1 + 2\Gamma t)^2 \sin^2\theta. \tag{10.28}$$

The formula above correctly predicts the angular dependence, and, at shorter times, also matches quite accurately the degree of squeezing for the $N = 120$ case. For larger N it should provide a good model of the squeezing for longer times, where it predicts that the degree of squeezing will continue to increase for a suitable choice of phase angle θ. Note also that Equation 10.28 is unchanged if a term $\omega_0'\hat{S}_z = \omega_0'(\hat{b}_{+1}^\dagger\hat{b}_{+1} - \hat{b}_{-1}^\dagger\hat{b}_{-1})$ is added to the Hamiltonian.

10.4.4 Spontaneous emission rates

Finally, we note that the rate of atomic spontaneous emission due to off-resonant excitation of the $5^2P_{1/2}$ state is estimated, for our configuration, as $\Gamma_{\mathrm{sp}} = \gamma(\Omega^2/12\Delta^2)$, which gives $\Gamma_{\mathrm{sp}}/(\Lambda/2) \approx 48\omega/(NC\kappa)$, where $C = 2g^2/(\kappa\gamma)$ is the single-atom cooperativity. For the parameters discussed above, this ratio is ~ 0.0006. With more atoms and/or increased cooperativity, this can evidently be reduced even further.

10.5 Conclusion

In conclusion, we have proposed a method for engineering spinor dynamics using cavity-mediated Raman transitions and demonstrated that such a scheme could be used to produce spin-nematic squeezing in an ensemble of spin-1 atoms. We believe this work opens up a range of exciting possibilities for emulating spinor BEC dynamics on much shorter timescales and extending this to explore a much wider range of spinor physics with significant flexibility.

Chapter 11

Preparing the spin singlet state of a spinor gas in an optical cavity

The spinor collisional Hamiltonian is of great interest because adjusting parameters can give a variety of ground states, varying from trivially prepared initial states to highly entangled many-body states. One particular ground state of interest is a state of zero spin length: the spin singlet. This can, in theory, be prepared by adiabatically varying parameters. Such approaches have so far yielded either states ruined by noise because the sweep is too long, or states with imperfect fidelity because the sweep was not truly adiabatic. In this Chapter, we present how such a "quasi-adiabatic" sweep could be performed using a cavity QED setup. The presence of the cavity also allows a different method to production: the spin singlet is a dark state to the cavity QED system. Therefore, a null measurement in the cavity output will prepare the spin singlet, and it will do so with a probability proportional to the initial population in that state. We show that using an imperfect sweep to increase the overlap with the spin singlet allows a greatly enhanced efficiency for our dissipative preparation scheme. The two methods used one after the other could thus prepare the spin singlet with remarkably high efficiency and near-perfect fidelity for very large ensembles. This work is presented in the form of a paper published in Physical Review A. It has been reformatted for this thesis, with added subsection headings, minor changes to figures and some notation and spelling altered to provide consistency throughout the thesis but is available in its original form at https://journals.aps.org/pra/abstract/10.1103/PhysRevA.99.013819.

11.1 Introduction

Spinor Bose gases - in particular, ensembles of ultracold Bose atoms with internal spin degrees of freedom - offer a remarkable platform for the study of quantum fluids and phenomena such as quantum phase transitions and superfluidity [172,173]. One reason for this is the rich variety of collision-induced, spin-mixing dynamics that are possible in spinor Bose-Einstein condensates (BECs), together with the exotic quantum states that may result from these dynamics. Of particular interest in this context, driven in part by potential application to quantum-enhanced metrology, have been highly entangled (e.g., spin squeezed) states [146,149,150,188,189], and remarkable experimental progress has been made in this field of research [14,99,100, 124,125,154–159].

One system that has been of interest is a small, tightly confined BEC of spin-1 atoms in the presence of a magnetic field. In the single-mode approximation, the interplay between collisions and the quadratic Zeeman shift is modelled by the Hamiltonian

$$\hat{H} = \frac{\Lambda}{N}\hat{\mathbf{S}}^2 + q\hat{N}_0 \tag{11.1}$$

where $\hat{\mathbf{S}} = \{\,\hat{S}_x, \hat{S}_y, \hat{S}_z\,\}$ and $\hat{S}_i$ are collective angular momentum operators for the ensemble of N spin-1 atoms, $\hat{N}_0$ is the population operator for the $m = 0$ state, and Λ and q characterise the interaction strength and quadratic Zeeman shift, respectively.

11.1.1 The spin singlet

Despite its apparent simplicity, the Hamiltonian in Equation 11.1 admits a variety of ground states dependent on the signs and relative magnitudes of Λ and q. One of those ground states is the macroscopic spin singlet. This is a state of N atoms where the *collective* angular momentum is zero. This state features strong entanglement and is given by the superposition

$$|S = 0\rangle = \sum_{j=0}^{N/2} c_j \,|j, N-2j, j\rangle \tag{11.2}$$

using the notation $|n_{-1}, n_0, n_{+1}\rangle$ for n_i atoms in the magnetic state $m = i$ and with coefficients given by

$$c_0 = \frac{1}{\sqrt{N+1}}, \quad c_j = -\sqrt{\frac{N-2j+2}{N-2j+1}}\,c_{j-1}. \tag{11.3}$$

This state features genuine multipartite entanglement of the entire ensemble [147, 148]. This entanglement is useful for quantum metrology [191] and could be of use in fields including quantum memory [202] and quantum information processing [192,203].

Preparing the spin singlet of a BEC as the ground state of the Hamiltonian given by Equation 11.1 is, in practice, a very challenging prospect, given the extremely small energy scales involved [173]. However, other methods have been proposed to produce the spin singlet state. One such method involves a sequence of quantum non-demolition measurements using pulses of light to probabilistically prepare a highly entangled macroscopic spin singlet [106, 204, 205].

11.1.2 Summary of the Chapter

In this work, we propose a method to produce the macroscopic spin singlet via interactions mediated by cavity-assisted Raman transitions. The imbalanced Dicke model for spin-1 atoms, as discussed in Chapters 7 and 10, or more simply a Tavis-Cummings model, as discussed in Chapter 8, can probabilistically produce the spin singlet heralded by the *absence* of measured photons in the cavity output. This protocol works with an efficiency equal to the overlap between the initial state and the spin singlet, which, however, is $1/(N+1)$. We thus propose the use of quasi-adiabatic sweep techniques - an established method for these systems in spinor BECs - to enhance that initial overlap. We then show that a protocol of a quasi-adiabatic sweep followed by the probabilistic distillation of the state using a Tavis-Cummings model offers a method to produce a singlet state with very high fidelity and a reasonably high efficiency.

11.2 Setup & model

11.2.1 General model

We consider an ensemble of ^{87}Rb atoms held tightly within an optical cavity. We assume that the ensemble is sufficiently dilute that we can ignore any direct atom-atom interactions, and instead engineer effective interactions via cavity-assisted Raman transitions [53, 161, 162], as illustrated in Figure 11.1. Here, as demonstrated recently in [71], we consider transitions within the complete $F = 1$ hyperfine ground state. In the limit that the detunings of the Raman transitions are much larger than the energy separations of the excited-state hyperfine levels, this gives an effective open Dicke model for an ensemble of spin-1 particles. In that case, as discussed in Chapter 7, the evolution of the density operator can be described by the master equation

$$\dot{\rho} = -i[\hat{H}, \rho] + \kappa\mathcal{D}[\hat{a}]\rho \tag{11.4}$$

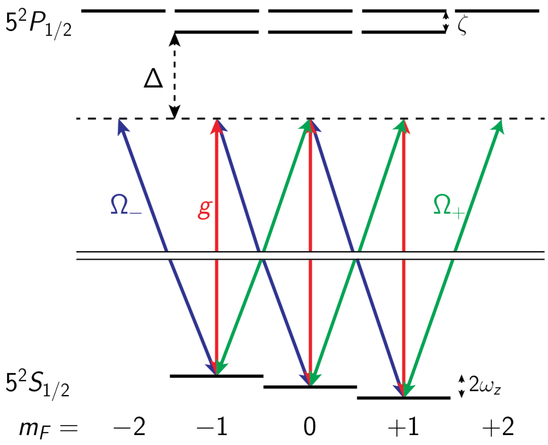

Figure 11.1: Implementation of an effective spin-1 Dicke model using the $F = 1$ ground state of ^{87}Rb. Interactions are mediated by detuned Raman transitions on the D_1 line composed of a cavity mode (red) and σ_-- (blue) and σ_+- (green) polarised lasers.

where $\hat{a}$ is the cavity mode annihilation operator, $\mathcal{D}[\hat{a}]\rho = 2\hat{a}\rho\hat{a}^\dagger - \rho\hat{a}^\dagger\hat{a} - \hat{a}^\dagger\hat{a}\rho$, and

$$\hat{H} = \omega\hat{a}^\dagger\hat{a} + \omega_0\hat{S}_z + \frac{\lambda_-}{\sqrt{2N}}(\hat{a}\hat{S}_+ + \hat{a}^\dagger\hat{S}_-) + \frac{\lambda_+}{\sqrt{2N}}(\hat{a}\hat{S}_- + \hat{a}^\dagger\hat{S}_+). \tag{11.5}$$

The coefficients of the various terms are determined by light shifts and Raman transition rates; in particular,

$$\omega = \omega_c - \frac{\omega_- + \omega_+}{2} + \frac{Ng^2}{3\Delta} \tag{11.6}$$

$$\omega_0 = \omega_z - \frac{\omega_- - \omega_+}{2} + \frac{\Omega_+^2 - \Omega_-^2}{24\Delta} \tag{11.7}$$

$$\lambda_\pm = \frac{\sqrt{N}g\Omega_\pm}{12\Delta}. \tag{11.8}$$

Here ω_c is the frequency of the cavity mode, $\omega_\pm(\Omega_\pm)$ are the bare frequencies (Rabi frequencies) of the $\sigma_\pm$-polarised laser fields, ω_z is the linear Zeeman splitting of the $F = 1$ levels, g is the single-atom-cavity coupling strength (for the ^{87}Rb D_2 line cycling transition), κ is the cavity field decay rate, and Δ is the detuning of the fields from the atomic resonance. Note that we assume that the atoms all couple to the cavity mode with the same strength g, which can in practice be achieved by confining the atoms tightly at cavity mode anti-nodes in an optical lattice potential (which may be created via another, far-detuned cavity mode at twice the wavelength of the other mode [71,72]).

11.2.2 Dissipative limit

By turning off the σ_+-polarised laser and choosing $\omega = \omega_0$, the above model reduces to the resonant Tavis-Cummings model for spin-1 atoms. We will consider this model in Section 11.4 in the context of a dissipative, probabilistic scheme for preparing the spin singlet state.

11.2.3 Hamiltonian limit

Alternatively, we can consider the above model in a dispersive limit, such that $\omega \gg \omega_0, \lambda_\pm$, in which case the cavity mode can be adiabatically eliminated. Considering again the case where $\Omega_+ = 0$, as shown in Chapter 9, the model can then be reduced to [163,164]

$$\dot{\rho} = -i[\hat{H}, \rho] + \frac{\Gamma}{N}\mathcal{D}[\hat{S}_-]\rho, \tag{11.9}$$

with

$$\hat{H} = \omega_0' \hat{S}_z + \frac{\Lambda}{N}(\hat{S}_x^2 + \hat{S}_y^2) \tag{11.10}$$

and in terms of the Dicke model parameters given above, we define new parameters

$$\omega_0' = \omega_0 + \frac{\Lambda}{N}, \quad \Lambda = -\frac{\omega\lambda^2}{2(\omega^2 + \kappa^2)} \quad \Gamma = -\frac{\kappa}{\omega}\Lambda. \tag{11.11}$$

By manipulating the microscopic parameters, it is possible to (at least approximately) set $\omega_0' = 0$, but given that we consider a system initiated with all atoms in the $m = 0$ level (i.e., with $\langle \hat{S}_z \rangle = 0$), and that $\hat{S}_z$ is conserved by the Hamiltonian evolution, this term does not impact the evolution in the absence of photon detections, which we show is the heralding condition for the production of the singlet. Hence, we see that the cavity-mediated, coherent spin interactions described by Equation 11.10 can emulate the collisional interactions of BECs in the single-mode approximation.

Further to this, an artificial quadratic Zeeman shift can, for example, be produced by a weak, auxiliary π-polarised laser field acting near the $F' = 1$ excited manifold. This shift is considered to be time dependent, and could be adjusted either by moving it closer or further from resonance, or by adjusting the power of the weak field. This leaves us with a Hamiltonian of the form

$$\hat{H} = \frac{\Lambda}{N}(\hat{S}_x^2 + \hat{S}_y^2) - q(t)\hat{N}_0. \tag{11.12}$$

11.3 Entanglement criteria

Due to the additional degrees of freedom for particles with spin $> 1/2$, entanglement in spinor particles can be quantified by a range of different inequalities [147,148].

From [148], we have that an ensemble of spin-1 particles with no entanglement satisfies

$$(\Delta\hat{S}_x)^2 + (\Delta\hat{S}_x)^2 + (\Delta\hat{S}_x)^2 \geq N. \tag{11.13}$$

Therefore, if an ensemble breaks the less strict bound

$$\langle\hat{S}_x^2\rangle + \langle\hat{S}_y^2\rangle + \langle\hat{S}_z^2\rangle \geq N \rightarrow \langle\hat{\mathbf{S}}^2\rangle \geq N \tag{11.14}$$

then that ensemble is entangled. This measure thus has two purposes: it shows us how the spin length decreases as well as acting as an entanglement witness. Furthermore, $\langle\hat{\mathbf{S}}^2\rangle$ gives a bound on the maximum number of atoms that are not entangled [204].

11.4 Dissipative evolution

We consider the master equation given in Equation 11.4 with $\omega = \omega_0 = 0$. An initial state with all the atoms in the $m = 0$ state can be decomposed into a superposition of Dicke states $|S, 0\rangle$ with different spin lengths as (for even N [46])

$$|n = 0\rangle \otimes |0, N, 0\rangle = |n = 0\rangle \otimes \sum_{k=0}^{N/2} d_k \, |2k, 0\rangle \tag{11.15}$$

where the distribution $\{d_k\}$ is strongly peaked around $k \simeq \sqrt{N}$, as shown in Chapter 8. Excitations are produced in the cavity in conjunction with a spin ladder operator, i.e., via terms in the Hamiltonian of the form $\hat{a}^\dagger\hat{S}_\pm$, and that ladder operator does not operate on the spin singlet (i.e., $\hat{S}_\pm |0, 0\rangle = 0$). This means that entanglement is generated between the cavity mode and the atoms: an empty cavity with the spin singlet, and non-zero photon numbers with the states of non-zero spin length occurring in Equation 11.15. Any photon emitted from the cavity must therefore collapse the state into a superposition of spin states not containing the spin singlet, while a null measurement will project the atomic state into the spin singlet. Monitoring the cavity output thus gives some probability of projecting the state into the spin singlet; the probability is simply the overlap of the initial state with the spin singlet, which is $1/(N + 1)$ for the state given in Equation 11.15.

If we turn off one of the lasers; in particular, if we set $\lambda_+ = 0$, then an initial atomic state $|2k, 0\rangle$ will evolve, subject to Equations 11.4 and 11.5 (i.e., the damped Tavis-Cummings model, when $\lambda_+ = 0$), to a steady state $|2k, -2k\rangle$, with the emission of $2k$ photons from the cavity, as discussed in Chapter 8. An ideal way to in which to

---

[46] Our scheme also works for the $F = 2$ hyperfine ground state, i.e., an ensemble of spin-2 atoms, where the initial state $|m = 0\rangle^{\otimes N}$ has a finite overlap with the spin singlet state regardless of whether the number of atoms is even or odd. Spin-1 atoms are considered here for simplicity.

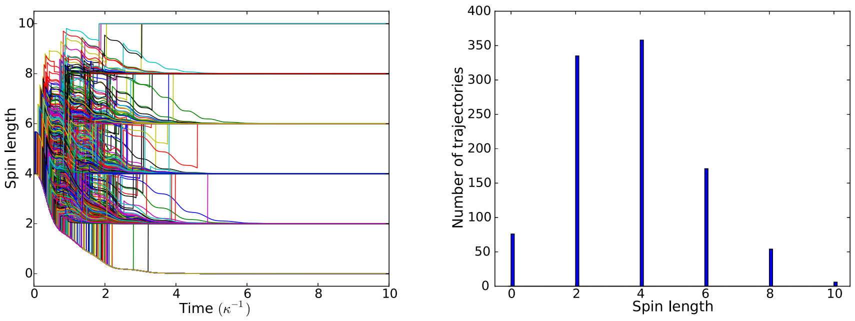

(a) (b)

Figure 11.2: Spin length, found by calculating $\langle \hat{S}^2 \rangle = S(S+1)$ and solving for S, (a) over time and (b) at $\kappa t = 10$ in 1000 quantum Monte Carlo trajectories for $N = 10$ atoms under the master equation given by Equation 11.4 with $\lambda_- = 6\kappa$, and $\omega = \omega_0 = \lambda_+ = 0$.

study this behaviour is to use the method of Monte Carlo wave function simulations (or quantum trajectories) [165], and in Figure 11.2 we present results of this approach applied to the model of Equations 11.4 and 11.5, where each "jump" in the simulations corresponds to the emission of a photon from the cavity. Figure 11.2a shows that, after a few cavity lifetimes, the state is always cleanly projected to a definite spin length. After a time $\kappa t = 10$ with $N = 10$ atoms, the overlap with the spin singlet is either (essentially) one or zero, depending on the output photon record (see Figure 11.2b).

The projection, for the parameters of Figure 11.2, occurs on a timescale on the order of the photon lifetime in the cavity, $1/\kappa$. This is because the production of photons in the cavity due to coupling to the atoms happens on a much faster timescale than cavity loss, and the rate of photon emission follows the rate of the slower process. For this to hold for arbitrary atom number we require that photon production happens for *all* states at a rate faster than κ. The slowest state to produce photons is $|S = 2, 0\rangle$, and so we require $\lambda_- \sqrt{3/N} \gg \kappa$. If that is not the case, the rate will instead be governed by the intracavity photon production rate, and so the singlet would be heralded by the absence of photon detections over some timescale more than a few cavity lifetimes.

With a more realistic photon detection scheme that has an efficiency η, the absence of emitted photons from the Tavis-Cummings system would project to a mixed state (a normalising factor is omitted):

$$\rho = |d_0|^2 \, |0,0\rangle \langle 0,0| + \sum_{k=1}^{N/2} (1-\eta)^{2k} |d_k|^2 \, |2k,-2k\rangle \langle 2k,-2k| \, . \tag{11.16}$$

For reasonably high efficiencies (in particular high enough such that $(1-\eta)^2 |d_2|^2 \ll$

$|d_0|^2$), this should still be dominated by the spin singlet. Alternatively, the Dicke model ($\lambda_+ = \lambda_-$), which produces a continuous stream of photons, could be used. This would allow for very high fidelity singlet production even without perfect detection efficiency. It should be noted that very high effective atom-cavity coupling, $\lambda_\pm$, or very long measurement times would be necessary to project out the lower spin state contributions.

The probability of this procedure working is simply the initial overlap with the singlet state, $1/(N+1)$. For small numbers of atoms this process offers an efficient method to prepare a highly entangled state. However, for 1000 atoms, the maximum efficiency would be 0.1%. Other experimental considerations, such as photon detection efficiency, would further reduce the overall efficiency.

This may be mitigated somewhat by multiple runs with a single atomic ensemble. Using a feedback system conditioned on a photon detection (or some threshold depending on dark count rates), switching back on the repumping system to reinitialise the state into the state $|0, N, 0\rangle$ would reintroduce an overlap with the spin singlet. Since the time required for each run is relatively short, this should allow for multiple runs over the course of the lifetime of the ensemble.

11.5 Quasi-adiabatic methods in spinor BECs

If we want to improve the efficiency of our procedure, we need to improve the overlap between the initial state and the spin singlet. To do so, we can make use of the various ground states admitted by the spin-collisional Hamiltonian in Equation 11.1. In the limit where the quadratic Zeeman shift dominates over the collisional interaction, i.e., $|q| \gg |\Lambda|$, and q is negative, the ground state of the system has all atoms in the $m = 0$ state, i.e., $|0, N, 0\rangle$, which is of course readily prepared via suitable optical pumping. If, instead, q is positive, then the ground state is degenerate between all states for which there are no atoms in the $m = 0$ state. Depending on the spread through the $\hat{S}_z$ states that satisfy this, the degeneracy includes entangled states, such as the twin Fock state $|N/2, 0, N/2\rangle$, as well as completely classical states such as $|N, 0, 0\rangle$ or coherent combinations.

In the other limit, where instead the collisional interaction dominates over the quadratic Zeeman shift, i.e., $|\Lambda| \gg |q|$, there are again two ground states. With ferromagnetic interactions ($\Lambda < 0$, as for ^{87}Rb) the ground state is degenerate for all states with a maximum spin length N. As above, this can range from a highly entangled Dicke state to a completely classical state, depending on how $\hat{S}_z$ is constrained. For anti-ferromagnetic interactions ($\Lambda > 0$, as for ^{23}Na), there is only one ground state: the spin singlet.

The existence of these different ground states allows, in theory, for preparation of entangled states by adiabatic passage. For example, an ensemble can be prepared in the (unentangled) state $|0, N, 0\rangle$, which is the ground state for large, negative q. An adiabatic sweep from there to $q = 0$ produces, depending on the sign of Λ, either the spin singlet [150, 159] or, due to the conservation of $\hat{S}_z$, the Dicke state $|S = N, S_z = 0\rangle$ [125]. Alternatively, an adiabatic sweep through to large, positive q would prepare the twin Fock state $|N/2, 0, N/2\rangle$ [124, 150].

However, a key issue with performing this experimentally is maintaining adiabaticity throughout the sweep. At the phase transition points, the energy gap between the ground and first excited states becomes extremely small (zero in the limit $N \to \infty$). Since an adiabatic sweep requires parameters to change on a timescale very slow compared to the inverse of the energy gap, the sweep has to be extremely slow through the transition. Hence, a true adiabatic sweep typically faces severe challenges associated with achievable experimental run times.

Hoang et al. [159] used an ensemble of 40000 atoms and a sweep time of 35 s (the minimum time for true adiabaticity). After such a long time, less than 25% of the original BEC remained trapped. Due to the noise that atom loss induces in the magnetisation, no measurable entanglement was left in the ensemble. The alternate approach is to ramp faster than adiabatic, introducing a small amount of energy to the system. This moves the state out of the true ground state, but into states near the ground state that still feature high entanglement. Luo et al. [124] instead ramped in 3 s to high negative q attempting to produce the twin Fock state, finding just 4% of the atoms remained in the $m = 0$ state. Such a quasiadiabatic sweep has also been shown to produce metrologically useful entanglement in a BEC [125].

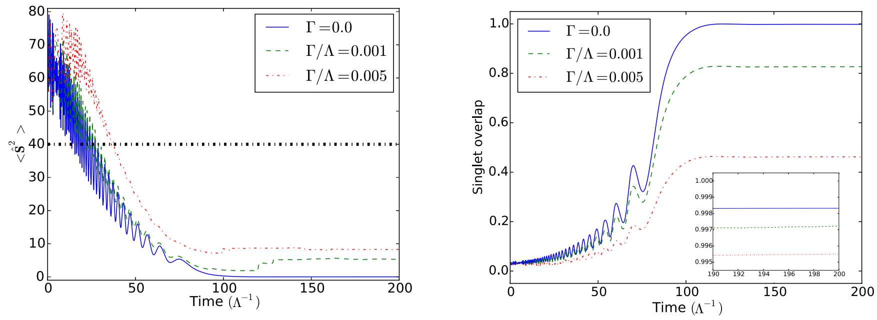

(a)

(b)

Figure 11.3: Simulations for $N = 40$ atoms. (a) Spin length squared and (b) overlap with the spin singlet state for a sweep $q(t)/\Lambda = 7.0\mathrm{e}^{-0.08\Lambda t}$ with and without losses. Results with losses, i.e., non-zero Γ, are plotted as an ensemble average of 1000 trajectories. Inset zooms in on the overlap at later times conditioned on zero jumps.

11.6 Hamiltonian evolution

We now consider evolution with the engineered master equation in Equation 11.9 with the Hamiltonian given by Equation 11.12. Here, the intention is to emulate results from BECs by sweeping the quadratic Zeeman shift, characterised by q, from some large value to essentially zero. To truly maximise the overlap, we should optimise the sweep such that it is as close to adiabatic as possible in the given timeframe [124,125,159]. However, in the interest of simplicity, we have instead considered just sweeps that are straightforward in form, but which still greatly enhance the overlap with the spin singlet. We find that an exponential decay, $q(t)/\Lambda = q_0 \mathrm{e}^{-\xi\Lambda t}$, produces a much higher fidelity spin singlet compared to linear-in-time or reciprocal-in-time decays.

In Figure 11.3 we use an average over an ensemble of quantum trajectories to approximate the master equation solution and show that the sweep greatly increases the overlap with the spin singlet and, concomitantly, greatly reduces the spin length. We also see that the non-adiabaticity adds energy to the system, resulting in large oscillations of the spin length during the sweep. These oscillations, and, in particular, their phase as they are "frozen out" by the quadratic Zeeman shift settling at zero, add considerable noise to the resultant spin length and overlap.

Using quantum trajectories, we find that the results can be split into two categories: with jumps and without jumps. With even a single jump, corresponding to the emission of a cavity photon, the overlap with the spin singlet becomes zero. This is because the spin singlet is a dark state to the jump operator, $\hat{S}_-$. Trajectories without a jump exhibit high overlap with the singlet state; in fact, for some sweep parameters, the overlap is higher than without losses. This is because the null measurement back-action increases the overlap with the dark state of the system: the spin singlet.

In line with the work in Section 11.4, there is the possibility of postselecting runs with a null photon output measurement, i.e., no jumps. As the spin length increases, so does the number of photons such a state produces. In particular, due to the spread of spin length, certain states in the initial superposition can release huge numbers of photons, greatly increasing $\langle \hat{\mathbf{S}}^2 \rangle$ for that trajectory. For example, with Γ/Λ in Figure 11.3, we find that 829 of the 1000 trajectories have no jumps and so have very high overlap with the spin singlet. Of other 171 trajectories, there are 139 with $\langle \hat{\mathbf{S}}^2 \rangle \approx 6$, i.e., $S \approx 2$, commensurate with the production of one or two photons. All bar two trajectories have $\langle \hat{\mathbf{S}}^2 \rangle < 40$, with the remaining two having a final value $\langle \hat{\mathbf{S}}^2 \rangle \sim 1600$. These states therefore each contribute a significant portion of the ensemble-averaged result, but, even with a realistic single photon detector, could easily be discared by postselection, since they emit ~ 40 photons to attain such a spin length.

Considering Figure 11.3, we obtain, with $\Gamma = 0$, a state with all 40 atoms entangled, while with $\Gamma > 0$ (i.e., finite cavity decay), we have more than 30 atoms

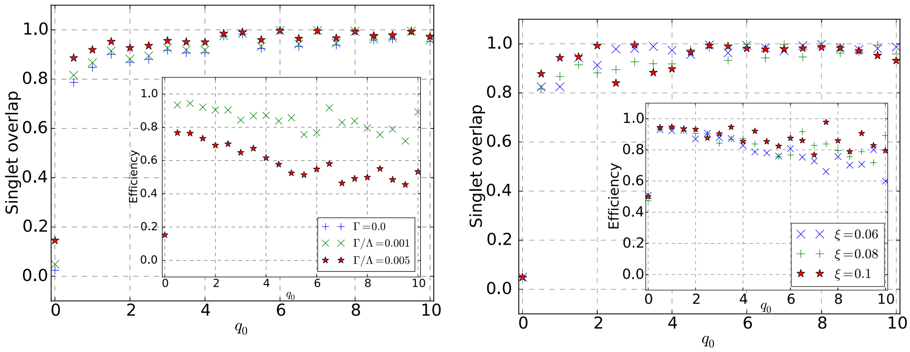

(a) (b)

Figure 11.4: Simulations for $N = 40$ atoms. (a,b) Final overlap with the spin singlet with zero emitted photons and (insets) postselection efficiency (i.e., no photons emitted) given (a) $q(t)/\Lambda = q_0 e^{-0.08\Lambda t}$, or (b) $q(t)/\Lambda = q_0 e^{-\xi\Lambda t}$ with $\Gamma/\Lambda = 0.001$. Postselection efficiencies are the percentage of 1000 trajectories that would produce zero photons.

entangled by the criterion introduced in Equation 11.14. Notably, the entanglement bound is strongly violated even for the master equation result, i.e., with no postselection, and even with the highest considered cavity-mediated damping $\Gamma/\Lambda = 0.005$.

Choosing the parameters for the sweep involves striking a balance between a slow ramp, finishing with the quadratic Zeeman shift close to zero, and limiting the cavity-mediated losses. However, clear dependences are not obvious due to the oscillations introduced by the non-adiabatic sweep. Instead, wide regions of sweep parameters offer reasonable results. We can see in Figure 11.4a that it is difficult to pinpoint an ideal value of the initial quadratic Zeeman shift q_0, with a general trend that $q_0 \gtrsim 4\Lambda$ produces higher overlap. However, higher q_0 reduces the probability of a trajectory without photon loss. Figure 11.4b shows that the rate of the exponential decay, ξ, is also difficult to choose so as to optimise the overlap, though, broadly speaking, higher ξ gives a higher success probability.

We note that, of course, optimising the quasi-adiabatic sweep in more complex ways should enhance the overlap of successful trajectories. However, such optimised sweeps might not necessarily be ideal for the probability that the sweep is successful and so that would need to be taken into consideration for the optimisation process.

11.7 Combination

We now show that for large atom numbers, the dissipative scheme can offer reasonable efficiency if it is preceded by the sort of quasi-adiabatic singlet preparation discussed above. The total efficiency of the scheme is now the postselection efficiency of the sweep (i.e., the probability of no photons being emitted during the sweep) multiplied by the efficiency of the dissipative scheme, which is the overlap at the end of the sweep:

$$p = p_s |\langle \psi | S = 0 \rangle|^2. \tag{11.17}$$

Since we are only interested in the final overlap with the singlet state, we can reduce our basis to those states accessible before a jump has occurred; that is, states with an exact number of pairs in the $m = \pm 1$ states, $|k, N - 2k, k\rangle$. Such a reduction in basis allows us to greatly increase the number of atoms we simulate. We model the backaction of the null measurement by adding a non-Hermitian term to the Hamiltonian,

$$\hat{H} = \frac{\Lambda - i\Gamma}{N}(\hat{S}_x^2 + \hat{S}_y^2) + q(t)\hat{N}_0 \tag{11.18}$$

and calculate the probability of a successful run from the jump operator expectation value,

$$p_s = \prod_{i=0}^{t_{\max}/\mathrm{d}t} \left\{ 1 - 2\Gamma \langle \hat{S}_x^2 + \hat{S}_y^2 \rangle_{t_i} \mathrm{d}t \right\} \tag{11.19}$$

where $\langle \hat{\mathcal{O}} \rangle_{t_i}$ is the expectation of the operator at time $t = i\,\mathrm{d}t$. This means that not only do we vastly reduce the basis size, but we also only have to integrate the Schrödinger equation once, rather than running a large number of trajectories.

Figure 11.5 shows the overlap and postselection efficiency for $N = 1000$ atoms. We can see a smooth relationship between the sweep parameters and the success probability. Simply, the sweep should be fast and from a small, non-zero q_0. Optimisation of the overlap is more complicated, though we see a wide range of parameters for which that overlap is significantly enhanced. The product of these thus gives a wide region of sweep parameters for which the total efficiency to produce a spin singlet of near perfect fidelity for 1000 atoms would be $\sim 10 - 20\%$. Even allowing for experimental reductions to this efficiency, such a method would produce the state frequently enough to allow for study and, potentially, use of the many-body entangled state.

For potential parameters, we consider parameters for the Tavis-Cummings model of $\{\lambda_-, \kappa\}/(2\pi) \simeq \{300, 10\}$ kHz. Large $\omega/2\pi \simeq 10$ MHz would then produce the spinor collisional model necessary for the quasi-adiabatic sweep. Switching to the dissipative method can then be performed by rapidly changing $\omega \to 0$. From a microscopic perspective, this involves shifting the frequency of the σ_--polarised laser closer to the cavity frequency. In this limit, we have an open Tavis-Cummings model, which would perfectly project the singlet state on the order of 1 ms or less. With these parameters, the scenario of Figure 11.5 corresponds to a sweep that lasts 3.2 ms, and hence to a time for the total procedure of approximately 4 ms.

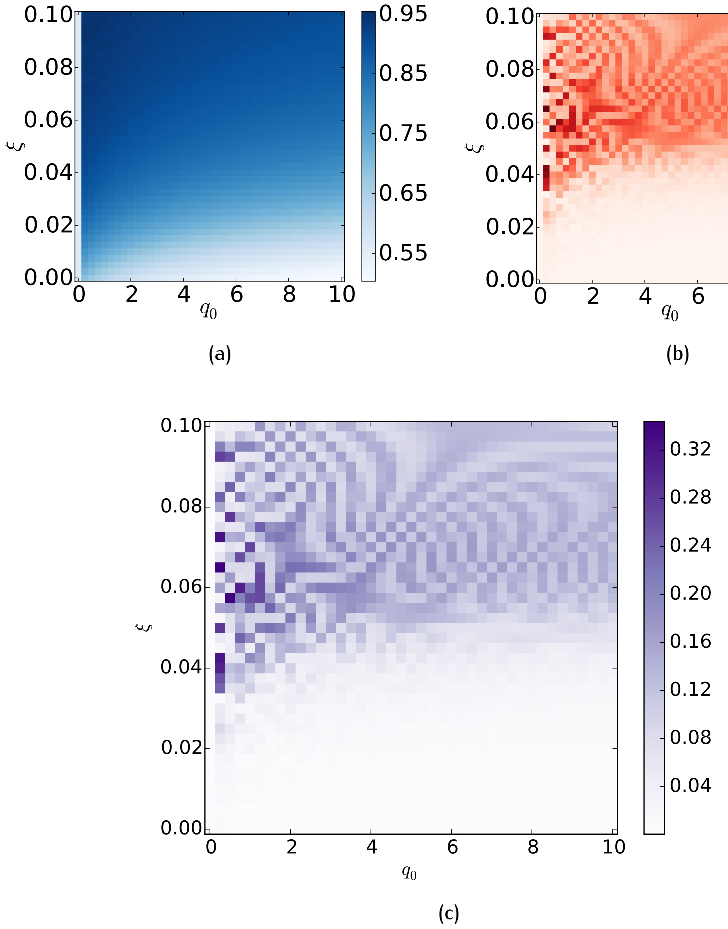

(a)

(b)

(c)

Figure 11.5: Simulations for $N = 1000$ atoms, with a sweep $q(t) = q_0 e^{-\xi \Lambda t}$, to a final time $\Lambda t = 200.0$. (a) Overlap with the spin singlet, (b) probability of no photons being emitted during the sweep, and (c) the product of those two, giving the efficiency of a combination of sweep and dissipative distillation.

11.8 Conclusion

We have proposed a method to prepare the spin singlet state of an ensemble of integer-spin atoms. Despite great interest in such a state, the production of the singlet is an open problem. Its preparation in spinor BEC experiments faces significant challenges; one potential method is that of adiabatic transformation, but this is made very difficult by the tiny energy gap at the phase transition, which greatly inflates the required timescales, as well as by the need to thoroughly minimise any residual magnetic field.

Our methods bypass these issues by using an alternative approach based upon engineered dynamics and projective measurement in cavity QED. Using a scheme of cavity-assisted Raman transitions to produce an effective spin-1 Tavis-Cummings model, we make use of the fact that the spin singlet is a unique dark state of the system. This means that the production of the singlet state is heralded by the *absence* of photons detected in the cavity output channel.

Using a slightly modified scheme of cavity-assisted Raman transitions enables us to emulate spinor BEC dynamics and thereby implement a quasi-adiabatic transformation to enhance the overlap of the atomic state with the singlet state prior to implementing the effective Tavis-Cummings model, thus enhancing the probabilistic distillation of the singlet state through monitoring of the dissipative output channel. We believe that this approach offers a realistic possibility of reliably producing the spin singlet state experimentally, and that it highlights the potential of augmenting spinor interaction models with dissipative channels such as cavity modes.

Chapter 12

Future extensions

This thesis has introduced a set of methods of how to engineer interactions between a cavity mode and an ensemble of spinor atoms *or* interactions within an ensemble of spinor atoms mediated by a cavity mode. My research focussed on using such methods to produce entanglement, in particular, *metrologically useful entanglement*. My experimental colleagues at the Centre for Quantum Technologies, and thus the theoretical work regarding those experiments, focussed on phase transition behaviour in fundamental models of physics. Of course, these engineered models have a great flexibility which opens up all sorts of possibilities that I did not have time to fully explore. In this Chapter, I discuss a few of the possibilities our methods might offer in the context of spinor physics, spinor Dicke models and spin-1 atoms in other quantum optics settings.

12.1 Spinor physics beyond collisions

In this thesis, when I have considered models of interacting spinor particles, the primary focus has been on the emulation of experiments in spinor BECs. However, the engineered schemes are certainly not limited in this way. Whilst experiments in spinor BECs are at a much more advanced stage than our proposals, it should be noted that there are distinct advantages to engineered schemes over spinor BECs.

- **Speed**. As pointed out in Chapters 10 and 11, these engineered models allow for much faster dynamics than collisional models. We proposed the production of the same types of entangled states that have been produced in spinor BECs, only with our methods we have access to them, and can thus use them for metrological purposes, much quicker. This could allow for "snapshot" measurements as a response to a change in environment, or a series of measurements tracking changes with a repetition rate much faster than available in BECs.

- **Dissipation**. When emulating spinor BEC dynamics, dissipation is an unwanted extra. Dissipation events break certain symmetries of the system, such as the conservation of $\langle \hat{S}_z \rangle$. However, it is precisely that breaking of the symmetry which allows for the production of the entangled states in Chapter 8 and the distillation of the spin singlet in Chapter 11. Without dissipation, the superposition of different spin length states is retained throughout the dynamics. With dissipation, elements of the superposition are heralded by the measurement of that dissipation. The addition of dissipative dynamics can allow us to prepare dark states of the system, but it could also be used to probe the state of the system non-destructively.

- **Flexibility**. We are not limited to spinor collisional physics. Instead, our Hamiltonian can simulate $\hat{S}_x^2$, $\hat{S}_y^2$ or sums of them. The Hamiltonian $\hat{S}_x^2$ has been mentioned multiple times during this thesis as the one-axis twisting Hamiltonian, meaning that we could produce spin squeezed states in that manner using our methods [199]. The same Hamiltonian also allows for the production of Schrödinger cat states [206]. Using such a scheme on a single large spin composed of a fully polarised ensemble of spinor atoms would allow for the production of a macroscopic superposition of a large atomic cloud [207].

- **Potential for extension**. If we overlay two copies of the Raman transition schemes on the same ensemble, we gain even greater flexibility allowing for fully arbitrary combinations of the operators $\hat{S}_x^2$ and $\hat{S}_y^2$ [161,162]. This allows us to produce the two-axis counter twisting Hamiltonian $\hat{S}_x^2 - \hat{S}_y^2$ [161,162,199]. As discussed in Chapter 10 and in [161,162], this range of Hamiltonians also encompasses the various Lipkin-Meshkov-Glick models, where spinor particles offer fascinating possibilities [197,198]. This could be done, for example, making use of multi-mode cavity implementations [75].

- **Other spinor phenomena**. Our methods used in this thesis operated in a limit where the "spinor" nature of the spins was suppressed in the Hamiltonian, arising only in the initial states we considered instead. If we operate with lower detuning, then we introduce distinctly spinor terms. The form of such systems is much more complex, and thus allows for far greater flexibility in the engineered interactions for the spins. It does not seem far-fetched to speculate that interesting and distinctly spinor physics could be found there, and that such physics would prove useful for the generation of exotic many-body quantum states or the study of many-body quantum dynamics.

12.2 Extensions to the Dicke model

The Dicke model and schemes of cavity-assisted Raman transitions that emulate such a model, or similar models, have generated lots of interest in recent years [51,84,85,208], with extensions such as the combination of spin and spatial degrees of freedom [73,74,209], multiple cavity modes [74,75] or even multiple cavities [76,77], and implementations in other schemes [210,211], in particular in trapped ions [212–216]. Motivations for such research includes the interest in phase transitions and novel states of matter described in this thesis [76,77,217–219], as well as being able to engineer spin glass physics [74,75,220,221] and quantum chaotic systems [216,222,223] that could potentially act as simulators for information scrambling in black holes [216,224,225]. The addition of spinor physics to these many-body cavity QED models, and the range of possibilities that would bring, is something that is just starting to be explored with experiments [163] and theory [164], along, of course, with the work detailed in this thesis. In this Section I discuss the flexibility that the methods in this thesis allow in terms of adding extra terms, in particular spinor terms, to the Hamiltonian. I talk in general terms about the resultant possibilities, as well as considering one specific limit where preliminary investigation has found interesting physics.

12.2.1 Augmenting the Dicke model with extra terms

Chapter 6 showed how the addition of the dispersive coupling can produce interesting and novel dynamics to the Dicke model. Chapter 7 discussed the extra intrigue added to the dynamical systems picture by simply relaxing the condition $\lambda_+ = \lambda_-$. The question is then what other additional terms can do.

Modulation of the coupling can be shown to destabilise the superradiant state such that increasing the coupling strength takes the system into superradiance, out of superradiance and then back into a second region of superradiance [226–228]. Such a scheme could be easily produced using a toolbox of cavity-assisted Raman transitions.

There is a huge variety of additional terms that can be added to such models with creative use of the tools available in cavity QED. One might expect that this means there is a huge variety of exciting and novel physics waiting to be explored.

Given the nature of this thesis, and its focus on spinor particles, the addition of distinctly spinor operators to the Dicke model is an obvious place to start. Our full derivation for the spin-1 Dicke model, before our assumption of a large detuning, included terms such as a quadratic cavity mediated light shift, operators that couple the two atomic end states without cavity involvement, and exchanges of excitations in entirely new ways. Terms of the form $\hat{a}\hat{q}_{xz}$, for example, annihilate a cavity excitation whilst moving the atomic population in a superposition of *both directions*. A Dicke model including those terms would therefore evolve in ways that the two-level system version cannot. This might allow for fundamentally different phases for the system, or perhaps alter the phase transition behaviour between different phases. We now give an example of how these extra terms produce different physics.

12.2.2 Superradiance shelving

Let us consider a single spin-1 atom under the Dicke Hamiltonian where we have taken $\omega_0 = 0$ and added a quadratic Zeeman shift

$$\hat{H} = \omega\hat{a}^\dagger\hat{a} + q\left|0\right\rangle\left\langle 0\right| + \frac{\lambda}{\sqrt{2}}(\hat{a}^\dagger + \hat{a})(\hat{\sigma}_+ + \hat{\sigma}_-). \tag{12.1}$$

Let us assume initially that the cavity field is empty, and that we start with the atom in one of the end magnetic states $|\pm 1\rangle$. The action of the Hamiltonian is then

$$\hat{H}\left|0\right\rangle \otimes \left|-1\right\rangle = \lambda\left|1\right\rangle \otimes \left|0\right\rangle \tag{12.2}$$

$$\hat{H}\left|0\right\rangle \otimes \left|+1\right\rangle = \lambda\left|1\right\rangle \otimes \left|0\right\rangle. \tag{12.3}$$

Both states produce a single photon and move to the central magnetic state. If we instead start with the superposition $\sqrt{1/2}(|-1\rangle - |1\rangle)$ then we can see that these two contributions will destructively interfere. This means that this anti-symmetric combination, due to the symmetry of the Hamiltonian in the two states, is blocked from producing any photons. If we start in the state $|-1\rangle$, we are half overlapped with that dark state and so the evolution will produce such a state half of the time heralded by the cavity output flux, as shown in Figure 12.1a.

We now consider the addition of a small ω_0 and direct coupling between $|-1\rangle \leftrightarrow$

$|1\rangle$ at strength h

$$\hat{H} = \omega\hat{a}^\dagger\hat{a} + \omega_0\hat{\sigma}_z + q\,|0\rangle\langle 0| + \frac{\lambda}{\sqrt{2}}(\hat{a}^\dagger + \hat{a})(\hat{\sigma}_+ + \hat{\sigma}_-) + h(\hat{\sigma}_+^2 + \hat{\sigma}_-^2). \tag{12.4}$$

The addition of the linear Zeeman shift does not break the coexistence of the bright and dark state, but instead provides a small coupling between the two that allows the state to jump between them. The dark state is destabilised and switches back to the bright state reasonably quickly, whilst the bright state appears to be much more stable. A significant value for h helps promote symmetry in the superradiant state and so encourages switches and stabilises the dark state. Figure 12.1b shows we have periods of strong emission interspersed with shorter periods without any emission. The process behind this is similar to electron shelving [229–231], yet here, the emission is superradiant in nature.

This quadratic Zeeman shift could be added with an auxiliary field, and the Raman transitions between $|-1\rangle \leftrightarrow |1\rangle$ could also be added on top of the Dicke model, but both of those terms also arise naturally in our model if we reduce the detuning such that the separation between the excited-state hyperfine levels is important. We can thus consider what the other terms in Equation 7.32 do to our picture. The quadratic cavity mediated light shift surely enhances the robustness of the system since it is similarly symmetric to $|\pm 1\rangle$ and inhibits the production of photons. $\hat{q}_{yz}$ is also symmetric to the two outer magnetic states, so should not impact the existence of either state. $\hat{q}_{xz}$ is not symmetric and so will also couple the dark and bright states slightly. This means that the full system of our derived Dicke model, with $\omega_0 \approx 0$, automatically gives us this superradiant blinking if we move to lower detuning. Simply adding spinor terms to the Hamiltonian creates a distinct change in response from the model.

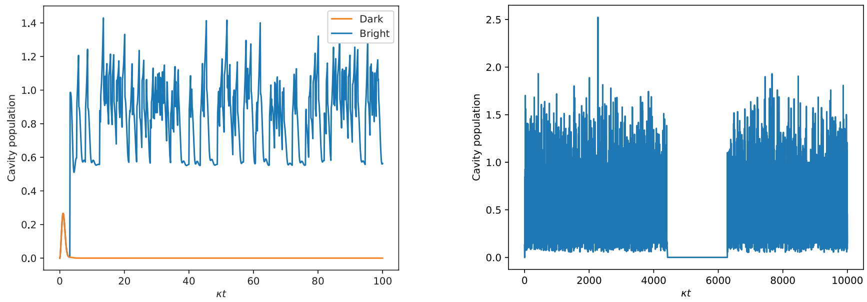

(a) (b)

Figure 12.1: The presence of (a) a bright state and dark state in a completely symmetric model and (b) switches between them with a slight asymmetry added to the Hamiltonian. Parameters for (a) are $\{\omega, \omega_0, q, \lambda, h\}/\kappa = \{1.0, 0.0, -2.0, 1.0, 0.0\}$ and (b) are $\{\omega, \omega_0, q, \lambda, h\}/\kappa = \{1.0, 0.05, -2.0, 1.0, 2.0\}$.

The interest in this result is the implication that this symmetric Dicke model protects anti-symmetric combinations for the spin. Moving to a collective picture, we would like to investigate whether such anti-symmetric dark states exist, and, if they do, their properties and the feasibility of preparing them.

12.3 Implementations in alternative configurations

This thesis used "traditional" cavity QED configurations throughout. However, the methods we describe are certainly not limited in such a way. We could instead trap atoms in the evanescent fields of, for example, nanoscale or photonic crystal waveguides. Whilst such systems have much more difficulty trapping large arrays as discussed in much of this thesis, the coupling for the atom to the field can be *much* stronger. This means that, even with the large detunings our methods generally use, we are not reliant on the $\sqrt{N}$ enhancement of the effective coupling. Instead, we can achieve interesting physics with small ensembles or even a *single* atom. This allows us to think of very different regimes. In this Section, I discuss examples of how our methods might be applied to such systems.

12.3.1 Superradiant pulses of exact photon number

The concept is fairly simple: trap a single ^{133}Cs atom next to a nanoscale cavity, where atom-cavity coupling of several GHz is possible [29, 30]. Alternatively, fabrication of cavities formed by polished optical fibre ends, such that the outputs of the cavity lead directly into a propagating fibre, have shown promising coupling strengths [232–234]. In both cases, we wish for the light to be emitted in one direction and so one of the mirrors should be much more transmissive than the other, as in [30].

Once we have such a system, we drive detuned Raman transitions with a laser and the fibre mode. If we pump our ^{133}Cs atom into the $F = 4$ manifold, we can thus produce a Tavis-Cummings model and, with an initial state $|4, 4\rangle$, an associated superradiant decay *for a single atom*. We can thus simulate the *collective* behaviour of a small, in this case eight spin-1/2 particles, ensemble without the added complexity of actually trapping and coupling a small ensemble.

In the direction of propagation, we have a superradiant pulse of *exactly* eight photons. Alternative preparation of the state into other magnetic sub-levels allows for different numbers of photons in that output pulse. An atom in a superposition state produces a superposition of Fock states, and so this method allows for the production of arbitrary Fock states and superpositions of Fock states with small photon numbers [235].

If we were to move to a multi-atom picture, this would allow for larger effective ensembles and the production of larger Fock states. Producing superpositions of

Fock states with multiple atoms becomes more complex because of the more complex collective picture for spinor particles. We would require superpositions of the magnetic number, *not* of the spin length. Each spin length produces a Fock state in the output field, but correlated to the final state of the spins such that the superposition of spin length states produces a mixed state of Fock states in the output field.

There are also other species outside of the alkali atom family with higher spin. Assuming these species have the same intrinsic symmetries to the dipole operator that allows us to simplify the higher spin model to a Dicke model, as in Section 7.1.1, then implementing the discussed scheme would allow an even larger effective ensemble size for a single atom. If we consider, for example, dysprosium atoms, which have electron spin $J = 8$, we might expect to be able to consider the generation of arbitrary superpositions of Fock states with a basis size up to 16.

12.3.2 Spinor models with tuneable range interactions

An emerging field in quantum optics is the interaction of trapped atoms with photonic crystal waveguide systems [200, 236–239]. One option in such systems is to trap an atom in the evanescent field of the waveguide where the atomic transition is within the band gap of the photonic crystal waveguide. This means that light of the atomic transition frequency cannot propagate along the waveguide. Instead, the photon must remain localised around the position of the atom, at which point the "defect" of the atom allows the photon to exist. If another atom is placed a short distance away along the waveguide, the photon can tunnel between the atoms. Thus, in a way that may sound familiar given what has been discussed in the thesis, the atoms interact mediated by photons.

Our engineered spinor models allow for interactions tuneable in form and in strength, but they are intrinsically infinite range because the atoms are coupled to the same cavity mode. Photonic crystal waveguides allow for interactions tuneable in form, strength *and* range. The interactions are mediated by the tunnelling, and the tunnelling interaction has an exponential form, so our range has exponential falloff. This could be tuned such that tunnelling happens only over one site, or that the interactions are effectively infinite range. It can also be theorised that, by overlapping different drives, sums of those exponentials can be used to approximate other types of interactions [200]. We note that non-infinite range interactions may also be possible with multimode cavity QED, where the different shapes of the various modes allow for atoms to have a different set of couplings to those modes [75, 220]. Such a setup is also amenable to our methods.

With a toolbox of atoms coupled to a 2D photonic crystal waveguide and interactions that we can tune so precisely, we can engineer all sorts of models for interacting spins. Using spinor atoms in this context, we could build spinor interaction models with all of this flexibility. This could be used to simulate condensed matter physics, probe topological physics and potentially explore new realms of physics interesting and useful in their own right.

Chapter 13

Conclusion

The interaction of light and matter has informed and influenced some of the most famous experiments in the history of physics. From Newton's use of a prism to split out the spectrum of light to the discovery of the photoelectric effect, and all the way to modern day searches for dark matter and the size of an electron, table top experiments making use of matter and light have been able to tell us fundamental truths about the very makeup of the universe. I do not, of course, wish to compare the research in this thesis with such lofty accomplishments; I fear that the thesis would not hold much weight under such comparisons. I instead wish to make the point of the fundamental importance of understanding and applying these light-matter interactions.

This thesis has described simulations of fundamental models of physics and proposed how to apply those methods and discoveries. The states that could be prepared using these proposals have practical applications, but are also of great interest to fundamental science. These many-body entangled states are one of the more mysterious areas of quantum mechanics and so, efficient production of such states would give scientists a resource to investigate the fundamental nature of entanglement.

The methods and concepts developed in our research have a wide range of applications. These applications could provide resources for quantum metrology and quantum information, but also resources to help answer questions on such varied topics as macroscopic superposition states, topological matter and chaos theory. Unlocking the secrets of the universe may seem like a grandiose and imposing goal, but when considered one problem at a time through the right lens with the right toolbox, it is, perhaps, one that is not so impossible after all.

Bibliography

[1] Scully, M. O. & Zubairy, M. S. *Quantum Optics* (Cambridge University Press, 1997).

[2] Hanbury Brown, R. & Twiss, R. Q. Correlation between photons in two coherent beams of light. *Nature* **177**, 27–29 (1956). URL `http://dx.doi.org/10.1038/177027a0`.

[3] Sudarshan, E. C. G. Equivalence of semiclassical and quantum mechanical descriptions of statistical light beams. *Phys. Rev. Lett.* **10**, 277–279 (1963). URL `https://link.aps.org/doi/10.1103/PhysRevLett.10.277`.

[4] Glauber, R. J. The quantum theory of optical coherence. *Phys. Rev.* **130**, 2529–2539 (1963). URL `https://link.aps.org/doi/10.1103/PhysRev.130.2529`.

[5] Glauber, R. J. Coherent and incoherent states of the radiation field. *Phys. Rev.* **131**, 2766–2788 (1963). URL `https://link.aps.org/doi/10.1103/PhysRev.131.2766`.

[6] Fox, M. *Quantum Optics: An Introduction* (Oxford University Press, 2006).

[7] Walls, D. F. & Milburn, G. J. *Quantum Optics* (Springer-Verlag Berlin Heidelberg, 1994).

[8] Carmichael, H. J. *Statistical Methods in Quantum Optics 1* (Springer-Verlag Berlin Heidelberg, 1999).

[9] Gardiner, C. & Zoller, P. *Quantum Noise* (Springer-Verlag Berlin Heidelberg, 2004).

[10] Carmichael, H. J. *Statistical Methods in Quantum Optics 2* (Springer-Verlag Berlin Heidelberg, 2008).

[11] Foot, C. J. *Atomic Physics* (Oxford University Press, 2005).

[12] Lewenstein, M., Sanpera, A. & Ahufinger, V. *Ultracold Atoms in Optical Lattices* (Oxford University Press, 2012).

[13] Yukawa, E., Ueda, M. & Nemoto, K. Classification of spin-nematic squeezing in spin-1 collective atomic systems. *Phys. Rev. A* **88**, 033629 (2013). URL `http://link.aps.org/doi/10.1103/PhysRevA.88.033629`.

[14] Hamley, C. D., Gerving, C. S., Hoang, T. M., Bookjans, E. M. & Chapman, M. S. Spin-nematic squeezed vacuum in a quantum gas. *Nat. Phys.* **8**, 305–308 (2012). URL `http://dx.doi.org/10.1038/nphys2245`.

[15] Huang, Y., Xiong, H.-N., Sun, Z. & Wang, X. Generation and storage of spin-nematic squeezing in a spinor Bose-Einstein condensate. *Phys. Rev. A* **92**, 023622 (2015). URL `http://link.aps.org/doi/10.1103/PhysRevA.92.023622`.

[16] Arecchi, F. T., Courtens, E., Gilmore, R. & Thomas, H. Atomic coherent states in quantum optics. *Phys. Rev. A* **6**, 2211–2237 (1972). URL `http://link.aps.org/doi/10.1103/PhysRevA.6.2211`.

[17] Gross, C. Spin squeezing, entanglement and quantum metrology with Bose–Einstein condensates. *J. Phys. B* **45**, 103001 (2012). URL `http://stacks.iop.org/0953-4075/45/i=10/a=103001`.

[18] Lee, C. T. *Q* representation of the atomic coherent states and the origin of fluctuations in superfluorescence. *Phys. Rev. A* **30**, 3308–3310 (1984). URL `https://link.aps.org/doi/10.1103/PhysRevA.30.3308`.

[19] Kitagawa, M. & Ueda, M. Squeezed spin states. *Phys. Rev. A* **47**, 5138–5143 (1993). URL `http://link.aps.org/doi/10.1103/PhysRevA.47.5138`.

[20] Ma, J., Wang, X., Sun, C. & Nori, F. Quantum spin squeezing. *Phys. Rep.* **509**, 89 – 165 (2011). URL `http://www.sciencedirect.com/science/article/pii/S0370157311002201`.

[21] Wineland, D. J., Bollinger, J. J., Itano, W. M., Moore, F. L. & Heinzen, D. J. Spin squeezing and reduced quantum noise in spectroscopy. *Phys. Rev. A* **46**, R6797–R6800 (1992). URL `http://link.aps.org/doi/10.1103/PhysRevA.46.R6797`.

[22] Pezzè, L., Smerzi, A., Oberthaler, M. K., Schmied, R. & Treutlein, P. Quantum metrology with nonclassical states of atomic ensembles. *Rev. Mod. Phys.* **90**, 035005 (2018). URL `https://link.aps.org/doi/10.1103/RevModPhys.90.035005`.

[23] Zhang, Z. & Duan, L. M. Quantum metrology with Dicke squeezed states. *New J. Phys.* **16**, 103037 (2014). URL `http://stacks.iop.org/1367-2630/16/i=10/a=103037`.

[24] Duan, L.-M. Entanglement detection in the vicinity of arbitrary Dicke states. *Phys. Rev. Lett.* **107**, 180502 (2011). URL `http://link.aps.org/doi/10.1103/PhysRevLett.107.180502`.

[25] Vetsch, E. *et al.* Optical interface created by laser-cooled atoms trapped in the evanescent field surrounding an optical nanofiber. *Phys. Rev. Lett.* **104**, 203603 (2010). URL `https://link.aps.org/doi/10.1103/PhysRevLett.104.203603`.

[26] Kato, S. & Aoki, T. Strong coupling between a trapped single atom and an all-fiber cavity. *Phys. Rev. Lett.* **115**, 093603 (2015). URL `https://link.aps.org/doi/10.1103/PhysRevLett.115.093603`.

[27] Aoki, T. *et al.* Observation of strong coupling between one atom and a monolithic microresonator. *Nature* **443**, 671–674 (2006). URL `http://dx.doi.org/10.1038/nature05147`.

[28] Junge, C., O'Shea, D., Volz, J. & Rauschenbeutel, A. Strong coupling between single atoms and nontransversal photons. *Phys. Rev. Lett.* **110**, 213604 (2013). URL `http://link.aps.org/doi/10.1103/PhysRevLett.110.213604`.

[29] Thompson, J. D. *et al.* Coupling a single trapped atom to a nanoscale optical cavity. *Science* **340**, 1202–1205 (2013). URL `http://science.sciencemag.org/content/340/6137/1202`.

[30] Tiecke, T. G. *et al.* Nanophotonic quantum phase switch with a single atom. *Nature* **508**, 241–244 (2014). URL `http://dx.doi.org/10.1038/nature13188`.

[31] Fraval, E., Sellars, M. J. & Longdell, J. J. Method of extending hyperfine coherence times in $\mathrm{Pr}^{3+}:\mathrm{Y}_2\mathrm{SiO}_5$. *Phys. Rev. Lett.* **92**, 077601 (2004). URL `http://link.aps.org/doi/10.1103/PhysRevLett.92.077601`.

[32] Jelezko, F. & Wrachtrup, J. Single defect centres in diamond: A review. *Phys. Status Solidi A* **203**, 3207–3225 (2006). URL `https://onlinelibrary.wiley.com/doi/abs/10.1002/pssa.200671403`.

[33] Devoret, M. H. & Martinis, J. M. Implementing qubits with superconducting integrated circuits. *Quantum Inf. Proc.* **3**, 163–203 (2004). URL `http://dx.doi.org/10.1007/s11128-004-3101-5`.

[34] Jaynes, E. T. & Cummings, F. W. Comparison of quantum and semiclassical radiation theories with application to the beam maser. *Proc. IEEE* **51**, 89–109 (1963). URL `https://ieeexplore.ieee.org/document/1443594`.

[35] Paul, H. Induzierte emission bei starker einstrahlung. *Ann. Phys. (Leipzig)* **466**, 411–412 (1963). URL `https://doi.org/10.1002/andp.19634660710`.

[36] Tian, L. & Carmichael, H. J. Quantum trajectory simulations of two-state behavior in an optical cavity containing one atom. *Phys. Rev. A* **46**, R6801–R6804 (1992). URL `https://link.aps.org/doi/10.1103/PhysRevA.46.R6801`.

[37] Birnbaum, K. M. *et al.* Photon blockade in an optical cavity with one trapped atom. *Nature* **436**, 87–90 (2005). URL `http://dx.doi.org/10.1038/nature03804`.

[38] Carmichael, H. J. Breakdown of photon blockade: A dissipative quantum phase transition in zero dimensions. *Phys. Rev. X* **5**, 031028 (2015). URL `https://link.aps.org/doi/10.1103/PhysRevX.5.031028`.

[39] Thompson, R. J., Rempe, G. & Kimble, H. J. Observation of normal-mode splitting for an atom in an optical cavity. *Phys. Rev. Lett.* **68**, 1132–1135 (1992). URL `https://link.aps.org/doi/10.1103/PhysRevLett.68.1132`.

[40] Boca, A. *et al.* Observation of the vacuum Rabi spectrum for one trapped atom. *Phys. Rev. Lett.* **93**, 233603 (2004). URL `https://link.aps.org/doi/10.1103/PhysRevLett.93.233603`.

[41] Brune, M. *et al.* Quantum Rabi oscillation: A direct test of field quantization in a cavity. *Phys. Rev. Lett.* **76**, 1800–1803 (1996). URL `https://link.aps.org/doi/10.1103/PhysRevLett.76.1800`.

[42] Wallraff, A. *et al.* Strong coupling of a single photon to a superconducting qubit using circuit quantum electrodynamics. *Nature* **431**, 162–167 (2004). URL `http://dx.doi.org/10.1038/nature02851`.

[43] Peter, E. *et al.* Exciton-photon strong-coupling regime for a single quantum dot embedded in a microcavity. *Phys. Rev. Lett.* **95**, 067401 (2005). URL `https://link.aps.org/doi/10.1103/PhysRevLett.95.067401`.

[44] Kaluzny, Y., Goy, P., Gross, M., Raimond, J. M. & Haroche, S. Observation of self-induced Rabi oscillations in two-level atoms excited inside a resonant cavity: The ringing regime of superradiance. *Phys. Rev. Lett.* **51**, 1175–1178 (1983). URL `https://link.aps.org/doi/10.1103/PhysRevLett.51.1175`.

[45] Dicke, R. H. Coherence in spontaneous radiation processes. *Phys. Rev.* **93**, 99–110 (1954). URL `http://link.aps.org/doi/10.1103/PhysRev.93.99`.

[46] Hepp, K. & Lieb, E. H. On the superradiant phase transition for molecules in a quantized radiation field: the Dicke maser model. *Ann. Phys. (N.Y.)* **76**, 360 – 404 (1973). URL `http://www.sciencedirect.com/science/article/pii/0003491673900390`.

[47] Wang, Y. K. & Hioe, F. T. Phase transition in the Dicke model of superradiance. *Phys. Rev. A* **7**, 831–836 (1973). URL `http://link.aps.org/doi/10.1103/PhysRevA.7.831`.

[48] Hepp, K. & Lieb, E. H. Equilibrium statistical mechanics of matter interacting with the quantized radiation field. *Phys. Rev. A* **8**, 2517–2525 (1973). URL `http://link.aps.org/doi/10.1103/PhysRevA.8.2517`.

[49] Hioe, F. T. Phase transitions in some generalized Dicke models of superradiance. *Phys. Rev. A* **8**, 1440–1445 (1973). URL `https://link.aps.org/doi/10.1103/PhysRevA.8.1440`.

[50] Carmichael, H. J., Gardiner, C. W. & Walls, D. F. Higher order corrections to the Dicke superradiant phase transition. *Phys. Lett. A* **46**, 47–48 (1973). URL `http://www.sciencedirect.com/science/article/pii/0375960173906798`.

[51] Kirton, P., Roses, M. M., Keeling, J. & Dalla Torre, E. G. Introduction to the Dicke model: From equilibrium to nonequilibrium, and vice versa. *Adv. Quantum Technol.* 1800043 (2018). URL `https://onlinelibrary.wiley.com/doi/abs/10.1002/qute.201800043`.

[52] Lambert, N., Emary, C. & Brandes, T. Entanglement and the phase transition in single-mode superradiance. *Phys. Rev. Lett.* **92**, 073602 (2004). URL `http://link.aps.org/doi/10.1103/PhysRevLett.92.073602`.

[53] Dimer, F., Estienne, B., Parkins, A. S. & Carmichael, H. J. Proposed realization of the Dicke-model quantum phase transition in an optical cavity QED system. *Phys. Rev. A* **75**, 013804 (2007). URL `https://link.aps.org/doi/10.1103/PhysRevA.75.013804`.

[54] Rzążewski, K., Wódkiewicz, K. & Żakowicz, W. Phase transitions, two-level atoms, and the A^2 term. *Phys. Rev. Lett.* **35**, 432–434 (1975). URL `http://link.aps.org/doi/10.1103/PhysRevLett.35.432`.

[55] Knight, J. M., Aharonov, Y. & Hsieh, G. T. C. Are super-radiant phase transitions possible? *Phys. Rev. A* **17**, 1454–1462 (1978). URL `https://link.aps.org/doi/10.1103/PhysRevA.17.1454`.

[56] Keeling, J. Coulomb interactions, gauge invariance, and phase transitions of the dicke model. *J. Phys. Condens. Matter* **19**, 295213 (2007). URL `https://doi.org/10.1088%2F0953-8984%2F19%2F29%2F295213`.

[57] Nataf, P. & Ciuti, C. No-go theorem for superradiant quantum phase transitions in cavity qed and counter-example in circuit qed. *Nat. Commun.* **1**, 72 (2010). URL `https://doi.org/10.1038/ncomms1069`.

[58] De Liberato, S. Light-matter decoupling in the deep strong coupling regime: The breakdown of the purcell effect. *Phys. Rev. Lett.* **112**, 016401 (2014). URL `https://link.aps.org/doi/10.1103/PhysRevLett.112.016401`.

[59] Vukics, A., Grießer, T. & Domokos, P. Elimination of the a-square problem from cavity qed. *Phys. Rev. Lett.* **112**, 073601 (2014). URL `https://link.aps.org/doi/10.1103/PhysRevLett.112.073601`.

[60] Grießer, T., Vukics, A. & Domokos, P. Depolarization shift of the superradiant phase transition. *Phys. Rev. A* **94**, 033815 (2016). URL `https://link.aps.org/doi/10.1103/PhysRevA.94.033815`.

[61] Jaako, T., Xiang, Z.-L., Garcia-Ripoll, J. J. & Rabl, P. Ultrastrong-coupling phenomena beyond the dicke model. *Phys. Rev. A* **94**, 033850 (2016). URL `https://link.aps.org/doi/10.1103/PhysRevA.94.033850`.

[62] Chan, H. W., Black, A. T. & Vuletić, V. Observation of collective-emission-induced cooling of atoms in an optical cavity. *Phys. Rev. Lett.* **90**, 063003 (2003). URL `https://link.aps.org/doi/10.1103/PhysRevLett.90.063003`.

[63] Black, A. T., Chan, H. W. & Vuletić, V. Observation of collective friction forces due to spatial self-organization of atoms: From rayleigh to bragg scattering. *Phys. Rev. Lett.* **91**, 203001 (2003). URL `https://link.aps.org/doi/10.1103/PhysRevLett.91.203001`.

[64] Arnold, K. J., Baden, M. P. & Barrett, M. D. Self-organization threshold scaling for thermal atoms coupled to a cavity. *Phys. Rev. Lett.* **109**, 153002 (2012). URL `http://link.aps.org/doi/10.1103/PhysRevLett.109.153002`.

[65] Ritsch, H., Domokos, P., Brennecke, F. & Esslinger, T. Cold atoms in cavity-generated dynamical optical potentials. *Rev. Mod. Phys.* **85**, 553–601 (2013). URL `https://link.aps.org/doi/10.1103/RevModPhys.85.553`.

[66] Nagy, D., Kónya, G., Szirmai, G. & Domokos, P. Dicke-model phase transition in the quantum motion of a Bose-Einstein condensate in an optical cavity. *Phys. Rev. Lett.* **104**, 130401 (2010). URL `http://link.aps.org/doi/10.1103/PhysRevLett.104.130401`.

[67] Baumann, K., Guerlin, C., Brennecke, F. & Esslinger, T. Dicke quantum phase transition with a superfluid gas in an optical cavity. *Nature* **464**, 1301–1306 (2010). URL `http://dx.doi.org/10.1038/nature09009`.

[68] Baumann, K., Mottl, R., Brennecke, F. & Esslinger, T. Exploring symmetry breaking at the Dicke quantum phase transition. *Phys. Rev. Lett.* **107**, 140402 (2011). URL `http://link.aps.org/doi/10.1103/PhysRevLett.107.140402`.

[69] Brennecke, F. *et al.* Real-time observation of fluctuations at the driven-dissipative Dicke phase transition. *Proc. Natl. Acad. Sci. USA* **110**, 11763–11767 (2013). URL `http://www.pnas.org/content/110/29/11763`. `http://www.pnas.org/content/110/29/11763.full.pdf`.

[70] Klinder, J., Keßler, H., Wolke, M., Mathey, L. & Hemmerich, A. Dynamical phase transition in the open Dicke model. *Proc. Natl. Acad. Sci. USA* **112**, 3290–3295 (2015). URL `http://www.pnas.org/content/112/11/3290`.

[71] Zhang, Z. *et al.* Nonequilibrium phase transition in a spin-1 Dicke model. *Optica* **4**, 424–429 (2017).

[72] Zhang, Z. *et al.* Dicke-model simulation via cavity-assisted Raman transitions. *Phys. Rev. A* **97**, 043858 (2018). URL `https://link.aps.org/doi/10.1103/PhysRevA.97.043858`.

[73] Landini, M. *et al.* Formation of a spin texture in a quantum gas coupled to a cavity. *Phys. Rev. Lett.* **120**, 223602 (2018). URL `https://link.aps.org/doi/10.1103/PhysRevLett.120.223602`.

[74] Kroeze, R. M., Guo, Y., Vaidya, V. D., Keeling, J. & Lev, B. L. Spinor self-ordering of a quantum gas in a cavity. *Phys. Rev. Lett.* **121**, 163601 (2018). URL `https://link.aps.org/doi/10.1103/PhysRevLett.121.163601`.

[75] Vaidya, V. D. *et al.* Tunable-range, photon-mediated atomic interactions in multimode cavity QED. *Phys. Rev. X* **8**, 011002 (2018). URL `https://link.aps.org/doi/10.1103/PhysRevX.8.011002`.

[76] Léonard, J., Morales, A., Zupancic, P., Esslinger, T. & Donner, T. Supersolid formation in a quantum gas breaking a continuous translational symmetry. *Nature* **543**, 87–90 (2017). URL `http://dx.doi.org/10.1038/nature21067`.

[77] Léonard, J., Morales, A., Zupancic, P., Donner, T. & Esslinger, T. Monitoring and manipulating Higgs and Goldstone modes in a supersolid quantum gas. *Science* **358**, 1415 (2017). URL `http://science.sciencemag.org/content/358/6369/1415.abstract`.

[78] Keeling, J., Bhaseen, M. J. & Simons, B. D. Collective dynamics of Bose-Einstein condensates in optical cavities. *Phys. Rev. Lett.* **105**, 043001 (2010). URL `http://link.aps.org/doi/10.1103/PhysRevLett.105.043001`.

[79] Bhaseen, M. J., Mayoh, J., Simons, B. D. & Keeling, J. Dynamics of nonequilibrium Dicke models. *Phys. Rev. A* **85**, 013817 (2012). URL `http://link.aps.org/doi/10.1103/PhysRevA.85.013817`.

[80] Grimsmo, A. L. & Parkins, A. S. Dissipative Dicke model with nonlinear atom–photon interaction. *J. Phys. B* **46**, 224012 (2013). URL `http://stacks.iop.org/0953-4075/46/i=22/a=224012`.

[81] Grimsmo, A. L. & Parkins, S. Cavity-QED simulation of qubit-oscillator dynamics in the ultrastrong-coupling regime. *Phys. Rev. A* **87**, 033814 (2013). URL `http://link.aps.org/doi/10.1103/PhysRevA.87.033814`.

[82] Stitely, K. C. *Nonlinear Dynamics and Bifurcations of a Semiclassical Unbalanced Dicke Model.* BSc Hons. dissertation, The University of Auckland (2018).

[83] Steck, D. A. Rubidium 87 D line data (2001). URL `https://steck.us/alkalidata/rubidium87numbers.pdf`.

[84] Dalla Torre, E. G., Shchadilova, Y., Wilner, E. Y., Lukin, M. D. & Demler, E. Dicke phase transition without total spin conservation. *Phys. Rev. A* **94**, 061802 (2016). URL `http://link.aps.org/doi/10.1103/PhysRevA.94.061802`.

[85] Gelhausen, J., Buchhold, M. & Strack, P. Many-body quantum optics with decaying atomic spin states: (γ, κ) Dicke model. *Phys. Rev. A* **95**, 063824 (2017). URL `https://link.aps.org/doi/10.1103/PhysRevA.95.063824`.

[86] Private correspondence between Chern Hui Lee, the author and Scott Parkins (2016).

[87] Private correspondence between Zhiqiang Zhang and the author (2016).

[88] Baden, M. P., Arnold, K. J., Grimsmo, A. L., Parkins, S. & Barrett, M. D. Realization of the Dicke model using cavity-assisted Raman transitions. *Phys. Rev. Lett.* **113**, 020408 (2014). URL `http://link.aps.org/doi/10.1103/PhysRevLett.113.020408`.

[89] Tino, G. & Kasevich, M. *Atom Interferometry.* EBL-Schweitzer (IOS Press, 2014).

[90] Bollinger, J. J. ., Itano, W. M., Wineland, D. J. & Heinzen, D. J. Optimal frequency measurements with maximally correlated states. *Phys. Rev. A* **54**, R4649–R4652 (1996). URL `http://link.aps.org/doi/10.1103/PhysRevA.54.R4649`.

[91] Tóth, G. & Apellaniz, I. Quantum metrology from a quantum information science perspective. *J. Phys. A* **47**, 424006 (2014). URL `http://stacks.iop.org/1751-8121/47/i=42/a=424006`.

[92] Wineland, D. J., Bollinger, J. J., Itano, W. M. & Heinzen, D. J. Squeezed atomic states and projection noise in spectroscopy. *Phys. Rev. A* **50**, 67–88 (1994). URL `http://link.aps.org/doi/10.1103/PhysRevA.50.67`.

[93] Gross, C., Zibold, T., Nicklas, E., Estève, J. & Oberthaler, M. K. Nonlinear atom interferometer surpasses classical precision limit. *Nature* **464**, 1165–1169 (2010). URL `http://dx.doi.org/10.1038/nature08919`.

[94] Riedel, M. F. *et al.* Atom-chip-based generation of entanglement for quantum metrology. *Nature* **464**, 1170–1173 (2010). URL `http://dx.doi.org/10.1038/nature08988`.

[95] Bookjans, E. M., Hamley, C. D. & Chapman, M. S. Strong quantum spin correlations observed in atomic spin mixing. *Phys. Rev. Lett.* **107**, 210406 (2011). URL `https://link.aps.org/doi/10.1103/PhysRevLett.107.210406`.

[96] Ockeloen, C. F., Schmied, R., Riedel, M. F. & Treutlein, P. Quantum metrology with a scanning probe atom interferometer. *Phys. Rev. Lett.* **111**, 143001 (2013). URL `http://link.aps.org/doi/10.1103/PhysRevLett.111.143001`.

[97] Muessel, W., Strobel, H., Linnemann, D., Hume, D. B. & Oberthaler, M. K. Scalable spin squeezing for quantum-enhanced magnetometry with Bose-Einstein condensates. *Phys. Rev. Lett.* **113**, 103004 (2014). URL `http://link.aps.org/doi/10.1103/PhysRevLett.113.103004`.

[98] Muessel, W. *et al.* Twist-and-turn spin squeezing in Bose-Einstein condensates. *Phys. Rev. A* **92**, 023603 (2015). URL `http://link.aps.org/doi/10.1103/PhysRevA.92.023603`.

[99] Linnemann, D. *et al.* Quantum-enhanced sensing based on time reversal of nonlinear dynamics. *Phys. Rev. Lett.* **117**, 013001 (2016). URL `http://link.aps.org/doi/10.1103/PhysRevLett.117.013001`.

[100] Kruse, I. *et al.* Improvement of an atomic clock using squeezed vacuum. *Phys. Rev. Lett.* **117**, 143004 (2016). URL `http://link.aps.org/doi/10.1103/PhysRevLett.117.143004`.

[101] Louchet-Chauvet, A. *et al.* Entanglement-assisted atomic clock beyond the projection noise limit. *New J. Phys.* **12**, 065032 (2010). URL `http://stacks.iop.org/1367-2630/12/i=6/a=065032`.

[102] Schleier-Smith, M. H., Leroux, I. D. & Vuletić, V. Squeezing the collective spin of a dilute atomic ensemble by cavity feedback. *Phys. Rev. A* **81**, 021804 (2010). URL `http://link.aps.org/doi/10.1103/PhysRevA.81.021804`.

[103] Leroux, I. D., Schleier-Smith, M. H. & Vuletić, V. Implementation of cavity squeezing of a collective atomic spin. *Phys. Rev. Lett.* **104**, 073602 (2010). URL `http://link.aps.org/doi/10.1103/PhysRevLett.104.073602`.

[104] Chen, Z., Bohnet, J. G., Sankar, S. R., Dai, J. & Thompson, J. K. Conditional spin squeezing of a large ensemble via the vacuum Rabi splitting. *Phys. Rev. Lett.* **106**, 133601 (2011). URL `http://link.aps.org/doi/10.1103/PhysRevLett.106.133601`.

[105] Sewell, R. J. *et al.* Magnetic sensitivity beyond the projection noise limit by spin squeezing. *Phys. Rev. Lett.* **109**, 253605 (2012). URL `http://link.aps.org/doi/10.1103/PhysRevLett.109.253605`.

[106] Behbood, N. *et al.* Feedback cooling of an atomic spin ensemble. *Phys. Rev. Lett.* **111**, 103601 (2013). URL `http://link.aps.org/doi/10.1103/PhysRevLett.111.103601`.

[107] Hosten, O., Engelsen, N. J., Krishnakumar, R. & Kasevich, M. A. Measurement noise 100 times lower than the quantum-projection limit using entangled atoms. *Nature* **529**, 505–508 (2016). URL `http://dx.doi.org/10.1038/nature16176`.

[108] Hald, J., Sørensen, J. L., Schori, C. & Polzik, E. S. Spin squeezed atoms: A macroscopic entangled ensemble created by light. *Phys. Rev. Lett.* **83**, 1319–1322 (1999). URL `http://link.aps.org/doi/10.1103/PhysRevLett.83.1319`.

[109] Cox, K. C., Norcia, M. A., Weiner, J. M., Bohnet, J. G. & Thompson, J. K. Reducing collective quantum state rotation errors with reversible dephasing. *Appl. Phys. Lett.* **105** (2014). URL `http://scitation.aip.org/content/aip/journal/apl/105/26/10.1063/1.4905148`.

[110] Bohnet, J. G. *et al.* Reduced spin measurement back-action for a phase sensitivity ten times beyond the standard quantum limit. *Nat. Photon.* **8**, 731–736 (2014). URL `http://dx.doi.org/10.1038/nphoton.2014.151`.

[111] Auccaise, R. *et al.* Spin squeezing in a quadrupolar nuclei NMR system. *Phys. Rev. Lett.* **114**, 043604 (2015). URL `https://link.aps.org/doi/10.1103/PhysRevLett.114.043604`.

[112] Cox, K. C., Greve, G. P., Weiner, J. M. & Thompson, J. K. Deterministic squeezed states with collective measurements and feedback. *Phys. Rev. Lett.* **116**, 093602 (2016). URL `https://link.aps.org/doi/10.1103/PhysRevLett.116.093602`.

[113] Holland, M. J. & Burnett, K. Interferometric detection of optical phase shifts at the Heisenberg limit. *Phys. Rev. Lett.* **71**, 1355–1358 (1993). URL `http://link.aps.org/doi/10.1103/PhysRevLett.71.1355`.

[114] Krischek, R. *et al.* Useful multiparticle entanglement and sub-shot-noise sensitivity in experimental phase estimation. *Phys. Rev. Lett.* **107**, 080504 (2011). URL `http://link.aps.org/doi/10.1103/PhysRevLett.107.080504`.

[115] Raghavan, S., Pu, H., Meystre, P. & Bigelow, N. Generation of arbitrary Dicke states in spinor Bose–Einstein condensates. *Opt. Commun.* **188**, 149 – 154 (2001). URL `http://www.sciencedirect.com/science/article/pii/S0030401800011639`.

[116] Duan, L.-M. & Kimble, H. J. Efficient engineering of multiatom entanglement through single-photon detections. *Phys. Rev. Lett.* **90**, 253601 (2003). URL `http://link.aps.org/doi/10.1103/PhysRevLett.90.253601`.

[117] Stockton, J. K., van Handel, R. & Mabuchi, H. Deterministic Dicke-state preparation with continuous measurement and control. *Phys. Rev. A* **70**, 022106 (2004). URL `http://link.aps.org/doi/10.1103/PhysRevA.70.022106`.

[118] Kiesel, N., Schmid, C., Tóth, G., Solano, E. & Weinfurter, H. Experimental observation of four-photon entangled Dicke state with high fidelity. *Phys. Rev. Lett.* **98**, 063604 (2007). URL `http://link.aps.org/doi/10.1103/PhysRevLett.98.063604`.

[119] Thiel, C., von Zanthier, J., Bastin, T., Solano, E. & Agarwal, G. S. Generation of symmetric Dicke states of remote qubits with linear optics. *Phys. Rev. Lett.* **99**, 193602 (2007). URL `http://link.aps.org/doi/10.1103/PhysRevLett.99.193602`.

[120] Prevedel, R. *et al.* Experimental realization of Dicke states of up to six qubits for multiparty quantum networking. *Phys. Rev. Lett.* **103**, 020503 (2009). URL `http://link.aps.org/doi/10.1103/PhysRevLett.103.020503`.

[121] Wieczorek, W. *et al.* Experimental entanglement of a six-photon symmetric Dicke state. *Phys. Rev. Lett.* **103**, 020504 (2009). URL `http://link.aps.org/doi/10.1103/PhysRevLett.103.020504`.

[122] Haas, F., Volz, J., Gehr, R., Reichel, J. & Estève, J. Entangled states of more than 40 atoms in an optical fiber cavity. *Science* **344**, 180–183 (2014). URL `http://science.sciencemag.org/content/344/6180/180`.

[123] Lücke, B. *et al.* Detecting multiparticle entanglement of Dicke states. *Phys. Rev. Lett.* **112**, 155304 (2014). URL `http://link.aps.org/doi/10.1103/PhysRevLett.112.155304`.

[124] Luo, X.-Y. *et al.* Deterministic entanglement generation from driving through quantum phase transitions. *Science* **355**, 620–623 (2017). URL `http://science.sciencemag.org/content/355/6325/620`.

[125] Zou, Y.-Q. *et al.* Beating the classical precision limit with spin-1 Dicke states of more than 10,000 atoms. *Proc. Natl. Acad. Sci. USA* **115**, 6381–6385 (2018). URL `http://www.pnas.org/content/115/25/6381`.

[126] Luo, Y., Yu, H. & Yao, W. Deterministic preparation of Dicke states of donor nuclear spins in silicon by cooperative pumping. *Phys. Rev. B* **85**, 155304 (2012). URL `http://link.aps.org/doi/10.1103/PhysRevB.85.155304`.

[127] Shammah, N., Lambert, N., Nori, F. & De Liberato, S. Superradiance with local phase-breaking effects. *Phys. Rev. A* **96**, 023863 (2017). URL `https://link.aps.org/doi/10.1103/PhysRevA.96.023863`.

[128] Chia, A. & Parkins, A. S. Entangled-state cycles of atomic collective-spin states. *Phys. Rev. A* **77**, 033810 (2008). URL `http://link.aps.org/doi/10.1103/PhysRevA.77.033810`.

[129] Christensen, S. L. *et al.* Toward quantum state tomography of a single polariton state of an atomic ensemble. *New J. Phys.* **15**, 015002 (2013). URL `http://stacks.iop.org/1367-2630/15/i=1/a=015002`.

[130] Casabone, B. *et al.* Heralded entanglement of two ions in an optical cavity. *Phys. Rev. Lett.* **111**, 100505 (2013). URL `https://link.aps.org/doi/10.1103/PhysRevLett.111.100505`.

[131] McConnell, R. *et al.* Generating entangled spin states for quantum metrology by single-photon detection. *Phys. Rev. A* **88**, 063802 (2013). URL `http://link.aps.org/doi/10.1103/PhysRevA.88.063802`.

[132] McConnell, R., Zhang, H., Hu, J., Cuk, S. & Vuletic, V. Entanglement with negative Wigner function of almost 3,000 atoms heralded by one photon. *Nature* **519**, 439–442 (2015). URL `http://dx.doi.org/10.1038/nature14293`.

[133] Christensen, S. L. *et al.* Quantum interference of a single spin excitation with a macroscopic atomic ensemble. *Phys. Rev. A* **89**, 033801 (2014). URL `http://link.aps.org/doi/10.1103/PhysRevA.89.033801`.

[134] Chen, W. *et al.* Carving complex many-atom entangled states by single-photon detection. *Phys. Rev. Lett.* **115**, 250502 (2015). URL `http://link.aps.org/doi/10.1103/PhysRevLett.115.250502`.

[135] Welte, S., Hacker, B., Daiss, S., Ritter, S. & Rempe, G. Cavity carving of atomic Bell states. *Phys. Rev. Lett.* **118**, 210503 (2017). URL `https://link.aps.org/doi/10.1103/PhysRevLett.118.210503`.

[136] Davis, E. J., Wang, Z., Safavi-Naeini, A. H. & Schleier-Smith, M. H. Painting nonclassical states of spin or motion with shaped single photons. *Phys. Rev. Lett.* **121**, 123602 (2018). URL `https://link.aps.org/doi/10.1103/PhysRevLett.121.123602`.

[137] Dür, W., Vidal, G. & Cirac, J. I. Three qubits can be entangled in two inequivalent ways. *Phys. Rev. A* **62**, 062314 (2000). URL `http://link.aps.org/doi/10.1103/PhysRevA.62.062314`.

[138] Shi, B.-S. & Tomita, A. Teleportation of an unknown state by *W* state. *Phys. Lett. A* **296**, 161 – 164 (2002). URL `http://www.sciencedirect.com/science/article/pii/S0375960102002578`.

[139] Agrawal, P. & Pati, A. Perfect teleportation and superdense coding with *W* states. *Phys. Rev. A* **74**, 062320 (2006). URL `http://link.aps.org/doi/10.1103/PhysRevA.74.062320`.

[140] Zheng, S.-B. Splitting quantum information via *W* states. *Phys. Rev. A* **74**, 054303 (2006). URL `http://link.aps.org/doi/10.1103/PhysRevA.74.054303`.

[141] Sames, C. *et al.* Antiresonance phase shift in strongly coupled cavity QED. *Phys. Rev. Lett.* **112**, 043601 (2014). URL `https://link.aps.org/doi/10.1103/PhysRevLett.112.043601`.

[142] Reimann, R. *et al.* Cavity-modified collective Rayleigh scattering of two atoms. *Phys. Rev. Lett.* **114**, 023601 (2015). URL `https://link.aps.org/doi/10.1103/PhysRevLett.114.023601`.

[143] Grimsmo, A. L. *Controlling the quantum state of light and matter with cavity QED*. Ph.D. thesis, Norwegian University of Science and Technology (2014).

[144] Nagy, D., Szirmai, G. & Domokos, P. Critical exponent of a quantum-noise-driven phase transition: The open-system Dicke model. *Phys. Rev. A* **84**, 043637 (2011). URL `https://link.aps.org/doi/10.1103/PhysRevA.84.043637`.

[145] Leroux, I. D., Schleier-Smith, M. H. & Vuletić, V. Orientation-dependent entanglement lifetime in a squeezed atomic clock. *Phys. Rev. Lett.* **104**, 250801 (2010). URL `https://link.aps.org/doi/10.1103/PhysRevLett.104.250801`.

[146] Sau, J. D., Leslie, S. R., Cohen, M. L. & Stamper-Kurn, D. M. Spin squeezing of high-spin, spatially extended quantum fields. *New J. Phys.* **12**, 085011 (2010). URL `http://stacks.iop.org/1367-2630/12/i=8/a=085011`.

[147] Vitagliano, G., Hyllus, P., Egusquiza, I. L. & Tóth, G. Spin squeezing inequalities for arbitrary spin. *Phys. Rev. Lett.* **107**, 240502 (2011). URL `https://link.aps.org/doi/10.1103/PhysRevLett.107.240502`.

[148] Vitagliano, G., Apellaniz, I., Egusquiza, I. L. & Tóth, G. Spin squeezing and entanglement for an arbitrary spin. *Phys. Rev. A* **89**, 032307 (2014). URL `http://link.aps.org/doi/10.1103/PhysRevA.89.032307`.

[149] Duan, L.-M., Cirac, J. I. & Zoller, P. Quantum entanglement in spinor Bose-Einstein condensates. *Phys. Rev. A* **65**, 033619 (2002). URL `http://link.aps.org/doi/10.1103/PhysRevA.65.033619`.

[150] Zhang, Z. & Duan, L.-M. Generation of massive entanglement through an adiabatic quantum phase transition in a spinor condensate. *Phys. Rev. Lett.* **111**, 180401 (2013). URL `http://link.aps.org/doi/10.1103/PhysRevLett.111.180401`.

[151] Sun, H., Xu, P., Pu, H. & Zhang, W. Efficient generation of many-body singlet states of spin-1 bosons in optical superlattices. *Phys. Rev. A* **95**, 063624 (2017). URL `https://link.aps.org/doi/10.1103/PhysRevA.95.063624`.

[152] Feldmann, P. *et al.* Interferometric sensitivity and entanglement by scanning through quantum phase transitions in spinor Bose-Einstein condensates. *Phys. Rev. A* **97**, 032339 (2018). URL `https://link.aps.org/doi/10.1103/PhysRevA.97.032339`.

[153] Kajtoch, D., Pawłowski, K. & Witkowska, E. Metrologically useful states of spin-1 Bose condensates with macroscopic magnetization. *Phys. Rev. A* **97**, 023616 (2018). URL `https://link.aps.org/doi/10.1103/PhysRevA.97.023616`.

[154] Lücke, B. *et al.* Twin matter waves for interferometry beyond the classical limit. *Science* **334**, 773 (2011). URL `http://science.sciencemag.org/content/334/6057/773.abstract`.

[155] Gross, C. *et al.* Atomic homodyne detection of continuous-variable entangled twin-atom states. *Nature* **480**, 219–223 (2011). URL `http://dx.doi.org/10.1038/nature10654`.

[156] Hoang, T. M. *et al.* Dynamic stabilization of a quantum many-body spin system. *Phys. Rev. Lett.* **111**, 090403 (2013). URL `http://link.aps.org/doi/10.1103/PhysRevLett.111.090403`.

[157] Peise, J. *et al.* Satisfying the Einstein–Podolsky–Rosen criterion with massive particles. *Nat. Commun.* **6**, 8984 (2015). URL `http://dx.doi.org/10.1038/ncomms9984`.

[158] Hoang, T. M. *et al.* Parametric excitation and squeezing in a many-body spinor condensate. *Nat. Commun.* **7**, 11233 (2016). URL `http://dx.doi.org/10.1038/ncomms11233`.

[159] Hoang, T. M. *et al.* Adiabatic quenches and characterization of amplitude excitations in a continuous quantum phase transition. *Proc. Natl. Acad. Sci. USA* **113**, 9475–9479 (2016). URL `http://www.pnas.org/content/113/34/9475.abstract`.

[160] Huang, X. Y., Sun, F. X., Zhang, W., He, Q. Y. & Sun, C. P. Spin-orbit-coupling-induced spin squeezing in three-component Bose gases. *Phys. Rev. A* **95**, 013605 (2017). URL `http://link.aps.org/doi/10.1103/PhysRevA.95.013605`.

[161] Morrison, S. & Parkins, A. S. Dynamical quantum phase transitions in the dissipative Lipkin-Meshkov-Glick model with proposed realization in optical cavity QED. *Phys. Rev. Lett.* **100**, 040403 (2008). URL `https://link.aps.org/doi/10.1103/PhysRevLett.100.040403`.

[162] Morrison, S. & Parkins, A. S. Collective spin systems in dispersive optical cavity QED: Quantum phase transitions and entanglement. *Phys. Rev. A* **77**, 043810 (2008). URL `https://link.aps.org/doi/10.1103/PhysRevA.77.043810`.

[163] Davis, E. J., Bentsen, G., Homeier, L., Li, T. & Schleier-Smith, M. H. Photon-mediated spin-exchange dynamics of spin-1 atoms. *Phys. Rev. Lett.* **122**, 010405 (2019). URL `https://link.aps.org/doi/10.1103/PhysRevLett.122.010405`.

[164] Marino, J., Shchadilova, Y. E., Schleier-Smith, M. & Demler, E. A. Spectrum, landau–zener theory and driven-dissipative dynamics of a staircase of photons. *New Journal of Physics* **21**, 013009 (2019). URL `https://doi.org/10.1088%2F1367-2630%2Faaf825`.

[165] Carmichael, H. J. *An Open Systems Approach to Quantum Optics*, vol. 18 of *Lecture Notes in Physics* (Springer-Verlag Berlin Heidelberg, 1993).

[166] Haine, S. A. Information-recycling beam splitters for quantum enhanced atom interferometry. *Phys. Rev. Lett.* **110**, 053002 (2013). URL `https://link.aps.org/doi/10.1103/PhysRevLett.110.053002`.

[167] Szigeti, S. S., Tonekaboni, B., Lau, W. Y. S., Hood, S. N. & Haine, S. A. Squeezed-light-enhanced atom interferometry below the standard quantum limit. *Phys. Rev. A* **90**, 063630 (2014). URL `https://link.aps.org/doi/10.1103/PhysRevA.90.063630`.

[168] Tonekaboni, B., Haine, S. A. & Szigeti, S. S. Heisenberg-limited metrology with a squeezed vacuum state, three-mode mixing, and information recycling. *Phys. Rev. A* **91**, 033616 (2015). URL `https://link.aps.org/doi/10.1103/PhysRevA.91.033616`.

[169] Haine, S. A. & Szigeti, S. S. Quantum metrology with mixed states: When recovering lost information is better than never losing it. *Phys. Rev. A* **92**, 032317 (2015). URL `https://link.aps.org/doi/10.1103/PhysRevA.92.032317`.

[170] Haine, S. A. & Lau, W. Y. S. Generation of atom-light entanglement in an optical cavity for quantum enhanced atom interferometry. *Phys. Rev. A* **93**, 023607 (2016). URL `https://link.aps.org/doi/10.1103/PhysRevA.93.023607`.

[171] Masson, S. J., Barrett, M. D. & Parkins, S. Cavity QED engineering of spin dynamics and squeezing in a spinor gas. *Phys. Rev. Lett.* **119**, 213601 (2017). URL `https://link.aps.org/doi/10.1103/PhysRevLett.119.213601`.

[172] Kawaguchi, Y. & Ueda, M. Spinor Bose–Einstein condensates. *Phys. Rep.* **520**, 253–381 (2012). URL `http://www.sciencedirect.com/science/article/pii/S0370157312002098`.

[173] Stamper-Kurn, D. M. & Ueda, M. Spinor Bose gases: Symmetries, magnetism, and quantum dynamics. *Rev. Mod. Phys.* **85**, 1191–1244 (2013). URL `https://link.aps.org/doi/10.1103/RevModPhys.85.1191`.

[174] Law, C. K., Pu, H. & Bigelow, N. P. Quantum spins mixing in spinor Bose-Einstein condensates. *Phys. Rev. Lett.* **81**, 5257–5261 (1998). URL `http://link.aps.org/doi/10.1103/PhysRevLett.81.5257`.

[175] Pu, H., Law, C. K., Raghavan, S., Eberly, J. H. & Bigelow, N. P. Spin-mixing dynamics of a spinor Bose-Einstein condensate. *Phys. Rev. A* **60**, 1463–1470 (1999). URL `https://link.aps.org/doi/10.1103/PhysRevA.60.1463`.

[176] Schmaljohann, H. *et al.* Dynamics of $F = 2$ spinor Bose-Einstein condensates. *Phys. Rev. Lett.* **92**, 040402 (2004). URL `http://link.aps.org/doi/10.1103/PhysRevLett.92.040402`.

[177] Chang, M.-S. *et al.* Observation of spinor dynamics in optically trapped ^{87}Rb Bose-Einstein condensates. *Phys. Rev. Lett.* **92**, 140403 (2004). URL `http://link.aps.org/doi/10.1103/PhysRevLett.92.140403`.

[178] Chang, M.-S., Qin, Q., Zhang, W., You, L. & Chapman, M. S. Coherent spinor dynamics in a spin-1 Bose condensate. *Nat Phys* **1**, 111–116 (2005). URL `http://dx.doi.org/10.1038/nphys153`.

[179] Kronjäger, J. *et al.* Evolution of a spinor condensate: Coherent dynamics, dephasing, and revivals. *Phys. Rev. A* **72**, 063619 (2005). URL `http://link.aps.org/doi/10.1103/PhysRevA.72.063619`.

[180] Sadler, L. E., Higbie, J. M., Leslie, S. R., Vengalattore, M. & Stamper-Kurn, D. M. Spontaneous symmetry breaking in a quenched ferromagnetic spinor Bose-Einstein condensate. *Nature* **443**, 312–315 (2006). URL `http://dx.doi.org/10.1038/nature05094`.

[181] Black, A. T., Gomez, E., Turner, L. D., Jung, S. & Lett, P. D. Spinor dynamics in an antiferromagnetic spin-1 condensate. *Phys. Rev. Lett.* **99**, 070403 (2007). URL `https://link.aps.org/doi/10.1103/PhysRevLett.99.070403`.

[182] Liu, Y. *et al.* Quantum phase transitions and continuous observation of spinor dynamics in an antiferromagnetic condensate. *Phys. Rev. Lett.* **102**, 125301 (2009). URL `http://link.aps.org/doi/10.1103/PhysRevLett.102.125301`.

[183] Leslie, S. R. *et al.* Amplification of fluctuations in a spinor Bose-Einstein condensate. *Phys. Rev. A* **79**, 043631 (2009). URL `https://link.aps.org/doi/10.1103/PhysRevA.79.043631`.

[184] Klempt, C. *et al.* Multiresonant spinor dynamics in a Bose-Einstein condensate. *Phys. Rev. Lett.* **103**, 195302 (2009). URL `http://link.aps.org/doi/10.1103/PhysRevLett.103.195302`.

[185] Klempt, C. *et al.* Parametric amplification of vacuum fluctuations in a spinor condensate. *Phys. Rev. Lett.* **104**, 195303 (2010). URL `http://link.aps.org/doi/10.1103/PhysRevLett.104.195303`.

[186] Anquez, M. *et al.* Quantum Kibble-Zurek mechanism in a spin-1 Bose-Einstein condensate. *Phys. Rev. Lett.* **116**, 155301 (2016). URL `http://link.aps.org/doi/10.1103/PhysRevLett.116.155301`.

[187] Payrits, M. & Barnett, R. Quantum rotor theory of systems of spin-2 bosons. *Phys. Rev. A* **94**, 023605 (2016). URL `https://link.aps.org/doi/10.1103/PhysRevA.94.023605`.

[188] Pu, H. & Meystre, P. Creating macroscopic atomic Einstein-Podolsky-Rosen states from Bose-Einstein condensates. *Phys. Rev. Lett.* **85**, 3987–3990 (2000). URL `https://link.aps.org/doi/10.1103/PhysRevLett.85.3987`.

[189] Müstecaplıoğlu, O. E., Zhang, M. & You, L. Spin squeezing and entanglement in spinor condensates. *Phys. Rev. A* **66**, 033611 (2002). URL `https://link.aps.org/doi/10.1103/PhysRevA.66.033611`.

[190] Scherer, M. *et al.* Spontaneous breaking of spatial and spin symmetry in spinor condensates. *Phys. Rev. Lett.* **105**, 135302 (2010). URL `https://link.aps.org/doi/10.1103/PhysRevLett.105.135302`.

[191] Urizar-Lanz, I., Hyllus, P., Egusquiza, I. L., Mitchell, M. W. & Tóth, G. Macroscopic singlet states for gradient magnetometry. *Phys. Rev. A* **88**, 013626 (2013). URL `https://link.aps.org/doi/10.1103/PhysRevA.88.013626`.

[192] Cabello, A. N-particle N-level singlet states: Some properties and applications. *Phys. Rev. Lett.* **89**, 100402 (2002). URL `https://link.aps.org/doi/10.1103/PhysRevLett.89.100402`.

[193] Damski, B. & Zurek, W. H. Dynamics of a quantum phase transition in a ferromagnetic Bose-Einstein condensate. *Phys. Rev. Lett.* **99**, 130402 (2007). URL `http://link.aps.org/doi/10.1103/PhysRevLett.99.130402`.

[194] Saito, H., Kawaguchi, Y. & Ueda, M. Kibble-Zurek mechanism in a quenched ferromagnetic Bose-Einstein condensate. *Phys. Rev. A* **76**, 043613 (2007). URL `http://link.aps.org/doi/10.1103/PhysRevA.76.043613`.

[195] Noh, C. & Angelakis, D. G. Quantum simulations and many-body physics with light. *Rep. Prog. Phys.* **80**, 016401 (2017). URL `http://stacks.iop.org/0034-4885/80/i=1/a=016401`.

[196] Behbood, N. *et al.* Generation of macroscopic singlet states in a cold atomic ensemble. *Phys. Rev. Lett.* **113**, 093601 (2014). URL `https://link.aps.org/doi/10.1103/PhysRevLett.113.093601`.

[197] Graß, T., Juliá-Díaz, B., Kuś, M. & Lewenstein, M. Quantum chaos in SU(3) models with trapped ions. *Phys. Rev. Lett.* **111**, 090404 (2013). URL `http://link.aps.org/doi/10.1103/PhysRevLett.111.090404`.

[198] Kronjäger, J., Sengstock, K. & Bongs, K. Chaotic dynamics in spinor Bose–Einstein condensates. *New J. Phys.* **10**, 045028 (2008). URL `http://stacks.iop.org/1367-2630/10/i=4/a=045028`.

[199] Yu, L. *et al.* Tunable two-axis spin model and spin squeezing in two cavities. *Chin. Phys. B* **25**, 050301 (2016). URL `http://stacks.iop.org/1674-1056/25/i=5/a=050301`.

[200] Douglas, J. S. *et al.* Quantum many-body models with cold atoms coupled to photonic crystals. *Nat. Photon.* **9**, 326–331 (2015). URL `http://dx.doi.org/10.1038/nphoton.2015.57`.

[201] Haldane, F. D. M. Nonlinear field theory of large-spin Heisenberg antiferromagnets: Semiclassically quantized solitons of the one-dimensional easy-axis Néel state. *Phys. Rev. Lett.* **50**, 1153–1156 (1983). URL `http://link.aps.org/doi/10.1103/PhysRevLett.50.1153`.

[202] Lidar, D. A., Chuang, I. L. & Whaley, K. B. Decoherence-free subspaces for quantum computation. *Phys. Rev. Lett.* **81**, 2594–2597 (1998). URL `https://link.aps.org/doi/10.1103/PhysRevLett.81.2594`.

[203] Bartlett, S. D., Rudolph, T. & Spekkens, R. W. Classical and quantum communication without a shared reference frame. *Phys. Rev. Lett.* **91**, 027901 (2003). URL `https://link.aps.org/doi/10.1103/PhysRevLett.91.027901`.

[204] Tóth, G. & Mitchell, M. W. Generation of macroscopic singlet states in atomic ensembles. *New J. Phys.* **12**, 053007 (2010). URL `http://stacks.iop.org/1367-2630/12/i=5/a=053007`.

[205] Hauke, P., Sewell, R. J., Mitchell, M. W. & Lewenstein, M. Quantum control of spin correlations in ultracold lattice gases. *Phys. Rev. A* **87**, 021601 (2013). URL `https://link.aps.org/doi/10.1103/PhysRevA.87.021601`.

[206] Chalopin, T. *et al.* Quantum-enhanced sensing using non-classical spin states of a highly magnetic atom. *Nat. Commun.* **9**, 4955 (2018). URL `https://doi.org/10.1038/s41467-018-07433-1`.

[207] Groiseau, C., Masson, S. J. & Parkins, S. *In preparation* .

[208] Ostermann, S., Piazza, F. & Ritsch, H. Spontaneous crystallization of light and ultracold atoms. *Phys. Rev. X* **6**, 021026 (2016). URL `https://link.aps.org/doi/10.1103/PhysRevX.6.021026`.

[209] Mivehvar, F., Piazza, F. & Ritsch, H. Disorder-driven density and spin self-ordering of a Bose-Einstein condensate in a cavity. *Phys. Rev. Lett.* **119**, 063602 (2017). URL `https://link.aps.org/doi/10.1103/PhysRevLett.119.063602`.

[210] Hamner, C. *et al.* Dicke-type phase transition in a spin-orbit-coupled Bose–Einstein condensate. *Nat. Commun.* **5**, 4023 (2014). URL `http://dx.doi.org/10.1038/ncomms5023`.

[211] Mezzacapo, A. *et al.* Digital quantum Rabi and Dicke models in superconducting circuits. *Sci. Rep.* **4**, 7482 (2014). URL `http://www.ncbi.nlm.nih.gov/pmc/articles/PMC4265784/`.

[212] Genway, S., Li, W., Ates, C., Lanyon, B. P. & Lesanovsky, I. Generalized Dicke nonequilibrium dynamics in trapped ions. *Phys. Rev. Lett.* **112**, 023603 (2014). URL `https://link.aps.org/doi/10.1103/PhysRevLett.112.023603`.

[213] Pedernales, J. S. *et al.* Quantum Rabi model with trapped ions. *Sci. Rep.* **5**, 15472 (2015). URL `http://dx.doi.org/10.1038/srep15472`.

[214] Lamata, L. Digital-analog quantum simulation of generalized Dicke models with superconducting circuits. *Sci. Rep.* **7**, 43768 (2017). URL `http://dx.doi.org/10.1038/srep43768`.

[215] Aedo, I. & Lamata, L. Analog quantum simulation of generalized Dicke models in trapped ions. *Phys. Rev. A* **97**, 042317 (2018). URL `https://link.aps.org/doi/10.1103/PhysRevA.97.042317`.

[216] Safavi-Naini, A. *et al.* Verification of a many-ion simulator of the Dicke model through slow quenches across a phase transition. *Phys. Rev. Lett.* **121**, 040503 (2018). URL `https://link.aps.org/doi/10.1103/PhysRevLett.121.040503`.

[217] Landig, R. *et al.* Quantum phases from competing short- and long-range interactions in an optical lattice. *Nature* **532**, 476–479 (2016). URL `http://dx.doi.org/10.1038/nature17409`.

[218] Mivehvar, F., Ostermann, S., Piazza, F. & Ritsch, H. Driven-dissipative supersolid in a ring cavity. *Phys. Rev. Lett.* **120**, 123601 (2018). URL `https://link.aps.org/doi/10.1103/PhysRevLett.120.123601`.

[219] Morales, A., Zupancic, P., Léonard, J., Esslinger, T. & Donner, T. Coupling two order parameters in a quantum gas. *Nat. Mater.* **17**, 686–690 (2018). URL `https://doi.org/10.1038/s41563-018-0118-1`.

[220] Gopalakrishnan, S., Lev, B. L. & Goldbart, P. M. Frustration and glassiness in spin models with cavity-mediated interactions. *Phys. Rev. Lett.* **107**, 277201 (2011). URL `https://link.aps.org/doi/10.1103/PhysRevLett.107.277201`.

[221] Strack, P. & Sachdev, S. Dicke quantum spin glass of atoms and photons. *Phys. Rev. Lett.* **107**, 277202 (2011). URL `https://link.aps.org/doi/10.1103/PhysRevLett.107.277202`.

[222] Emary, C. & Brandes, T. Quantum chaos triggered by precursors of a quantum phase transition: The Dicke model. *Phys. Rev. Lett.* **90**, 044101 (2003). URL `http://link.aps.org/doi/10.1103/PhysRevLett.90.044101`.

[223] Emary, C. & Brandes, T. Chaos and the quantum phase transition in the Dicke model. *Phys. Rev. E* **67**, 066203 (2003). URL `http://link.aps.org/doi/10.1103/PhysRevE.67.066203`.

[224] Swingle, B., Bentsen, G., Schleier-Smith, M. & Hayden, P. Measuring the scrambling of quantum information. *Phys. Rev. A* **94**, 040302 (2016). URL `https://link.aps.org/doi/10.1103/PhysRevA.94.040302`.

[225] Gärttner, M. *et al.* Measuring out-of-time-order correlations and multiple quantum spectra in a trapped-ion quantum magnet. *Nat. Phys.* **13**, 781 (2017). URL `http://dx.doi.org/10.1038/nphys4119`.

[226] Bastidas, V. M., Emary, C., Regler, B. & Brandes, T. Nonequilibrium quantum phase transitions in the Dicke model. *Phys. Rev. Lett.* **108**, 043003 (2012). URL `https://link.aps.org/doi/10.1103/PhysRevLett.108.043003`.

[227] Cosme, J. G., Georges, C., Hemmerich, A. & Mathey, L. Dynamical control of order in a cavity-BEC system. *Phys. Rev. Lett.* **121**, 153001 (2018). URL `https://link.aps.org/doi/10.1103/PhysRevLett.121.153001`.

[228] Georges, C., Cosme, J. G., Mathey, L. & Hemmerich, A. Light-induced coherence in an atom-cavity system. *Phys. Rev. Lett.* **121**, 220405 (2018). URL `https://link.aps.org/doi/10.1103/PhysRevLett.121.220405`.

[229] Nagourney, W., Sandberg, J. & Dehmelt, H. Shelved optical electron amplifier: Observation of quantum jumps. *Phys. Rev. Lett.* **56**, 2797–2799 (1986). URL `http://link.aps.org/doi/10.1103/PhysRevLett.56.2797`.

[230] Bergquist, J. C., Hulet, R. G., Itano, W. M. & Wineland, D. J. Observation of quantum jumps in a single atom. *Phys. Rev. Lett.* **57**, 1699–1702 (1986). URL `http://link.aps.org/doi/10.1103/PhysRevLett.57.1699`.

[231] Sauter, T., Neuhauser, W., Blatt, R. & Toschek, P. E. Observation of quantum jumps. *Phys. Rev. Lett.* **57**, 1696–1698 (1986). URL `http://link.aps.org/doi/10.1103/PhysRevLett.57.1696`.

[232] Hunger, D. *et al.* A fiber Fabry–Perot cavity with high finesse. *New J. Phys.* **12**, 065038 (2010). URL `http://stacks.iop.org/1367-2630/12/i=6/a=065038`.

[233] Volz, J., Gehr, R., Dubois, G., Estève, J. & Reichel, J. Measurement of the internal state of a single atom without energy exchange. *Nature* **475**, 210–213 (2011). URL `http://dx.doi.org/10.1038/nature10225`.

[234] Ballance, T. G. *et al.* Cavity-induced backaction in Purcell-enhanced photon emission of a single ion in an ultraviolet fiber cavity. *Phys. Rev. A* **95**, 033812 (2017). URL `https://link.aps.org/doi/10.1103/PhysRevA.95.033812`.

[235] Groiseau, C., Masson, S. J. & Parkins, S. *Work in progress* .

[236] Liu, Y. & Houck, A. A. Quantum electrodynamics near a photonic bandgap. *Nat. Phys.* **13**, 48–52 (2016). URL `http://dx.doi.org/10.1038/nphys3834`.

[237] Hood, J. D. *et al.* Atom–atom interactions around the band edge of a photonic crystal waveguide. *Proc. Natl. Acad. Sci. USA* **113**, 10507–10512 (2016). URL `http://www.pnas.org/content/113/38/10507`.

[238] Chang, D. E., Douglas, J. S., González-Tudela, A., Hung, C.-L. & Kimble, H. J. Colloquium: Quantum matter built from nanoscopic lattices of atoms and photons. *Rev. Mod. Phys.* **90**, 031002 (2018). URL `https://link.aps.org/doi/10.1103/RevModPhys.90.031002`.

[239] Sundaresan, N. M., Lundgren, R., Zhu, G., Gorshkov, A. V. & Houck, A. A. Interacting qubit-photon bound states with superconducting circuits. *Phys. Rev. X* **9**, 011021 (2019). URL `https://link.aps.org/doi/10.1103/PhysRevX.9.011021`.